Université catholique de Louvain

Institute of Condensed Matter and Nanosciences

Molecular Chemistry, Materials, and Catalysis

Synthesis and Dehydrogenation of Novel N-substituted Ammonia Borane Derivatives

Dissertation submitted for the Degree of Doctor in Sciences

by

Ting Zhang

Supervisors: Prof. Yaroslav Filinchuk

Prof. Michel Devillers

Members of the Jury

Prof. Dr. Jean-François Gohy (UCLouvain, President)

Prof. Dr. Haiwen Li (Hefei General Machinery Research Institute, China)

Dr. Iurii Dovgaliuk (PSL University, France)

Prof. Dr. Sophie Hermans (UCLouvain)

Prof. Dr. Tom Leyssens (UCLouvain)

Prof. Dr. Michel Devillers (UCLouvain, Supervisor)

Prof. Dr. Yaroslav Filinchuk (UCLouvain, Supervisor)

Acknowledgments

Time has flown by faster than expected, and it is hard to believe that five years have passed since I embarked on my Ph.D. journey at UCLouvain. Looking back, I can confidently say that these years have been some of the best in my life, spent at this esteemed institution.

During this five-year period, there are many people whom I am immensely grateful to. First and foremost, I would like to express my deepest appreciation to my supervisors, Prof. Yaroslav Filinchuk and Prof. Michel Devillers for their exceptional supervision, guidance, suggestions, encouragement, and unwavering enthusiasm during my Ph.D. I am particularly indebted to them for their invaluable assistance and valuable suggestions in my research work and writing, which have played a crucial role in producing this thesis. Without their unwavering support and guidance, this thesis would have been an insurmountable challenge.

I would also like to extend my heartfelt gratitude to the members of my Ph.D. supervisory panel, Prof. Jean-François Gohy and Prof. Tom Leyssens, for their suggestions and great feedback to enhance the quality of my research. I would like to express my sincere thanks to all the jury members of my Ph.D. defense, Prof. Jean-François Gohy, Prof. Sophie Hermans, Prof. Tom Leyssens, Prof. Haiwen Li, and Dr. Iurii Dovgaliuk. Their willingness to serve on my Ph.D. defense jury and their dedicated efforts in carefully reviewing this thesis are deeply appreciated. I am truly grateful for their kindness, patience, and invaluable advice, which has greatly contributed to the improvement of both me and this thesis.

I am also indebted to Dr. Koen Robeyns, Dr. François Devred, and Dr. Jean-François Statsyns for their invaluable assistance in high-resolution powder X-ray diffraction measurements, thermal gravimetric analysis, and mass spectrometry, respectively. My heartfelt thanks go to all my colleagues, Anne-Christine Baudouin, Marie Claire Umutoni, Céline Brochier, Timothy Steenhaut, Xiao Li, Igor Golub, Jian Wang, Yuqin Fan, Robin Crits, Iago Maye, Fang Xia, Guillaume Esser, Guillaume Wéry, Camila Caro Garrido, Ting Wen,

Inna Kozak, Carole Body, and Joséphine de Meester. Their support, collaboration, and camaraderie have made my Ph.D. journey all the more enriching and enjoyable.

Furthermore, I would like to express my warm and special acknowledgment to my family and friends for their unwavering understanding, encouragement, and support throughout these five years. Their belief in me and their constant presence have provided me with the strength and motivation to embrace the challenges of my Ph.D. studies and enjoy a fulfilling work-life balance.

Last but not least, I would like to extend my gratitude to the China Scholarship Council (CSC) for awarding me the scholarship that made it possible for me to study in Belgium and pursue this Ph.D. I am also thankful to UCLouvain for their co-funding, which has further supported my academic journey.

With profound appreciation and heartfelt thanks to all, I sincerely acknowledge your significant contributions to my Ph.D. success.

Author's Contribution

The author and the supervisors Prof. Yaroslav Filinchuk and Prof. Michel Devillers have designed this project.

The author carried out the experiments, recorded the analytical data and interpreted the results that are presented in this thesis with the following exceptions:

Thermogravimetric analysis (TGA) were recorded by Dr. Xiao Li (Hefei General Machinery Research Institute, China), Dr. Timothy Steenhaut (UCLouvain), and Dr. Jean-François Statsyns (UCLouvain).

Mass spectrometry were recorded and analyzed by Dr. François Devred (UCLouvain) and Dr. Xiao Li (Hefei General Machinery Research Institute, China).

High-resolution powder X-ray diffraction (PXRD) was recorded by Dr. Koen Robeyns (UCLouvain).

All the crystal structures in this work were determined by Prof. Yaroslav Filinchuk (UCLouvain) together with the author.

List of abbreviations

˚: Degree
˚C: Celsius degree
K: Kelvin
T: Temperature
t: Time
h: Hour(s)
s: Second(s)
min: Minute
d: Distance
rt: Room temperature
a.u.: Arbitrary unit(s)
α: Alpha
β: Belta
γ: Gamma
δ: Delta
ζ: Zeta
λ: Lambda
Å: ångström
Θ: Theta
Rp: Profile Factor
Rwp: Weighted Profile Factor
Rexp: Expected Weighted Profile Factor
χ2: Reduced chi-square
wt.%: Weight percent
~: Approximate
>: More than
<: Less than
1st: First
2rd: Second
l: Liquid state

s: Solid state
HT: High temperature
LT: Light temperature
Temp.: temperature
1D: One-dimensional
2D: Two-dimensional
3D: Three-dimensional
QGA: Quantitative gas analyser
NMR: Nuclear magnetic resonance
MS: Mass spectrometry
PXRD: Powder X-ray diffraction
HR-PXRD: High-resolution powder X-ray diffraction
SR-PXRD: Synchrotron radiation powder X-ray diffraction
TGA: Thermalgravimetric analysis
DSC: Differential scanning calorimetry
ATR: Attenuated total reflectance
IR: Infrared radiation
FTIR: Fourier-transform infrared spectroscopy
TPD: Temperature programmed desorption
ESRF: European Synchrotron Radiation Facility in Grenoble
SNBL: Swiss-Norwegian Beamlines at the ESRF
M: Metal
MH: Metal hydrides
$M(AlH_4)_n$: Metal alanates
$M(NH_2)_n$: Metal amides
$M(BH_4)_n$: Metal borohydrides
MABs: Metal amidoboranes
$M(NH_2BH_3)_n$: Mono-metallic amidoboranes
$M_1[M_2(NH_2BH_3)_n]$: Bi-metallic amidoboranes
$[B_3N_2]^-$: $[BH_3NH_2BH_2NH_2BH_3]^-$
AB: Ammonia borane
MeAB: Methylamine borane
EDAB: Ethane-1,2-diamineborane
DETAB: Diethylenetriamine-borane
TETAB: Triethylenetetramine-borane

TEPAB: Tetraethylenepentamine-borane

1,2-TMDAB: 1,2-di-aminopropane-borane

1,2/1,3-TMDAB: 1,3-di-aminopropane-borane

NaEDAB: $NaBH_3NHCH_2CH_2NH_2BH_3$

RHCs: Reactive hydride composites

VB: 2,8,9-triisobutyl-2,5,8,9-tetraaza-1-phosphabicyclo [3.3.3] undecane

Me: Methyl group

$[Et_4N]$: Tetraethylammonium cation

$[Bu_4N]$: Tetrabutylammonium cation

$[C(N_3H_6)]$: Guanidinium cation

$[C(N_3H_5CH_3)]$: methylguanidinium cation

$NaN(SiMe_3)_2$: Sodium bis(trimethylsilyl)amide

$M[Al\{OC(CF_3)_3\}_4]$: metal perfluorinated tetraalkoxyaluminate

$Na[B_3(MeN)_2]$: $Na[BH_3(CH_3NH)BH_2(CH_3NH)BH_3]$

THF: Tetrahydrofuran

DSMO: Dimethylsulfoxide

MOFs: Metal organic frameworks

COFs: Covalent organic frameworks

DFT: Density functional theory

Abstract

Hydrogen is considered one of the most promising alternatives to fossil fuels as an energy carrier due to its high energy density and environmental friendliness and sustainability. However, a significant obstacle to the widespread application of hydrogen is the lack of a compact, safe, and cost-effective storage method. Solid hydrogen storage is regarded as a long-term solution among various hydrogen storage methods. Solid materials based on chemical sorption include interstitial hydrides, metal hydrides, complex hydrides, chemical hydrides, and reactive hydride composites, all of them have garnered significant attention due to their higher hydrogen content. Nevertheless, these solid materials possess both advantages and limitations for hydrogen storage. Regarding this thesis, the primary focus was on developing solid materials based on ammonia borane derivatives for hydrogen storage. This work is divided into two different but complementary approaches: 1) synthesis of ammonia borane derivatives solid materials for optimizing hydrogen storage properties by introducing functional groups on the nitrogen atoms, 2) understanding the relationship between material structure and hydrogen storage properties to establish new design principles of hydrogen storage materials.

In this thesis, the properties of ammonia borane derivatives were fine-tuned by introducing $-CH_3$ and $-CH_2CH_2-$ groups. A series of corresponding metallic complexes were synthesized through the optimized mechanochemical or solution syntheses, as discussed in Chapters 3-6. Chapter 3 and 5 focus on synthesis and hydrogen storage properties of compounds containing $-CH_3$ and $-CH_2CH_2-$ substituent on nitrogen atoms of the parent compound, $Na[BH_3NH_2BH_2NH_2BH_3]$. These substitutions effectively suppress the release of by-products such as NH_3, B_2H_6, and other large fragments. Consequently, these modifications significantly enhance the production of pure hydrogen. Notably, the derivative with $-CH_2CH_2-$ releases approximately 7.4 wt.% of pure hydrogen below 260°C. However, the impact of substitution with $-CH_3$ and $-CH_2CH_2-$ on the nitrogen atoms in

$Na[Al(NH_2BH_3)_4]$ on hydrogen storage properties is slightly different, as explored in Chapters 4 and 6. $Na[Al(CH_3NHBH_3)_4]$ exhibits significant mass loss upon heating. These results indicate the substituents on ammonia borane derivatives and the structure of metallic complexes, including all the specific network of intermolecular interactions, define together the hydrogen storage properties. This cooperative effect is also illustrated in Chapter 6, where the derivatives $Li[Al(BH_3NHCH_2CH_2NHBH_3)_2]$ and $Na[Al(BH_3NHCH_2CH_2NHBH_3)_2]$ featuring $-CH_2CH_2-$ substitutions, exhibit high ability to suppress the release of ammonia, diborane, and ethylenediamine. Specifically, $Li[Al(BH_3NHCH_2CH_2NHBH_3)_2]$ releases about 6.6 wt.% pure hydrogen below 280°C.

As with any complex materials, the optimization of ammonia borane derivatives for hydrogen storage inherently demands systematic control over multiple factors, encompassing the substitution patterns on ammonia borane, the choice of metal, and the intermolecular interactions. Our findings, however, unequivocally demonstrate that the introduction of $-CH_3$ and $-CH_2CH_2-$ groups onto nitrogen atoms of ammonia borane derivatives positively impacts hydrogen storage performance. This substitution helps to suppress the release of unwanted by-products such as NH_3 and B_2H_6. Therefore, the incorporation of alkyl-groups and the electron donating groups onto nitrogen atoms of NH_3BH_3 emerges as a promising strategy for optimizing the hydrogen storage properties of amidoboranes and their metal complexes.

Table of Contents

Acknowledgments ..... **III**

Author's Contribution ..... **V**

List of abbreviations ..... **VII**

Abstract ..... **XI**

Chapter 1 ..... **1**

Introduction **1**

1.1 Hydrogen: a promising energy carrier 1

1.2 Solid-state hydrogen storage systems 2

1.3 Interstitial Hydrides as chemisorption hydrogen storage materials 5

1.4 Magnesium hydride (MgH_2) as chemisorption hydrogen storage material 5

1.5 Complex/chemical hydrides as chemisorption hydrogen storage materials 7

1.5.1 Metal alanates 7

1.5.2 Metal amides 17

1.5.3 Metal borohydrides 21

1.5.4 B-N-H compounds 27

1.6 Reactive hydride composites (RHCs) 39

1.7 The objective of this thesis 43

1.8 Summary of this thesis 44

Chapter 2 ..... **61**

Methodology **61**

2.1 Mechanochemical synthesis 61

2.2 Powder X-ray diffraction 62

2.2.1 Fundamental principles of X-ray powder diffraction 62

2.2.2 Crystal structure determination from Powder X-ray Diffraction 67
2.3 Infrared spectra 68
2.4 NMR Spectroscopy 68
2.5 Thermal gravimetric analysis (TGA) 68
2.6 Mass spectrometry (MS) 69

Chapter 3 71

The synthesis, structure and hydrogen release of $Na[BH_3(CH_3NH)BH_2(CH_3NH)BH_3]$ 71

3.1 Introduction 72
3.2 The synthesis of $Na[BH_3(CH_3NH)BH_2(CH_3NH)BH_3]$ 75
3.3 The IR spectra of $Na[BH_3(CH_3NH)BH_2(CH_3NH)BH_3]$ 77
3.4 The structure of $Na[BH_3(CH_3NH)BH_2(CH_3NH)BH_3]$ 78
3.5 Thermal dehydrogenation of $Na[BH_3(CH_3NH)BH_2(CH_3NH)BH_3]$ 80
3.6 Conclusion 82
3.7 Experimental section 82
3.7.1 Chemicals 82
3.7.2 The formula of VB 82
3.7.3 The products of $NaH\text{-}NH_3BH_3$ in different molar ratio 83
3.7.4 Synthesis of $CH_3NH_2BH_3$ (MeAB) 83
3.7.5 Synthesis of $Na[BH_3(CH_3NH)BH_2(CH_3NH)BH_3]$ 83
3.7.6 Nuclear magnetic resonance (NMR) 84
3.7.7 PXRD measurement 84
3.7.8 Structure determination 84
3.7.9 Fourier transform infrared spectroscopy (FTIR) 86
3.7.10 Thermogravimetric analysis (TGA) 86
3.7.11 Mass spectrometry 87

Chapter 4 95

Aluminum methylamidoborane complexes: mechanochemical synthesis, structure, stability, and reactive hydride composites 95

4.1 Introduction 96
4.2 The synthesis and structure characterization of $Na[Al(CH_3NHBH_3)_4]$

.....98
4.3 Investigation of the reaction mechanism and isolation of the intermediate.....102
4.4 The thermal decomposition of Na[Al(CH_3NHBH_3)$_4$] 106
4.4.1 The stability of Na[Al(CH_3NHBH_3)$_4$] in air 106
4.4.2 The thermal decomposition of Na[Al(CH_3NHBH_3)$_4$].....106
4.5 The thermal dehydrogenation of RHCs based on Na[Al(CH_3NHBH_3)$_4$].....108
4.5.1 The thermal dehydrogenation of Na[Al(CH_3NHBH_3)$_4$] + 12NaH 108
4.5.2 The thermal dehydrogenation of Na[Al(CH_3NHBH_3)$_4$] + 6$NaNH_2$ 109
4.6 Conclusion..... 111
4.7 Experimental section 111
4.7.1 Chemicals 111
4.7.2 Synthesis of $CH_3NH_2BH_3$ (MeAB)..... 112
4.7.3 Synthesis of Na[Al(CH_3NHBH_3)$_4$]..... 112
4.7.4 Isolation of Na[AlH(CH_3NHBH_3)$_3$] 113
4.7.5 Powder X-ray diffraction (PXRD) 114
4.7.6 Crystal structure determination..... 114
4.7.7 Fourier-transform infrared spectroscopy (FTIR) 116
4.7.8 Thermogravimetric analysis (TGA) 116
4.7.9 Mass spectrometry..... 116

Chapter 5.....125

Enhancing Hydrogen (H_2) Release from Boron-nitrogen-hydrogen Metal Oligomers via Di-methylene Substitution.....125
5.1 Introduction.....126
5.2 Optimization of the reaction between NaH and EDAB.....128
5.3 Structure characterization of sample Na-ii 131
5.4 Thermal decomposition of sample Na-ii.....134
5.4.1 Stability of sample Na-ii in air 134
5.4.2 Thermal decomposition of sample Na-ii 134
5.5 Thermal dehydrogenation of sample Na-ii 136

5.6 Conclusion 137
5.7 Experimental section 137
5.7.1 Chemicals 137
5.7.2 Synthesis of $BH_3NH_2CH_2CH_2NH_2BH_3$ (EDAB) 137
5.7.3 Optimization of the reaction between NaH and EDAB. 138
5.7.4 Reaction between $NaNH_2$ and EDAB 139
5.7.5 Reaction between LiH and EDAB 140
5.7.6 The reaction between $LiNH_2$ and EDAB 142
5.7.7 Powder X-ray diffraction (PXRD) 143
5.7.8 Fourier transform infrared spectroscopy (FTIR) 143
5.7.9 Nuclear magnetic resonance (NMR) 144
5.7.10 Thermogravimetric analysis (TGA) 144
5.7.11 Mass spectrometry 144

Chapter 6 149

Synthesis, Structural Characterization, and Hydrogen Release of Al-Based Amidoboranes Derived from $MAlH_4$-EDAB 149
6.1 Introduction 150
6.2 The syntheses of four- and six-coordinated Al-based amidoboranes with EDAB 152
6.2.1 Synthesis of $Li[Al(BH_3NHCH_2CH_2NHBH_3)_2]$ 153
6.2.2 Synthesis of $Na[Al(BH_3NHCH_2CH_2NHBH_3)_2]$ 155
6.2.3 Attempted synthesis of $Li_3[Al(BH_3NHCH_2CH_2NHBH_3)_3]$ 162
6.2.4 Attempted synthesis of $Na_3[Al(BH_3NHCH_2CH_2NHBH_3)_3]$ 163
6.2.5 Attempted synthesis of $Na_2Li[Al(BH_3NHCH_2CH_2NHBH_3)_3]$ ... 165
6.3 Characterization of $M[Al(BH_3NHCH_2CH_2NHBH_3)_2]$ (M = Li, Na) .. 166
6.3.1 Structure of $Na[Al(BH_3NHCH_2CH_2NHBH_3)_2]$ 166
6.3.2 The IR spectra of $M[Al(BH_3NHCH_2CH_2NHBH_3)_2]$ (M = Li and Na) 168
6.4 Thermal decomposition of $M[Al(BH_3NHCH_2CH_2NHBH_3)_2]$ (M = Li, Na) 169
6.4.1 Stability of $Li[Al(BH_3NHCH_2CH_2NHBH_3)_2]$ in air 169
6.4.2 Thermal dehydrogenation of $Li[Al(BH_3NHCH_2CH_2NHBH_3)_2]$ 171
6.4.3 Stability of $Na[Al(BH_3NHCH_2CH_2NHBH_3)_2]$ in air 174

6.4.4 Thermal dehydrogenation of $Na[Al(BH_3NHCH_2CH_2NHBH_3)_2]$ 175
6.5 Conclusion 177
6.6 Experimental section 178
6.6.1 Chemicals 178
6.6.2 Synthesis of EDAB ($BH_3NH_2CH_2CH_2NH_2BH_3$) 178
6.6.3 Synthesis of Li_3AlH_6 178
6.6.4 Synthesis of Na_3AlH_6 179
6.6.5 Synthesis of Na_2LiAlH_6 179
6.6.6 Synthesis of $Li[Al(BH_3NHCH_2CH_2NHBH_3)_2]$ 180
6.6.7 Synthesis of $Na[Al(BH_3NHCH_2CH_2NHBH_3)_2]$ 180
6.6.8 Synthesis of $Li_3[Al(BH_3NHCH_2CH_2NHBH_3)_3]$ 181
6.6.9 Synthesis of $Na_3[Al(BH_3NHCH_2CH_2NHBH_3)_3]$ 182
6.6.10 Synthesis of $Na_2Li[Al(BH_3NHCH_2CH_2NHBH_3)_3]$ 183
6.6.11 Powder X-ray diffraction 183
6.6.12 Crystal structure determination 184
6.6.13 Fourier transform infrared spectroscopy (FTIR) 184
6.6.14 Thermogravimetric analysis (TGA) 184
6.6.15 Mass spectrometry 185

Chapter 7 191

Attempts to synthesize $M_3[Al(NH_2BH_3)_6]$ 191
7.1 Introduction 192
7.2 Exploring the synthesis of $Li_3[Al(NH_2BH_3)_6]$ 193
7.3 Exploring the synthesis of $Na_3[Al(NH_2BH_3)_6]$ 197
7.4 Exploring the synthesis of $Na_2Li[Al(NH_2BH_3)_6]$ 200
7.5 Experimental section 202
7.5.1 Chemicals 202
7.5.2 Synthesis of Li_3AlH_6 202
7.5.3 Syntheses of Samples Li3Al-01 to Li3Al-14 202
7.5.4 Synthesis of Na_3AlH_6 205
7.5.5 Synthesis of $NaNH_2BH_3$ 205
7.5.6 Syntheses of Samples Na3Al-01 to Na3Al-14 206
7.5.7 Synthesis of Na_2LiAlH_6 208

7.5.8 Syntheses of Samples Na_2LiAl-01 to Na_2LiAl-04 208

Chapter 8 213

Conclusions and perspectives 213

8.1 General conclusions 213

8.2 Perspectives 215

Annex 219

Chapter 1

Introduction

1.1 Hydrogen: a promising energy carrier

The continued growth of the world population and economy, coupled with rapid urbanization, as well as the increasing standard of lifestyle have resulted in a rapidly increasing demand for energy. [1-3] However, the non-renewable fossil fuels such as coal, oil and natural gas are depleted and limited by geographical distribution. It was speculated that current fossil fuels servers can support a maximum of 40 years for oil, 60 years for natural gas and 200 years for coal if the world continues to consume fossil fuels at 2006 rates.[4] The development of alternative fuels is an urgent need to cope with the future energy demand when those classic fossil fuels become unavailable. In addition, the classic fossil fuels have an adverse effect on the environment as they release plenty of CO_2 when burned, which is causing greenhouse effect, climate change and global negative consequences.[5] Therefore, clean, renewable, sustainable energy sources are being actively searched for. The intermittent nature of renewable energies requires to find solutions for storage in a much large scale than for the currently used fossil-based model, which is capable to quickly satisfy demand, for example by burning natural gas.

Hydrogen is the most abundant element in the universe, and hydrogen molecule is the lightest colorless, odorless, flammable gas. Importantly, it has much higher energy content than that of most fuels (Table 1.1).[6] Unlike oil, natural gas and coal, hydrogen is environmentally friendly since water is the only exhaust product during conversion to energy. In addition, hydrogen can be generated from renewable sources such as hydro, wind, wave, solar, biomass and geothermal energy sources. For these reasons, hydrogen is considered as a key solution to the current prevailing energy challenge and planet-warming which threatens to cripple energy security and environmental safety worldwide.

Table 1.1 Comparison of some selected energy contents of fuels.[6]

Fuel	Energy contents [MJ/kg]	
	Lower heating value	**Higher heating value**
Gaseous hydrogen	119.96	141.88
Liquid hydrogen	120.04	141.77
Natural gas	47.13	52.21
Liquefied natural gas	46.6	50.14
Conventional gasoline	43.44	46.52
Reformulated or low-Sulfur gasoline	42.35	45.42
Conventional diesel	42.78	45.76
Low-Sulfur diesel	42.6	45.56
Coal (wet basis)	22.73	23.96
Bituminous coal (wet basis)	26.12	27.26
Coking coal (wet basis)	28.6	29.86
Methanol	20.09	22.88
Ethanol	26.95	29.84

1.2 Solid-state hydrogen storage systems

The development of hydrogen economy includes hydrogen production, hydrogen storage and hydrogen use. Currently, the main obstacle in its wide applications is the lack of methods to store hydrogen in a compact, safe, and cost-effective manner, due to its poor energy density by volume (0.0108 MJ/L)[7] under normal pressure and temperature condition. At present, compressed H_2 gas (30-70 MPa) and liquid hydrogen (20 K) are the currently accepted solutions, but solid-state hydrogen storage appears to be an interesting mid- and long-term alternative (Figure 1.1).

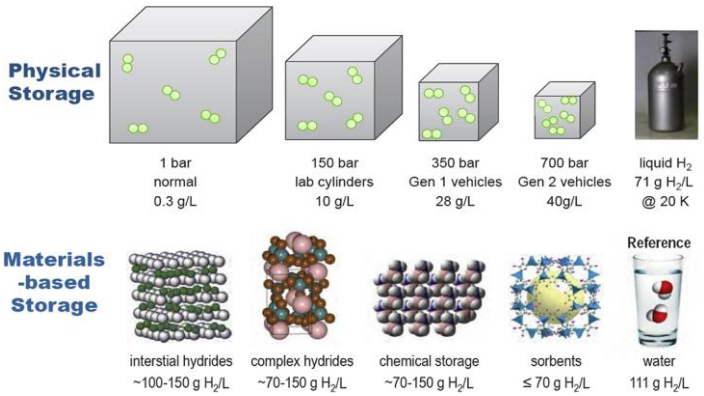

Figure 1.1 Compressed hydrogen vs. materials-based hydrogen storage.[2]

In solid-state storage systems, hydrogen is stored either by physisorption or chemisorption (Figure 1.3).[2, 6, 8] In physisorption, hydrogen does not dissociate, but binds to the surface of the materials by van der Waals interactions. This interaction is very weak, which makes the process of physisorption fast and reversible. Generally, these weak interactions occur in carbon materials[9, 10], zeolites[11], carbon nanotubes, on graphene[12], in metal organic frameworks (MOFs)[13-15] and covalent organic frameworks (COFs)[16]. Although many of the physisorption based materials have acceptable hydrogen storage capacities at cryogenic temperatures (77 K) and high pressures, their capacities drop to below 1 wt.% at ambient temperature and pressure in the range of 50-100 bar.

In chemisorption, hydrogen molecules are first dissociated on the surface and then migrate and form chemical bonds with metals/alloys. The hydrogen storage properties are widely characterized by the Pressure-Composition-Isotherm (PCI) curve, which includes three regions, as shown in Figure 1.2. The amount of absorbed hydrogen is measured with the hydrogen pressure increment at a given temperature. The hydrogen concentration increases with hydrogen pressure before it reaches the plateau pressure, appearing as a slope at the left side of plateau. At this region, the hydrogen concentration is relatively low and hydrogen atoms dissolve into the sublattice of metal/alloy to form a solid solution (α-phase). At higher hydrogen pressures, the hydride phase (β-phase) begins to form. The hydrogen concentration increases within the constant pressure region (plateau region), where the saturated α-phase is converted into the β-phase. The temperature-dependent plateau pressure represents the equilibrium dissociation pressure of the hydride (β-phase), serving as a measure of the hydride's stability. In other words, increasing the plateau pressure at a given temperature, in accordance with the van't Hoff equation, can reduce the thermodynamic stability of the hydride.

$$\frac{1}{2}\ln\left(\frac{P_T}{P_0}\right) = \frac{\Delta H}{RT} - \frac{\Delta S}{R}$$

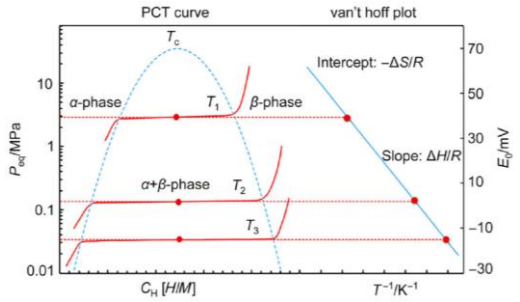

Figure 1.2 PCT curve (left) and van't Hoff plot (right).[19]

Compared with physisorption, materials based on chemisorption have high gravimetric storage capacities for hydrogen, but poor kinetics of dehydrogenation and high temperature required to release hydrogen. For instance, MgH_2 possesses 7.7 wt.% hydrogen but requires a temperature of about 300 °C. Each method has its cons and pros. To enable hydrogen to be stored in a solid-state materials-based system at ambient temperature with acceptable storage density, different strategies have been investigated and evaluated. For porous materials-based physisorption systems, research is focused on improving hydrogen storage capacities at closer to ambient temperatures. For metal/chemical hydrides-based chemisorption systems, research is focused on improving kinetics and thermodynamics of the investigated materials as well as developing new materials and catalysts that will enable the achievement of high storage capacities at significantly lower temperatures.

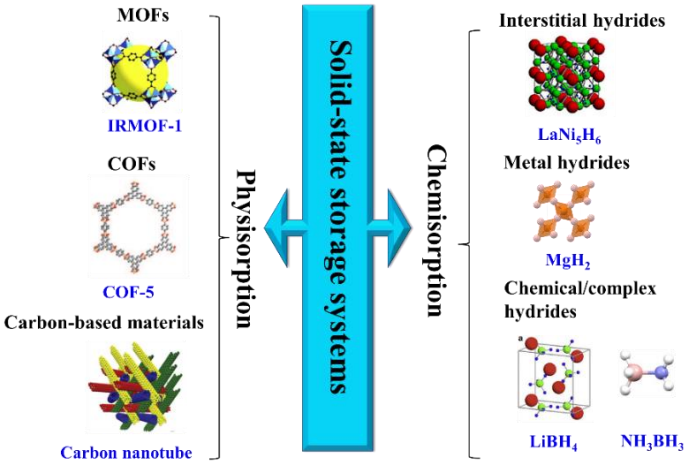

Figure 1.3 Classification of solid-state hydrogen storage systems.

1.3 Interstitial Hydrides as chemisorption hydrogen storage materials

Interstitial hydrides[6, 17-19] (also called hydrogen storage alloys) are composed of the hydride easily forming metals A (typically rare-earth or alkaline earth metal e.g., Ca, Ti, Y, Zr, Hf, La, Ce, etc.) and the non-hydride forming metals B (typically a transition metal ex. Cr, Mn, Fe). Unlike the covalent and/or ionic bond in the complex/chemical hydrides, in interstitial hydrides, hydrogen forms an alloy structure (but often with a significant contribution of covalent or ionic nature of metal-hydrogen interaction) with metal atoms by occupying the interstitial spaces of tetrahedral and/or octahedral sites in sublattice of interstitial hydrides. This makes the interstitial hydrides have lower hydrogen desorption temperature and faster kinetics compared to chemical/complex hydrides. Furthermore, the hydrogenation and de-hydrogenation processes of interstitial hydrides mainly depend on the dissociation and recombination on the surface and diffusion in the bulk of hydrogen atoms, whereas the metallic structure does not change significantly, which makes the interstitial hydrides have better cycling behavior than that of complex/chemical hydrides.

$LaNi_5H_6$ is one of the most studied interstitial hydrides for hydrogen storage. It can reversibly store 1.4 wt.% of hydrogen at room temperature.[20] AB_2 alloys, such as $TiCr_2$, $TiMn_{1.5}$, $ZrCr_2$, $ZrMn_2$ and ZrV_2, absorb more hydrogen than $LaNi_5$, and the maximum hydrogen capacity reaches 1.9 wt.% of hydrogen in $TiMn_{1.5}$.[19] BCC (body centered cubic structure) alloy like $Ti_{0.22}Cr_{0.39}V_{0.39}$ (Ti-Cr-V) absorbs and desorbs 2.2 wt.% of hydrogen at 296 K.[21] The limited gravimetric capacity and high cost of these materials hinder their widespread use in large-scale hydrogen storage applications.

1.4 Magnesium hydride (MgH_2) as chemisorption hydrogen storage material

MgH_2 attracted significant attention for hydrogen storage due to rich resources of magnesium, thus its low price, and high hydrogen storage capacity of its hydride (7.7 wt.%) and good reversibility. The de-hydrogenation of MgH_2 occurs slowly at 300–400 °C under atmospheric pressure, re-

hydrogenation can be achieved under over 3 MPa hydrogen pressure also at rather high temperatures of 300–400 °C. The high thermodynamic stability and sluggish dehydrogenation kinetics limit the further development of MgH_2.

To address these issues, various strategies have been explored to reduce thermodynamic stability and enhance the dehydrogenation kinetics of MgH_2:[23] 1). Catalyst doping: The introduction of catalysts, such as coating Mg with different transition metals (e.g., Ti, Nb, V, Co, Mo, or Ni) at the nanoscale to create a core-shell structure (Mg-TM)[22], was proven effective. Catalysts provide active sites for hydrogen absorption and desorption reactions, significantly accelerating these processes. This approach is the simplest and most effective way to improve kinetic performance. 2). Nano-engineering: Reducing the crystal grain size to the nanoscale promotes the Mg-H bond interaction process, disrupts the stability of the Mg-H bond and enhances thermodynamic performance of MgH_2. Additionally, numerous boundaries of nanostructures components can also accelerate the rate of hydrogen absorption and dehydrogenation thus enhancing the de/re-hydrogenation kinetics of MgH_2. 3). Metastable alloys Preparation: The high thermal stability of MgH_2 is mainly due to the strong Mg-H bond. Introducing other metal elements to replace some of the magnesium in MgH_2 to form Mg-M-H compounds (where 'M' represents other metals) can reduce the stability of the M-H bond, lower the reaction enthalpy of the compound, and enhance the thermodynamic properties of Mg-based hydrogen storage materials. This can lead to reductions in hydrogen absorption and dehydrogenation temperatures. For instance, Mg_2Ni had a reversible hydrogen storage capacity of 2.8 wt.%, and the enthalpy dropped from 75 kJ/mol to 64 kJ/mol;[24] 4). Composite Formation: Creating composites with light metal complexes like $LiBH_4$, $LiAlH_4$, and other metal hydrides (see sections 1.5.2, 1.5.3 and 1.6) can alter the reaction pathway. For example, the interface area between MgH_2 and $LiBH_4$ plays a key role in the nucleation and growth of LiH and MgB_2, affecting the dehydrogenation kinetics of MgH_2+0.5 $LiBH_4$ mixture and the storage capacity of H_2. However, the complexity of the reaction process, involving multiple steps and potential formation of irreversible substances, poses challenges and requires a detailed study of the hydrogen absorption and desorption mechanisms in composite systems. These approaches represent key strategies for mitigating the challenges associated with MgH_2 as a hydrogen

storage material.

1.5 Complex/chemical hydrides as chemisorption hydrogen storage materials

In contrast to interstitial hydrides, in complex/chemical hydrides, hydrogen is covalently bonded to central atoms. It includes a number of materials groups, such as metal alanates ($M(AlH_4)_n$), metal amides ($M(NH_2)_n$), metal borohydrides ($M(BH_4)_n$) and B-N-H compounds. Most of the complex/chemical hydrides are comprised of light elements and thus possess higher hydrogen capacity than all the above-mentioned ways of storage, which also attracted considerable attention to re-valuate or improve the hydrogen storage properties of the known complex hydrides or to synthesize the new ones. In this section, we will mainly introduce the hydrogen storage properties, as well as the synthesis and structure, of light metal alanates, light metal borohydrides and B-N-H compounds, all owing to their high hydrogen content and promising hydrogen storage performance.

1.5.1 Metal alanates

Metal alanates are also called metal aluminum hydrides, in which hydrogen is covalently bound to aluminum forming complex anions $[AlH_4]^-$ or $[AlH_6]^{3-}$. The known metal alanates include alkali, alkaline earth, rare earth and even transition metals aluminum hydrides, as shown in Figure 1.4. In this section, the general synthesis procedures, structure, thermodynamics, and hydrogen storage capacity of the alanates of Li, Na, K, Mg, Ca are mainly introduced, due to their high hydrogen content and mild hydrogen storage conditions. Additionally, double cation alanates are also presented and discussed.

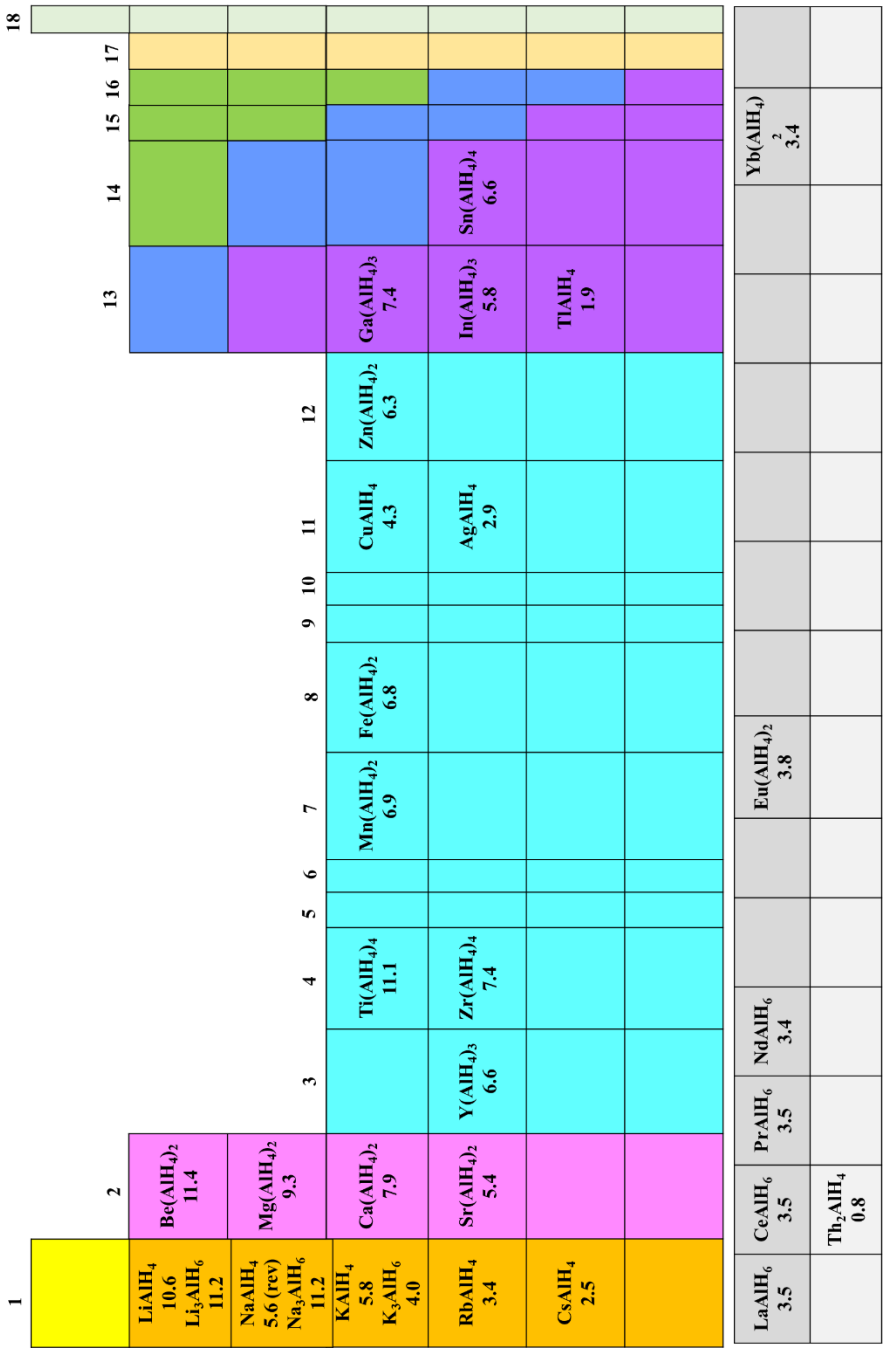

Figure 1.4 "Periodic table" of metal alanates, with hydrogen content in wt.%.[25-38]

1) Tetrahedrally coordinated aluminum-based metal hydrides

Li, Na, K, Mg and Ca alanates with high hydrogen content (>5.5 wt.%) reveal that Al is tetrahedrally coordinated. In these complexes, aluminum is covalently bonded to four hydrogen atoms (Figure 1.5), and more electropositive metals counterbalance the charge of the complex anion, while having different coordination numbers. To obtain a more precise hydrogen position and bond length between Al and H, and M and H, powder neutron diffraction data were used to determine the structure of almost all metal alanates using $M(AlD_4)_n$ instead of $M(AlH_4)_n$.

$LiAlH_4$ and $NaAlH_4$ are commercially available, which favors the synthesis of other metal alanates by metathesis reaction between $LiAlH_4$/$NaAlH_4$ and metal halides in organic solvents. The structures of $LiAlH_4$ include α-[26], β- and γ-$LiAlH_4$[27] polymorphs. The high-pressure phases have higher hydrogen density, however the high transition pressures of these two phases (26-71.5 kbar for α-$LiAlH_4$ to β-$LiAlH_4$, 338 kbar for β-$LiAlH_4$ to γ-$LiAlH_4$), limit the application in hydrogen storage. Here we mainly describe the structure of α-$LiAlH_4$ ($LiAlD_4$). The structure of α-$LiAlD_4$ was determined by powder neutron diffraction and this compound is found to crystallize in the space group $P2_1/c$. The Al-D distances average 1.616 Å at 295 K. The Li-D distances range from 1.831 to 1.978 Å at 295 K and from 1.841 to 1.978 Å at 8 K (see Table 1.2). $NaAlH_4$ crystallizes in a tetragonal unit cell with space group $I4_1/a$.[28] In $NaAlH_4$, the central Al^{3+} ions are tetrahedrally coordinated by four H and the Na atoms are surrounded by eight H-atoms from $[AlH_4]^-$ tetrahedra in a distorted square antiprismatic geometry. The Al-D distances were found to be 1.626 and 1.627 Å at 8 and 295 K, respectively based on the powder neutron diffraction data at 8 K and 295 K. And the Na-D bond distances were nearly equal, 2.403 and 2.405 Å at 8 K and 2.431 and 2.439 Å at 295 K.[39]

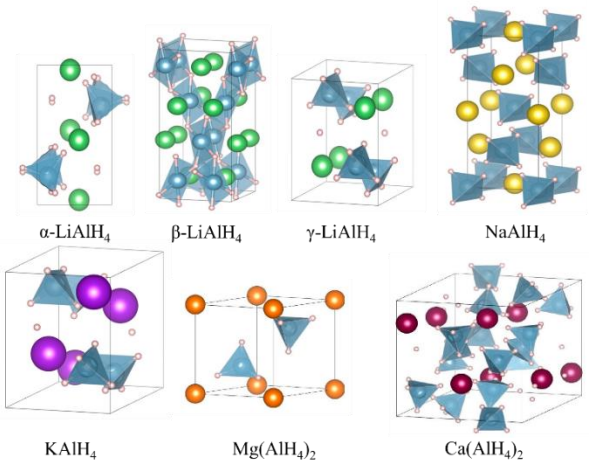

Figure 1.5 Crystal structure of Li, Na, K, Mg and Ca alanates.[25-30,41]

$KAlH_4$ can be prepared through one-step synthesis in organic solvents or directly in a powder form using KH and Al under high hydrogen pressure and temperature of 543 K. Like Li/$NaAlD_4$, neutron diffraction experiments at 8 K and 295 K were used to determine the structure of $KAlD_4$. $KAlD_4$ has a $BaSO_4$-type structure with space group *Pnma*. The structure (Figure 1.5) consists of isolated $[AlD_4]^-$ tetrahedra in which potassium atoms are surrounded by seven of the tetrahedra (ten D atoms in total). The average Al-D distance is 1.631 Å at 8 K and 1.618 Å at 295 K. The minimum Al-Al distance between the tetrahedra is 4.052 Å at 295 K. The shortest K-D distance is 2.596 Å at 295 K (larger than the Na-D distance in $NaAlD_4$ and the Li-D distance in $LiAlD_4$).

Many different synthetic methods were proposed to obtain $Mg(AlH_4)_2$. Among them, the synthesis method of Fichtner and Fuhr[40] based on the metathesis reaction between $NaAlH_4$ and $MgCl_2$ was mainly followed because the pure $Mg(AlH_4)_2$ could be obtained. The crystal structure of $Mg(AlH_4)_2$ is trigonal with space group *P*3*m*1. The tetrahedral $[AlH_4]^-$ groups are coordinated to Mg atoms in a distorted octahedral geometry, giving a sheet-like structure along the crystallographic *c*-axis. The Al-H distances range from 1.606 to 1.634 Å at 8 K and from 1.561 to 1.672 Å at 295 K. These distances are in the same range as those found for lithium, sodium, and potassium alanates.

As with $Mg(AlH_4)_2$, $Ca(AlH_4)_2$ can be synthesized through the metathesis reaction between $NaAlH_4$ or $LiAlH_4$ and $CaCl_2$ in an organic solvent or by

mechanical milling. The latter is nowadays popular due to the complicated purification aiming to avoid a decomposition of the alanate obtained by a solution method. The structure of $Ca(AlD_4)_2$[41] takes an orthorhombic $Ca(BF_4)_2$-type structure in the space group *Pbca*. The Ca atom is surrounded by eight D atoms in a distorted square antiprism with Ca–D distances of 2.199–2.333 Å such that each corner in the square antiprism is shared by one AlD_4 tetrahedron. The AlD_4 tetrahedra (Figure 1.5) in $Ca(AlD_4)_2$ are formed from two crystallographically different Al atoms (Al1 and Al2) with Al–D distances between 1.598 and 1.639 Å and D–Al–D angles in the range 104.5(8)–115.4(7)◦. Although the AlD_4 tetrahedra are slightly distorted, the Al–D distances are similar to other alanates.

Table 1.2 Parameters of $LiAlH_4$, $NaAlH_4$, $KAlH_4$, $Mg(AlH_4)_2$ and $Ca(AlH_4)_2$.[39, 42]

Compound	Space group	Al-D length (average) Å at 295 K and 8 K		M-D distance Å at 295 K and 8 K	
α-$LiAlH_4$	*P*2$_1$/*c*	1.616	1.622	1.831-1.978	1.841-1.978
$NaAlH_4$	*I*4$_1$/*a*	1.626	1.627	2.431-2.439	2.403-2.405
$KAlH_4$	*Pnma*	1.618	1.631	2.596-3.182	2.627-3.137
$Mg(AlH_4)_2$	*P*3*m*1	1.617	1.620	1.833	1.870
$Ca(AlH_4)_2$	*Pbca*	1.603/1.620 (room temperature)		2.199-2.34 (room temperature)	

The thermal dehydrogenation of $LiAlH_4$ goes through three steps and one phase transition at 160-177 ˚C before the first thermal dehydrogenation event. The three thermal decomposition reactions occur as shown in Table 1.3 The first dehydrogenation process was determined to be exothermic at 187-218 ˚C, which makes the re-hydrogenation nonspontaneous under all conditions. A second dehydrogenation reaction was observed to occur at 228-282 ˚C and to be endothermic. The two processes provide for a hydrogen release of 7.9 wt.%. The dehydrogenation on the third step occurs in the range of 370-483 ˚C, which is beyond any practical hydrogen storage operational temperature. It was found that ball milling and the use of additives like $TiCl_3$, VCl_3, etc[43] can enhance the hydrogenation kinetics of $LiAlH_4$. For instance, $LiAlH_4$ could be transformed into Li_3AlH_6 and Al at room temperature upon the addition of 3

mol % $TiCl_4$ upon 5 min of mechanical milling[44]; the addition of a few mole percent VCl_3 can also reduce the thermal decomposition temperature of $LiAlH_4$ by 60 °C[43]; and the doped Li_3AlH_6 with 2 mol % $TiCl_3$ can convert to LiH and Al at temperatures as low as 100 °C.[45]

The thermal decomposition of undoped $NaAlH_4$ goes through several steps, like $LiAlH_4$ (Table 1.3).[46] $NaAlH_4$ transforms to Na_3AlH_6 at 185–230 ˚C and releases about 3.7 wt.% of hydrogen. Further elimination of hydrogen (~1.9 wt.%) to give Al and NaH occurs at ~260 ˚C. And the dehydrogenation of NaH occurs only at temperatures over 400 ˚C, which is too high for technical applications.[47] Besides the thermal decomposition of the hydride also involves the melting of $NaAlH_4$ at about 183 ˚C and the conversion of pseudo-cubic α-Na_3AlH_6 to face-centered cubic β-Na_3AlH_6 (Table 1.3).[42]

It was found that the activation energies for the first two steps transforming $NaAlH_4$ first to Na_3AlH_6 and then to Al are 118 and 124 kJ/mol H_2[48], respectively. And the formation of Na_3AlH_6 from $NaAlH_4$ takes place in 3 h at 210–220 ˚C, while to obtain an appreciable speed for the dissociation of the newly formed compound, temperatures higher than 250 ˚C are required.[49, 50] Concerning the re-hydrogenation, a complete conversion from NaH and Al to $NaAlH_4$ was achieved in 3 h under 175 bar of hydrogen pressure at 270 ˚C.[51] Considering the practical application these two steps are too slow and require rather high temperatures. To enhance the hydrogen storage performance of $NaAlH_4$, various types of catalysts have been used. In summary, the catalysts not only enhance the de-/re-hydrogenation kinetics and cycling performances of $NaAlH_4$ but also reduce the activation energies of the composite sample compared to undoped $NaAlH_4$. For instance, to enhance the dehydrogenation kinetics, the system of $NaAlH_4$ + 7 mol% Ti[52] desorbs a large amount of hydrogen, with a total capacity of ~3.5 wt.% in 180 min, whereas undoped $NaAlH_4$ only desorbed a small amount of hydrogen (0.25 wt.%); the CeB_6-doped $NaAlH_4$[53] sample absorbs around 4.9 wt.% of hydrogen within 20 min at 120 ˚C. After 15 cycles, the doped sample still exhibited a high H-capacity of 4.5 wt.%, with ultrafast kinetics. To enhance the cyclability of the de- and re-hydrogenation of $NaAlH_4$, Srivinisan et al.[54] and Sun et al[55] found that a $Ti(OBu^n)_4$-doped sample revealed good cyclability. The Ti-doped $NaAlH_4$ sample maintained a high hydrogen capacity of 4.0 wt.% for the first two dehydrogenation steps after completing the 40th cycle, showing

remarkable reproducibility. This outcome was in good agreement with the study of Sun and co-workers. They found that the initial capacity of the sample was 3.6 wt.%, and after completing the 100th cycle, the hydrogen capacity only decreased slightly to 3.0 wt.% without showing degradation trends after completing the 100th cycle, which showed that only a small degradation occurred. The reduction of the activation energy resulted in lower temperature for the release of hydrogen. For instance, 7 mol % $MnFe_2O_4$-doped $NaAlH_4$[56] sample significantly reduced the temperatures of the desorption steps to 95 ˚C, 152 ˚C and 327 ˚C, which are lower by 84 ˚C, 88 ˚C and 84 ˚C, respectively, compared to the undoped $NaAlH_4$ in the three-decomposition step process. In addition, the activation energies of the NbF_5-$NaAlH_4$[57] sample were 88.2 and 102.9 kJ/mol, which are lower than for the pristine $NaAlH_4$, showing a significant reduction of the kinetic barriers. From the temperature programmed desorption (TPD) data, the NbF_5-doped sample showed a reduction of 71 ˚C for the first two dehydrogenation steps compared to the pristine $NaAlH_4$. The pristine $NaAlH_4$ started to decompose over 200 ˚C, the dehydrogenation process was completed at around 300 ˚C, and the NbF_5-doped sample decomposed at around 120 ˚C and completed at around 229 ˚C.

$KAlH_4$ has an acceptable total hydrogen content of 5.8 wt.% and a reversible hydrogen storage capacity of 4.3 wt.% without catalysts addition over a temperature range 250–340 °C under <10 bar of hydrogen. Morioka et al.[58] proposed the dehydrogenation mechanism as the equations in Table 1.3, based on the temperature programmed desorption (TPD) analyses. The addition of $TiCl_3$, or salts, such as NaCl and LiCl were able to modify the reaction kinetics.[59]

In contrast to Li, Na, K alanates, the dehydrogenation of $Mg(AlH_4)_2$[60] (Table 1.3) showed that the $[AlH_6]_3^-$ as an intermediate phase did not form but transformed directly into MgH_2 at about 163 °C during the first step. And the obtained MgH_2 undergoes further dehydrogenation at 287 °C to produce magnesium metal that will react with aluminum at 400 °C to give Al_3Mg_2. It was found that the dehydrogenation temperature can be reduced by additional milling,[61] the addition of materials,[62, 63] such as TiF_4, TiF_3, and Ti, or the reduction of particle size.[64] The re-hydrogenation is partially achieved by the formation of MgH_2 instead of $Mg(AlH_4)_2$.

$Ca(AlH_4)_2$ has a total hydrogen content of 7.9 wt.%. This is not the same

result for the thermal decomposition of $Ca(AlH_4)_2$ samples because there is always a by-product mixed with $Ca(AlH_4)_2$ obtained by the currently used synthesis methods. Weidenthaler and co-workers found that $Ca(AlH_4)_2$ complete decomposition occurs in four steps as shown below (Table 1.3) and the first two steps liberate 5.2–5.9 wt.% of hydrogen of the theoretical 7.2 wt.% for $Ca(AlH_4)_2$ + 2NaCl system.[65] Adding TiF_3 decreased the decomposition temperature for the first two-step decomposition reactions to 116 °C and 218 °C respectively, and activation energy for the second step decreases to 96 kJ/mol.[66]

Table. 1.3 The thermal dehydrogenation of $LiAlH_4$, $NaAlH_4$, $KAlH_4$, $Mg(AlH_4)_2$ and $Ca(AlH_4)_2$ (all the reactions occurred under inert atmosphere).

Compound (hydrogen content)	Reaction
$LiAlH_4$ (10.6 wt.%)	$LiAlH_4\ (s) \longrightarrow LiAlH_4\ (l)$ (160-177°C)
	$LiAlH_4 \longrightarrow 1/3\ Li_3AlH_6 + 2/3\ Al + H_2\uparrow$ (187-281°C; 5.3 wt.%)
	$1/3\ Li_3AlH_6 \longrightarrow LiH + 1/3\ Al + 3/2\ H_2\uparrow$ (228-282°C; 2.6 wt.%)
	$LiH + Al \longrightarrow LiAl + 1/2\ H_2\uparrow$ (370-483°C; 2.6 wt.%)
$NaAlH_4$ (7.5 wt.%)	$NaAlH_4\ (s) \longrightarrow NaAlH_4\ (l)$ (~183°C)
	$NaAlH_4 \longrightarrow 1/3\ Na_3AlH_6 + 2/3\ Al + H_2\uparrow$ (185-230°C; 3.7 wt.%)
	$NaAlH_4\ (\alpha) \longrightarrow NaAlH_4\ (\beta)$ (~250°C)
	$1/3\ Na_3AlH_6 \longrightarrow NaH + 1/3\ Al + 3/2\ H_2\uparrow$ (260°C; 1.9 wt.%)
	$NaH \longrightarrow Na + 1/2\ H_2\uparrow$ (435°C; 1.9 wt.%)
$KAlH_4$ (5.8 wt.%)	$KAlH_4 \longrightarrow 1/3\ K_3AlH_6 + 2/3\ Al + H_2\uparrow$ (300°C; 2.9 wt.%)
	$1/3\ K_3AlH_6 \longrightarrow KH + 1/3\ Al + 3/2\ H_2\uparrow$ (340°C; 1.4 wt.%)
	$KH \longrightarrow K + 1/2\ H_2\uparrow$ (430°C; 1.4 wt.%)
$Mg(AlH_4)_2$ (9.3 wt.%)	$Mg(AlH_4)_2 \longrightarrow MgH_2 + 2\ Al + 3\ H_2\uparrow$ (110-200°C; 7 wt.%)
	$MgH_2 \longrightarrow Mg + H_2\uparrow$ (240-380°C; 2.3 wt.%)
	$2\ Al + Mg \longrightarrow 1/2\ Al_3Mg_2 + 1/2\ Al\uparrow$ (400°C)
$Ca(AlH_4)_2$ (7.9 wt.%)	$Ca(AlH_4)_2 \longrightarrow CaAlH_5 + Al + 3/2\ H_2\uparrow$ (100-160°C; 2.4 wt.%)
	$CaAlH_5 \longrightarrow CaH_2 + Al + 3/2\ H_2\uparrow$ (220-270°C; 2.8 wt.%)
	$CaH_2 + 4\ Al \longrightarrow Al_4Ca + H_2\uparrow$ (~ 350°C)
	$CaH_2 + Al_4Ca \longrightarrow 2\ Al_2Ca + H_2\uparrow$ (~ 400°C)

The bi-metallic alanates also show tetrahedral coordinated Al, as for instance in $LiMg(AlH_4)_3$ and $LiCa(AlH_4)_3$. As in the mono-metallic alanates, aluminum is covalently bound to four hydrogen atoms, and Li and Mg/Ca counterbalance the charge of the anion $[AlH_4]^-$ (Figure 1.6). $LiMg(AlH_4)_3$ and $LiCa(AlH_4)_3$ can be produced by the metathesis reaction between $LiAlH_4$ and $MgCl_2/CaCl_2$.

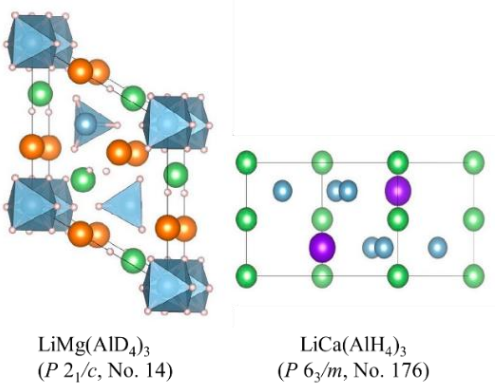

Figure 1.6 Crystal structures of $LiMg(AlD_4)_3$ and $LiCa(AlH_4)_3$.[31,32]

The $LiMg(AlH_4)_3$ has a hydrogen content of 9.7 wt.%. And its thermal decomposition occurs at 100-130 °C for the first step and at 150-180 °C for the second step. The addition of graphitic nanofibers can reduce the dehydrogenation temperatures. $LiCa(AlH_4)_3$ is an attractive hydrogen storage material too due to its high hydrogen content of 8.6 wt.%. $LiCa(AlH_4)_3$ (plus LiCl) starts decomposing at 120 °C and ends at about 180 °C. It was proposed that $LiCaAlH_6$ forms in the first de-hydrogenation step and converts to Al, CaH_2, and LiH in the second de-hydrogenation step. These two steps released 6 wt.% of hydrogen and there is no information regarding possible re-hydrogenation found.

2) Octahedrally coordinated aluminum in metal hydrides

The metal alanates showing six-coordinated geometry include the products of the first step of thermal decomposition of $MAlH_4$ (Li_3AlH_6, Na_3AlH_6 and K_3AlH_6)[33-35] and of mixed-cation alanates (Na_2LiAlH_6, K_2LiAlH_6, K_2NaAlH_6)[36-38] (Figure 1.7). All of them can be obtained through $MAlH_4$ and MH/M′H according to the following equation:

$$MAlH_4 + 2\,MH \longrightarrow M_3AlH_6$$

$$MAlH_4 + MH + M'H \longrightarrow M_2M'AlH_6$$

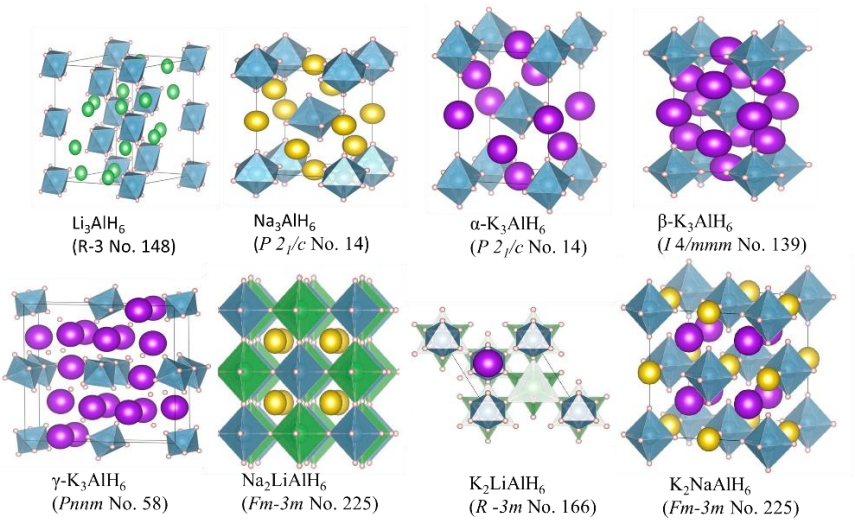

Figure 1.7 Crystal structures of some hexa-coordinated alanates.[33-38]

Na_2LiAlH_6 has a total hydrogen content of 7.03 wt.% and a theoretical reversible hydrogen storage of 3.51 wt.% (see the equation below). The de-hydrogenation of Na_2LiAlH_6 occurs between 190–250 °C and about 3.35 wt.% of hydrogen is released at the first step. Further hydrogen release involves NaH decomposition at 320–380 °C and finally the reaction of LiH with Al occurs at 380–480 °C with the formation of LiAl and H_2. It was demonstrated that the use of catalysts, such as TiF_3, $TiFe_3$, $TiCl_3$, CeO_2, $ZrCl_4$, $TiBr_4$, $CrCl_3$, $AlCl_3$, TiO_2, Y_2O_3, or $MnCl_2$ can enhance the reversibility of Na_2LiAlH_6. TiF_3 decreased the starting temperature of Na_2LiAlH_6 decomposition to ~50 °C.

$$Na_2LiAlH_6 \rightleftharpoons 2\,NaH + LiH + Al + 3/2\,H_2 \uparrow$$

K_2LiAlH_6 has a total hydrogen content of 5.11 wt.% and a reversible hydrogen storage of 2.56 wt.%. The de-hydrogenation of K_2LiAlH_6 was performed at 227 °C while re-hydrogenation was performed at 300 °C and up to 10 bar.

The only reported mixed Na-K alanate, K_2NaAlH_6, has a total hydrogen content of 4.46 wt.%. The decomposition occurs at about 352 °C and produces simple hydrides, Al and hydrogen gas. It was reported that K_2NaAlH_6

can show a partially reversible de-/re-hydrogenation. Also, the addition of $TiCl_3$, TiF_3, graphene, or carbon nanotubes slightly reduced the dehydrogenation temperature.

All in all, $NaAlH_4$ and $KAlH_4$ stand out among all the alanates due to their acceptable hydrogen content and reversibility. Metal alanates can not only be used as hydrogen storage materials directly, but also be precursors in synthesis of more complex Al-based solids, as for instance amidoboranes, like $Na[Al(NH_2BH_3)_4]$, $K[Al(NH_2BH_3)_4]$, which will be given more details in the section on B-N-H compounds.

1.5.2 Metal amides

Table 1.4 Dehydrogenation properties of some metal amide-based composites.

Composites	Hydrogen capacity (wt.%)	Dehydrogenation temperature (°C)		References
		Onset	Peak(s)	
$LiNH_2$-LiH	6.0 @ 200 °C	100	270	67
$LiNH_2$-2 LiH	6.5 @ 190 °C	-	245	67
2 $LiNH_2$-MgH_2	2.8 @ 210 °C	-	166	68
2 $LiNH_2$-3 MgH_2	6.4 @ 395 °C	190	-	69
2 $LiNH_2$-CaH_2	-	100	140, 206	68
$LiNH_2$-$LiBH_4$	11.7 @ 450 °C	170	295, 410	70, 71
2 $LiNH_2$-$LiBH_4$	10.2 @ 364 °C	220	324	72
3 $LiNH_2$-$LiBH_4$	10.3 @ 400 °C	270	378	73, 74
$LiNH_2$-$Mg(BH_4)_2$	11.4 @ 500 °C	160	216, 412	75
$LiNH_2$-$Ca(BH_4)_2$	8.0 @ 480 °C	150	281, 387	76, 77
2 $LiNH_2$-$Ca(BH_4)_2$	7.2 @ 480 °C	230	306, 396	76, 77
3 $LiNH_2$-$Ca(BH_4)_2$	7.6 @ 480 °C	240	315, 390	76, 77
4 $LiNH_2$-$Ca(BH_4)_2$	9.0 @ 480 °C	250	320	77
2 $NaNH_2$-3 MgH_2	5.0 @ 395 °C	130	-	69
2 $NaNH_2$-3 $LiBH_4$	5.1 @ 400 °C	50	330	78
$NaNH_2$-$NaBH_4$	7.0 @ 480 °C	290	-	79
2 $NaNH_2$-$NaBH_4$	6.86 @ 400 °C	124	346	80
$NaNH_2$-$Ca(BH_4)_2$	6.2 @ 400 °C	210	340, 418	81
$Mg(NH_2)_2$-2 LiH	4.5 @ 200 °C	100		82
3 $Mg(NH_2)_2$-8 LiH	7	140	190	83
$Mg(NH_2)_2$-4 LiH	6.5 @ 600 °C	146	-	84
$Mg(NH_2)_2$- $LiBH_4$	8.0 @ 340 °C	300	-	85
$Mg(NH_2)_2$- $Mg(BH_4)_2$	10.0 @ 450 °C	195	240,415	86
2 $Mg(NH_2)_2$- $Ca(BH_4)_2$	8.3 @ 480 °C	220	305	87
2 $Ca(NH_2)_2$- $Ca(BH_4)_2$	6.8 @ 480 °C	220	313	87

Metal amides, denoted as $M(NH_2)_n$ (where n represents the valence of a metal M, typically an alkali or alkaline-earth metal), do not release hydrogen when heated but ammonia gas. In order for hydrogen absorption/desorption to occur, metal amide is typically used in the form of a composite with other hydrides such as binary hydrides, metal borohydrides and metal alanates. Therefore, when discussing hydrogen storage, metal amide systems are commonly referred to as amide-hydrides composite systems, like those shown in above Table 1.4.

One of the most interesting systems, at present, is the system $LiNH_2$ + 2 LiH, studied by Ping in 2002.[88] The system of $LiNH_2$ + 2 LiH can be fully and reversibly desorbed and re-adsorbed at about 9.3 wt.% hydrogen below 300 ˚C according to the reaction equation shown below. On the contrary, pure lithium amide and lithium hydride, separately, decompose at temperatures above 300 ˚C and 550 ˚C, respectively.

$$LiNH_2 + 2\,LiH \rightleftharpoons Li_2NH + H_2 + LiH \rightleftharpoons Li_3N + 2\,H_2$$

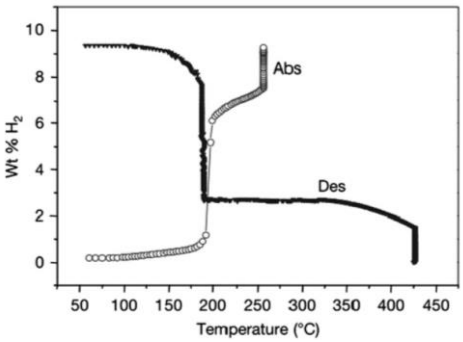

Figure 1.8 Weight variations during hydrogen absorption and desorption process over Li_3N samples. (Abs: absorption; Des: Desorption).[88]

Another interesting system is made of $LiNH_2$ and MgH_2 (or $Mg(NH_2)_2$ and LiH). Xiong et al.[68] heated lithium amide and magnesium hydride in a 2:1 molar ratio up to 350 ˚C, and, similar to the Li-N-H system, only hydrogen, without any ammonia, is desorbed. Thermal dehydrogenation of the system $2LiNH_2$ + MgH_2 occurred as the reaction shown below.

$$2\,LiNH_2 + MgH_2 \longrightarrow Li_2Mg(NH)_2 + 2\,H_2 \rightleftharpoons Mg(NH_2)_2 + 2\,LiH$$

$Li_2Mg(NH)_2$ can be re-hydrogenated under 90 bar of H_2 pressure at 180 ˚C. Upon cycling of the ternary imide, the XRD pattern showed that the

products are represented by $Mg(NH_2)_2$ and LiH rather than the original starting materials $LiNH_2$ and MgH_2. Later the hydrogen storage of the system $Mg(NH_2)_2$ + 2LiH was also reported. $Li_2Mg(NH)_2$ also formed upon dehydrogenation of ball-milled system $Mg(NH_2)_2$ + 2LiH at 250 ˚C with a considerable amount of hydrogen (5.0 wt.%) released.[82] It was also reported that $LiBH_4$ can significantly improve the de-hydrogenation/re-hydrogenation properties of the $Mg(NH_2)_2$–2LiH system. For example, 5 wt.% H_2 can be desorbed at 140 ˚C and fully reabsorbed at 100 ˚C. The rates of hydrogen desorption/absorption are 3 times as fast as those of the pristine system. They concluded that addition of $LiBH_4$ not only improved the kinetics but also changed the thermodynamics of Li–Mg–N–H system, because the $LiBH_4$ can react with $LiNH_2$ to form $Li_4(BH_4)(NH_2)_3$, which weakens the N-H bonds of $LiNH_2$ and changes the reaction path of Li–Mg–N–H.[89]

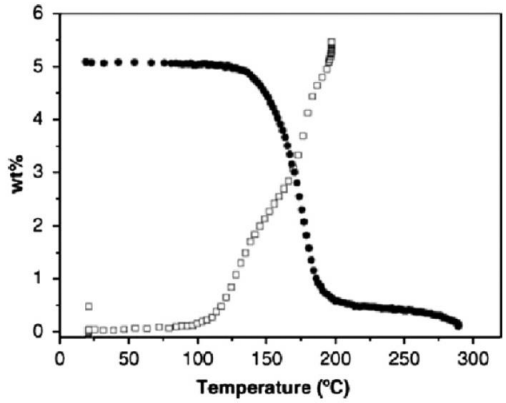

Figure 1.9 Hydrogen absorption in a $Li_2Mg(NH)_2$ sample and desorption from $Mg(NH_2)_2$–2LiH sample.[82]

For the $LiAlH_4$–$2LiNH_2$ system [90], more than 5 wt.% of hydrogen can be reversibly stored by Li_3AlN_2 by means of heating to 500 ˚C under 80 bar of hydrogen pressure (Figure 1.10). The whole dehydrogenation reaction can be expressed by the following equation:

$$2\ LiNH_2 + LiAlH_4 \longrightarrow (Li_3AlN_2H_4) + 2\ H_2 \longrightarrow Li_3AlN_2 + 4\ H_2$$

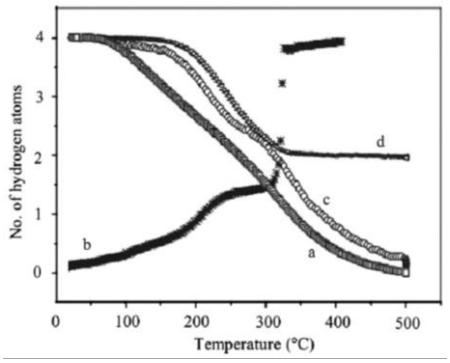

Figure 1.10 Volumetric measurements of: (a) hydrogen release from post-12h-milled $LiNH_2$–$LiAlH_4$ (2:1) sample; (b) hydrogen absorption over Li_3AlN_2; (c) hydrogen desorption from the fully hydrogenated Li_3AlN_2 sample and (d) hydrogen release from the $LiNH_2$–LiH (1:2) mixture.[90]

$NaNH_2$ and its composites have attracted a lot of attention too because of its considerable amount of hydrogen, low cost, and interesting thermodynamic properties. For example, Pecharsky et al.[69] reported that the $2NaNH_2 + 3MgH_2$ system released hydrogen in the temperature range of 130–400 ˚C with a total release of 5.1 wt.% at 400 ˚C in the following reaction. And 2.1 wt.% of hydrogen could be re-absorbed at 395 ˚C under 190 bars of hydrogen.

$$2\ NaNH_2 + 3\ MgH_2 \longrightarrow Mg_3N_2 + 2\ NaH + H_2$$

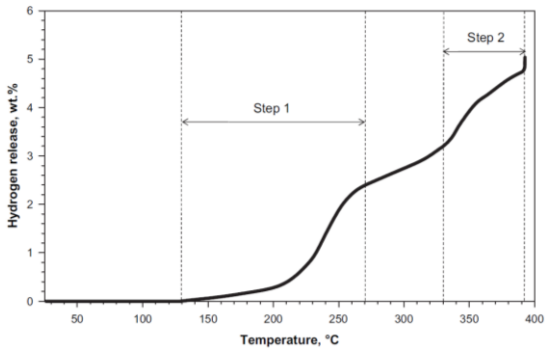

Figure 1.11 Temperature programmed decomposition of the $2NaNH_2$–$3MgH_2$ mixture.[69]

A further way to destabilize $NaNH_2$ to enhance the hydrogen storage properties is represented by the addition of metal borohydrides, such as $NaBH_4$, $Ca(BH_4)_2$ and $Mg(BH_4)_2$ in stochiometric amount.[80, 81, 91] For example,

the starting reagents $2NaNH_2$–$NaBH_4$ when subjected to intensive ball milling, react producing $Na_3(NH_2)_2BH_4$. This new phase desorbed hydrogen (6.85 wt. %) gas forming Na_3BN_2.[80] The desorption path is characterized by two main steps: the first in the temperature range 70–170 ˚C, while the second one between 190–420 ˚C. At higher temperatures, Na_3BN_2 decomposes to Na. Also mixed with metal alanates to improve the hydrogen storage properties of $NaNH_2$. For instance, Xiong et al. proved that during ball milling a solid-state interaction between $NaNH_2$ and $LiAlH_4$ took place, leading to the formation of the tetramide $Li_3Na(NH_2)_4$ which seems to favor the desorption at lower temperatures.[92]

Other combinations based on the metal amide were also studied for hydrogen storage, such as $LiAlH_4$/$NaAlH_4$ + $LiNH_2$, $LiBH_4$ + $LiNH_2$, $Ca(BH_4)_2$ + $NaNH_2$, $LiAlH_4$ + $Mg(NH_2)_2$ and so on.

1.5.3 Metal borohydrides

Metal borohydrides $M(BH_4)_n$ contain boron and hydrogen atoms forming negatively charged BH_4^-, counterbalanced by metal cations. Metal borohydrides include mono-metallic ($LiBH_4$, $Mg(BH_4)_2$, $Al(BH_4)_3$ and so on) and multi-metallic borohydrides (like $LiK(BH_4)_2$, $Na[Al(BH_4)_4]$, $KZn(BH_4)_3$ etc.). The multi-metallic borohydrides can be obtained by combining mono-metallic borohydrides or by the reaction of mono-metallic borohydrides with metal chlorides through metathesis reaction. The pure bimetallic borohydrides usually yield back the mono-metallic components upon thermal decomposition. The chloride-based products, however, are more difficult to study, as these systems involve a number of chloride-based phases, where borohydride-chloride solid-solutions are forming depending on the temperature. The mono-metallic borohydrides involve alkali, alkaline earth, transition, and rare-earth metal borohydrides, as shown in Figure 1.12. The heavier members have low hydrogen content, which limits the application for hydrogen storage. KBH_4 has considerable hydrogen content, while hydrogen releases only near 680 °C and few reports exist in how to improve its hydrogen storage properties. There are no complete studies about the hydrogen storage properties of $Be(BH_4)_2$, $Ti(BH_4)_3$, $Zr(BH_4)_4$, $Hf(BH_4)_4$, $Fe(BH_4)_2$ and $Al(BH_4)_3$, all having high hydrogen content. However, all of them are not very stable at room temperature. $V(BH_4)_3$ and $Mn(BH_4)_2$ have considerable hydrogen

content (12.7 wt.%, 9.5 wt.% respectively), while they are usually mixed with LiCl or NaCl, decreasing their hydrogen content. Therefore, we mainly introduced the hydrogen storage properties of mono-metallic borohydrides with lighter metals (Li, Na, Mg, Ca, and Y) due to their high hydrogen content and good stability at ambient conditions.

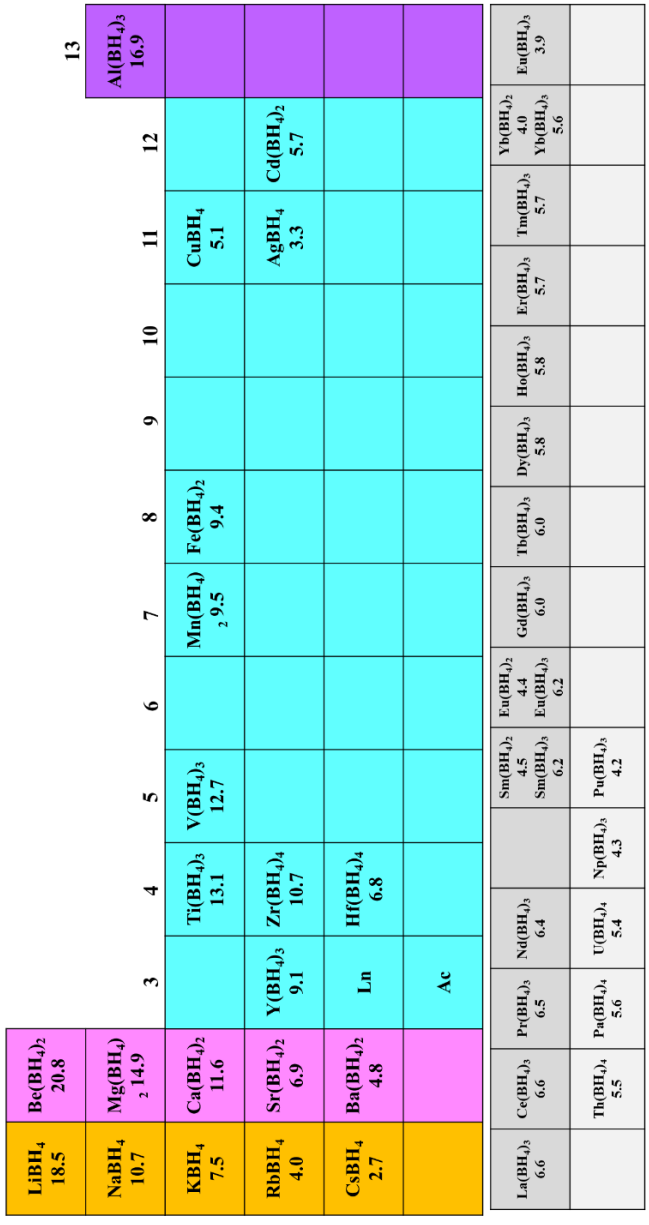

Figure 1.12 "Periodic table" of experimentally known mono-metallic borohydrides with hydrogen content in wt.%.[93, 94]

In general, metal borohydrides have high thermal stability, and generate highly inert elemental boron after full hydrogen release, which affects its reverse reaction to absorb hydrogen again. Therefore, a lot of efforts were focused on enhancing the thermodynamics and de-/re-hydrogenation kinetics of metal borohydrides, especially for Li, Na, Mg and Ca borohydrides, along the strategies introduced below. At present, Li, Na, Mg and Ca borohydrides are commercially available. Their structures, as well as for $Y(BH_4)_3$, including different phases, are shown in Table 1.5.

Table 1.5 Experimental structures of $LiBH_4$, $NaBH_4$, $Mg(BH_4)_2$, $Ca(BH_4)_2$ and $Y(BH_4)_3$.[95]

Compound	Space group	Stability
o-$LiBH_4$[96]	*Pnma*	RT
h-$LiBH_4$[96]	*P*6$_3$*mc*	>380 K
hp1-$LiBH_4$[97]	*Ama2*	RT, 1.2-10 GPa
hp2-$LiBH_4$[97]	*Fm*-3*m*	RT, >10 GPa
α-$NaBH_4$[98]	*Fm*-3*m*	RT
lt-$NaBH_4$[99]	*P*4$_2$/*nmc*	<190 K or RT, >6 GPa
hp-$NaBH_4$[100]	*Pnma*	>9 GPa
α-$Mg(BH_4)_2$[101, 102]	*P*6$_1$22	RT
β-$Mg(BH_4)_2$[103, 104]	*Fddd*	RT, metastable, HT polymorph
γ-$Mg(BH_4)_2$[105]	*Ia*-3*d*	RT, metastable
δ-$Mg(BH_4)_2$[105]	*P*4$_2$*nm*	RT, >2.1 GPa
ζ-$Mg(BH_4)_2$[106]	*P*3$_1$12	~ 500 K
α-$Ca(BH_4)_2$[107]	*F*2*dd*	RT
α'-$Ca(BH_4)_2$[107]	*I*-42*d*	>495 K
β-$Ca(BH_4)_2$[107, 108]	*P*-4	RT, metastable, HT polymorph
α-$Y(BH_4)_3$[109]	*Pa*-3	RT
β-$Y(BH_4)_3$[110]	*Fm*-3*c*	RT, HT polymorph

$LiBH_4$ has high gravimetric and volumetric hydrogen densities: 18.5 wt.% and 122 g/L[94], respectively, which attracted significate attention for hydrogen storage. Direct decomposition without the presence of intermediate compounds, leads to the production of boron, lithium hydride and release of 13.8 wt.% hydrogen, in the range of 380−680 °C under one bar of H_2 pressure as specified by the reaction below.[111] Partial dehydrogenation can also occur, forming lithium closo-borane, $Li_2B_{12}H_{12}$, via less endothermic reactions, as shown below.[95]

$$LiBH_4 \longrightarrow LiH + B + 3/2\ H_2\uparrow$$

$$LiBH_4 \longrightarrow 5/6\ LiH + 1/12\ Li_2B_{12}H_{12} + 13/12\ H_2\uparrow$$

The re-hydrogenation of $LiBH_4$ from LiH and B can be completed at 600 °C and 35 MPa for 12 h.[111] Although pure $LiBH_4$ is a high-capacity hydrogen storage material, it has high hydrogen absorption and desorption temperature, slow hydrogen releasing rate, and poor reversibility. Two common methods have been used to improve the hydrogen storage properties of $LiBH_4$. The rehydrogenation enthalpy of bulk $LiBH_4$ is estimated at -82 kJ/mol H_2[112], so the rehydrogenation is exothermic, but in reality, this process will require energy as the reaction mixture should be kept at high temperature and the hydrogen pressure should be very high to achieve an acceptable kinetics.

One is to thermodynamically destabilize $LiBH_4$ by adding metals, metal halides, oxides, amides or metal hydrides to form composite materials or alloys after dehydrogenation. Like, $LiBH_4$-1/2 MgH_2 system including 2-3 mol % $TiCl_3$, the dehydrogenation of this system proceeds as follows:

$$LiBH_4 + 1/2\ MgH_2 \longrightarrow LiH + 1/2\ MgB_2 + 2\ H_2\uparrow$$

This system reversibly stores 8-10 wt.% hydrogen. Isothermal measurements were performed in the range of 315–400 °C, the enthalpy of hydrogen lowers the hydrogenation/dehydrogenation enthalpy by 25 kJ/(mol of H_2) compared with pure $LiBH_4$.[113] This approach not only reduces the enthalpy of the dehydrogenation, which decreases the decomposition temperature, but also kinetically enhances the re-hydrogenation reaction. That is, in contrast to the formation of pure $LiBH_4$ (35 MPa, 600 °C), $LiBH_4$ and MgH_2 form simultaneously under fairly moderate conditions: 5 MPa hydrogen pressure and in the temperature range of 250–300 °C.[114]

Another method is to use catalysts or nanoconfinement, confining $LiBH_4$ in mesoporous scaffolds or mixing $LiBH_4$ with nanotubes or mesoporous gels etc. to improve the kinetics. Like, the $LiBH_4 + 0.2MgCl_2 + 0.1TiCl_3$ composite starts desorbing 5 wt.% of hydrogen at 60 °C and can be re-hydrogenated to 4.5 wt.% at 600 °C and 7 MPa.[115] And the nanoconfined $LiBH_4$ obtained from the confined LiH in graphene reacts with B_2H_6, and can dehydrogenate about

7.6 wt.% at 280 °C, and dehydrogenate about 9.7 wt.% within 60 min at 340 °C. After absorbing hydrogen at 320 °C and 100 bar, it still has 7.5 wt.% of capacity after five cycles of hydrogen absorption/desorption.[116]

$NaBH_4$ has 10.7 wt.% and 114 g/L[94] gravimetric and volumetric hydrogen density respectively. The evolution of hydrogen starts at lower temperatures (240 °C) and continues by several steps at different temperatures. The most significant H_2 emission starts at about 450 °C and continues at higher temperatures with a total of 10.4 wt.% of H_2 released, following the equation,

$$NaBH_4 \longrightarrow NaH + B + 3/2\ H_2\uparrow \longrightarrow Na + B + 2\ H_2\uparrow$$

At present, the methods to improve the performance of $NaBH_4$ include anion and cation substitution, chemical destabilization, catalysis, and particle size modification. For instance, Ngene et al. used the liquid melting method to obtain nano-$NaBH_4$ to achieve reversible hydrogen absorption and desorption performances. The initial hydrogen desorption temperature of nano sized $NaBH_4$ was reduced from 470 °C to below 250 °C, and the reactant after dehydrogenation can be re-hydrogenated to $NaBH_4$ under the condition of 60 bar H_2 and 325 °C. However, since the pores in this template are open, Na is volatile during the hydrogen evolution process, and only 43 % of hydrogen are stored during the cycle.[117]

The mass and volume hydrogen storage density of $Mg(BH_4)_2$ is 14.8 wt.% and 147.4 g/L[94], respectively. $Mg(BH_4)_2$ has a variety of crystal structures, and each crystal structure can transform into several others at certain pressure and temperature conditions. However, all crystal forms transform to high temperature stable β phase before hydrogen evolution, and this will lead to different crystal forms having little effect on its hydrogen absorption and desorption properties.

The decomposition of α-$Mg(BH_4)_2$ first undergoes a phase transition at 190°C, and then decomposes into MgH_2, Mg and MgB_2 with the increase of temperature to 290–500 °C.[118] The decomposition reaction is suggested as below:

$$Mg(BH_4)_2 \longrightarrow MgH_2 + 2B + 3\ H_2 \longrightarrow MgB_2 + 4\ H_2\uparrow$$

The decomposition mechanism of magnesium borohydride is quite complex and highly dependent on reaction conditions.[95] Amorphous or

nanocrystalline closo-borane, $MgB_{12}H_{12}$, was reported to be a major intermediate product during decomposition of $Mg(BH_4)_2$ in vacuum. However, the different reaction pathway occurred when $Mg(BH_4)_2$ was decomposed in dynamic vacuum in the temperature range 265 to 400 °C. $Mg(B_3H_8)_2$ was observed as the major decomposition product when $Mg(BH_4)_2$ was heated to 265 °C. Trace amounts of $Mg(B_3H_8)_2$ were observed after heating to 285 °C, and none of the boranes $Mg(BH_4)_2$, $Mg(B_3H_8)_2$ or $MgB_{12}H_{12}$ were observed in samples heated at T > 285 °C. Recently, MgB_4H_{10} was also proposed as an intermediate in the decomposition reaction.

$Mg(BH_4)_2$ has high thermodynamic stability and kinetic barrier due to the generation of stable intermediate(s) during its thermal decomposition. And $Mg(BH_4)_2$ can only be recovered under the conditions of 95 MPa and 400 °C, so much research focused on improving its hydrogen storage performance. A common method is adding transition metals or their compounds. Like Bardaji et al. combined $TiCl_3$ and $Mg(BH_4)_2$ into nanocomposite materials, and found that the initial hydrogen desorption temperature was reduced to above 100 °C; and further study shows that $Mg(BH_4)_2$ doped with $NbCl_5$–$TiCl_3$ nanocomposite could lead to that 5 wt.% hydrogen released while the dehydrogenation temperature was lowered below 300 °C. The cycle performance of $Mg(BH_4)_2$ was not improved by doping.[119] Investigation showed that adding NbF_5 into the composites can also lead to better hydrogen storage properties than pristine $Mg(BH_4)_2$ or the sample obtained by ball milling $LiBH_4$ and $MgCl_2$. The catalyzed composite starts to release hydrogen at about 120 °C with a total capacity of 10 wt.%. The reversibility of the catalytic composite was also improved, and the catalytic composite could still release 4 wt.% H_2 in the third and fourth cycles.[120]

Although researchers have tried various methods to improve the hydrogen storage performance of $Mg(BH_4)_2$, its initial hydrogen desorption temperature is still high, and the kinetic performance of $Mg(BH_4)_2$ at low temperature still needs to be improved.

The theoretical mass and volume hydrogen storage density of $Ca(BH_4)_2$ is 11.6 wt.% and 124.1 g/L[94], respectively, while 9.6 wt.% of hydrogen can practically be released. The decomposition of $Ca(BH_4)_2$ is a multi-step reaction process accompanied by the formation of various possible intermediates. The reaction equation is shown below. At 347–387 °C, $Ca(BH_4)_2$ decomposes to

form CaH_2 and some intermediate products, and at 397–497 °C, the intermediate products decompose to form amorphous B and CaB_6.

$$3\ Ca(BH_4)_2 \longrightarrow 2\ CaH_2 + CaB_6 + 10\ H_2\uparrow$$

Since it is a high-capacity hydrogen storage material, there is a potential to improve the performance of $Ca(BH_4)_2$ by introducing catalysts and or by other means. However, the dehydrogenation temperature still remains high and the purity of hydrogen in the released gas is not high enough.

The theoretical mass hydrogen storage density of $Y(BH_4)_3$ is 9.1 wt.%. It can be obtained through the metathesis synthesis[109] between YCl_3 and $LiBH_4$, or a gas–solid reaction[121] promoted by mechanical milling, avoiding the formation of LiCl, like in the reactions below:

$$YCl_3 + 3\ LiBH_4 \longrightarrow Y(BH_4)_3 + 3\ LiCl$$

$$YH_3 + 3/2\ B_2H_6 \longrightarrow Y(BH_4)_3$$

The $Y(BH_4)_3$ without LiCl starts decomposing at about 187 °C, and shows high decomposition rate at 250 °C with a 6.8 wt.% of total mass loss.[121]

The common metal borohydrides like $LiBH_4$, $NaBH_4$, $Mg(BH_4)_2$, and $Ca(BH_4)_2$ all have a high hydrogen capacity higher than 10 wt.%, which is much higher than that of the materials that have been practically applied. However, they still require high temperatures to release considerable amount of H_2 (> 6 wt.% at least), although numerous methods have been used to improve hydrogen storage performance.

1.5.4 B-N-H compounds

Compared to alanates and metal borohydrides, B-N-H compounds usually demonstrate a higher hydrogen capacity under a moderate thermal de-hydrogenation condition. A kind of typical representative of B-N-H materials is ammonia borane (NH_3BH_3, or AB) and its derivatives. NH_3BH_3 has one of the highest gravimetrical hydrogen contents (19.6 wt.%) among all known chemical compounds, possesses low toxicity and good stability under ambient conditions. However, its thermal decomposition proceeds in multiple steps, at around 120 °C, 200 °C and 500 °C, respectively, that are accompanied by the evolution of some toxic volatile by-products (B_2H_6, NH_3, $N_3B_3H_6$). The thermal decomposition of AB is furthermore paired with severe

foaming and volume expansion. Compared to being used as hydrogen storage material directly, it is better to be used as starting material for preparation of other hydrogen-rich compounds, like $M(NH_2BH_3)_n$ (mono-metallic amidoboranes) or $M_1[M_2(NH_2BH_3)_n]$ (bi-metallic amidoboranes). In this section, we will give a short account on $M(NH_2BH_3)_n$ and $M_1M_2(NH_2BH_3)_n$ from the synthesis, structure and hydrogen storage properties perspectives.

1) Mono-metallic amidoboranes

Table 1.6 Synthesis reactions to access MABs.

Compound	Reaction Equation
$LiNH_2BH_3$	$LiH + NH_3BH_3 \longrightarrow LiNH_2BH_3 + H_2\uparrow$
	$LiNH_2 + NH_3BH_3 \longrightarrow LiNH_2BH_3 + NH_3\uparrow$
	$RLi + NH_3BH_3 \longrightarrow LiNH_2BH_3 + RH$
$LiNH_2BH_3{\cdot}NH_3BH_3$	$LiH + 2\ NH_3BH_3 \longrightarrow LiNH_2BH_3{\cdot}NH_3BH_3 + H_2\uparrow$
	$LiNH_2BH_3 + NH_3BH_3 \longrightarrow LiNH_2BH_3{\cdot}NH_3BH_3$
$NaNH_2BH_3$	$NaH + NH_3BH_3 \longrightarrow NaNH_2BH_3 + H_2\uparrow$
	$NaNH_2 + NH_3BH_3 \longrightarrow NaNH_2BH_3 + NH_3\uparrow$
KNH_2BH_3	$KH + NH_3BH_3 \longrightarrow KNH_2BH_3 + H_2\uparrow$
	$K + NH_3BH_3 \longrightarrow KNH_2BH_3 + 1/_2\ H_2\uparrow$
$Mg(NH_2BH_3)_2$	$MgH_2 + 2\ NH_3BH_3 \longrightarrow Mg(NH_2BH_3)_2 + 2\ H_2\uparrow$
	$Mg + 2\ NH_3BH_3 \longrightarrow Mg(NH_2BH_3)_2 + H_2\uparrow$
	$Mg(BH_4)_2 + 2\ LiNH_3BH_3 \longrightarrow Mg(NH_2BH_3)_2 + 2\ LiBH_4$
	$MgI_2 + 2\ LiNH_3BH_3 \longrightarrow Mg(NH_2BH_3)_2 + 2\ LiI$
$Ca(NH_2BH_3)_2$	$CaH_2 + 2\ NH_3BH_3 \longrightarrow Ca(NH_2BH_3)_2 + 2\ H_2\uparrow$

The mono-metallic amidoboranes $M(NH_2BH_3)_n$ include M = Li (α- , β-phases and $LiNH_2BH_3{\cdot}NH_3BH_3$), Na, K, Rb, Cs, Mg, Ca, Sr, Ba, Y, Al, Zn. There are more studies for the mono-metallic amidoboranes with light metal amidoboranes and good stability in ambient conditions like Li, Na, K, Mg, Ca (hydrogen content is higher than 7 wt.%). $Zn(NH_2BH_3)_2$ is unstable at ambient condition, although it has 8.1 wt.% hydrogen content. $Y/Al(NH_2BH_3)_3$ were synthesized from MNH_2BH_3 and their chlorides, obtaining $Y/Al(NH_2BH_3)_3$

mixed with Y/$AlCl_3$, the latter caused the so called “dead mass” and further decreased the hydrogen content of these two systems.

Usually, $M(NH_2BH_3)_n$ (M = Li, Na, K, Mg, Ca) can be obtained simply from metal hydrides (MH) and AB through ball milling or vigorous stirring in solvents as shown in Table 1.6. One hydrogen atom connected with N atom of AB is replaced in the process, where the hydrogen atom can be exchanged on the interface of the two solid compounds. The specific synthesis reactions are also shown in Table 1.6.[122]

Table 1.7 Interatomic distances in crystal structures of amidoborane salts. Note that the positions of H atoms cannot be determined with large accuracy and thus the BH and NH bond lengths usually have much larger errors than those indicated in brackets. Presented data are rounded and shown without standard deviation.[122]

Compound	N-H (Å)	B-H (Å)	B-N (Å)	M-B (Å)	M-N (Å)
α-$LiNH_2BH_3$	1.03	1.24-1.25	1.55	2.51-2.97	2.06
β-$LiNH_2BH_3$	0.99	1.18-1.22	1.58-1.59	2.50-2.93	1.93-2.04
$LiNH_2BH_3{\cdot}NH_3BH_3$					
NH_3BH_3 unit	1.03-1.04	1.23	1.61	2.63	-
NH_2BH_3 unit	1.03	1.23	1.56	2.47	1.95
$NaNH_2BH_3$	1.04-1.05	1.29-1.32	1.56	2.68-2.93	2.14
KNH_2BH_3	0.78-1.05	1.08-1.26	1.53	3.28-3.59	2.91-3.36
$Ca(NH_2BH_3)_2$	1.04-1.10	1.25-1.32	1.55	3.00-3.18	2.47
NH_3BH_3 (HT)	0.85	1.11	1.58	-	-
NH_3BH_3 (LT)	0.96-1.07	1.15-1.18	1.58	-	-

$M(NH_2BH_3)_n$ (M = Li, Na, K, Mg, Ca) exhibit properties typical of protic–hydridic hydrogen storage materials, like their parent AB, because of the presence of $H^{\delta+}$ in NH_2 groups and $H^{\delta-}$ in BH_3 groups. The crystal structures of metal amidoboranes are often unprecedented and show great variety; this is due to a low symmetry of the amidoborane anion, and its flexibility to bind to metal cations, involving both the lone pair on N atom, and the three-hydride terminal at B atom (Figure 1.13). Among these metal amidoboranes, $LiNH_2BH_3$ and $NaNH_2BH_3$ are isostructural. In $LiNH_2BH_3$, $NaNH_2BH_3$ and $LiNH_2BH_3{\cdot}NH_3BH_3$, both Li and Na tetrahedrally coordinated to one N and

three BH_3 groups by $H^{\delta-}$ of BH_3.[123, 124] In KNH_2BH_3, there are two distinct K, N, and B atomic sites, and each K^+ ion is octahedrally coordinated by three N atoms and three BH_3 units.[125] To our knowledge, the structure of $Mg(NH_2BH_3)_2$ has not been reported. In the crystal structure of $Ca(NH_2BH_3)_2$[126] every Ca has an octahedral coordination environment with two N and four BH_3 units of the $NH_2BH_3^-$ anion. The bond lengths in the above amidoborane anions are comparable with the corresponding bond lengths in ammonia borane molecules (Table 1.7). It is worth mentioning that the B–N bond length is usually slightly shorter in amidoborane anions than in ammonia borane molecules.[122]

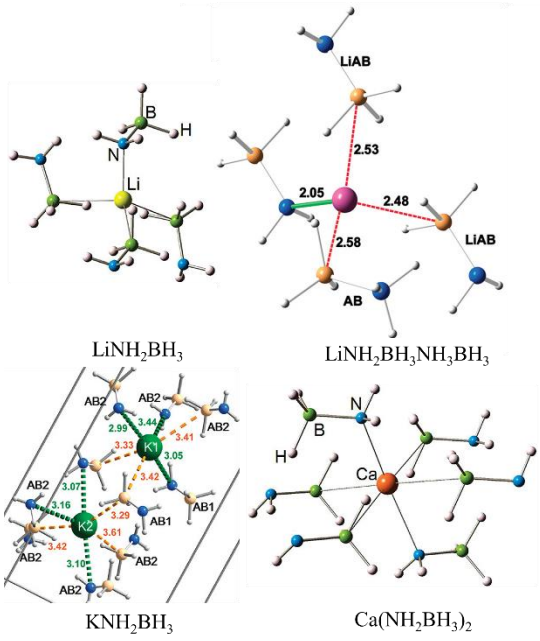

Figure 1.13 Coordination environments of Li^+, K^+ and Ca^{2+} in $LiNH_2BH_3$, $LiNH_2BH_3{\cdot}NH_3BH_3$, KNH_2BH_3 and $Ca(NH_2BH_3)_2$.

The thermal dehydrogenation of $M(NH_2BH_3)_n$ (M = Li, Na, K, Mg, Ca) usually occurs at moderate temperature (below 300 ˚C) with a significant hydrogen release. α- and β-$LiNH_2BH_3$ both can release 10.8 wt.% of hydrogen with slight amounts of NH_3 up to 180 ˚C. $LiNH_2BH_3{\cdot}NH_3BH_3$ has high gravimetric and volumetric hydrogen density (16.4 wt.% and 137.3 g/L), which is about 3 times and 2 times of volumetric hydrogen density of 70 MPa and liquid hydrogen, respectively. $LiNH_2BH_3{\cdot}NH_3BH_3$ prepared by directly milling

a 1:2 molar ratio of LiH/NH_3BH_3 was observed to release 6.0 wt.% (ca. ~2 mol equiv.) H_2 at 91 °C and 8.3 wt.% (ca. ~3 mol equiv.) H_2 at 180 °C, a total of 14.3 wt.%H_2, which is close to its theoretical capacity of five mole hydrogen per $LiNH_2BH_3 \cdot NH_3BH_3$ 14.8 wt.%.[123, 126]

The thermal dehydrogenation of $NaNH_2BH_3$ resembles that of $LiNH_2BH_3$, but at a slightly lower peak temperature of 89 ˚C. Volumetric-release measurements showed that about 6 wt.% of hydrogen is released from the $NaNH_2BH_3$ sample within the first hour at ~91 ˚C. Extending the reaction period to 19 h enables about 7.4 wt.% or about 2.0 equivalent moles of H_2 to fully desorb without borazine.[123] Further investigation of Xiong et al. showed two step thermal decomposition with evolution of 4.4 wt.% of borazine-free hydrogen below 87 ˚C, when heating with a high heating rate. The second decomposition step occurs at temperatures exceeding 100 ˚C and results in evolution of 3.1 wt.% of hydrogen together with reformation of crystalline NaH. Fijalkowski et al. reported desorption of hydrogen contaminated with ammonia, which was later confirmed by Sandra et al. Luedke et al. did not confirm the evolution of ammonia upon thermolysis of $NaNH_2BH_3$ by sampling the gas evolved through a Drägar tube detecting ammonia in the range of 10–1000 ppm. Later Fijalkowski et al. observed upon slow heating (1 ˚C /min) of $NaNH_2BH_3$, the evolution of 3 wt.% ammonia at 50–60 ˚C separated from evolution of 4 wt.% of hydrogen at 70–80 ˚C. According to Fijalkowski et al., $NaNH_2BH_3$ undergoes slow spontaneous decomposition at room temperature. $Na(BH_3NH_2BH_2NH_2BH_3)$ salt can be detected in this solid residue after this slow room-temperature decomposition. Regeneration of decomposed $NaNH_2BH_3$ with gaseous hydrogen at high pressure was not achieved.[122]

KNH_2BH_3 undergoes a two-step decomposition releasing pure hydrogen: 4.0 wt.% (1.5 mol equivalent H_2) is released at ca. 65–110 ˚C with a hydrogen release peak at 98 ˚C; and additional 2.0 wt.% (0.75 mol equivalent H_2) evolves at ca. 110–225 ˚C with a peak at 179 ˚C.[125]

$Mg(NH_2BH_3)_2$ thermally decomposes via a multi-step process while evolving pure hydrogen upon heating to 300 ˚C. In the first step at ca. 75–110 ˚C, $Mg(NH_2BH_3)_2$ evolves ca. 2 wt.% of hydrogen with a peak of evolution at 104 ˚C. At higher temperatures a continuous mass loss and slow evolution of hydrogen with a maximum rate at ca. 225 ˚C can be observed. Overall mass loss is equal to 9 wt.% below 300 ˚C.[128]

Thermolysis of $Ca(NH_2BH_3)_2$ was described in several papers. According to Wu et al., decomposition of $Ca(NH_2BH_3)_2$ starts at ca. 80 ˚C, and a vigorous dehydrogenation can be observed at ca. 100 ˚C and ca. 140 ˚C. Below 250 ˚C, $Ca(NH_2BH_3)_2$ desorbs four equivalents of borazine-free hydrogen which corresponds to 8 wt.% mass loss. According to Diyabalanage et al., 0.3 equivalents of hydrogen is being evolved at 90 ˚C, 1.1 equivalent at 120 ˚C, 2.4 at 150 ˚C and 3.6 at 170 ˚C. In summary $Ca(NH_2BH_3)_2$ desorbs 7.4 wt.% of hydrogen slightly contaminated with ammonia and borazine below 170 ˚C which gives 90 % of theoretical dehydrogenation yield. According to Spielmann et al., $Ca(NH_2BH_3)_2$ undergoes a head-to-tail dimerization of amidoborane anions leading towards $[HN\text{-}BH\text{-}NH\text{-}BH_3]^{2-}$ ions upon dehydrogenation.[122]

Table 1.8 Dehydrogenation data of metal amidoborane salts. Experimental data of the thermal decomposition: temperature range, mass loss, contamination of hydrogen evolved.

Compound	H content (wt.%)	decomposition: Temp., mass loss	Contaminants of H_2
α-$LiNH_2BH_3$[123, 127]	13.5	isothermal at 91 ˚C, 10.9 wt.%[123]	Borazine-free
		isothermal at 91 ˚C, 8.8 wt.%; isothermal at 180 ˚C, ca. 10.8 wt.%[127]	NH_3
β-$LiNH_2BH_3$[127]	13.5	isothermal at 180 ˚C, ca. 10.8 wt.%[127]	NH_3
$LiNH_2BH_3{\cdot}NH_3BH_3$[124, 127]	16.4	1st isothermal at 91 ˚C, ca. 6.0 wt %, 2rd isothermal at 180 ˚C, ca. 8.3 wt %[124, 127]	NH_3
$NaNH_2BH_3$[123, 129]	9.5	isothermal at 89 ˚C, 7.4 wt.%[123]	Borazine-free
		50 – 90 ˚C, 7.0 wt.%[129]	NH_3
KNH_2BH_3[125]	7.3	rt - 160 ˚C, 5.8 wt.%[125]	No
$Mg(NH_2BH_3)_2$[128]	12.0	50 – 300 ˚C, ~10 wt %[128]	No
$Ca(NH_2BH_3)_2$[130]	10.1	At 170 ˚C, ~7.2 wt %[129]	NH_3, borazine

2) Multi-metallic amidoboranes

The multi-metallic amidoboranes $M_1[M_2(NH_2BH_3)_n]$ include $Na[Li(NH_2BH_3)_2]$, $Na/K/Rb[Mg(NH_2BH_3)_3]$, $Li_2/Na_2/K_2[Mg(NH_2BH_3)_4]$,

$Li_2/Na_2[Ca(NH_2BH_3)_4]$, $Li/Na/K[Al(NH_2BH_3)_4]$ and $Li_3[AlH_2(NH_2BH_3)_4]$. Different from the mono-metallic amidoborane, two or more metal centers of $[M_1M_2(NH_2BH_3)_n]$ (multi metal amidoborane) often improve the hydrogen purity in the decomposition, because both of them suppress the liberation of ammonia and diborane at the meantime.

Table 1.9 The synthesis reactions of $M_1[M_2(NH_2BH_3)_n]$.

Compound	Reactions
$Na[Li(NH_2BH_3)_2]$	$LiH + NaH + 2\ NH_3BH_3 \longrightarrow Na[Li(NH_2BH_3)_2] + 2\ H_2\uparrow$
$Na/K/Rb[Mg(NH_2BH_3)_3]$	$Na/K/RbMgH_3 + 3\ NH_3BH_3 \longrightarrow Na/K/Rb[Mg(NH_2BH_3)_3] + 3\ H_2\uparrow$
$Li_2[Mg(NH_2BH_3)_4]$	$2\ LiH + MgH_2 + 4\ NH_3BH_3 \longrightarrow Li_2[Mg(NH_2BH_3)_4] + 4\ H_2\uparrow$
$Na_2[Mg(NH_2BH_3)_4]$	$2\ NaH + MgH_2 + 4\ NH_3BH_3 \longrightarrow Na_2[Mg(NH_2BH_3)_4] + 4\ H_2\uparrow$
	$2\ Mg(NH_2BH_3)_2{\cdot}NH_3 + 2\ NaH \longrightarrow Na_2[Mg(NH_2BH_3)_4] + Mg(NH_2)_2 + 2\ H_2\uparrow$
$K_2[Mg(NH_2BH_3)_4]$	$2\ Mg(NH_2BH_3)_2{\cdot}NH_3 + 2\ KH \longrightarrow K_2[Mg(NH_2BH_3)_4] + Mg(NH_2)_2 + 2\ H_2\uparrow$
$Li_2/Na_2[Ca(NH_2BH_3)_4]$	$2\ Li/NaH + CaH_2 + 4\ NH_3BH_3 \longrightarrow Li_2/Na_2[Ca(NH_2BH_3)_4] + 4\ H_2\uparrow$
$Li/Na/K[Al(NH_2BH_3)_4]$	$Li/Na/KAlH_4 + 4\ NH_3BH_3 \longrightarrow Li/Na/K[Al(NH_2BH_3)_4] + 4\ H_2\uparrow$
$Li_3[AlH_2(NH_2BH_3)_4]$	$Li_3AlH_6 + 4\ NH_3BH_3 \longrightarrow Li_3[AlH_2(NH_2BH_3)_4] + 4\ H_2\uparrow$

Like mono-metallic amidoboranes, most of the multi-metallic amidoboranes also can be obtained from the M_1H, M_2H_{n-1} or $M_1M_2H_n$ and NH_3BH_3 by mechanochemical synthesis except for $K_2[Mg(NH_2BH_3)_4]$ (Table 1.9). $K_2[Mg(NH_2BH_3)_4]$, as well as $Na_2[Mg(NH_2BH_3)_4]$ was synthesized via a

mechanochemical reaction of $Mg(NH_2BH_3)_2 \cdot NH_3$ and KH or NaH in molar ratio 1:1. $Li_3[AlH_2(NH_2BH_3)_4]$ shows a little bit different from others, there only four of six H^- in Li_3AlH_6 were replaced by $NH_2BH_3^-$.

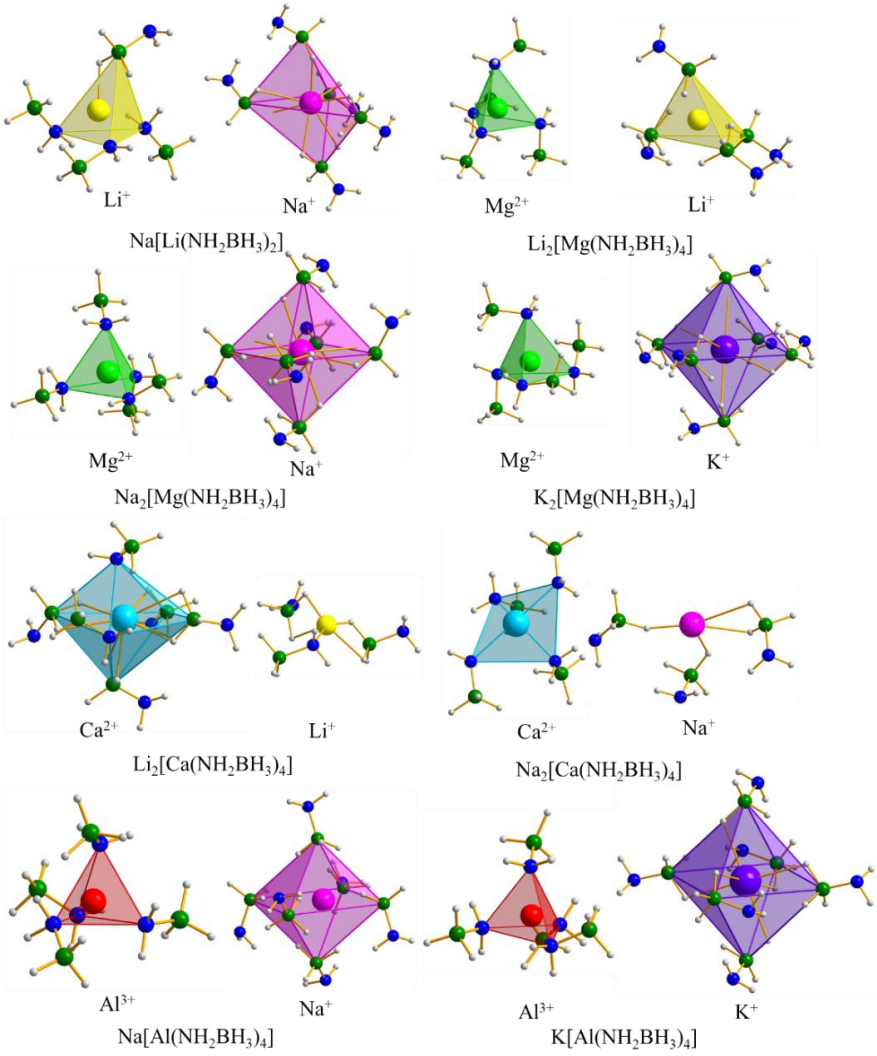

Figure 1.14 Perspective projections of coordination spheres of metal cations in the crystal structures of $Na[Li(NH_2BH_3)_2]$, $Li_2/Na_2/K_2[Mg(NH_2BH_3)_4]$, $Li_2/Na_2[Ca(NH_2BH_3)_4]$ and $Na/K[Al(NH_2BH_3)_4]$.

Not all the structure of the above multi-metallic amidoboranes have been determined. Up to now, eight structures of multi-metallic amidoboranes have been reported. Different from the mono-metallic amidoboranes, in

$M_1[M_2(NH_2BH_3)_n]$, almost all the strong Lewis bases (NH_2) coordinate to a stronger Lewis acid (like Li^+ in $Na[Li(NH_2BH_3)_2]$, Mg^{2+} in $Na_2[Mg(NH_2BH_3)_4]$ and so on) and simultaneously the weaker Lewis acid (Na^+ in $Na[Li(NH_2BH_3)_2]$ and $Na_2[Mg(NH_2BH_3)_4]$) is found in the homoleptic environment of weaker Lewis bases, BH_3, except the metals in $Li_2[Ca(NH_2BH_3)_4]$ (Figure.1.14).

Table 1.10 Interatomic distances in crystal structures of bi-metallic amidoboranes.

Compound	Space group	B-N (Å)	M-N (Å)	M-B (Å)
$Na[Li(NH_2BH_3)_2]$	*P*-1	1.51-1.61	2.16-2.26 Li-N	2.86-3.11 Na-B
$Li_2[Mg(NH_2BH_3)_4]$	*Pbcn*	1.562	2.09-2.10 Mg-N	2.39-2.88 Li-B
$Na_2[Mg(NH_2BH_3)_4]$	$I4_1/a$	1.56	2.11 Mg-N	2.96-3.03 Na-B
$K_2[Mg(NH_2BH_3)_4]$	$I4_1/a$	1.56	2.21 Mg-N	3.34-3.46 K-B
$Li_2[Ca(NH_2BH_3)_4]$	*Fdd*2	1.56	2.43 Ca-N	2.39-2.63 Li-B
$Na_2[Ca(NH_2BH_3)_4]$	*C*2	1.56	2.32-2.47 Ca-N	2.634-3.059 Na-B
$Na[Al(NH_2BH_3)_4]$	*P*-1	1.58-1.63	1.84-1.93 Al-N	2.92-2.97 Na-B
$K[Al(NH_2BH_3)_4]$	*P*-1	1.59	1.84-1.91 Al-N	3.13-3.60 K-B

In $Na[Li(NH_2BH_3)_2]$[131], Li^+ is coordinated by three N atoms from $[NH_2]$ groups and by one $H^{\delta-}$ atom from $[BH_3]$ group. A $[Li(NH_2BH_3)_2^-]_2$ anionic dimers can be observed in the crystal structure. Na^+ is in trigonal bipyramid coordination surrounded by five hydride atoms from $[BH_3]$ groups. In $Li_2/Na_2/K_2[Mg(NH_2BH_3)_4]$[132-134], Mg^{2+} is coordinated exclusively by four amidoborane anions via their nitrogen atoms while forming the $[Mg(NH_2BH_3)_4]^{2-}$ tetrahedra. Li^+, Na^+ and K^+ are in tetrahedral, octahedral, and octahedral coordination of four, six and six $[BH_3]$ groups, respectively. In $Li_2[Ca(NH_2BH_3)_4]$[135], The Ca^{2+} ion is coordinated by two N atoms of two $NH_2BH_3^-$ anion, and four B atoms from the BH_3 to form a octahedral coordinated environment. Li^+ is coordinated by four hydrogen atoms of two BH_3 moieties and one N atom, in a distorted coordination environment. In $Na_2[Ca(NH_2BH_3)_4]$[135] the Ca^{2+} ion is coordinated by four N atoms of four $NH_2BH_3^-$ anion, forming a distorted $[Ca(NH_2BH_3)_4]^{2-}$ tetrahedron. The Na^+ ion is coordinated by four hydrogen atoms of the BH_3 moiety in a distorted coordination environment. $Na[Al(NH_2BH_3)_4]$[136] crystallizes in a triclinic space

group *P*–1, The central Al^{3+} cation is coordinated by four nitrogen atoms from the $[NH_2BH_3]^-$ anions, whereas Na^+ is octahedrally coordinated by six BH_3 groups. $K[Al(NH_2BH_3)_4]$[137], is isostructural to $Na[Al(NH_2BH_3)_4]$, the Al^{3+} ions are tetrahedrally coordinated to $[NH_2BH_3]^-$ through the nitrogen lone pair. The K^+ ion is octahedrally coordinated to $[NH_2BH_3]^-$ through the BH_3 group in zig-zag 1D chain. (Table 1.10)

Table 1.11 Dehydrogenation data of multi-metallic amidoborane salts. Experimental data of the thermal decomposition: temperature range, mass loss, contaminants of hydrogen evolved.

Compound	H content (wt.%)	Decomposition: Temp., mass loss	Contaminants of H_2
$Na[Li(NH_2BH_3)_2]$[131]	11.1	1st step: 75-100 ˚C, 6.0 wt.% 2rd step: 130-220 ˚C, 3.0 wt.%	NH_3, $(NH_2BH_2)H$
$Na/K/Rb[Mg(NH_2BH_3)_3]$[139, 140]	11.0, 9.9, 7.6	Isotherm at 80 ˚C for 2 min: 9.8 wt% (Na), 9.2 wt.% (K) and 6.2 wt.% (Rb)	
$Li_2[Mg(NH_2BH_3)_4]$[134]	7 .0	70-250 ˚C	NH_3, B_2H_6
$Na_2[Mg(NH_2BH_3)_4]$[132]	10.6	1st step: 65–150 ˚C, 2 wt.% 2rd step: 150-200 ˚C, 6.4 wt.%	NH_3, $N_3B_3H_6$
$K_2[Mg(NH_2BH_3)_4]$ + $Mg(NH_2)_2$[133]	8.6	1st step: 75–150 ˚C, 3.7 wt.% 2rd step: 150-200 ˚C, 4.4 wt.%	NH_3
$Li_2[Ca(NH_2BH_3)_4]$[135]	11.6	85 -95 ˚C	NH_3
$Na_2[Ca(NH_2BH_3)_4]$ [135]	9.8	50-300 ˚C	NH_3
$Li[Al(NH_2BH_3)_4]$ [141]	13.1	80-190 ˚C, 7.0 wt.%	No NH_3
$Na[Al(NH_2BH_3)_4]$[136]	11.9	1st step: 115–130 ˚C, 3.0 wt.% 2rd step: 130-250 ˚C, 6.0 wt.%	Slight NH_3
$K[Al(NH_2BH_3)_4]$[137]	10.9	1st step: 92–119 ˚C, 1.3 wt.% 2rd step: 119-260 ˚C, 4.7 wt.%	NH_3, $N_3B_3H_6$, and B_2H_6
$Li_3[AlH_2(NH_2BH_3)_4]$[142]	13.1	1st step: 80–110 ˚C, 3.85 wt.% 2rd step: 110-175 ˚C, 6.25 wt.%	No NH_3, $N_3B_3H_6$, and B_2H_6

The results of thermal decomposition of bi-metallic amidoboranes are summarized in Table 1.11. The thermal dehydrogenation of

$Na[Li(NH_2BH_3)_2]$[131] at elevated temperatures proceeds in two steps: 75–100 ˚C and 130–220 ˚C. In the first decomposition step 6 % mass loss is observed which is attributed to evolution of hydrogen contaminated with ammonia and volatile $(NH_2BH_2)H$ by-product. It is worth noticing that in the temperature range ca. 75–90 ˚C the level of impurities evolved is significantly lower than in the temperature range 90–100 ˚C. In the second step 3 wt.% of hydrogen is evolved. Total observed mass loss is equal to 9 wt.% below 220 ˚C. $Na[Li(NH_2BH_3)_2]$ slowly decomposes at room temperature while forming $Na(BH_3NH_2BH_2NH_2BH_3)$ salt[138].

$Na[Mg(NH_2BH_3)_3]$, $K[Mg(NH_2BH_3)_3]$ and $Rb[Mg(NH_2BH_3)_3]$ are analogues and showed similar thermal decomposition behavior.[139, 140] They thermally decompose via a slightly endothermic process at temperature range of 75–225 ˚C without foaming. Besides H_2, trace amounts of ammonia were detected in the temperature range of 100-180 ˚C, peaking at about 130 ˚C. Interestingly, milled composites $MMgH_3/3NH_3BH_3$ (M = Na, K, Rb) are able to rapidly evolve 9.8 wt.%, 9.2 wt.% and 6.2 wt.%, respectively, of pure hydrogen during 2 min isothermal heating at 80 ˚C.

$Li_2[Mg(NH_2BH_3)_4]$[134] released about 7 wt.% of hydrogen with trace amounts of NH_3 and B_2H_6 contamination, and no detectable borazine from 70-250 ˚C. $Na_2[Mg(NH_2BH_3)_4]$[132] thermally decomposes releasing 8.4 wt.% of hydrogen contaminated with traces of ammonia and borazine. The first decomposition step is seen in the temperature range of 65–150 ˚C and results in evolution of 2 wt.% of hydrogen. The process proceeds slowly until ca. 120 ˚C when a rapid hydrogen evolution is observed. The second decomposition step yields 6.4 wt.% of mass loss in the form of hydrogen gas in the temperature range of 150–200 ˚C. The as prepared $K_2[Mg(NH_2BH_3)_4]$ + $Mg(NH_2)_2$[133] composite decomposes with evolution of both hydrogen and ammonia. It was reported that the 3.7 wt.% mass loss up to 150 ˚C is mainly related to NH_3 release. Further decomposition occurs at 150–200 ˚C with hydrogen evolution peak at 158 ˚C and a concomitant mass loss of ca. 4.4 wt.%. This process is endothermic based on the TGA/DSC measurement. The hydrogen storage capacity in $K_2[Mg(NH_2BH_3)_4]$ + $Mg(NH_2)_2$ was further quantified by volumetric release measurements. The results showed a total of ca. 7 wt.% up to 285 ˚C released, which corresponds to 9.7 equivalents of hydrogen per formula unit of the composite $K_2[Mg(NH_2BH_3)_4]$ + $Mg(NH_2)_2$.

$Li_2[Ca(NH_2BH_3)_4]$[135] shows three intense maxima between 83 and 91 ˚C, while a less intense event takes place at 112 ˚C. Temperature-programmed desorption with mass spectroscopy (TPD-MS) shows that $Li_2[Ca(NH_2BH_3)_4]$ desorbs all H_2 between 85 and 95 ˚C. This is accompanied by a release of NH_3, but in a trace amount, a few orders of magnitude lower amount with respect to H_2, as well as ammonia from $Na_2[Ca(NH_2BH_3)_4]$. $Na_2[Ca(NH_2BH_3)_4]$[135] starts to decompose very fast at 66 ˚C. Until 100 ˚C, four thermal events are observed, with the most intensive one at 89 ˚C. The other two very broad exothermal maxima are positioned between 150 and 240 ˚C. TPD-MS shows that these transitions are mainly associated with chemical transformations resulting in NH_3, followed by intense H_2 release. The release of significant amounts of ammonia occurs above 80 ˚C and remains more or less constant by further heating (up to 300 ˚C). H_2 is released over a broad 80−120 ˚C temperature range, peaking at 98 ˚C.

$Li[Al(NH_2BH_3)_4]$[141] was reported to start releasing hydrogen at 80 ˚C, peaking at around 170 ˚C. Heating to 190 ˚C, approximately 5.2 moles of hydrogen (which corresponds to around 7 wt.% hydrogen based on material) are released. And no NH_3 was detected at that process. $Na[Al(NH_2BH_3)_4]$[136] decomposes while releasing borazine and diborane-free hydrogen, contaminated with traces of ammonia and yielding crystalline $NaBH_4$ and an amorphous phase $AlN_4B_3H_{(0\text{-}3.6)}$ as solid residue. Thermolysis of $Na[Al(NH_2BH_3)_4]$ occurs via two overlapping steps at 115–130 ˚C and 130–250 ˚C with a mass loss of ca. 3 wt.% and ca. 6 wt.%. Both steps are exothermic. Total observed mass loss up to 250 ˚C is equal to 9 wt.% which corresponds to eight equivalents of hydrogen per formula unit. The analogue of $Na[Al(NH_2BH_3)_4]$, $K[Al(NH_2BH_3)_4]$[137] has similar thermal decomposition. There are also two exothermic steps at T ~ 92 ˚C (maximum at T ~ 104 ˚C with a mass loss of 1.3 wt.%) and at T ~ 139 ˚C (peaks at T ~ 153 ˚C with a mass loss of 4.2 wt.%). Tiny amounts of NH_3, $N_3B_3H_6$, and B_2H_6 were observed accompanied with H_2 releasing. A total mass loss of 6.0 wt.% is observed at ~262 ˚C.

$Li_3[AlH_2(NH_2BH_3)_4]$, obtained as a post-milled Li_3AlH_6–$4NH_3BH_3$,[142] release high purity hydrogen via two steps. The first step occurred in the region of 80–110 ˚C with 3.85 wt.% weight loss. And the second step from 110 ˚C to 175 ˚C with 6.25 wt.% mass loss.

1.6 Reactive hydride composites (RHCs)

Reactive hydride composites are the combinations of different metal hydrides and/or complex hydrides. Once combined, they are capable of releasing hydrogen through chemical reactions unique to these mixtures, and not to the individual components. The gravimetric hydrogen storage capacity remains as high as for the individual hydrides. However, the thermodynamics of the decomposition reaction is very different, since the dehydrogenated phases have a different stability from the ones obtained from the individual components (Figure 1.15). Therefore, some reactive hydride composites release a lot of hydrogen at lower temperature than their pure components. Moreover, the resulting solid phases may be able to adsorb hydrogen reversibly.

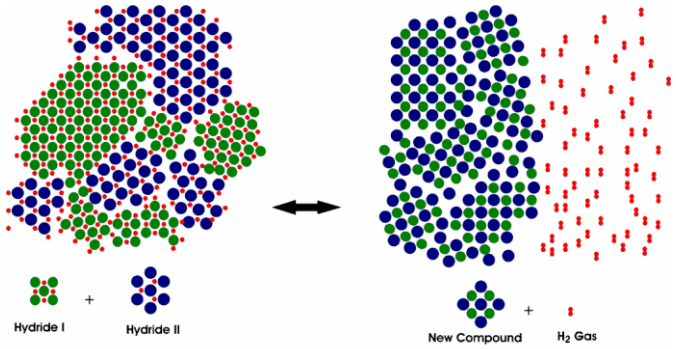

Figure 1.15 The simplified scheme of the RHCs.[143]

A typical example of reactive hydride composites is the metal amide mixed with binary hydrides (like LiH, MgH_2, introduced in the section on metal amides) and complex hydrides, such as the composites $2LiNH_2 + LiBH_4$, $LiAlH_4 + 2LiNH_2$, $Mg(NH_2)_2 + LiAlH_4$ etc.

The composites of alanates and metal borohydride are also studied for their hydrogen storage, for instance, $NaBH_4 + Li_3AlH_6$. Compared to the milled $NaBH_4$, the composites $NaBH_4 + Li_3AlH_6$ obtained by milling has lower decomposition temperature (170 and 400 ˚C) and higher hydrogen desorption/absorption capacity (Table 1.12). It was reported that the formation of Al and AlB_2 during dehydrogenation are the keys to the improvement of hydrogenation properties.

Table 1.12 Hydrogen storage properties of $NaBH_4$, Li_3AlH_6 and $NaBH_4$–Li_3AlH_6 RHC.[144]

System (milled)	Decomposition temperature (˚C)	Desorption capacity (60 min at 330/420 ˚C)	Absorption capacity (60 min at 330/420 ˚C under 30 atom)
Li_3AlH_6	170	-	-
$NaBH_4$	495	0.3/2.1 wt.%	3.4/3.7 wt.%
$NaBH_4$–Li_3AlH_6	170 and 400	2.0/4.1 wt.%	4.2/6.1 wt.%

The formation of composites is also a good strategy to destabilize MgH_2 to improve the poor performance of MgH_2. For example, the compositions of $4MgH_2 + NaAlH_4$ showed a strong improvement of releasing hydrogen kinetics than MgH_2 (Figure 1.16). Especially at 320 ˚C, $4MgH_2 + NaAlH_4$ released about 3.5 wt.% hydrogen in 12 min, in contrast to the milled MgH_2 with 0.5 wt.% hydrogen releasing at the same condition and at the same time.[145]

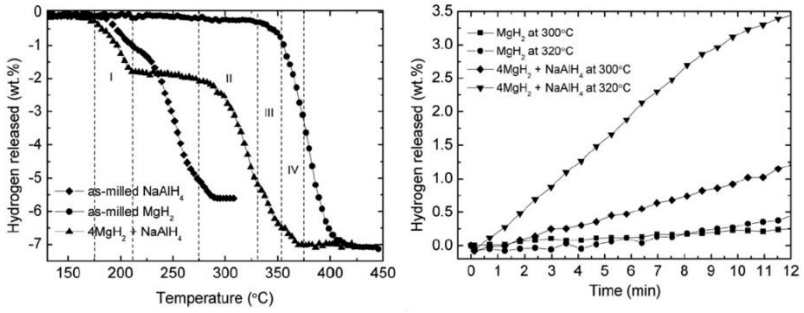

Figure 1.16 TPD (temperature programmed desorption) curves of the as-milled MgH_2, the as-milled $NaAlH_4$, and the MgH_2 - $NaAlH_4$ composite. (I, II, III, and IV refer to the first, second, third, and fourth dehydrogenation stage, respectively) (left); Isothermal dehydrogenation kinetics of the MgH_2 and the MgH_2 - $NaAlH_4$ composite at 300 ˚C and 320 ˚C.[145]

The combination of $Ca(BH_4)_2$ and MgH_2 yields a higher hydrogen capacity, approximately 9.0 wt.%, which is nearly identical to the theoretical value of 9.1 wt.%. Furthermore, the introduction of NbF_5 as a dopant enhances the performance of $Ca(BH_4)_2$-MgH_2 while maintaining high hydrogen content even after several cycles. In the initial cycle, both $Ca(BH_4)_2$-MgH_2 and NbF_5-doped $Ca(BH_4)_2$-MgH_2 sample exhibit a hydrogen storage capacity close to the theoretical capacity (9.1 wt.%). However, after completing 10 cycles, the

remaining hydrogen storage capacity for the $Ca(BH_4)_2$-MgH_2 is 2.9 wt.%, whereas the NbF_5-doped $Ca(BH_4)_2$-MgH_2 sample retains a higher capacity of 4.1 wt.%.[146] The $2LiBH_4$-MgH_2 system was studied and found to exhibit reversible behavior, following the reaction described below. Volumetric experiments demonstrate the composite $2LiBH_4$-MgH_2 can reversibly store approximately 10 wt.% of hydrogen with no noticeable degradation during five cycles.[147]

$$2\ LiBH_4 + MgH_2 \rightleftharpoons 2\ LiH + MgB_2 + 4\ H_2$$

In addition, the ternary composites were also studied for their hydrogen storage properties. For instance, in the case of $Ca(BH_4)_2 + 2LiBH_4 + 2MgH_2$, hydrogen desorption begins at 320 °C and is completed at 370 °C under a heating rate of 2 °C min^{-1}, releasing ~ 8.1 wt.% H_2. These desorption properties, including the end temperature and capacity surpass those of any of the two-hydride mixtures within the ternary system. In particular, hydrogenation of the ternary system commences at an exceptionally low temperature of around 75 °C, and the onset dehydrogenation temperature is significantly reduced by 90 °C after the initial dehydrogenation/hydrogenation cycle. The reversibility of this process is remarkable, reaching up to 97 %, with a dehydrogenation capacity of approximately 6.2 wt.% H_2 observed during the 10th cycle.

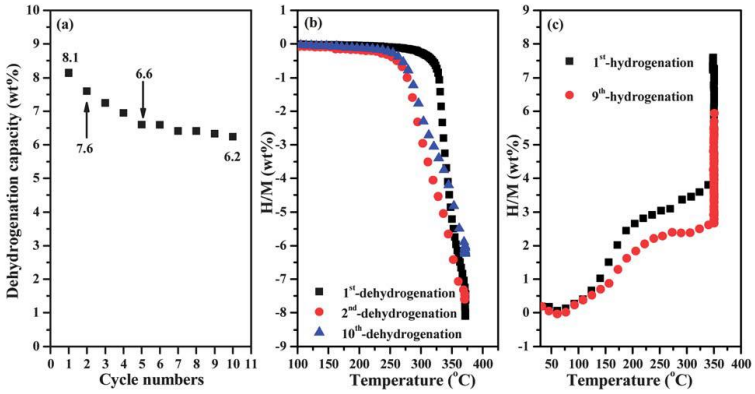

Figure 1.17 Cycling properties of the $Ca(BH_4)_2 + 2LiBH_4 + 2MgH_2$ system: (a) the dehydrogenation capacity at different dehydrogenation/hydrogenation cycles; (b) dehydrogenation curves at the 1st, 2nd and 10th cycles upon heating to 370 °C and dwelling for 30 min; (c) hydrogenation curves of the 1st and 9th cycles upon heating to 350 °C and dwelling for 18 h at 90 bar H_2.[148]

The $LiBH_4$-$LiNH_2$-LiH composite commenced hydrogen desorption at 192 °C, which is 35 °C lower than that of the $LiNH_2$-LiH composite. At 250 °C, the $LiBH_4$-$LiNH_2$-LiH composite released 4.0 wt.% of H_2 within 30 min and absorbed 4.8 wt.% of H_2 within 2 min. Conversely, the $LiNH_2$-LiH composite desorbed 1.44 wt.% of H_2 and absorbed 2.1 wt.% under the same conditions. Additionally, the addition of $LiBH_4$ could hinder the release of NH_3.[149] Gizer et al. demonstrated that the addition of $LiBH_4$ enhanced the thermodynamic properties of the $6Mg(NH_2)_2$-9LiH. It reduced the desorption temperature by 25 °C and lowered the activation energy by 43 kJ/mol. Additionally, the presence of $LiBH_4$ promoted faster sorption kinetics. At 180 °C, the $Mg(NH_2)_2$-LiH sample desorbed 1.1 wt.% of H_2 within 20 min, whereas the $6Mg(NH_2)_2$-9LiH-$LiBH_4$ sample desorbed >3.0 wt.% of H_2 under the same conditions. Similarly, there was a notable improvement in absorption kinetics. Within 10 minutes, the $6Mg(NH_2)_2$-9LiH-$LiBH_4$ sample absorbed 3.6 wt.% of H_2, whereas the $Mg(NH_2)_2$-LiH sample only absorbed 1.4 wt.% of H_2. A series of 20 dehydrogenation/hydrogenation cycles were performed on the $Mg(NH_2)_2$-LiH and $6Mg(NH_2)_2$-9LiH-$LiBH_4$ samples isothermally at 180 °C. For the $Mg(NH_2)_2$-LiH sample, the amount of hydrogen desorbed was reduced from 4.0 wt.% to 3.6 wt.% of hydrogen within 10 cycles even after measurement time is extended. However, the $LiBH_4$-containing sample presents superior cycling stability with no observable capacity loss with the 20 cycles. In terms of dehydrogenation/hydrogenation time necessary to achieve 80 % of maximum capacity, the $6Mg(NH_2)_2$-9LiH-$LiBH_4$ sample required only 10 min while the $Mg(NH_2)_2$-LiH sample takes 70 min.[150]

It has been demonstrated that the formation of the intermediate phases plays a significant role in enhancing the hydrogen storage properties of the RHCs. It is the formation of intermediate compounds during the heating process (dehydrogenation process) that alters the reaction pathway and modifies the thermodynamic properties (reducing the enthalpy Figure 1.18) of the RHC systems. Therefore, the new high hydrogen content compounds have the potential to be used as a component to the formation of new reactive hydride composites for hydrogen storage.

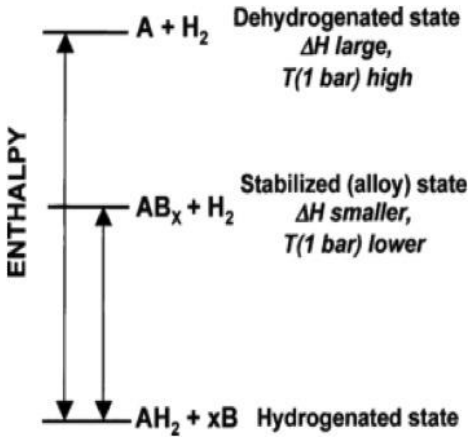

Figure 1.18 The addition of B lowers the temperature (1 bar) because AB_x is formed during dehydrogenation. The formation of AB_x reduces the dehydrogenation enthalpy, which in turn alters the thermodynamics properties of AH_2.[151]

1.7 The objective of this thesis

At present, the lack of compact, safe, and cost-effective manners for hydrogen storage is one of the main obstacles for wide application of hydrogen as a main energy carrier. To solve this problem, researchers are focusing on designing and synthesizing new materials or re-evaluating the known materials doped with catalysis or other additives to obtain promising hydrogen storage materials. Among the solid-state hydrogen storage materials, ammonia borane, (NH_3BH_3) is a promising precursor for the synthesis of new compounds with high hydrogen content and low decomposition temperature for thermal dehydrogenation. For instance, the metallic amidoboranes usually release a large amount of hydrogen (> 6 wt.%) under moderate condition, without borazine and sometime with traces of NH_3 or B_2H_6. It was reported that the introduction of alkyl-N groups on NH_3BH_3 can disrupt the dihydrogen bonding network, which not only lowers dehydrogenation exothermicity and alters the activation energy but also enhances the B–N dative bond, resulting in decreasing volatile nitrogen-based impurities during the decomposition. Therefore, my doctoral research focused on the synthesis and structure characterization of simple and light alkyl groups ($-CH_3$ and $-CH_2CH_2-$) substituted on metal amidoboranes to obtain new

materials which can release pure hydrogen under practical conditions (<200 °C, <200 bar of H_2 pressure), with the aim to understand the relationships between structure and properties at molecular level. To achieve this goal, two precursors, $CH_3NH_2BH_3$ and $BH_3NH_2CH_2CH_2NH_2BH_3$ were used to synthesize different derivatives of mono- and bi-metallic amidoboranes. These works are organized according to the following aspects:

a. Introducing methyl groups on N atoms of NH_3BH_3 to weaken the N–H bond and enhance the B–N dative bond to suppress the release of NH_3. In addition, decrease the number of protic hydrogens on $H^{\delta+}$-N, further reducing the number of intermolecular dihydrogen bonds in the corresponding derivatives of metallic amidoboranes. This is aiming to destabilize the amidoborane and therefore potentially make it release hydrogen at a lower temperature. Moreover, the introduction of an alkyl group on the N atom would increase the steric hindrance, additionally influencing the geometry of the structure, offering more information about the structure-property relationship in metal amidoboranes.

b. Introduction of di-methylene on N atoms as a bridge to connect two ammonia boranes not only to keep the positive effect on the N-H and B-N bonds described above but also to decrease the weight of hydrocarbon substituent, also making it heavier and thus less volatile. Interestingly, there are no reports on structure and properties of metallic di-aminoboranes.

c. Improve the hydrogen desorption properties of ammonia borane derivatives by introducing functional groups onto nitrogen atoms to gain insights into the impact of materials structure modifications on hydrogen desorption properties. Further to guide the structure design to find new materials suitable for practical applications with safety and cost-efficient in large scale.

1.8 Summary of this thesis

This thesis is dedicated to the chemistry and hydrogen storage properties of novel boron-nitrogen-hydrogen (B-N-H) compounds. The main efforts were focused on the synthesis, structural characterization, and hydrogen release

properties of the derivatives of metal amidoborane complexes. The objective was to investigate and comprehend the hydrogen storage properties of ammonia borane derivatives, focusing primarily on the effects of introducing alkyl-groups on the nitrogen atoms of amidoborane and metal amidoborane complexes, as well as the coordination geometry of Aluminum in metal aluminum amidoboranes, on hydrogen storage performance. The prior research conducted in our laboratory on the synthesis, structure, and hydrogen storage properties of $M[Al(NH_2BH_3)_4]$ (M = Na, K)[136,137] laid the foundation for this thesis. The work presented in this thesis further advances the exploration of Al-based metal amidoboranes.

The alkyl-groups used in this thesis were $-CH_3$ and $-CH_2CH_2-$, utilizing $CH_3NH_2BH_3$ and $BH_3NH_2CH_2CH_2NH_2BH_3$ as precursors. Reactions between these precursors and binary metal hydrides (mainly NaH and LiH) or alanates ($NaAlH_4$ and $LiAlH_4$) were investigated. In summary, mechanochemical synthesis methods and wet chemical synthesis approaches were employed to synthesize $Na[BH_3(CH_3NH)BH_2(CH_3NH)BH_3]$ ($Na[B_3(MeN)_2]$), $Na[Al(CH_3NHBH_3)_4]$, Na-ii (a B-N-H metal oligomer compound with a ten B-N-membered ring), $Li[Al(BH_3NHCH_2CH_2NHBH_3)_2]$ and $Na[Al(BH_3NHCH_2CH_2NHBH_3)_2]$. The structures of these compounds were typically characterized using powder X-ray diffraction (PXRD), infrared spectra (IR) and ^{11}B NMR. Crystal structures of $Na[B_3(MeN)_2]$, $Na[Al(CH_3NHBH_3)_4]$ and a $Na[AlH(CH_3NHBH_3)_3]$ intermediate, and $Na[Al(BH_3NHCH_2CH_2NHBH_3)_2]$ were determined based on high-resolution laboratory or synchrotron PXRD.

The thermal decomposition of these novel metal amidoborane complexes was investigated by thermogravimetric analysis while thermal dehydrogenation was studied by mass spectrometry. The results revealed that $Na[B_3(MeN)_2]$ can release approximately 4.6 wt.% pure hydrogen below 150 ˚C. The higher hydrogen purity, compared with the unsubstituted $Na[B_3N_2]$, can be attributed to the introduction of $-CH_3$ on nitrogen atoms. The presence of $-CH_3$ on nitrogen atoms strengthens the B-N bonds, resulting in a reduction in the release of volatile gases containing nitrogen and boron during thermal dehydrogenation. Additionally, the introduction of $-CH_3$ on the nitrogen atoms disrupts some intermolecular dihydrogen bonds and induces a kink in the B-N-B-N-B geometry, promoting the formation of intramolecular dihydrogen bonds. This facilitates the release of hydrogen molecules while suppressing

the release of larger fragments during thermal decomposition. These findings are detailed in Chapter 3.

The introduction of -CH_3 on nitrogen atoms of Na[Al(NH_2BH_3)$_4$] promotes the formation of Al-N bonds in Na[Al(CH_3NHBH_3)$_4$], resulting in a lower energy input required for synthesizing Na[Al(CH_3NHBH_3)$_4$] compared to the unsubstituted Na[Al(NH_2BH_3)$_4$]. Furthermore, we isolated the intermediate Na[AlH(CH_3NHBH_3)$_3$], providing valuable insights into the formation mechanism of Al-based amidoborane compounds. The thermal dehydrogenation of the reactive hydrides composites Na[Al(CH_3NHBH_3)$_4$] + 12NaH and Na[Al(CH_3NHBH_3)$_4$] + 6$NaNH_2$ was investigated at 180 ˚C and found to enable the release of high-purity hydrogen. These findings are discussed in Chapter 4.

The introduction of -CH_2CH_2- on the nitrogen atoms of NH_3BH_3 forming a sodium oligomer with a ten B-N membered ring when reacted with NaH, resulted in the release of approximately 7.4 wt.% pure hydrogen below 260°C. This novel metal oligomer exhibited higher hydrogen storage capacity compared to the -CH_3-substituted sodium oligomer, Na[B_3(MeN)$_2$]. These findings are presented in Chapter 5.

Both Li[Al($BH_3NHCH_2CH_2NHBH_3$)$_2$] and Na[Al($BH_3NHCH_2CH_2NHBH_3$)$_2$] released hydrogen without the presence of ammonia, diborane, and ethylenediamine. Specifically, Li[Al($BH_3NHCH_2CH_2NHBH_3$)$_2$] released about 6.6 wt.% pure hydrogen below 280 ˚C. These findings are detailed in Chapter 6.

At last, we give a very short introduction about our attempt of the six-coordinated metal aluminum amidoboranes in Chapter 7. The aim was to give a deeper understanding for the hydrogen storage properties from the structures.

References

1. Desa, U., World Population Prospects 2019: Highlights. *New York (US): United Nations Department for Economic and Social Affairs* **2019**, *11*, 125.

2. Ren, J.; Musyoka, N. M.; Langmi, H. W.; Mathe, M.; Liao, S., Current Research Trends and Perspectives on Materials-Based Hydrogen Storage Solutions: A Critical Review. *International Journal of Hydrogen Energy* **2017**, *42*, 289-311.

3. Yearbook, G. E. S., Total Energy Consumption. *Global Energy Statistical Yearbook* **2019**.
4. Shafiee, S.; Topal, E., When Will Fossil Fuel Reserves Be Diminished? *Energy Policy* **2009**, *37*, 181-189.
5. Veziroglu, T. N., Conversion to Hydrogen Economy. *Energy Procedia* **2012**, *29*, 654-656.
6. Abe, J. O.; Popoola, A. P. I.; Ajenifuja, E.; Popoola, O. M., Hydrogen Energy, Economy and Storage: Review and Recommendation. *International Journal of Hydrogen Energy* **2019**, *44*, 15072-15086.
7. Durbin, D. J.; Malardier-Jugroot, C., Review of Hydrogen Storage Techniques Foronboard Vehicle Applications. *International Journal of Hydrogen Energy* **2013**, *38*, 14595-14617.
8. Faye, O.; Szpunar, J.; Eduok, U., A Critical Review on the Current Technologies for the Generation, Storage, and Transportation of Hydrogen. *International Journal of Hydrogen Energy* **2022**, *47*, 13771-13802.
9. Yang, Z.; Xia, Y.; Mokaya, R., Enhanced Hydrogen Storage Capacity of High Surface Area Zeolite-Like Carbon Materials. *Journal of the American Chemical Society* **2007**, *129*, 1673-1679.
10. Blankenship Ii, T. S.; Balahmar, N.; Mokaya, R., Oxygen-Rich Microporous Carbons with Exceptional Hydrogen Storage Capacity. *Nature Communications* **2017**, *8*, 1545.
11. Takagi, H.; Hatori, H.; Soneda, Y.; Yoshizawa, N.; Yamada, Y., Adsorptive Hydrogen Storage in Carbon and Porous Materials. *Materials Science and Engineering: B* **2004**, *108*, 143-147.
12. Faye, O., Metal Adatom Adsorption on Graphehe Sheet: A First-Principle Study. *African Review of Physics* **2012**, *7*, 313-318.
13. Rosi, N. L.; Eckert, J.; Eddaoudi, M.; Vodak, D. T.; Kim, J.; Keeffe, M.; Yaghi, O. M., Hydrogen Storage in Microporous Metal-Organic Frameworks. *Science* **2003**, *300*, 1127.
14. Belof, J. L.; Stern, A. C.; Eddaoudi, M.; Space, B., On the Mechanism of Hydrogen Storage in a Metal−Organic Framework Material. *Journal of the American Chemical Society* **2007**, *129*, 15202-15210.
15. Berenguer-Murcia, Á.; Marco-Lozar, J. P.; Cazorla-Amorós, D., Hydrogen Storage in Porous Materials: Status, Milestones, and Challenges. *The Chemical Record* **2018**, *18*, 900-912.

16. Han, S. S.; Furukawa, H.; Yaghi, O. M.; Goddard, W. A., Covalent Organic Frameworks as Exceptional Hydrogen Storage Materials. *Journal of the American Chemical Society* **2008**, *130*, 11580-11581.

17. Eberle, U.; Felderhoff, M.; Schüth, F., Chemical and Physical Solutions for Hydrogen Storage. *Angewandte Chemie International Edition* **2009**, *48*, 6608-6630.

18. Kojima, Y., Hydrogen Storage Materials for Hydrogen and Energy Carriers. *International Journal of Hydrogen Energy* **2019**, *44*, 18179-18192.

19. Chen, Z.; Ma, Z.; Zheng, J.; Li, X.; Akiba, E.; Li, H.-W., Perspectives and Challenges of Hydrogen Storage in Solid-State Hydrides. *Chinese Journal of Chemical Engineering* **2021**, *29*, 1-12.

20. Iwakura, C.; Asaoka, T.; Yoneyama, H.; Sakai, T.; Ishikawa, H.; Oguro, K., Electrochemical Characteristics of Lani5 System Hydrogen-Absorbing Alloys as Negative Electrode Materials for Nickel-Hydrogen Batteries. *J Chem Soc Jpn, Chem Ind Chem* **1988**, 1481-1488.

21. Kojima, Y.; Kawai, Y.; Towata, S.-i.; Matsunaga, T.; Shinozawa, T.; Kimbara, M., Development of Metal Hydride with High Dissociation Pressure. *Journal of Alloys and Compounds* **2006**, *419*, 256-261.

22. Cui, J.; Liu, J.; Wang, H.; Ouyang, L.; Sun, D.; Zhu, M.; Yao, X., Mg–Tm (Tm: Ti, Nb, V, Co, Mo or Ni) Core–Shell Like Nanostructures: Synthesis, Hydrogen Storage Performance and Catalytic Mechanism. *Journal of Materials Chemistry A* **2014**, *2*, 9645-9655.

23. Hou, Q.; Yang, X.; Zhang, J., Review on Hydrogen Storage Performance of MgH_2: Development and Trends. *ChemistrySelect* **2021**, *6*, 1589-1606.

24. Nobuki, T.; Okuzumi, Y.; Hatate, M.; Crivello, J.-C.; Cuevas, F.; Joubert, J.-M., Mechanosynthesis and Reversible Hydrogen Storage of Mg_2Ni and Mg_2Cu Alloys. *Materials Transactions* **2019**, *60*, 441-449.

25. Suárez-Alcántara, K.; Tena-Garcia, J. R.; Guerrero-Ortiz, R., Alanates, a Comprehensive Review. *Materials (Basel)* **2019**, *12*, 2724.

26. Hauback, B.C.; Brinks, H.W.; Fjellvåg, H. Accurate structure of $LiAlD_4$ studied by combined powder neutron and X-ray diffraction. *Journal of Alloys and Compounds* **2002**, 346, 184–189.

27. Vajeeston, P.; Ravindran, P.; Vidya, R.; Fjellvåg, H.; Kjekshus, A. Huge-pressure-induced volume collapse in $LiAlH_4$ and its implications to hydrogen storage. *Physical Review B* **2003**, 68, 212101.

28. Lauher, J. W.; Dougherty, D.; Herley, P. J., Sodium Tetrahydroaluminate. *Acta Crystallographica Section B* **1979**, *35*, 1454-1456.

29. Hauback, B.C.; Brinks, H.W.; Heyn, R.H.; Blom, R.; Fjellvag, H. The crystal structure of $KAlD_4$. *Journal of Alloys and Compounds* **2005**, 394, 35–38.

30. Fossdal, A.; Brinks, H.W.; Fichtner, M.; Hauback, B.C. Determination of the crystal structure of $Mg(AlH_4)_2$ by combined X-ray and neutron diffraction. *Journal of Alloys and Compounds* **2005**, 387, 47–51.

31. Grove, H.; Brinks, H.W.; Heyn, R.H.; Wu, F.-J.; Opalka, S.M.; Tang, X.; Laube, B.L.; Hauback, B.C. The structure of $LiMg(AlD_4)_3$. *Journal of Alloys and Compounds* **2008**, 455, 249–254.

32. Liu, D.M.; Qian, Z.X.; Si, T.Z.; Zhang, Q.A. Synthesis, crystal structure and thermal decomposition of $LiCa(AlH_4)_3$. *Journal of Alloys and Compounds* **2012**, 520, 202–206.

33. Løvvik, O.; Opalka, S.; Brinks, W.H.; Hauback, B.C. Crystal structure and thermodynamic stability of the lithium alanates $LiAlH_4$ and Li_3AlH_6. *Physical Review B* **2004**, 69, 134117.

34. Canton, P.; Fichtner, M.; Frommen, C.; Léon, A. Synchrotron X-ray studies of Ti-doped $NaAlH_4$. *The Journal of Physical Chemistry B* **2006**, 110, 3051–3054.

35. Vajeeston, P.; Ravindran, P.; Kjekhus, A.; Fjellvåg, H. First-principles investigations of aluminum hydrides: M_3AlH_6 (M = Na, K). *Physical Review B* **2005**, 71, 092103.

36. Brinks, H.W.; Huback, B.C.; Jensen, C.M.; Zidan, R. Synthesis and crystal structure of Na_2LiAlD_6. *Journal of Alloys and Compounds* **2005**, 392, 27–30.

37. Rönnebro, E.; Majzoub, E.H. Crystal structure, Raman spectroscopy and Ab initio calculations of a new bialkali alanate K_2LiAlH_6. *The Journal of Physical Chemistry B* **2006**, 110, 25686–25691.

38. Sørby, M.H.; Brinks, H.W.; Fossdal, A.; Thorshaung, K.; Hauback, B.C. The crystal structure and stability of K_2NaAlH_6. Journal of Alloys and Compounds **2006**, 415, 284–287.

39. Hauback, B. C.; Brinks, H. W.; Jensen, C. M.; Murphy, K.; Maeland, A. J., Neutron Diffraction Structure Determination of $NaAlD_4$. *Journal of Alloys and Compounds* **2003**, *358*, 142-145.

40. Fichtner, M.; Fuhr, O., Synthesis and Structures of Magnesium Alanate and Two Solvent Adducts. *Journal of Alloys and Compounds* **2002**, *345*, 286-296.

41. Sato, T.; Sørby, M. H.; Ikeda, K.; Sato, S.; Hauback, B. C.; Orimo, S., Syntheses, Crystal Structures, and Thermal Analyses of Solvent-Free $Ca(AlD_4)_2$ and $CaAlD_5$. *Journal of Alloys and Compounds* **2009**, *487*, 472-478.

42. Orimo, S.-i.; Nakamori, Y.; Eliseo, J. R.; Züttel, A.; Jensen, C. M., Complex Hydrides for Hydrogen Storage. *Chemical Reviews* **2007**, *107*, 4111-4132.

43. Blanchard, D.; Brinks, H. W.; Hauback, B. C.; Norby, P., Desorption of $LiAlH_4$ with Ti- and V-Based Additives. *Materials Science and Engineering: B* **2004**, *108*, 54-59.

44. Balema, V. P.; Dennis, K. W.; Pecharsky, V. K., Rapid Solid-State Transformation of Tetrahedral [AlH] into Octahedral [AlH] in Lithium Aluminohydride. *Chemical Communications* **2000**, 1665-1666.

45. Chen, J.; Kuriyama, N.; Xu, Q.; Takeshita, H. T.; Sakai, T., Reversible Hydrogen Storage Via Titanium-Catalyzed $LiAlH_4$ and Li_3AlH_6. *The Journal of Physical Chemistry B* **2001**, *105*, 11214-11220.

46. Claudy, P.; Bonnetot, B.; Chahine, G.; Letoffe, J. M., Etude Du Comportement Thermique Du Tetrahydroaluminate De Sodium $NaAlH_4$ Et De L'hexahydroaluminate De Sodium Na_3AlH_6 De 298 a 600 K. *Thermochimica Acta* **1980**, *38*, 75-88.

47. Ali, N. A.; Ismail, M., Modification of Naalh4 Properties Using Catalysts for Solid-State Hydrogen Storage: A Review. *International Journal of Hydrogen Energy* **2021**, *46*, 766-782.

48. Bogdanović, B.; Sandrock, G., Catalyzed Complex Metal Hydrides. *MRS Bulletin* **2002**, *27*, 712-716.

49. Ashby, E. C.; Kobetz, P., The Direct Synthesis of Na_3AlH_6. *Inorganic Chemistry* **1966**, *5*, 1615-1617.

50. Dilts, J. A.; Ashby, E. C., Thermal Decomposition of Complex Metal Hydrides. *Inorganic Chemistry* **1972**, *11*, 1230-1236.

51. Dymova, T.; Eliseeva, N.; Bakum, S.; Dergachev, Y. M., Direct Synthesis of Alcali Metal Alumohydrides in Melts. *Doklady Akademii Nauk SSSR* **1974**, *215*, 1369-1372.

52. Wang, P.; Jensen, C. M., Method for Preparing Ti-Doped $NaAlH_4$ Using

Ti Powder: Observation of an Unusual Reversible Dehydrogenation Behavior. *Journal of Alloys and Compounds* **2004**, *379*, 99-102.

53. Fan, X.; Xiao, X.; Chen, L.; Zhang, L.; Shao, J.; Li, S.; Ge, H.; Wang, Q., Significantly Improved Hydrogen Storage Properties of $NaAlH_4$ Catalyzed by Ce-Based Nanoparticles. *Journal of Materials Chemistry A* **2013**, *1*, 9752-9759.

54. Srinivasan, S. S.; Brinks, H. W.; Hauback, B. C.; Sun, D.; Jensen, C. M., Long Term Cycling Behavior of Titanium Doped $NaAlH_4$ Prepared through Solvent Mediated Milling of NaH and Al with Titanium Dopant Precursors. *Journal of Alloys and Compounds* **2004**, *377*, 283-289.

55. Sun, D.; Srinivasan, S. S.; Chen, G.; Jensen, C. M., Rehydrogenation and Cycling Studies of Dehydrogenated $NaAlH_4$. *Journal of Alloys and Compounds* **2004**, *373*, 265-269.

56. Wan, Q.; Li, P.; Li, Z.; Zhao, K.; Liu, Z.; Wang, L.; Zhai, F.; Qu, X.; Volinsky, A. A., $NaAlH_4$ Dehydrogenation Properties Enhanced by $MnFe_2O_4$ Nanoparticles. *Journal of Power Sources* **2014**, *248*, 388-395.

57. Mao, J.; Guo, Z.; Liu, H., Improved Hydrogen Sorption Performance of NbF_5-Catalysed $NaAlH_4$. *International Journal of Hydrogen Energy* **2011**, *36*, 14503-14511.

58. Morioka, H.; Kakizaki, K.; Chung, S.-C.; Yamada, A., Reversible Hydrogen Decomposition of $KAlH_4$. *Journal of Alloys and Compounds* **2003**, *353*, 310-314.

59. Ares, J. R.; Aguey-Zinsou, K.-F.; Leardini, F.; Ferrer, I. J.; Fernandez, J.-F.; Guo, Z.-X.; Sánchez, C., Hydrogen Absorption/Desorption Mechanism in Potassium Alanate ($KAlH_4$) and Enhancement by $TiCl_3$ Doping. *The Journal of Physical Chemistry C* **2009**, *113*, 6845-6851.

60. Fichtner, M.; Fuhr, O.; Kircher, O., Magnesium Alanate—a Material for Reversible Hydrogen Storage? *Journal of Alloys and Compounds* **2003**, *356-357*, 418-422.

61. Pang, Y.; Liu, Y.; Zhang, X.; Gao, M.; Pan, H., Role of Particle Size, Grain Size, Microstrain and Lattice Distortion in Improved Dehydrogenation Properties of the Ball-Milled $Mg(AlH_4)_2$. *International Journal of Hydrogen Energy* **2013**, *38*, 1460-1468.

62. Wang, J.; Ebner, A. D.; Ritter, J. A., On the Reversibility of Hydrogen Storage in Novel Complex Hydrides. *Adsorption* **2005**, *11*, 811-816.

63. Pang, Y.; Liu, Y.; Zhang, X.; Gao, M.; Pan, H., TiF_4-Doped $Mg(AlH_4)_2$ with Significantly Improved Dehydrogenation Properties. *International Journal of Hydrogen Energy* **2013**, *38*, 13343-13351.

64. Xiao, X.; Qin, T.; Jiang, Y.; Jiang, F.; Li, M.; Fan, X.; Li, S.; Ge, H.; Wang, Q.; Chen, L., Significantly Enhanced Hydrogen Desorption Properties of $Mg(AlH_4)_2$ Nanoparticles Synthesized Using Solvent Free Strategy. *Progress in Natural Science: Materials International* **2017**, *27*, 112-120.

65. Mamatha, M.; Weidenthaler, C.; Pommerin, A.; Felderhoff, M.; Schüth, F., Comparative Studies of the Decomposition of Alanates Followed by in Situ XRD and DSC Methods. *Journal of Alloys and Compounds* **2006**, *416*, 303-314.

66. Li, C.; Xiao, X.; Ge, P.; Xue, J.; Li, S.; Ge, H.; Chen, L., Investigation on Synthesis, Structure and Catalytic Modification of $Ca(AlH_4)_2$ Complex Hydride. *International Journal of Hydrogen Energy* **2012**, *37*, 936-941.

67. Chen, P.; Xiong, Z.; Luo, J.; Lin, J.; Tan, K. L., Interaction between Lithium Amide and Lithium Hydride. *Journal of Physical Chemistry B* **2003**, *107*, 10967-10970.

68. Xiong, Z.; Wu, G.; Hu, J.; Chen, P., Ternary Imides for Hydrogen Storage. *Advanced Materials* **2004**, *16*, 1522-1525.

69. Dolotko, O.; Paulson, N.; Pecharsky, V. K., Thermochemical Transformations in 2 MNH_2–3 MgH_2 Systems (M=Li or Na). *International Journal of Hydrogen Energy* **2010**, *35*, 4562-4568.

70. Chater, P. A.; David, W. I. F.; Anderson, P. A., Synthesis and Structure of the New Complex Hydride $Li_2BH_4NH_2$. *Chemical Communications* **2007**, 4770-4772.

71. Zheng, X.; Wu, G.; He, T.; Chu, H.; Chen, H.; Chen, P., Improved Hydrogen Desorption Properties of Co-Doped Li_2BNH_6. *Chinese Science Bulletin* **2011**, *56*, 2481-2485.

72. Pinkerton, F. E.; Meisner, G. P.; Meyer, M. S.; Balogh, M. P.; Kundrat, M. D., Hydrogen Desorption Exceeding Ten Weight Percent from the New Quaternary Hydride $Li_3BN_2H_8$. *The Journal of Physical Chemistry B* **2005**, *109*, 6-8.

73. Pinkerton, F. E.; Meyer, M. S., Hydrogen Desorption Behavior of Nickel-Chloride-Catalyzed Stoichiometric $Li_4BN_3H_{10}$. *The Journal of Physical Chemistry C* **2009**, *113*, 11172-11176.

74. Zheng, X.; Xiong, Z.; Lim, Y.; Wu, G.; Chen, P.; Chen, H., Improving Effects of Lih and Co-Catalyst on the Dehydrogenation of $Li_4BN_3H_{10}$. *The Journal of Physical Chemistry C* **2011**, *115*, 8840-8844.

75. Yu, X. B.; Guo, Y. H.; Sun, D. L.; Yang, Z. X.; Ranjbar, A.; Guo, Z. P.; Liu, H. K.; Dou, S. X., A Combined Hydrogen Storage System of $Mg(BH_4)_2$−$LiNH_2$ with Favorable Dehydrogenation. *The Journal of Physical Chemistry C* **2010**, *114*, 4733-4737.

76. Chu, H.; Xiong, Z.; Wu, G.; Guo, J.; He, T.; Chen, P., Improved Dehydrogenation Properties of $Ca(BH_4)_2$-$LiNH_2$ Combined System. *Dalton Transactions* **2010**, 39, 10585-10587.

77. Yu, X. B.; Yang, Z. X.; Guo, Y. H.; Li, S. G., Thermal Decomposition Performance of $Ca(BH_4)_2$/$LiNH_2$ Mixtures. *Journal of Alloys and Compounds* **2011**, *509*, S724-S727.

78. Zhang, Y.; Tian, Q., The Reactions in $LiBH_4$–$NaNH_2$ Hydrogen Storage System. *International Journal of Hydrogen Energy* **2011**, *36*, 9733-9742.

79. Somer, M.; Acar, S.; Koz, C.; Kokal, I.; Höhn, P.; Cardoso-Gil, R.; Aydemir, U.; Akselrud, L., A- and B-$Na_2[BH_4][NH_2]$: Two Modifications of a Complex Hydride in the System $NaNH_2$–$NaBH_4$; Syntheses, Crystal Structures, Thermal Analyses, Mass and Vibrational Spectra. *Journal of Alloys and Compounds* **2010**, *491*, 98-105.

80. Wu, C.; Bai, Y.; Yang, J.-h.; Wu, F.; Long, F., Characterizations of Composite $NaNH_2$–$NaBH_4$ Hydrogen Storage Materials Synthesized Via Ball Milling. *International Journal of Hydrogen Energy* **2012**, *37*, 889-893.

81. Poonyayant, N.; Stavila, V.; Majzoub, E. H.; Klebanoff, L. E.; Behrens, R.; Angboonpong, N.; Ulutagay-Kartin, M.; Pakawatpanurut, P.; Hecht, E. S.; Breit, J. S., An Investigation into the Hydrogen Storage Characteristics of $Ca(BH_4)_2$/$LiNH_2$ and $Ca(BH_4)_2$/$NaNH_2$: Evidence of Intramolecular Destabilization. *The Journal of Physical Chemistry C* **2014**, *118*, 14759-14769.

82. Xiong, Z.; Hu, J.; Wu, G.; Chen, P.; Luo, W.; Gross, K.; Wang, J., Thermodynamic and Kinetic Investigations of the Hydrogen Storage in the Li–Mg–N–H System. *Journal of Alloys and Compounds* **2005**, *398*, 235-239.

83. Leng, H. Y.; Ichikawa, T.; Hino, S.; Kanada, N.; Isobe, S.; Fujii, H., New Metal-N-H System Composed of $Mg(NH_2)_2$ and LiH for Hydrogen Storage. *Journal of Physical Chemistry B* **2004**, *108*, 8763-8765.

84. Nakamori, Y.; Kitahara, G.; Orimo, S., Synthesis and Dehydriding Studies

of Mg–N–H Systems. *Journal of Power Sources* **2004**, *138*, 309-312.

85. Chen, X. Y.; Guo, Y. H.; Yu, X. B., Enhanced Dehydrogenation Properties of Modified $Mg(NH_2)_2$−$LiBH_4$ Composites. *The Journal of Physical Chemistry C* **2010**, *114*, 17947-17953.

86. Noritake, T.; Miwa, K.; Aoki, M.; Matsumoto, M.; Towata, S.-i.; Li, H.-W.; Orimo, S.-i., Dehydrogenation Properties and Crystal Structure Analysis of $Mg(BH_4)(NH_2)$. *Journal of Alloys and Compounds* **2013**, *580*, S85-S89.

87. Chu, H.; Wu, G.; Zhang, Y.; Xiong, Z.; Guo, J.; He, T.; Chen, P., Improved Dehydrogenation Properties of Calcium Borohydride Combined with Alkaline-Earth Metal Amides. *The Journal of Physical Chemistry C* **2011**, *115*, 18035-18041.

88. Chen, P.; Xiong, Z.; Luo, J.; Lin, J.; Tan, K. L., Interaction of Hydrogen with Metal Nitrides and Imides. *Nature* **2002**, *420*, 302-304.

89. Hu, J.; Weidner, E.; Hoelzel, M.; Fichtner, M., Functions of $LiBH_4$ in the Hydrogen Sorption Reactions of the 2 LiH–$Mg(NH_2)_2$ System. *Dalton Transactions* **2010**, *39*, 9100-9107.

90. Xiong, Z.; Wu, G.; Hu, J.; Liu, Y.; Chen, P.; Luo, W.; Wang, J., Reversible Hydrogen Storage by a Li–Al–N–H Complex. *Advanced Functional Materials* **2007**, *17*, 1137-1142.

91. Morelle, F.; Jepsen, L. H.; Jensen, T. R.; Sharma, M.; Hagemann, H.; Filinchuk, Y., Reaction Pathways in $Ca(BH_4)_2$–$NaNH_2$ and $Mg(BH_4)_2$–$NaNH_2$ Hydrogen-Rich Systems. *The Journal of Physical Chemistry C* **2016**, *120*, 8428-8435.

92. Chua, Y. S.; Wu, G.; Xiong, Z.; Chen, P., Investigations on the Solid State Interaction between $LiAlH_4$ and $NaNH_2$. *Journal of Solid State Chemistry* **2010**, *183*, 2040-2044.

93. Suárez-Alcántara, K.; Tena García, J. R., Metal Borohydrides Beyond Groups I and II: A Review. *Materials* **2021**, *14*.

94. Li, H.-W.; Yan, Y.; Orimo, S.-i.; Züttel, A.; Jensen, C. M. Recent Progress in Metal Borohydrides for Hydrogen Storage *Energies* **2011**, DOI: 10.3390/en4010185.

95. Paskevicius, M.; Jepsen, L. H.; Schouwink, P.; Černý, R.; Ravnsbæk, D. B.; Filinchuk, Y.; Dornheim, M.; Besenbacher, F.; Jensen, T. R., Metal Borohydrides and Derivatives – Synthesis, Structure and Properties. *Chemical Society Reviews* **2017**, *46*, 1565-1634.

96. Soulié, J. P.; Renaudin, G.; Černý, R.; Yvon, K., Lithium Boro-Hydride $LiBH_4$: I. Crystal Structure. *Journal of Alloys and Compounds* **2002**, *346*, 200-205.
97. Filinchuk, Y.; Chernyshov, D.; Nevidomskyy, A.; Dmitriev, V., High-Pressure Polymorphism as a Step Towards Destabilization of $LiBH_4$. *Angewandte Chemie International Edition* **2008**, *47*, 529-532.
98. Abrahams, S. C.; Kalnajs, J., The Lattice Constants of the Alkali Borohydrides and the Low‐Temperature Phase of Sodium Borohydride. *The Journal of Chemical Physics* **2004**, *22*, 434-436.
99. Babanova, O. A.; Soloninin, A. V.; Stepanov, A. P.; Skripov, A. V.; Filinchuk, Y., Structural and Dynamical Properties of $NaBH_4$ and KBH_4: NMR and Synchrotron X-Ray Diffraction Studies. *The Journal of Physical Chemistry C* **2010**, *114*, 3712-3718.
100. Filinchuk, Y.; Talyzin, A. V.; Chernyshov, D.; Dmitriev, V., High-Pressure Phase of $NaBH_4$: Crystal structure from synchrotron powder diffraction data:. *Physical Review B* **2007**, *76*, 092104.
101. Filinchuk, Y.; Černý, R.; Hagemann, H., Insight into $Mg(BH_4)_2$ with Synchrotron X-Ray Diffraction: Structure Revision, Crystal Chemistry, and Anomalous Thermal Expansion. *Chemistry of Materials* **2009**, *21*, 925-933.
102. Černý, R.; Filinchuk, Y.; Hagemann, H.; Yvon, K., Magnesium Borohydride: Synthesis and Crystal Structure. *Angewandte Chemie International Edition* **2007**, *46*, 5765-5767.
103. Her, J.-H.; Stephens, P. W.; Gao, Y.; Soloveichik, G. L.; Rijssenbeek, J.; Andrus, M.; Zhao, J.-C., Structure of Unsolvated Magnesium Borohydride $Mg(BH_4)_2$. *Acta Crystallographica Section B* **2007**, *63*, 561-568.
104. Pitt, M. P.; Webb, C. J.; Paskevicius, M.; Sheptyakov, D.; Buckley, C. E.; Gray, E. M., In Situ Neutron Diffraction Study of the Deuteration of Isotopic $Mg^{11}B_2$. *The Journal of Physical Chemistry C* **2011**, *115*, 22669-22679.
105. Filinchuk, Y.; Richter, B.; Jensen, T. R.; Dmitriev, V.; Chernyshov, D.; Hagemann, H., Porous and Dense Magnesium Borohydride Frameworks: Synthesis, Stability, and Reversible Absorption of Guest Species. *Angewandte Chemie International Edition* **2011**, *50*, 11162-11166.
106. Richter, B.; Ravnsbæk, D. B.; Tumanov, N.; Filinchuk, Y.; Jensen, T. R., Manganese Borohydride; Synthesis and Characterization. *Dalton Transactions* **2015**, *44*, 3988-3996.

107. Filinchuk, Y.; Rönnebro, E.; Chandra, D., Crystal Structures and Phase Transformations in $Ca(BH_4)_2$. *Acta Materialia* **2009**, *57*, 732-738.
108. Buchter, F., et al., Structure of $Ca(BD_4)_2$ B-Phase from Combined Neutron and Synchrotron X-Ray Powder Diffraction Data and Density Functional Calculations. *The Journal of Physical Chemistry B* **2008**, *112*, 8042-8048.
109. Sato, T.; Miwa, K.; Nakamori, Y.; Ohoyama, K.; Li, H.-W.; Noritake, T.; Aoki, M.; Towata, S.-i.; Orimo, S.-i., Experimental and Computational Studies on Solvent-free Rare-earth Metal Borohydrides $R(BH_4)_3$ (R=Y, Dy, and Gd). *Physical Review B* **2008**, *77*, 104114.
110. Frommen, C.; Aliouane, N.; Deledda, S.; Fonneløp, J. E.; Grove, H.; Lieutenant, K.; Llamas-Jansa, I.; Sartori, S.; Sørby, M. H.; Hauback, B. C., Crystal Structure, Polymorphism, and Thermal Properties of Yttrium Borohydride $Y(BH_4)_3$. *Journal of Alloys and Compounds* **2010**, *496*, 710-716.
111. Orimo, S.; Nakamori, Y.; Kitahara, G.; Miwa, K.; Ohba, N.; Towata, S.; Züttel, A., Dehydriding and Rehydriding Reactions of $LiBH_4$. *Journal of Alloys and Compounds* **2005**, *404-406*, 427-430.
112. Huang, Z.-Q.; Chen, W.-C.; Chuang, F.-C.; Majzoub, E. H.; Ozoliņš, V., First-Principles Calculated Decomposition Pathways for $LiBH_4$ *Nanoclusters. Scientific Reports* **2016**, *6*, 26056.
113. Vajo, J. J.; Skeith, S. L.; Mertens, F., Reversible Storage of Hydrogen in Destabilized $LiBH_4$. *The Journal of Physical Chemistry B* **2005**, *109*, 3719-3722.
114. Bösenberg, U., et al., Hydrogen Sorption Properties of MgH_2–$LiBH_4$ Composites. *Acta Materialia* **2007**, *55*, 3951-3958.
115. Au, M.; Jurgensen, A.; Zeigler, K., Modified Lithium Borohydrides for Reversible Hydrogen Storage (2). *The Journal of Physical Chemistry B* **2006**, *110*, 26482-26487.
116. Xia, G.; Tan, Y.; Chen, X.; Fang, F.; Sun, D.; Li, X.; Guo, Z.; Yu, X., Oxygen-Free Layer-by-Layer Assembly of Lithiated Composites on Graphene for Advanced Hydrogen Storage. *Advanced Science* **2017**, *4*, 1600257.
117. Ngene, P.; van den Berg, R.; Verkuijlen, M. H. W.; de Jong, K. P.; de Jongh, P. E., Reversibility of the Hydrogen Desorption from $NaBH_4$ by Confinement in Nanoporous Carbon. *Energy & Environmental Science* **2011**, *4*, 4108-4115.
118. Chłopek, K.; Frommen, C.; Léon, A.; Zabara, O.; Fichtner, M., Synthesis

and Properties of Magnesium Tetrahydroborate, $Mg(BH_4)_2$. *Journal of Materials Chemistry* **2007**, *17*, 3496-3503.

119. Bardají, E. G.; Hanada, N.; Zabara, O.; Fichtner, M., Effect of Several Metal Chlorides on the Thermal Decomposition Behaviour of α-$Mg(BH_4)_2$. *International Journal of Hydrogen Energy* **2011**, *36*, 12313-12318.

120. Wang, X.; Xiao, X.; Zheng, J.; Huang, X.; Chen, M.; Chen, L., In-Situ Synthesis of Amorphous $Mg(BH_4)_2$ and Chloride Composite Modified by NbF_5 for Superior Reversible Hydrogen Storage Properties. *International Journal of Hydrogen Energy* **2020**, *45*, 2044-2053.

121. Yan, Y.; Li, H.-W.; Sato, T.; Umeda, N.; Miwa, K.; Towata, S.-i.; Orimo, S.-i., Dehydriding and Rehydriding Properties of Yttrium Borohydride $Y(BH_4)_3$ Prepared by Liquid-Phase Synthesis. *International Journal of Hydrogen Energy* **2009**, *34*, 5732-5736.

122. Owarzany, R.; Leszczyński, P. J.; Fijalkowski, K. J.; Grochala, W. Mono- and Bimetalic Amidoboranes *Crystals* **2016**, DOI: 10.3390/cryst6080088.

123. Xiong, Z., et al., High-Capacity Hydrogen Storage in Lithium and Sodium Amidoboranes. *Nature Materials* **2007**, *7*, 138.

124. Wu, C.; Wu, G.; Xiong, Z.; Han, X.; Chu, H.; He, T.; Chen, P., $LiNH_2BH_3{\cdot}NH_3BH_3$: Structure and Hydrogen Storage Properties. *Chemistry of Materials* **2010**, *22*, 3-5.

125. Diyabalanage, H. V. K., et al., Potassium(I) Amidotrihydroborate: Structure and Hydrogen Release. *Journal of the American Chemical Society* **2010**, *132*, 11836-11837.

126. Wu, H.; Zhou, W.; Yildirim, T., Alkali and Alkaline-Earth Metal Amidoboranes: Structure, Crystal Chemistry, and Hydrogen Storage Properties. *Journal of the American Chemical Society* **2008**, *130*, 14834-14839.

127. Wu, C.; Wu, G.; Xiong, Z.; David, W. I. F.; Ryan, K. R.; Jones, M. O.; Edwards, P. P.; Chu, H.; Chen, P., Stepwise Phase Transition in the Formation of Lithium Amidoborane. *Inorganic Chemistry* **2010**, *49*, 4319-4323.

128. Luo, J.; Kang, X.; Wang, P., Synthesis, Formation Mechanism, and Dehydrogenation Properties of the Long-Sought $Mg(NH_2BH_3)_2$ Compound. *Energy & Environmental Science* **2013**, *6*, 1018-1025.

129. Fijałkowski, K. J.; Grochala, W., Substantial Emission of NH_3 During Thermal Decomposition of Sodium Amidoborane, $NaNH_2BH_3$. *Journal of*

Materials Chemistry **2009**, *19*, 2043-2050.

130. Diyabalanage, H. V. K.; Shrestha, R. P.; Semelsberger, T. A.; Scott, B. L.; Bowden, M. E.; Davis, B. L.; Burrell, A. K., Calcium Amidotrihydroborate: A Hydrogen Storage Material. *Angewandte Chemie International Edition* **2007**, *46*, 8995-8997.

131. Fijalkowski, K. J.; Genova, R. V.; Filinchuk, Y.; Budzianowski, A.; Derzsi, M.; Jaroń, T.; Leszczyński, P. J.; Grochala, W., $Na[Li(NH_2BH_3)_2]$ – the First Mixed-Cation Amidoborane with Unusual Crystal Structure. *Dalton Transactions* **2011**, *40*, 4407-4413.

132. Wu, H.; Zhou, W.; Pinkerton, F. E.; Meyer, M. S.; Yao, Q.; Gadipelli, S.; Udovic, T. J.; Yildirim, T.; Rush, J. J., Sodium Magnesium Amidoborane: The First Mixed-Metal Amidoborane. *Chemical Communications* **2011**, *47*, 4102-4104.

133. Chua, Y. S.; Li, W.; Wu, G.; Xiong, Z.; Chen, P., From Exothermic to Endothermic Dehydrogenation – Interaction of Monoammoniate of Magnesium Amidoborane and Metal Hydrides. *Chemistry of Materials* **2012**, *24*, 3574-3581.

134. Biliškov, N.; Borgschulte, A.; Užarević, K.; Halasz, I.; Lukin, S.; Milošević, S.; Milanović, I.; Novaković, J. G., In-Situ and Real-Time Monitoring of Mechanochemical Preparation of $Li_2Mg(NH_2BH_3)_4$ and $Na_2Mg(NH_2BH_3)_4$ and Their Thermal Dehydrogenation. *Chemistry – A European Journal* **2017**, *23*, 16274-16282.

135. Milanović, I.; Biliškov, N.; Užarević, K.; Lukin, S.; Etter, M.; Halasz, I., Mechanochemical Synthesis and Thermal Dehydrogenation of Novel Calcium-Containing Bimetallic Amidoboranes. *ACS Sustainable Chemistry & Engineering* **2021**, *9*, 2089-2099.

136. Dovgaliuk, I.; Jepsen, L. H.; Safin, D. A.; Łodziana, Z.; Dyadkin, V.; Jensen, T. R.; Devillers, M.; Filinchuk, Y., A Composite of Complex and Chemical Hydrides Yields the First Al-Based Amidoborane with Improved Hydrogen Storage Properties. *Chemistry – A European Journal* **2015**, *21*, 14562-14570.

137. Møller, K. T.; Jørgensen, M.; Andreasen, J. G.; Skibsted, J.; Łodziana, Z.; Filinchuk, Y.; Jensen, T. R., Synthesis and Thermal Decomposition of Potassium Tetraamidoboranealuminate, $K[Al(NH_2BH_3)_4]$. *International Journal of Hydrogen Energy* **2018**, *43*, 311-321.

138. Fijalkowski, K. J.; Jaroń, T.; Leszczyński, P. J.; Magos-Palasyuk, E.; Palasyuk, T.; Cyrański, M. K.; Grochala, W., $M(BH_3NH_2BH_2NH_2BH_3)$ – the Missing Link in the Mechanism of the Thermal Decomposition of Light Alkali Metal Amidoboranes. *Physical Chemistry Chemical Physics* **2014**, *16*, 23340-23346.

139. Kang, X.; Luo, J.; Zhang, Q.; Wang, P., Combined Formation and Decomposition of Dual-Metal Amidoborane $NaMg(NH_2BH_3)_3$ for High-Performance Hydrogen Storage. *Dalton Transactions* **2011**, *40*, 3799-3801.

140. Kang, X.-D.; Luo, J.-H.; Wang, P., Efficient and Highly Rapid Hydrogen Release from Ball-Milled 3 $NH_3BH_3/MMgH_3$ (M=Na, K, Rb) Mixtures at Low Temperatures. *International Journal of Hydrogen Energy* **2012**, *37*, 4259-4266.

141. Hawthorne, M. F.; Jalisatgi, S. S.; Safronov, A. V.; Lee, H. B.; Wu, J. *Chemical Hydrogen Storage Using Polyhedral Borane Anions and Aluminum-Ammonia-Borane Complexes*; United States, 2010-10-01, 2010.

142. Xia, G.; Tan, Y.; Chen, X.; Guo, Z.; Liu, H.; Yu, X., Mixed-Metal (Li, Al) Amidoborane: Synthesis and Enhanced Hydrogen Storage Properties. *Journal of Materials Chemistry A* **2013**, *1*, 1810-1820.

143. Martin, D., Thermodynamics of Metal Hydrides: Tailoring Reaction Enthalpies of Hydrogen Storage Materials. *Rijeka*, **2011**, *33*, 891-918

144. Yahya, M. S.; Ali, N. A.; Sazelee, N. A.; Mustafa, N. S.; Halim Yap, F. A.; Ismail, M., Intensive Investigation on Hydrogen Storage Properties and Reaction Mechanism of the $NaBH_4$-Li_3AlH_6 Destabilized System. *International Journal of Hydrogen Energy* **2019**, *44*, 21965-21978.

145. Ismail, M.; Zhao, Y.; Yu, X. B.; Mao, J. F.; Dou, S. X., The Hydrogen Storage Properties and Reaction Mechanism of the MgH_2–$NaAlH_4$ Composite System. *International Journal of Hydrogen Energy* **2011**, *36*, 9045-9050.

146. Li Y, Li P, Tan Q, Zhang Z, Wan Q, Liu Z, et al. Thermal properties and cycling performance of $Ca(BH_4)_2/MgH_2$ composite for energy storage. *Chemical Physics Letters* **2018**, *700*, 44-49.

147. Vajo JJ, Salguero TT, Gross AF, Skeith SL, Olson GL. Thermodynamic destabilization and reaction kinetics in light metal hydride systems. *Journal of Alloys and Compounds* **2007**, *446-447*, 409-414.

148. Gao M, Gu J, Pan H, Wang Y, Liu Y, Liang C, et al. $Ca(BH_4)_2$-$LiBH_4$-MgH_2: a novel ternary hydrogen storage system with superior long-term cycling performance. *Journal of Materials Chemistry A* **2013**, *1*, 12285-12292.

149. Wei J, Leng H, Li Q, Chou K-C. Improved hydrogen storage properties of $LiBH_4$ doped Li-N-H system. *International Journal of Hydrogen Energy* **2014**, *39*,13609-13615.
150. Gizer G, Puszkiel J, Cao H, Pistidda C, Le TT, Dornheim M, et al. Tuning the reaction mechanism and hydrogenation/dehydrogenation properties of $6Mg(NH_2)_2$-9LiH system by adding $LiBH_4$. *International Journal of Hydrogen Energy* **2019**, *44*, 11920-11929.
151. Ali, N. A.; Sazelee, N. A.; Ismail, M., An Overview of Reactive Hydride Composite (RHC) for Solid-State Hydrogen Storage Materials. *International Journal of Hydrogen Energy* **2021**, *46*, 31674-31698.

Chapter 2

Methodology

Several techniques were employed in this thesis, including Powder X-ray diffraction (PXRD), Fourier transform infrared spectroscopy (IR), Nuclear magnetic resonance (NMR), Thermogravimetric analysis (TGA), and Mass spectrometry. In the following section, we provide a brief overview of these essential methods frequently utilized throughout this thesis.

2.1 Mechanochemical synthesis

Mechanochemical synthesis is a synthesis method that utilizes mechanical energy input, typically through grinding in ball mills, to induce reactions. Shaker mills and planetary mills are commonly employed machines for mechanochemical synthesis. In a shaker mill, jars oscillate back and forth, with the milling intensity determined by the frequency of oscillation. Shaker mills are often utilized for small samples, such as in pharmaceutical solid screening. On the other hand, in a planetary mill, the jar rotates around a central axis while simultaneously spinning around its own axis. This "planetary" motion generates centrifugal forces that mimic the effects of gravity in large-scale roller mills, making it directly applicable for scaling up processes.

In this thesis, we employed a Fritsch Planetary Micro Mill PULVERISETTE 7 for the majority of our syntheses. Comminution primarily occurs through the high-energy impact of grinding balls and partially through friction between the grinding balls and the walls of the grinding bowl. To achieve this, the grinding bowl, containing the material to be ground and grinding balls, rotates around its own axis on a main disk rotating in the opposite direction. At a certain speed, the centrifugal force causes the ground sample material and grinding balls to bounce off the inner wall of the grinding

bowl, cross the bowl diagonally at an extremely high speed and impact the material to be ground on the opposite wall of the bowl.

There is also an EASY GTM-bowl available, featuring a special lid and transmitter, which enables the transformation of a Planetary Mills premium line into an analytical measuring system for monitoring pressure and temperature during the grinding process. In addition, the actual rotational speed and power consumption can be monitored and documented. The software is a distinct safety feature, since overpressure and a rise in temperature are avoided and defects on the mill and sticking of the sample material prevented.

Figure 2.1 The photograph of the Planetary Micro Mill PULVERISETTE 7 (right) and EASY GTM-bowl (left).

In the process of the milling, the rotating speed, milling time, milling cycles and ratio of ball to powder can be used to adjust the input energy. And the break time can be used to diminish or avoid over-milling and over-heating.

2.2 Powder X-ray diffraction

2.2.1 Fundamental principles of X-ray powder diffraction

X-ray diffraction is a phenomenon where the uniform spacing of atoms in a crystal lead to the creation of an interference pattern for the waves present in an incident X-ray beam. This interaction is like the effect of a uniformly ruled diffraction grating on a beam of light. When X-rays come into contact with a crystal at an angle of incidence θ, they are “reflected” off the crystal's atoms at the same angle θ. The X-rays reflect off atomic planes within the crystal that are separated by a distance *d*. To form an interference pattern, the X-rays reflecting off different planes must interfere constructively; otherwise,

destructive interference would occur, resulting in no pattern. Consequently, the path length difference between the beams reflecting off two atomic planes must be an integer multiple (n) of the wavelength (λ), satisfying Bragg's Law: $n\lambda = 2d \cdot \sin\theta$ (Figure 2.2).

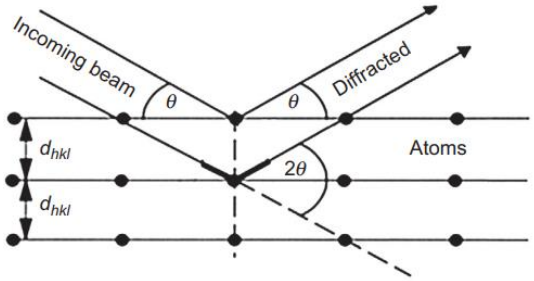

Figure 2.2 A schematic diagram of Bragg diffraction.[1]

A powder sample consists of a large number of very small crystals. In the ideal case, these crystals are much smaller than the overall size of the sample and are randomly oriented. For any given lattice spacing between planes, *d*, there are many crystals oriented in such a way that their planes make the correct Bragg angle with the incident X-ray beam. The correctly oriented crystals have all possible orientations about the incident beam, hence the diffracted beams form a cone of a semi-vertex angle of 2θ (θ is the angle between the incident beam and the *d*-planes, whereas 2θ is the angle between the incident and diffracted beams) around the incident beam. For each different lattice spacing, *d*, there is a separate cone of angle 2θ (shown in Figure 2.3). As a result, instead of observing a single point on the detector, a ring is observed, which is often referred to as a Debye-Scherrer ring.

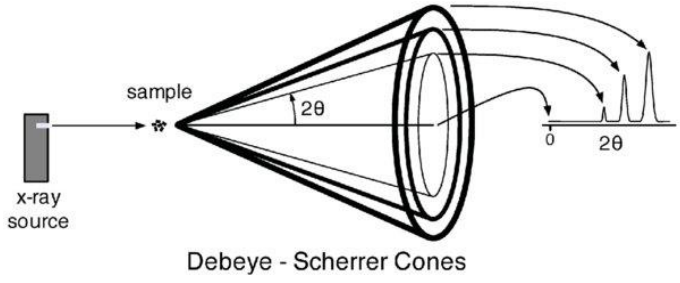

Figure 2.3 A schematic diagram of diffraction cones.[2]

X-ray Sources

1) X-ray tubes

X-rays are generated in a cathode ray tube by heating a filament to produce electrons. These electrons are then accelerated towards a target by applying a voltage, resulting in the bombardment of the target material. When the energy of the electrons is sufficient to dislodge inner shell electrons of the target material, characteristic X-ray spectra are produced. These spectra consist of several components, with the most common ones being Kα and Kβ. Kα includes Kα1 and Kα2, with Kα1 having a slightly shorter wavelength and twice the intensity compared to Kα2. The specific wavelengths depend on the target material, such as Cu, Fe, Mo, or Cr.

Table 2.1 Common target materials and corresponding wavelength of Kα and Kβ radiation in nm together with the minimum excitation potential in kV and the appropriate filter material.[1]

Target	Kα1 Kα2 Kα mean	Kβ	Excitation potential	Filter
Cr	0.22897263 0.22936513 0.22910346	0.20848881	5.98	V
Mn	0.21018543 0.21058223 0.21031770	0.19102164	6.54	Cr
Fe	0.19360413 0.19399733 0.19373520	0.17566055	7.11	Mn
Co	0.17889961 0.17928351 0.17902758	0.16208263	7.71	Fe
Ni	0.16579301 0.16617561 0.16592054	0.15001523	8.33	Co
Cu	0.15405929 0.15444274 0.15418711	0.13922346	8.98	Ni
Mo	0.07093000 0.07135900 0.07107300	0.06322880	20.0	Zr

To obtain monochromatic X-rays required for diffraction, filtering techniques using foils or crystal monochromators are necessary. Various target materials can be employed for this purpose, as listed in Table 2.1. Since Kα1 and Kα2 have wavelengths close enough, a weighted average of the two is typically used. In our laboratory, molybdenum (Mo) is utilized for powder X-ray diffraction, with Mo Kα radiation having a wavelength of 0.71073 Å.

In our Lab we used a new generation of X-ray tubes, having low power (30 or 50 W) and thus cooled by air, but producing high bright X-ray beams thanks to a multilayer focusing optic. These machines are equipped with large area detectors, MAR345 imaging plates, allowing to azimuthally integrate the Debye-Scherrer rings, thus producing low-noise data despite at moderate angular resolution. The high-resolution Lab data were obtained at Stoe Stadi M diffractometer working in Debye-Scherrer, thus also using glass capillaries containing samples. This system uses classical water-cooled X-rays tubes.

2) Synchrotron radiation

In contrast to an X-ray tube, synchrotron radiation is electromagnetic radiation generated when electrons or positrons, traveling close to the speed of light, change their direction of movement. This results in a much more intense and highly collimated beam with a tunable wavelength compared to an X-ray tube source.

The first observation of synchrotron radiation was in the laboratory in 1947 (Elder et al. 1947).[3] To date, synchrotron radiation has undergone four generations of development.[4] First-generation hard X-ray sources were parasitic on accelerators used for high-energy physics, and provision of time for materials scientists was erratic. As an accelerator became obsolete for high-energy physics, more time was released for X-ray research so long as the accelerator was not closed down. Second-generation synchrotrons were designed for fully dedicated operation using an array of bending magnets spaced around the entire ring. Third generation synchrotrons[5] were designed to optimize the number of straight sections to take advantage of the increased brilliance provided by undulators, and to a lesser extent by wigglers. The ESRF (Europe Synchrotron Radiation Faculty) was started in 1988, as the world's first third-generation synchrotron light source. There are two more powerful light sources with the potential for significantly increased peak

brilliance compared to third generation undulator sources.[6] The first is the Energy Recovery Linac (ERL). This device would use a linear accelerator with energy recovered from the electrons after a single pass (or a few passes) around a ring with undulator beamlines. The horizontal emittance would be significantly less than a storage ring, and so the brilliance could be more than 10 times that of a third-generation source. A more radically new source is the Free Electron Laser (FEL), which would increase the brilliance by 4-5 orders of magnitude compared to an undulator. If hard X-ray FEL's are successfully built they will probably be limited to specialized experiments where problems of low repetition rates and sample damage are not important. On 25 august 2020, the ESRF launched its Extremely Brilliant Source[7], the first high-energy fourth-generation synchrotron light source, with X-ray performances increased by a factor 100 compared to the previous source and with a 30% reduction in electricity consumption.

The generation process of synchrotron radiation involves accelerating the electrons in a linear accelerator and then in a booster ring before emitting them into the storage ring. Undulators and wigglers are used to induce oscillations of relativistic electrons, producing a strong X-ray beam. The radiation is subsequently modified by optical elements and directed towards the sample to record the scattering (Figure 2.4).

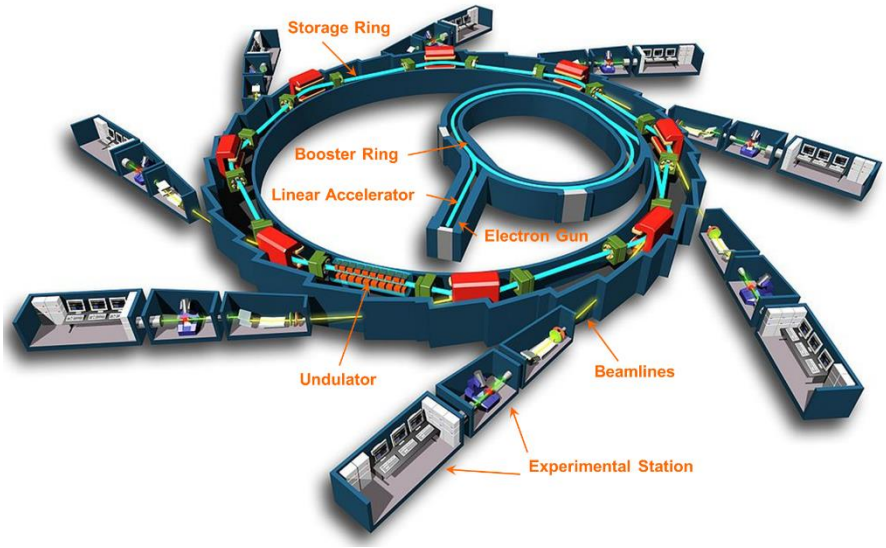

Figure 2.4 A schematic representation of a synchrotron source.

In this work, all the synchrotron diffraction data were collected using X-ray diffraction at SNBL (one of the two Swiss-Norwegian Beam Lines, namely BM01) at the ESRF, Grenoble, France. The beamline is equipped with a PILATUS 2M detector from Dectris, Switzerland. This detector utilizes pixel detector technology, providing benefits such as low noise, fast readout, and no correlation between pixels. The beamline also offers flexible goniometry, allowing for easy repositioning of both the detector and the goniometer in vertical and horizontal directions.

2.2.2 Crystal structure determination from Powder X-ray Diffraction

Due to the air sensitivity of our samples, growing single crystals is challenging. Therefore, the crystal structures in this work were determined using high-resolution or synchrotron powder X-ray diffraction. The general processes involved several steps: phase analysis, peaks indexing, selection of space group, profile fitting, crystal structure determination, and refinement.

All the reactions in this work theoretically produce single-phase solid products. As a result, the phase analysis primarily focused on screening to detect the presence of unreacted substances or the occurrence of side reactions. We mainly employed two methods: comparing with the reactants and conducting temperature ramping monitored by PXRD. The new series of peaks were indexed by using DICVOL[8] and the possible unit cells would be found. We then used CHECKCELL to analyze the obtained unit cells for systematic absences and check for possible derived lattices that could account for superstructure peaks. Profile fitting was performed using Le Bail modeling in the Fullprof Suite software package,[9] aiming to obtain the best fit for the intensities and peak profiles of the indexed phases.

For crystal structure solution, we utilized the FOX software package,[10] which employed global optimization methods. In this thesis, for molecular units either partly flexible z-matrix or in some cases, like for $[BH_3CH_2NHBH_2CH_3NHBH_3]^-$ and $[Al(BH_3NHCH_2CH_2NHBH_3)_2]^-$ anions, a rigid-body model was applied. The refinements of the obtained structures were performed in Fullprof Suite using the Rietveld method. This method works as least-squares refinement, which minimizes the difference between the observed and calculated profiles from the entire recorded pattern (every

point), rather than individual reflections. To evaluate the refinement results, several factors were considered, including the Profile Factor R_p, Weighted Profile Factor R_{wp}, Expected Weighted Profile Factor R_{exp} and the reduced chi-square χ^2. Ideally, the values of R_{wp} and R_p should be as low as possible. Importantly, the number of refined parameters was considered in order not to over-refine the model to the data. The corresponding values for our structures can be found in the respective chapters of this thesis.

2.3 Infrared spectra

Infrared spectra were collected to confirm the structural models of the complexes determined by powder X-ray diffraction (PXRD) and to analyze the presence of characteristic peaks, such as the N-H, B-H, Al-N bond in $Na[Al(CH_3NHBH_3)_4]$ and $Li/Na[Al(BH_3NHCH_2CH_2NHBH_3)_2]$, and so on. We used an ATR cell (Bruker Alfa spectrometer) in an argon glovebox, avoiding making KBr pellets and the contact with air.

2.4 NMR Spectroscopy

Multinuclear NMR spectra were primarily used to characterize the purity of the precursors $CH_3NH_2BH_3$ and $BH_3NH_2CH_2CH_2NH_2BH_3$ through the ^1H, ^{11}B and ^{13}C NMR. Additionally, the ^{11}B NMR spectra were employed to confirm the structural models of the complexes determined by PXRD.

2.5 Thermal gravimetric analysis (TGA)

Thermogravimetric analysis (TGA) was employed to analyze the thermal decomposition behavior of the newly obtained compounds in this thesis. It provided valuable information about mass loss and decomposition temperature, which served as a primary reference for the thermal dehydrogenation process. The TGA instruments used in this work were the Netzsch STA 449 F3 TGA/DSC, which was installed in a glovebox to prevent air contact with the sample throughout the process, and the Mettler Toledo TGA/SDTA 851e.

2.6 Mass spectrometry (MS)

Mass spectrometry is an analytical technique used to measure the mass-to-charge ratio of ions. The results are presented as a mass spectrum, which depicts the intensity as a function of the mass-to-charge ratio. In this study, mass spectrometry was employed to analyze the release of H_2 and other volatile gases, such as NH_3, B_2H_6, H_2O etc. to investigate the hydrogen release properties of the newly synthesized compounds.

For this purpose, we utilized the Hiden Catlab reactor in conjunction with a Quantitative Gas Analyser (QGA) Hidden quadrupole mass spectrometer, which is installed outside of the glovebox. This setup provided high-quality signals of the released gases due to its large sample holding capacity. Additionally, the Hiden Analytical HPR-20 QMS sampling system was utilized, which was installed in a glovebox to ensure better protection for air-sensitive samples.

References

1. Epp, J., 4 - X-Ray Diffraction (XRD) Techniques for Materials Characterization. In *Materials Characterization Using Nondestructive Evaluation (NDE) Methods*, Hübschen, G.; Altpeter, I.; Tschuncky, R.; Herrmann, H.-G., Eds. *Woodhead Publishing*: **2016**; 81-124.

2. Burrows, S.; Brewer, K.; Long, G., Infrared Spectroscopic Measurement of Titanium Dioxide Nanoparticle Shallow Trap State Energies. **2023**.

3. Robinson, A. L., History of Synchrotron Radiation. *Synchrotron Radiation News* **2015**, *28*, 4-9.

4. Sham, T. K.; Rivers, M. L., A Brief Overview of Synchrotron Radiation. *Reviews in Mineralogy and Geochemistry* **2002**, *49*, 117-147.

5. Kunz, C., Synchrotron Radiation: Third Generation Sources. *Journal of Physics: Condensed Matter* **2001**, *13*, 7499.

6. Shin, S., New Era of Synchrotron Radiation: Fourth-Generation Storage Ring. *AAPPS Bulletin* **2021**, *31*, 21.

7. https://indico.psi.ch/event/5589/event.ics

8. Boultif, A.; Louer, D., Powder Pattern Indexing with the Dichotomy Method. *Journal of Applied Crystallography* **2004**, *37*, 724-731.

9. Rodríguez-Carvajal, J., Recent Advances in Magnetic Structure Determination by Neutron Powder Diffraction. *Physica B: Condensed Matter* **1993**, *192*, 55-69.
10. Favre-Nicolin, V.; Cerny, R., Fox, `Free Objects for Crystallography': A Modular Approach to Ab Initio Structure Determination from Powder Diffraction. *Journal of Applied Crystallography* **2002**, *35*, 734-743.

Chapter 3

The synthesis, structure and hydrogen release of $Na[BH_3(CH_3NH)BH_2(CH_3NH)BH_3]$

Abstract

Over the last 10 years, hydrogen-rich compounds based on five-membered boron–nitrogen chain anions have attracted attention as potential hydrogen storage candidates. In this work, we synthesized $Na[BH_3(CH_3NH)BH_2(CH_3NH)BH_3]$ through a simple mechanochemical approach. The structure of this compound, obtained through synchrotron powder X-ray diffraction, is presented here for the first time. Its hydrogen release properties were studied by thermogravimetric analysis and mass spectrometry. It is shown here that $Na[BH_3(CH_3NH)BH_2(CH_3NH)BH_3]$, on the contrary of its parent counterpart, $Na[BH_3NH_2BH_2NH_2BH_3]$, is able to release up to 4.6 wt.% of pure hydrogen below 150 ˚C. These results demonstrate that the introduction of a methyl group on nitrogen atom may be a good strategy to efficiently suppress the release of commonly encountered undesired gaseous by-products during the thermal dehydrogenation of B-N-H compounds.

This chapter is based on the following publication:

Ting Zhang, Timothy Steenhaut, Michel Devillers and Yaroslav Filinchuk, Release of Pure H_2 from $Na[BH_3(CH_3NH)BH_2(CH_3NH)BH_3]$ by Introduction of Methyl Substituents, *Inorganics* **2023**, 11, 202 (DOI: 10.3390/inorganics11050202)

3.1 Introduction

In the field of chemical hydrogen storage[1-3], boron–nitrogen–hydrogen (B–N–H) compounds have emerged as promising candidates owing to the light weight of boron and nitrogen and to their ability of bearing multiple hydrogens. Additionally, B–H and N–H bonds tend to be hydridic and protic, respectively, resulting in normally facile hydrogen release[4-10]. A typical representative of B–N–H materials is ammonia borane (NH_3BH_3, or AB), which contains three hydridic and protic hydrogens on the N and B atoms, respectively. Ammonia borane has attracted consideration attention for hydrogen storage due to its high gravimetric storage density (up to 19.6 wt.%), high stability under ambient conditions, low toxicity, and high solubility in common solvents[11-15]. However, one of the drawbacks of NH_3BH_3 for hydrogen storage is the decomposition temperature. It starts releasing the first equivalent of hydrogen at about 120 ˚C, and a second hydrogen elimination step occurs at approximately 145 ˚C; the remaining amount of hydrogen is not released until more than 500 ˚C. Moreover, its decomposition is exothermic and thus irreversible, and it releases multiple volatile byproducts such as NH_3, $N_3B_3H_6$, and B_2H_6, making the chemical hydrogenation process more challenging. In addition, the thermal decomposition of AB is furthermore paired with severe foaming and volume expansion[12, 16, 17]. To overcome these disadvantages, several strategies have been employed, including nanoconfinement using nano-scaffolds, catalytic effects, ionic liquid assistance, the hydrolysis reaction, and chemical modification of NH_3BH_3 through replacing one of the H atoms in the $–NH_3$ group of NH_3BH_3 by a metal, forming metal amidoboranes (MABs)[9, 13, 18-25]. Among these strategies, the formation of metal amidoboranes as a popular option show a number of advantages over neutral NH_3BH_3: (i) lower hydrogen release temperatures than that of pristine NH_3BH_3[26]; (ii) generally the released hydrogen is not contaminated with undesirable borazine by-products [19, 27, 28]; (iii) the de-hydrogenation process is much less exothermic, about 3 to 5 kJ/mol[26, 29], vs. 22.5 kJ/mol for NH_3BH_3[16, 30]. Furthermore, the introduction of metals increases the diversity of hydrogen storage candidates based on B–N–H compounds. Recently, five-membered chain anions having the general formula $[BH_3NH_2BH_2NH_2BH_3]^-$, also known under the abbreviation $[B_3N_2]^-$, have

emerged as a novel group of ammonia borane derivatives[31-38]. $M[B_3N_2]$ compounds have a higher hydrogen content than MABs, and the Li and Na $[B_3N_2]^-$ derivatives are stable at room temperature, on the contrary of their respective MABs[33]. However, the interest in $M[B_3N_2]$ is much more recent than for MAB, and therefore there are only few reports about their synthesis, structure, characterization, and hydrogen storage properties. In 2011, the salt of Verkade's base (2,8,9-triisobutyl-2,5,8,9-tetraaza-1-phosphabicyclo[3.3.3]undecane, $C_{18}H_{39}N_4P$, VB, chemical formula see Figure 3.7 in Experimental section) with $[B_3N_2]$ was synthesized, and its structure was characterized, with the aim of studying the activating effect of VB on the rate and extent of H_2 release from NH_3BH_3[31]. Two years later, the same authors reported the synthesis of the sodium salt and two substituted $Na[BH_3N(R)HBH_2N(R)HBH_3]$ salts (R = H, Me, and benzyl), to further study the growth of aminoborane oligomers through the de-hydrocoupling reactions of NH_3BH_3[32]. Interestingly, since 2014, the salts of the $[BH_3NH_2BH_2NH_2BH_3]^-$ anion with different cations have been synthesized with a focus on the study of their hydrogen storage properties (see Table 3.5 in Experimental section). Generally, these kinds of complexes that are studied for their hydrogen storage properties can be classified into three types, based on their cations: ionic liquids, ammonium, and alkali metal salts. A total of four $[B_3N_2]^-$ ionic liquids have been described: $[Bu_4N][B_3N_2]$, $[Et_4N][B_3N_2]$, $[C(N_3H_6)][B_3N_2]$, and $[C(N_3H_5CH_3)][B_3N_2]$[35]. Among them, $[Bu_4N][B_3N_2]$ and $[Et_4N][B_3N_2]$ release pure hydrogen below 160 °C [35]. $[NH_4][B_3N_2]$ was reported this year, as the minor component of a 1:3 mixture with $NH_3BH_2NH_2BH_2NH_2BH_3$. Despite its impressive hydrogen content, this system releases H_2 with substantial contamination by borazine and traces of ammonia and diborane[38]. Among alkali metal (Li-Cs) salts of $[B_3N_2]^-$, only $Li[B_3N_2]$ was shown to release pure hydrogen during thermal decomposition[33, 34]. However, it is the sodium salt, $Na[B_3N_2]$, that was studied the most in the literature until now, with five synthesis approaches (four wet chemical and one dry mechanochemical) reported between 2013 and 2021. In 2013, Sneddon and co-workers reported that $Na[B_3N_2]$ could be obtained from $NaN(SiMe_3)_2$–$3NH_3BH_3$ in fluorobenzene at 50 °C for 24 hours[32]. Grochala et al. synthesized the same compound from NaH–$3NH_3BH_3$ in THF at room temperature for 24 hours and obtained $Li[B_3N_2]$ by a similar approach[33]. The same authors later used a

metathesis method to obtain $Na[B_3N_2]$ from $VBH[B_3N_2]$ and $M[Al\{OC(CF_3)_3\}_4]$ (M = Na) in CH_2Cl_2 at room temperature for 1 hour and were able to obtain the related K, Rb, and Cs salts by this method as well[34]. Although the metathesis is fast, the two precursors involved in this kind of reaction need to be synthesized first, adding a second step to the preparation of the salt. In 2021, Chen et al. reported a facile synthetic method to obtain $Na[B_3N_2]$, based on the reaction of $NaNH_2BH_3$ with $NiBr_2$ or $CoCl_2$ as a catalyst[36]. Results showed that the reaction with 0.05 equiv. of $NiBr_2$ in THF at 0 °C could produce the final $Na[B_3N_2]$ after 10 hours, with a yield of 60%. The main advantages of the dry mechanochemical synthesis are that it avoids the use of solvent and usually simplifies the drying process[39, 40]. However, the reported procedures for the synthesis of $Li[B_3N_2]$ and $Na[B_3N_2]$ require two stages of milling at room temperature, followed by a removal of the by-products (NH_3) upon heating[33, 34]. Moreover, long time reaction times and/or complicated operating processes are usually needed for the synthesis of the alkali metal $[B_3N_2]$ compounds.

With its 12.7 wt.% hydrogen content, $Na[B_3N_2]$ has potential for hydrogen storage. However, the hydrogen released when heating this compound is contaminated by unwanted by-products, including NH_3, B_2H_6, and larger fragments detected by mass spectrometry[33, 34]. To suppress these by-products during hydrogen releasing, one strategy is to enhance the dative bond B-N and diminish the N–H or B–H bond. It was reported that the introduction of alky-groups on N of NH_3BH_3 can strengthen the N–B bond and weaken the N–H bond. In addition, this method can lower dehydrogenation exothermicity and activation energy, thereby improving the hydrogen storage properties of NH_3BH_3.[41, 42] Similarly, this approach can be employed to modify the thermal dehydrogenation of $Na[B_3N_2]$. Additionally, the introduction of alkyl-groups on N would affect the geometry of the B–N–B–N–B skeleton and change the inter-anion dihydrogen bonds, potentially positively affecting the hydrogen properties of the compound, due to the steric hindrance. With this in mind, we synthesized $Na[BH_3(CH_3NH)BH_2(CH_3NH)BH_3]$ (abbreviated here as $Na[B_3(MeN)_2]$) through a new convenient mechanochemical synthesis method from easily accessible NaH and $CH_3NH_2BH_3$. We also report that its structure, solved from synchrotron powder X-ray diffraction (PXRD), enables a better understanding of the structure–properties relationships. Its thermal

dehydrogenation was also investigated, by thermogravimetric analysis (TGA) and mass spectrometry, revealing a release of pure hydrogen and thus confirming our hypothesis. The purity of hydrogen released from $Na[BH_3NH_2BH_2NH_2BH_3]$ was enhanced by the introduction of methyl groups on N atoms. This achievement represents the first successful suppression of the unwanted by-product release through the introduction of -CH_3 groups on the nitrogen atoms of $[B_3N_2]^-$. Furthermore, the structure of $Na[BH_3(CH_3NH)BH_2(CH_3NH)BH_3]$ was analyzed for the first time helping to understand the potential reasons behind the improved hydrogen purity. This study provides valuable insights into the relationship between the hydrogen release properties and the structure of B–N–H compounds. The introduction of methyl groups on the nitrogen atoms of $Na[B_3N_2]$ to enhance hydrogen purity could potentially be extended to the other $M[B_3N_2]$ or even other M–B–N–H compound. It could even be expanded to include the use of other small alkyl groups or small electron–donating groups instead of the methyl group.

3.2 The synthesis of $Na[BH_3(CH_3NH)BH_2(CH_3NH)BH_3]$

The reaction between NaH and NH_3BH_3 in various molar ratios was reported to produce different hydrogen rich B–N compounds, i.e., $NaNH_2BH_3$ (1:1), $NaBH_3NH_2BH_3$ (1:2), $NaBH_3NH_2BH_2NH_2BH_3$ (1:3), $NaBH_3NH_2BH_2NH_2BH_2NH_2BH_3$, and $NaBH_3NH_2BH(NH_2BH_3)_2$ (1:4)[43]. All of those have potential for application in hydrogen storage due to their high H content (see Table 3.1 in Experimental section 3.7.3). Despite the potential of this system, there is only one report of the reaction between the methyl–substituted $CH_3NH_2BH_3$ and NaH, in a 1:3 molar ratio[32]. We thus investigated the reaction of NaH and $CH_3NH_2BH_3$ by mechanochemistry (Figure 1A), to avoid an incorporation of or a reaction with solvents. Upon milling NaH–$CH_3NH_2BH_3$ systems in different molar ratios, new peaks appeared on the PXRD pattern of all the tested ratios, along with some unreacted NaH for the 1:1 system (Figure 1B). The ^{11}B NMR spectra of the resulting products furthermore showed the appearance of a new quadruplet signal located between -14.45 and -16.07 ppm, which likely belongs to the BH_3 unit of $Na[CH_3NHBH_3]$. When the NaH:$CH_3NH_2BH_3$ ratio was increased to 1:2, the PXRD pattern of the obtained product shows peaks corresponding to

crystalline $Na[BH_3(CH_3NH)BH_2(CH_3NH)BH_3]$. Although the ^{11}B NMR spectrum of the product displays a triplet signal of BH_2 (-2.24 ppm) and quadruplet signal of BH_3 (-16.39 ppm), expected for the $[BH_3(CH_3NH)BH_2(CH_3NH)BH_3]^-$ anion, other signals on the spectrum reveal the presence of unknown non-crystalline by–products (Figure 1C). Further increasing the ratio to 1:3 leads to the appearance of only the signals of BH_2 and BH_3 from the $[BH_3(CH_3NH)BH_2(CH_3NH)BH_3]^-$ anion on the ^{11}B NMR spectra.

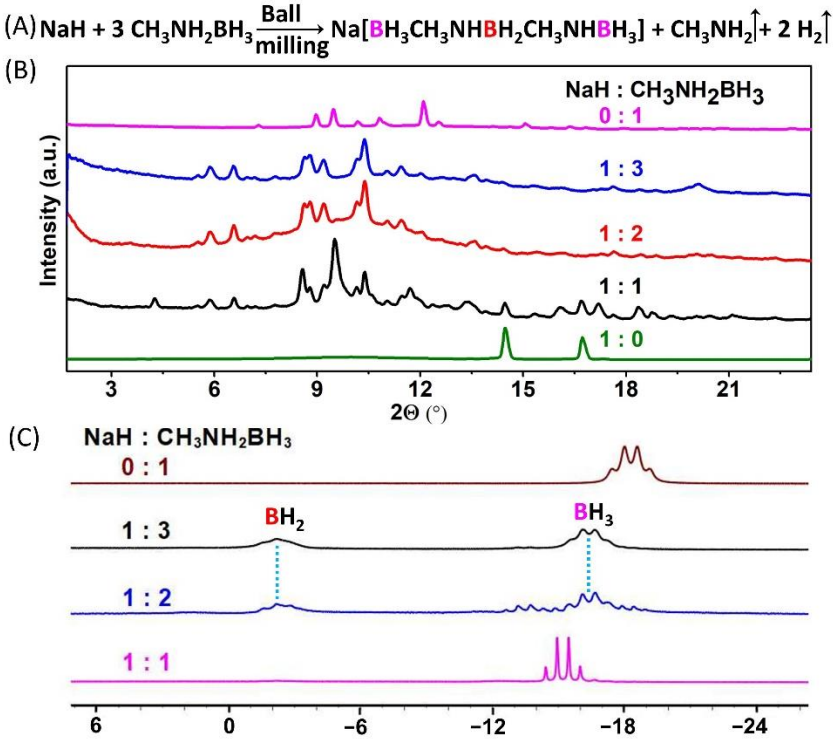

Figure 3.1 (**A**) Equation of the mechanochemical reaction; (**B**) PXRD patterns of NaH and $CH_3NH_2BH_3$ ball-milled in different molar ratios, along with patterns of NaH and $CH_3NH_2BH_3$ (λ = 0.71073 Å); (**C**) ^{11}B NMR spectra of ball-milled NaH and $CH_3NH_2BH_3$ mixtures in different molar ratios, along with the spectrum of $CH_3NH_2BH_3$.

The phase purity of the compound obtained upon 27 hours of ball milling the 1:3 mixture was confirmed by temperature programmed synchrotron powder X-ray diffraction (PXRD) measurements. Indeed, the complete set of peaks of the pattern disappeared at once at around 150 °C (Figure 3.2).

Based on the ^{11}B NMR spectrum and the temperature ramping synchrotron PXRD experiment, we deduce that relatively pure $Na[B_3(MeN)_2]$ with five membered B–MeN–B–MeN–B chains was formed and that the reaction shown in Figure 1A was complete.

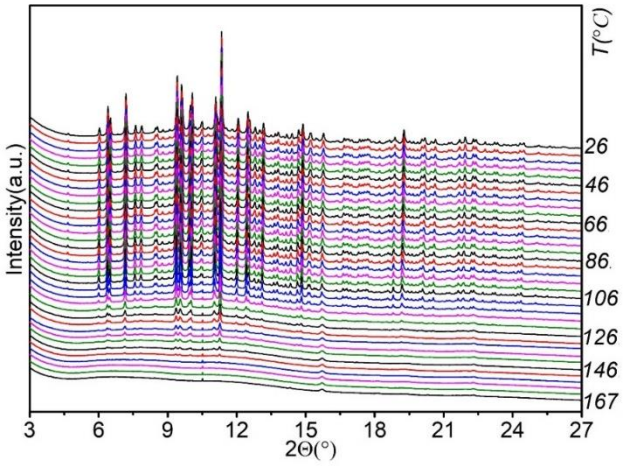

Figure 3.2 Synchrotron PXRD patterns of $Na[B_3(MeN)_2]$ (λ = 0.77509 Å).

3.3 The IR spectra of $Na[BH_3(CH_3NH)BH_2(CH_3NH)BH_3]$

The obtained $Na[B_3(MeN)_2]$ was further characterized by infrared (IR) spectroscopy (Figure 3.3). On the spectrum, it can be seen that the asymmetry of the N–H stretching band (3162 cm^{-1}) disappeared, compared with the $CH_3NH_2BH_3$ precursor. This is because one hydrogen on the nitrogen of $CH_3NH_2BH_3$ is released, combined with a hydride atom from NaH to form H_2. In addition, the N–H bending of $Na[B_3(MeN)_2]$ (1457–1491 cm^{-1}) is redshifted compared to $CH_3NH_2BH_3$ (1596 cm^{-1}). This can be attributed to the introduction of weak electron donating methyl group on N atom, influencing the electron density of N and further having an effect on the N–H band. The broad band located in the region of 2000–2500 cm^{-1} belongs to the B–H stretching band. There is no significant difference compared to the $CH_3NH_2BH_3$ precursor. However, the signal of the B–N stretching is widened and split in $Na[B_3(MeN)_2]$ (692–716 cm^{-1}), due to the presence of two types of B–N bands in $Na[B_3(MeN)_2]$, whereas $CH_3NH_2BH_3$ exhibits only one B–N band.

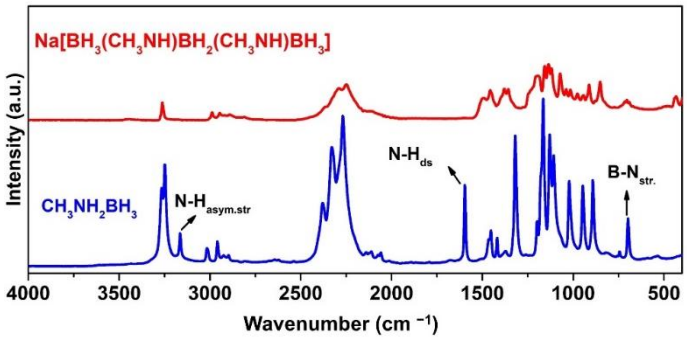

Figure 3.3 IR spectra of $Na[B_3(MeN)_2]$ and $CH_3NH_2BH_3$.

All of the aforementioned differences between $Na[B_3(MeN)_2]$ and $CH_3NH_2BH_3$ align with our previous analysis based on XRD and ^{11}B NMR, further confirming the proposed formula of the product as shown in Figure 3.1A.

3.4 The structure of $Na[BH_3(CH_3NH)BH_2(CH_3NH)BH_3]$

The structure of $Na[B_3(MeN)_2]$ was determined by direct space methods from synchrotron powder X-ray diffraction (PXRD) data, indexed in the monoclinic space group $P2_1/n$; the final Rietveld refinement profile is shown in Figure 3.4. The $[BH_3(CH_3NH)BH_2(CH_3NH)BH_3]^-$ anion is a five–membered B–N chain with an alternance of B and N atoms connected in a similar way as in the reported $[BH_3NH_2BH_2NH_2BH_3]^-$[33]. Although the N atoms in $Na[B_3(MeN)_2]$ have four different substituents and are therefore chiral, the crystal structure reveals that the anions are integrated in the solid as a meso compound, as both N atoms possess opposite chirality. This is in agreement with reported DFT calculations, which indicate that the meso isomer is the preferred stereoisomer for this anion[32]. Due to the introduction of the methyl substituents, the skeleton of the B–N–B–N–B chain shows a twisted geometry, which is in contrast with the linear geometry adopted by the $[B_3N_2]^-$ anion in the Li, Na, and K salts but is similar to the reported Rb and Cs $[B_3N_2]^-$ salts[34]. This type of geometry enables the formation of intramolecular dihydrogen bonds, of 2.04 and 2.12 Å (Figure 3.4A). With this type of geometry of the chain anion, an increase in the intramolecular interactions is expected, which should have a positive influence on the hydrogen release properties of $Na[B_3(MeN)_2]$. Interanion dihydrogen bonds are also present between H atoms of the NH and

terminal BH_3 groups, as well as between H atoms of the NH and the ones of the central BH_2, as can be seen in Figure 3.4B and in Table 3.2. Unlike in the reported $K[B_3N_2]$ and $Rb[B_3N_2]$, the N–BH_2 distances are not shorter than the N–BH_3 ones (Table 3.3)[34, 44]. Na^+ cations have a distorted triangular bipyramidal coordination geometry with five B atoms from four distinct $[BH_3(CH_3NH)BH_2(CH_3NH)BH_3]^-$ anions (Figure 3.4B,C). The coordination is performed through six hydridic H atoms of the BH_3 (green balls in Figure 3.4C) groups from four different chain anions. Two other hydridic H atoms from the BH_2 (red balls in Figure 3.4C) of one of above four chain anions complete the coordination around Na. This is different from the unsubstituted $Na[BH_3NH_2BH_2NH_2BH_3]$, where Na atoms are coordinated only to hydrogen atoms of the terminal $[BH_3]$ groups. This may be one reason of the release of large undesirable gaseous species during the thermal dehydrogenation of $Na[B_3N_2]$[33].

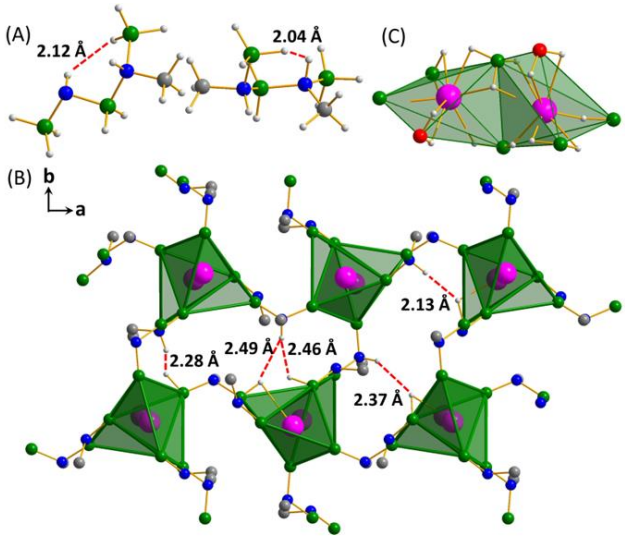

Figure 3.4 Ball and stick plot of the $[BH_3(CH_3NH)BH_2(CH_3NH)BH_3]^-$ anion with indication of the intramolecular dihydrogen bond (**A**), crystal packing of Na coordination polyhedra with boron atoms (hydrogen atoms are omitted for clarity) in $Na[BH_3(CH_3NH)BH_2(CH_3NH)BH_3]$ projected along the *c* axis, indicating interanion dihydrogen bonds (**B**), and coordination of H atoms around the Na^+ cation (central B was highlighted by red color) (**C**). Color code: N = blue, B = green, C = grey, H = white, and Na = pink. Dihydrogen bonds are displayed by red dotted lines.

3.5 Thermal dehydrogenation of $Na[BH_3(CH_3NH)BH_2(CH_3NH)BH_3]$

The thermal stability of $Na[B_3(MeN)_2]$ was investigated by thermogravimetric analysis (TGA) under inert argon atmosphere, from room temperature to 150 °C. A single step decomposition event occurs at about 80 °C, accompanied by a weight oscillation due to the so–called "jet" effect[12, 45] (Figure 3.5A). The solid decomposition products isolated upon heating at 150 °C were identified as being crystalline $NaBH_4$, along with some unknown crystalline and possibly amorphous compounds, based on PXRD and IR analyses (Figure 3.5B and C). Those by-products are expected to contain B, C, and N atoms, based on 4.6 wt.% the experimental weight loss as compared to 26.2 wt.% B, 19.4 wt.% C, and 22.7 wt.% N (calculated) in the sample before decomposition. It is interesting to note that thermally decomposing alkali metal salts of the unsubstituted anion (Li – Cs $[B_3N_2]$) also leads to the formation of BH_4^- compounds, similarly to the title compound. The observed mass loss during the thermal decomposition of $Na[B_3(MeN)_2]$, of 4.6 wt.%, is in accordance with the possible release of pure H_2, as the compound has a theoretical hydrogen content of 8.1 wt.% (excluding H atoms from the methyl groups). This is interesting, as the parent $Na[B_3N_2]$ shows a larger mass loss (~20 wt.%) than its theoretical hydrogen content (12.7 wt.%) when heating below 200 °C, resulting in the single-step release of undesirable gaseous decomposition by-products like diborane and ammonia[34].

The purity of the gas released during the thermal de-hydrogenation of $Na[B_3(MeN)_2]$ was analysed by means of temperature-programmed mass spectrometry between 40 °C and 150 °C. Hydrogen was the only gas detected, and the experiment confirmed that NH_3, B_2H_6, CH_4, and CH_3NH_2 were not released during the decomposition (Figure 3.6). This confirms that the methyl-substituted $Na[B_3(MeN)_2]$ indeed releases about 4.6 wt.% of pure hydrogen upon heating to 150 °C. This confirmed that the introduction of a methyl group on the nitrogen atoms efficiently suppresses the release of unwanted by-products during thermal hydrogen desorption (Table 3.5).

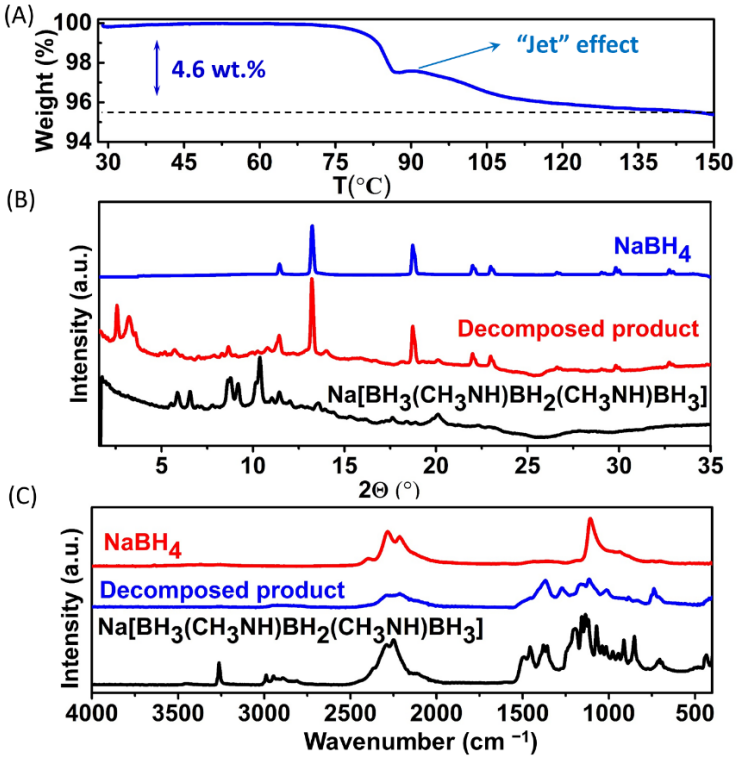

Figure 3.5 TG analysis of $Na[B_3(MeN)_2]$ (**A**); PXRD patterns (λ = 0.71073 Å) (**B**) and IR spectra (**C**) of the product upon heating at 150 °C, compared to the starting $Na[B_3(MeN)_2]$ and $NaBH_4$.

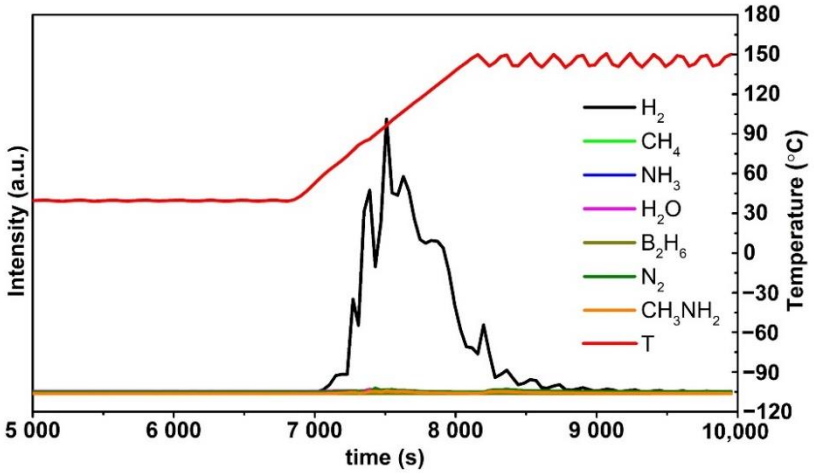

Figure 3.6 Mass spectrometry analysis of gases released during the thermal decomposition of $Na[B_3(MeN)_2]$ under argon, between 40 °C and 150 °C.

3.6 Conclusion

We synthesized $Na[BH_3(CH_3NH)BH_2(CH_3NH)BH_3]$ ($Na[B_3(MeN)_2]$, 130.5 g H_2/kg, 126 g H_2/L, Table 3.4), a methyl-substituted Na salt with five-membered B–N chain anions, by a novel mechanochemical approach from NaH and $CH_3NH_2BH_3$. Its crystal structure was determined for the first time based on synchrotron PXRD, showing that the introduction of -CH_3 groups on the N atoms leads to the introduction of the anion in a kinked geometry into the solid, unlike its unsubstituted parent counterpart ($Na[B_3N_2]$), that possesses straight B-N chains. $Na[B_3(MeN)_2]$ releases up to 4.6 wt.% of pure hydrogen below to 150 °C, contrary to its unsubstituted analogue that releases undesirable gaseous by-products during heating. This indicates that the introduction of methyl (or other) substituents on the nitrogen atoms of similar compounds is a promising approach to suppress the release of unwanted volatile by-products during thermal hydrogen release.

3.7 Experimental section

3.7.1 Chemicals:

All samples were obtained from commercially available NaH (95%), $NaBH_4$ (97%), $CH_3NH_2{\cdot}HCl$ (98%), and anhydrous THF (≥99.9%) that were purchased from Sigma Aldrich Co., Ltd. (St. Louis, MI, USA). All operations were performed in gloveboxes with a high purity argon atmosphere.

3.7.2 The formula of VB:

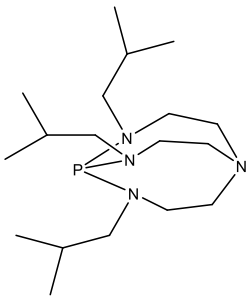

Figure 3.7 Chemical formula of $C_{18}H_{39}N_4P$ (VB).

3.7.3 The products of NaH-NH_3BH_3 in different molar ratio:

Table 3.1 H-content in $NaNH_2BH_3$, $NaBH_3NH_2BH_3$, $NaBH_3NH_2BH_2NH_2BH_3$, $NaBH_3NH_2BH_2NH_2BH_2NH_2BH_3$ and $NaBH_3NH_2BH(NH_2BH_3)_2$.

Compound	Molar mass (g/mol)	H-content (wt. %)
$NaNH_2BH_3$	52.85	9.54
$NaBH_3NH_2BH_3$	66.68	12.09
$NaBH_3NH_2BH_2NH_2BH_3$	95.53	12.66
$NaBH_3NH_2BH_2NH_2BH_2NH_2BH_3$	124.38	12.97
$NaBH_3NH_2BH(NH_2BH_3)_2$	124.38	12.97

3.7.4 Synthesis of $CH_3NH_2BH_3$ (MeAB)

$CH_3NH_2BH_3$ was synthesized following a procedure adapted from the literature[46]. Initially, powdered $NaBH_4$ (3.79 g, 0.1 mol), $CH_3NH_2{\cdot}HCl$ (13.50 g, 0.1 mol), and THF (300 mL) were added to a 500 mL three-neck round-bottom flask. The resulting mixture was then vigorously stirred at ambient temperature under an argon atmosphere for 48 hours. Filtration was performed to remove the solid by-product (NaCl) from the reaction mixture, and the collected filtrate was subjected to evaporation under reduced pressure using a rotary evaporator. The resulting white solid of $CH_3NH_2BH_3$ was then dried under vacuum overnight to eliminate any residual THF. The purity of the product was confirmed through characterization using ^{1}H, ^{11}B, and ^{13}C NMR and PXRD, as depicted in Figures S1–S4 in Annex.

3.7.5 Synthesis of $Na[BH_3(CH_3NH)BH_2(CH_3NH)BH_3]$:

Totals of 1 eq. of NaH (30.0 mg) and 3 eqs. of $CH_3NH_2BH_3$ (168.4 mg) were placed into an 80 mL stainless steel vial with three 10 mm diameter stainless steel balls (ball-to-powder mass ratio of 60:1). The reactants were then milled in a planetary ball mill (Fritsch Pulverisette 7 Premium line), with a rotation speed of 500 rpm for 55 milling cycles of 30 min interrupted by 5 min cooling breaks. The product was obtained as a white powder. We have repeated this synthesis several times and found this method reproducible.

3.7.6 Nuclear magnetic resonance (NMR):

Multinuclei NMR spectra were acquired in DMSO on a Bruker Avance 500 MHz spectrometer operating at 500 MHz for ^{1}H NMR, 160 MHz for ^{11}B and 126 MHz for ^{13}C).

3.7.7 PXRD measurement:

Samples were carefully filled into 0.7 mm thin-walled glass capillaries (Hilgenberg GmbH, Malsfeld, Germany) within an argon-filled glovebox. To prevent contact with air, the capillaries were sealed with grease before being taken out of the glovebox. The sealed capillaries were then cut and promptly placed into wax on a goniometer head, ensuring that no air entered the capillary. Diffraction data were immediately collected using a MAR345 image-plate detector equipped with an Incoatec Mo (λ = 0.71073 Å) Microfocus (IμS 2.0) X-ray source operating at 50 kV and 1000 μA. The resulting two-dimensional images were azimuthally integrated using the Fit2D software, with LaB_6 serving as a calibrant.

3.7.8 Structure determination:

Synchrotron PXRD patterns were collected with a PILATUS@SNBL diffractometer (SNBL, ESRF, Grenoble, France) equipped with a Dectris PILATUS 2M single-photon counting pixel area detector (λ = 0.77509 Å). Powder patterns were obtained by using raw data processed by the SNBL Toolbox software using data for LaB_6 standard. The synchrotron PXRD data for $Na[BH_3(CH_3NH)BH_2(CH_3NH)BH_3]$ were indexed in a monoclinic unit cell, and its structure was solved by global optimization using the FOX software[47]. The anions were modelled by conformationally free z-matrices with restrained bond distances and angles. Since the N-atom of methylamidoborane is chiral, all combinations of these chiral centres were examined. The final structure showed the best fit to the data but also satisfied crystal-chemical expectations, such as the formation of dihydrogen bonds (N–H···H–B) and the coordination of Na^+ to H atoms of BH_3 and BH_2 groups. Rietveld refinements were done in Fullprof[48], refining all non-hydrogen atoms of the anions individually using restraints from DFT-refined geometry. Hydrogen atoms were refined using the

rigiding model, with Na as free atoms. The symmetry was confirmed with ADDSYM routine in the PLATON[49] software. R_B = 7.9%, R_p = 14.2, R_{wp} = 12.5, χ^2 = 424 (mind that the counting statistics is very high).

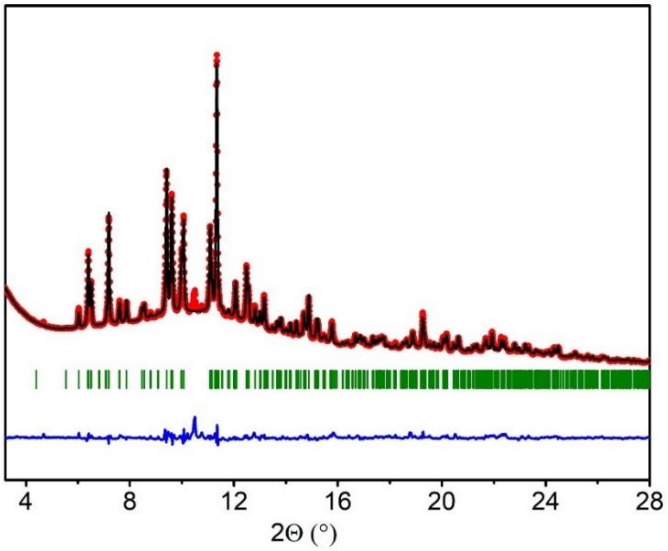

Figure 3.8 Rietveld refinement of the synchrotron PXRD pattern of $Na[B_3(MeN)_2]$ (λ = 0.77509 Å, T = 300 K). Observed data (Yobs) are displayed in red, the Rietveld refinement profile (Ycalc) in black and the difference plot (Yobs – Ycalc) in blue. Agreement factors, with background correction, are R_B = 7.9 %, R_p = 14.2, R_{wp} = 12.5, χ^2 = 424.

Table 3.2 Inter-anion dihydrogen bond lengths and angles in $Na[B_3(MeN)_2]$.

N–H$^{\delta+}$…H$^{\delta-}$–B	D(H···H) / Å	∠(N–H···H) / °
N(12)–H(121) …H(212)–B(21) (terminal B)	2.37	135.6
N(22)–H(221) …H(131)–B(13) (central B)	2.13	173.8
N(14)–H(141) …H(251)–B(25) (terminal B)	2.28	124.0
N(24)–H(241) …H(151)–B(15) (terminal B)	2.46	159.4
N(24)–H(241) …H(232)–B(23) (central B)	2.49	136.6

Table 3.3 B–N bond lengths in $CH_3NH_2BH_3$, $M[B_3N_2]$ (M = Li – Cs), and $Na[B_3(MeN)_2]$ (Because of the significant disorder and presence of peaks from unidentified impurities, they modeled the structure of $Na/Li[B_3N_2]$ in Jana2006. And B–N distances in $Na[B_3N_2]$ were restrained to 1.60(1) Å).

Compound	Identification of B-N bond	Bond length (Å)
$CH_3NH_2BH_3$[44]	B–N	1.587(3)
$Li[B_3N_2]$[33]	B–N	-
$Na[B_3N_2]$[33]	B–N	1.60(1)
$K[B_3N_2]$[34]	B–N (terminal B)	1.609(1)
	B–N (central B)	1.551(1)
$Rb[B_3N_2]$[34]	B–N (terminal B)	1.62(2) – 1.65(2)
	B–N (central B)	1.60(2)
$Cs[B_3N_2]$[34]	B-N	1.56(7) – 1.57(7)
$Na[B_3(MeN)_2]$[*(this work)*]	B11–N12 (terminal B)	1.638(9)
	B13–N12 (central B)	1.620(9)
	B13–N14 (central B)	1.626(10)
	B15-N14 (terminal B)	1.592(9)
	B21–N22 (terminal B)	1.603(8)
	B23–N22 (central B)	1.635(11)
	B23–N24 (central B)	1.601(8)
	B25–N24 (terminal B)	1.632(10)

3.7.9 Fourier transform infrared spectroscopy (FTIR):

Attenuated total reflectance (ATR)-IR spectra were recorded using a Bruker Alpha spectrometer. The spectrometer was equipped with a Platinum ATR sample holder, which featured a diamond crystal for single bounce measurements. The entire experimental setup was located within an argon-filled glovebox to maintain an inert atmosphere during the measurements.

3.7.10 Thermogravimetric analysis (TGA):

TGA measurements were conducted using a Netzsch STA 449 F3 TGA/DSC. The TGA/DSC was equipped with a stainless-steel oven and located within an argon-filled glovebox to ensure an inert atmosphere during

the measurements. The samples were loaded into Al_2O_3 crucibles and subjected to a heating rate of 5 K/min under an argon flow of 100 mL/min.

3.7.11 Mass spectrometry:

Mass spectrometry measurements were conducted using a Hiden Catlab reactor coupled with a Quantitative Gas Analyser (QGA) Hiden quadrupole mass spectrometer, which is installed outside of the glovebox. Prior to the experiment, the samples were loaded into a quartz tube with two layers of quartz wool, all within the protective atmosphere of an argon-filled glovebox. The ends of the quartz tube were sealed with Parafilm before being removed from the glovebox. Subsequently, the quartz tube was placed in the sample holder outside the glovebox after quickly removing the Parafilm. The argon flow (40 mL/min) was immediately initiated to prevent any contact of the sample with air. The samples were then heated to 40 °C and held isothermally for approximately 2 hours to stabilize the temperature. Heating was then performed at a rate of 5 °C/min until reaching 150 °C, followed by an one hour isotherm. Gas evolution was monitored by recording the peak with the highest intensity for each gas, specifically the *m*/*z* values of 2, 15, 17, 18, 26, 28, and 30, corresponding to H_2, CH_4, NH_3, H_2O, B_2H_6, N_2, and CH_3NH_2, respectively. The absence of H_2O and N_2 signals in the collected data confirmed the absence of leaks, ensuring that the sample remained under a protective argon atmosphere throughout the measurement.

Table 3.4 The mole mass, density, gravimetric and volumetric hydrogen density of $Na[B_3(MeN)_2]$

Mole mass	δ	Gravimetric hydrogen density	Volumetric hydrogen density
123.58 g/mol	973 g/L	13.05 %	126 g/L

Table 3.5 H-contents, mass losses and by-products formed during thermal treatment of several $M[B_3N_2]$ compounds.

Compound[reference]	**H-content (wt. %, excluding hydrogen on carbon)**	**Mass loss below 200 ˚C (%)**	**By-products**
$[Bu_4N][B_3N_2]$[35]	3.8	3.0	None
$[Et_4N][B_3N_2]$[35]	6.0	6.0	None
$[C(N_3H_6)][B_3N_2]$[35]	13.7	18.5	NH_3, CH_4
$[C(N_3H_5CH_3)][B_3N_2]$[35]	11.7	8.0	NH_3, CH_4
$[NH_4][B_3N_2]$ - $3NH_3BH_2NH_2BH_2NH_2BH_3$[38]	16.4	~ 45	$B_3N_3H_6$, B_2H_6, NH_3
$Li[B_3N_2]$[33]	15.2	~ 5	None
$Na[B_3N_2]$[33]	12.7	~ 20	NH_3, BNH_5, B_2NH_7
$K[B_3N_2]$[34]	10.8	~ 36	NH_3, B_2H_6
$Rb[B_3N_2]$[34]	7.6	~ 23	NH_3, B_2H_6
$Cs[B_3N_2]$[34]	5.9	~ 19	NH_3, B_2H_6

References

1. Milanese, C., et al., Complex Hydrides for Energy Storage. *International Journal of Hydrogen Energy* **2019**, *44*, 7860-7874.

2. Chen, Z.; Ma, Z.; Zheng, J.; Li, X.; Akiba, E.; Li, H.-W., Perspectives and Challenges of Hydrogen Storage in Solid-State Hydrides. *Chinese Journal of Chemical Engineering* **2021**, *29*, 1-12.

3. Dematteis, E. M., et al., Hydrogen Storage in Complex Hydrides: Past Activities and New Trends. *Progress in Energy* **2022**, *4*, 032009.

4. Hamilton, C. W.; Baker, R. T.; Staubitz, A.; Manners, I., B–N Compounds for Chemical Hydrogen Storage. *Chemical Society Reviews* **2009**, *38*, 279-293.

5. Huang, Z.; Autrey, T., Boron–Nitrogen–Hydrogen (B-N-H) Compounds: Recent Developments in Hydrogen Storage, Applications in Hydrogenation and Catalysis, and New Syntheses. *Energy & Environmental Science* **2012**, *5*, 9257-9268.

6. Dovgaliuk, I.; Filinchuk, Y., Aluminium Complexes of B- and N-Based Hydrides: Synthesis, Structures and Hydrogen Storage Properties. *International Journal of Hydrogen Energy* **2016**, *41*, 15489-15504.

7. Kumar, R.; Karkamkar, A.; Bowden, M.; Autrey, T., Solid-State Hydrogen Rich Boron–Nitrogen Compounds for Energy Storage. *Chemical Society Reviews* **2019**, *48*, 5350-5380.

8. Wang, K.; Pan, Z.; Yu, X., Metal B-N-H Hydrogen-Storage Compound: Development and Perspectives. *Journal of Alloys and Compounds* **2019**, *794*, 303-324.

9. Castilla-Martinez, C. A.; Moury, R.; Demirci, U. B., Amidoboranes and Hydrazinidoboranes: State of the Art, Potential for Hydrogen Storage, and Other Prospects. *International Journal of Hydrogen Energy* **2020**, *45*, 30731-30755.

10. Paskevicius, M.; Jepsen, L. H.; Schouwink, P.; Černý, R.; Ravnsbæk, D. B.; Filinchuk, Y.; Dornheim, M.; Besenbacher, F.; Jensen, T. R., Metal Borohydrides and Derivatives – Synthesis, Structure and Properties. *Chemical Society Reviews* **2017**, *46*, 1565-1634.

11. Stephens, F. H.; Pons, V.; Tom Baker, R., Ammonia–Borane: The Hydrogen Source Par Excellence? *Dalton Transactions* **2007**, 2613-2626.

12. Staubitz, A.; Robertson, A. P. M.; Manners, I., Ammonia-Borane and Related Compounds as Dihydrogen Sources. *Chemical Reviews* **2010**, *110*, 4079-4124.
13. Wang, K.; Zhang, J.-G.; Man, T.-T.; Wu, M.; Chen, C.-C., Recent Process and Development of Metal Aminoborane. *Chemistry – An Asian Journal* **2013**, *8*, 1076-1089.
14. Demirci, U. B., Ammonia Borane, a Material with Exceptional Properties for Chemical Hydrogen Storage. *International Journal of Hydrogen Energy* **2017**, *42*, 9978-10013.
15. Akbayrak, S.; Özkar, S., Ammonia Borane as Hydrogen Storage Materials. *International Journal of Hydrogen Energy* **2018**, *43*, 18592-18606.
16. Baitalow, F.; Baumann, J.; Wolf, G.; Jaenicke-Rößler, K.; Leitner, G., Thermal Decomposition of B–N–H Compounds Investigated by Using Combined Thermoanalytical Methods. *Thermochimica Acta* **2002**, *391*, 159-168.
17. Demirci, U. B., Mechanistic Insights into the Thermal Decomposition of Ammonia Borane, a Material Studied for Chemical Hydrogen Storage. *Inorganic Chemistry Frontiers* **2021**, *8*, 1900-1930.
18. Chua, Y. S.; Chen, P.; Wu, G.; Xiong, Z., Development of Amidoboranes for Hydrogen Storage. *Chemical Communications* **2011**, *47*, 5116-5129.
19. Owarzany, R.; Leszczyński, J. P.; Fijalkowski, J. K.; Grochala, W., Mono- and Bimetalic Amidoboranes. *Crystals* **2016**, *6*.
20. Hügle, T.; Hartl, M.; Lentz, D., The Route to a Feasible Hydrogen-Storage Material: Mofs Versus Ammonia Borane. *Chemistry – A European Journal* **2011**, *17*, 10184-10207.
21. Li, L., et al., Lithium-Catalyzed Dehydrogenation of Ammonia Borane within Mesoporous Carbon Framework for Chemical Hydrogen Storage. *Advanced Functional Materials* **2009**, *19*, 265-271.
22. Huang, X.; Liu, Y.; Wen, H.; Shen, R.; Mehdi, S.; Wu, X.; Liang, E.; Guo, X.; Li, B., Ensemble-Boosting Effect of Ru-Cu Alloy on Catalytic Activity Towards Hydrogen Evolution in Ammonia Borane Hydrolysis. *Applied Catalysis B: Environmental* **2021**, *287*, 119960.
23. Kang, N., et al., Fast Au-Ni@Zif-8-Catalyzed Ammonia Borane Hydrolysis Boosted by Dramatic Volcano-Type Synergy and Plasmonic Acceleration. *Applied Catalysis B: Environmental* **2023**, *320*, 121957.

24. Mehdi, S., et al., P-Induced Co-Based Interfacial Catalysis on Ni Foam for Hydrogen Generation from Ammonia Borane. *Applied Catalysis B: Environmental* **2023**, *325*, 122317.

25. Himmelberger, D. W.; Yoon, C. W.; Bluhm, M. E.; Carroll, P. J.; Sneddon, L. G., Base-Promoted Ammonia Borane Hydrogen-Release. *Journal of the American Chemical Society* **2009**, *131*, 14101-14110.

26. Xiong, Z., et al., High-Capacity Hydrogen Storage in Lithium and Sodium Amidoboranes. *Nature Materials* **2007**, *7*, 138.

27. Diyabalanage, H. V. K., et al., Potassium(I) Amidotrihydroborate: Structure and Hydrogen Release. *Journal of the American Chemical Society* **2010**, *132*, 11836-11837.

28. Luo, J.; Kang, X.; Wang, P., Synthesis, Formation Mechanism, and Dehydrogenation Properties of the Long-Sought $Mg(NH_2BH_3)_2$ Compound. *Energy & Environmental Science* **2013**, *6*, 1018-1025.

29. Diyabalanage, H. V. K.; Shrestha, R. P.; Semelsberger, T. A.; Scott, B. L.; Bowden, M. E.; Davis, B. L.; Burrell, A. K., Calcium Amidotrihydroborate: A Hydrogen Storage Material. *Angewandte Chemie International Edition* **2007**, *46*, 8995-8997.

30. Wolf, G.; Baumann, J.; Baitalow, F.; Hoffmann, F. P., Calorimetric Process Monitoring of Thermal Decomposition of B–N–H Compounds. *Thermochimica Acta* **2000**, *343*, 19-25.

31. Ewing, W. C.; Marchione, A.; Himmelberger, D. W.; Carroll, P. J.; Sneddon, L. G., Syntheses and Structural Characterizations of Anionic Borane-Capped Ammonia Borane Oligomers: Evidence for Ammonia Borane H_2 Release Via a Base-Promoted Anionic Dehydropolymerization Mechanism. *Journal of the American Chemical Society* **2011**, *133*, 17093-17099.

32. Ewing, W. C.; Carroll, P. J.; Sneddon, L. G., Syntheses and Characterizations of Linear Triborazanes. *Inorganic Chemistry* **2013**, *52*, 10690-10697.

33. Fijalkowski, K. J.; Jaroń, T.; Leszczyński, P. J.; Magos-Palasyuk, E.; Palasyuk, T.; Cyrański, M. K.; Grochala, W., $M(BH_3NH_2BH_2NH_2BH_3)$ – the Missing Link in the Mechanism of the Thermal Decomposition of Light Alkali Metal Amidoboranes. *Physical Chemistry Chemical Physics* **2014**, *16*, 23340-23346.

34. Owarzany, R.; Fijalkowski, K. J.; Jaroń, T.; Leszczyński, P. J.; Dobrzycki, Ł.; Cyrański, M. K.; Grochala, W., Complete Series of Alkali-Metal M($BH_3NH_2BH_2NH_2BH_3$) Hydrogen-Storage Salts Accessed Via Metathesis in Organic Solvents. *Inorganic Chemistry* **2016**, *55*, 37-45.

35. Chen, X.-M.; Jiang, X.; Jing, Y.; Chen, X., Synthesis and Dehydrogenation of Organic Salts of a Five-Membered B/N Anionic Chain, a Novel Ionic Liquid. *Chemistry – An Asian Journal* **2021**, *16*, 2475-2480.

36. Ju, M.-Y.; Guo, Y.; Chen, X.-M.; Chen, X., Facile Synthetic Method of Na[$BH_3(NH_2BH_2)_2H$] Based on the Reactions of Sodium Amidoborane ($NaNH_2BH_3$) with $NiBr_2$ or $CoCl_2$. *Inorganic Chemistry* **2021**, *60*, 7101-7107.

37. Nawrocka, E. K.; Prus, A.; Owarzany, R.; Koźmiński, W.; Kazimierczuk, K.; Fijalkowski, K. J., The Assignment of ^{11}B and ^{1}H Resonances in the Post-Reaction Mixture from the Dry Synthesis of Li($BH_3NH_2BH_2NH_2BH_3$). *Magnetic Resonance in Chemistry* **2023**, *61*, 49-54.

38. Owarzany, R.; Jaroń, T.; Kazimierczuk, K.; Malinowski, P. J.; Grochala, W.; Fijalkowski, K. J., Towards Hydrogen-Rich Ionic (NH_4)($BH_3NH_2BH_2NH_2BH_3$) and Related Molecular $NH_3BH_2NH_2BH_2NH_2BH_3$. *Dalton Transactions* **2023**, *52*, 3586-3595.

39. James, S. L., et al., Mechanochemistry: Opportunities for New and Cleaner Synthesis. *Chemical Society Reviews* **2012**, *41*, 413-447.

40. Do, J.-L.; Friščić, T., Mechanochemistry: A Force of Synthesis. *ACS Central Science* **2017**, *3*, 13-19.

41. Li, L.; Gu, Q.; Tang, Z.; Chen, X.; Tan, Y.; Li, Q.; Yu, X., Two Novel Derivatives of Ammonia Borane for Hydrogen Storage: Synthesis, Structure, and Hydrogen Desorption Investigation. *Journal of Materials Chemistry A* **2013**, *1*, 12263-12269.

42. Li, S.; Tang, Z.; Gong, Q.; Yu, X.; Beaumont, P. R.; Jensen, C. M., Phenyl Introduced Ammonium Borohydride: Synthesis and Reversible Dehydrogenation Properties. *Journal of Materials Chemistry* **2012**, *22*, 21017-21023.

43. Chen, X.-M.; Wang, J.; Liu, S.-C.; Zhang, J.; Wei, D.; Chen, X., Controllable Syntheses of B/N Anionic Aminoborane Chain Complexes by the Reaction of NH_3BH_3 with NaH and the Mechanistic Study. *Dalton Transactions* **2019**, *48*, 14984-14988.

44. Bowden, M. E.; Brown, I. W. M.; Gainsford, G. J.; Wong, H., Structure and Thermal Decomposition of Methylamine Borane. *Inorganica Chimica Acta* **2008**, *361*, 2147-2153.

45. Dovgaliuk, I.; Jepsen, L. H.; Safin, D. A.; Łodziana, Z.; Dyadkin, V.; Jensen, T. R.; Devillers, M.; Filinchuk, Y., A Composite of Complex and Chemical Hydrides Yields the First Al-Based Amidoborane with Improved Hydrogen Storage Properties. *Chemistry – A European Journal* **2015**, *21*, 14562-14570.

46. Dovgaliuk, I.; Møller, K. T.; Robeyns, K.; Louppe, V.; Jensen, T. R.; Filinchuk, Y., Complexation of Ammonia Boranes with Al^{3+}. *Inorganic Chemistry* **2019**, *58*, 4753-4760.

47. Favre-Nicolin, V.; Cerny, R., Fox, `Free Objects for Crystallography': A Modular Approach to Ab Initio Structure Determination from Powder Diffraction. *Journal of Applied Crystallography* **2002**, *35*, 734-743.

48. Rodríguez-Carvajal, J., Recent Advances in Magnetic Structure Determination by Neutron Powder Diffraction. *Physica B: Condensed Matter* **1993**, *192*, 55-69.

49. Spek, A., Single-Crystal Structure Validation with the Program Platon. *Journal of Applied Crystallography* **2003**, *36*, 7-13.

Chapter 4

Aluminum methylamidoborane complexes: mechanochemical synthesis, structure, stability, and reactive hydride composites

Abstract

Methyl-substituted Al-based amidoborane $Na[Al(CH_3NHBH_3)_4]$ was designed and synthesized as a potential candidate for hydrogen-storage purposes. Its structure as well as that of $Na[AlH(CH_3NHBH_3)_3]$, forming as an intermediate in mechanochemical synthesis, were determined by high-resolution powder X-ray diffraction. The synthesis of $Na[Al(CH_3NHBH_3)_4]$ required the much cheaper $CH_3NH_2BH_3$ and could be performed under less harsh conditions compared to the unsubstituted analogue. $Na[AlH(CH_3NHBH_3)_3]$ is the first example of an Al-based compound containing both hydride and amidoborane species. Despite $Na[Al(CH_3NHBH_3)_4]$ not being suitable for hydrogen storage on its own, reactive hydride composites (RHCs) made of $Na[Al(CH_3NHBH_3)_4]$ and 12 eq. of NaH, or 6 eq. of $NaNH_2$, showed the release of pure hydrogen at moderate temperatures, making this and similar systems interesting candidates for hydrogen storage.

This chapter is based on the following publication:

Ting Zhang, Timothy Steenhaut, Xiao Li, François Devred, Michel Devillers and Yaroslav Filinchuk, Aluminum methylamidoborane complexes: mechanochemical synthesis, structure, stability, and reactive hydride composites, *Sustainable Energy & Fuels*, **2023**, 7, 1119 (DOI: 10.1039/d2se01558g)

4.1 Introduction

Environmental pollution and the increasing demand for more energy are driving the search for new sustainable and ecofriendly alternatives for energy production and storage. Hydrogen appears to be an ideal candidate for the latter owing to its highest energy density (120 MJ/kg) and its generation from renewable energy sources, as well as the fact that water is the only waste product during the back-conversion to energy.[1-3] However, its storage in a compact, safe, and cost-effective manner remains a challenging problem that needs to be overcome before its use in widespread applications. Compressed H_2 gas is the currently accepted solution, but solid-state hydrogen storage appears to be an interesting mid- and long-term alternative.[2, 4-13] Unfortunately, up to now, no single hydrogen storage material fulfills all the essential application requirements (like the volumetric and gravimetric hydrogen capacities, handling pressure and temperature, and regeneration of dehydrogenated products) despite several decades of intensive investigation.[14] Therefore, developing new and better materials for this purpose is still a major requirement.

Ammonia borane (NH_3BH_3, AB) has received significant attention for hydrogen storage due to its high hydrogen content (19.6 wt.%), low toxicity, and good stability under ambient conditions.[15-20] However, it undergoes thermal decomposition in multiple steps at about 120 °C, 200 °C, and 500 °C, respectively,[16] accompanied by the evolution of some toxic volatile byproducts (B_2H_6, NH_3, $N_3B_3H_6$) and severe foaming and volume expansion during the thermal decomposition.[21-23] Many strategies have been explored to overcome these problems; for example, by forming metal amidoboranes (MABs),[6, 24-27] including mono-metallic[28-38] and multi-metallic[39-50] derivatives. Compared to pristine AB, MABs often have lower decomposition temperatures and/or release hydrogen with improved purity. This is the case, for example, for $LiNH_2BH_3$ and $NaNH_2BH_3$, which release ~10.9 wt.% and ~7.5 wt.% hydrogen, respectively, at lower temperatures (~90 °C) than the pure AB, with no borazine emission.[29] Other promising compounds comprise KNH_2BH_3, which decomposes at 80 °C and releases 6.5 wt.% of pure H_2,[33] and $Mg(NH_2BH_3)_2$, which releases ca.10 wt.% of high-purity H_2 upon heating to 300 °C.[35] Among the multi-metallic MABs, the first described was $Na_2Mg(NH_2BH_3)_4$, which could

release 8.4 wt.% of predominantly hydrogen with small amounts of ammonia and borazine.[42] Other examples include $Li_2Ca(NH_2BH_3)_4$ and $Na_2Ca(NH_2BH_3)_4$, which have shown low H_2 desorption temperatures of 91 °C and 98 °C, respectively. Also, $Li_2Ca(NH_2BH_3)_4$ decomposes with minimal ammonia contamination.[50]

$Na[Al(NH_2BH_3)_4]$ was studied by our group and was shown to release ~9 wt.% of high-purity hydrogen in two steps (at 120 °C and 168 °C). Furthermore, the final amorphous residue obtained upon the thermal decomposition of $Na[Al(NH_2BH_3)_4]$ could reversibly absorb about 27% of the released hydrogen at 250 °C and a H_2 pressure of 150 bar.[44] The high gravimetric hydrogen density, low decomposition temperature, and pure released hydrogen encouraged us to further investigate aluminum-based amidoboranes. Other known Al-based amidoboranes include $Li/Na/K[Al(NH_2BH_3)_4]$,[39, 44, 48, 49] $[Al(NH_3)_6]$ $[Al(NH_2BH_3)_6]$,[45] and $Li_3[AlH_2(NH_2BH_3)_4]$[43]. Among those, only the crystal structures of $Na[Al(NH_2BH_3)_4]$ and $K[Al(NH_2BH_3)_4]$ have been reported, limiting the understanding of the relationship between the structure and properties of Al-based amidoboranes.

With this in mind, and with the aim to enlarge the class of Al-based amidoboranes using cheaper substituted molecules, we synthesized $Na[Al(CH_3NHBH_3)_4]$ by a mechanochemical approach. Mechanochemical synthesis refers to reactions, normally of solids, induced by the input of mechanical energy, such as by grinding in a ball mill, which is extensively used for the synthesis of hydrides.[51-54] Such synthesis minimizes the use of toxic solvents, clearly promoting reactions between solids, often quickly and with quantitative yields, and enables access to products or processes not encountered in solution, as well as being easy to scale up. In addition, milling vials allow for synthesis under reactive conditions and/or offer access to the pressure and temperature of the reacting mixture, such as with the Easy GTM system (gas pressure and temperature detection system). Compared to “blind” milling, this approach allows following a reaction pathway, isolating the intermediates, and avoiding the degradation of a sample by over-milling.

The synthesis of $Na[Al(CH_3NHBH_3)_4]$ started from the more accessible (as compared to NH_3BH_3) methyl-substituted $CH_3NH_2BH_3$, which was easily obtainable from commercially available and cheap precursors. In addition, the presence of the weak electron–donating methyl substituent was expected to

affect the coordination bonds between N and Al atoms in the final complex. This, in particular, allowed doing the mechanochemical synthesis under much less harsh conditions compared to the non-substituted NH_3BH_3 based system. The crystal structure of the obtained $Na[Al(CH_3NHBH_3)_4]$ complex was determined from high-resolution powder X-ray diffraction (HR-PXRD), as well as that of $Na[AlH(CH_3NHBH_3)_3]$, which appeared as an intermediate in the mechanochemical synthesis. The thermal decomposition of $Na[Al(CH_3NHBH_3)_4]$ was accompanied by a large weight loss, making it unsuitable for hydrogen storage on its own. However, the dehydrogenation of the reactive hydride composites (RHCs) based on the newly obtained complex and sodium hydride, as well as sodium amide, demonstrated a release of significant amounts of pure hydrogen. This makes this Al-based system a potential candidate for solid-state hydrogen storage.

4.2 The synthesis and structure characterization of $Na[Al(CH_3NHBH_3)_4]$

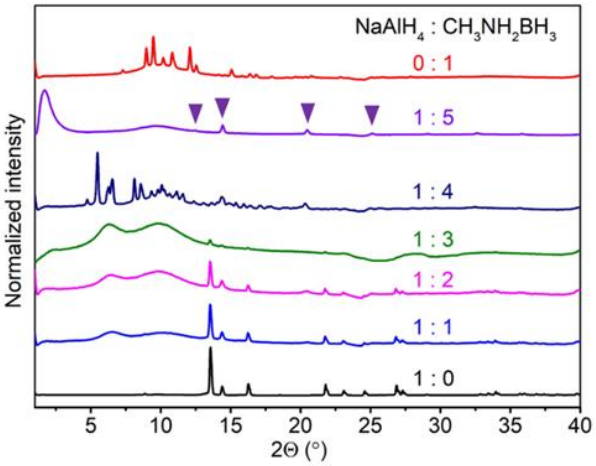

Figure 4.1 PXRD patterns of products obtained upon milling $NaAlH_4$ and $CH_3NH_2BH_3$ in different ratios, along with the patterns of reagents, the peaks of the residual NaCl are pointed by purple triangles (λ = 0.71073 Å).

Although the synthesis of $Na[Al(NH_2BH_3)_4]$[44] has been reported, methyl substitution on the ligand may lead to different reactivity, and potential steric hindrance may lead to the formation of different structures. Therefore, we

screened several conditions for the mechanochemical synthesis, exploring different mole ratios for $NaAlH_4$ and $CH_3NH_2BH_3$. We found that a new crystalline product was obtained only when using the mole ratio of 1: 4 of $NaAlH_4$ and $CH_3NH_2BH_3$ (see the powder X-ray diffraction, PXRD, results in Figure 4.1).

Structure solution and subsequent Rietveld refinement (Figure 4.2) for the $NaAlH_4$-$4CH_3NH_2BH_3$ sample revealed a 97 weight % of the new phase $Na[Al(CH_3NHBH_3)_4]$ and ~3 wt.% of the NaCl, the impurity from the synthesis of $CH_3NH_2BH_3$. NaCl is a solid by-product during the synthesis of $CH_3NH_2BH_3$ in THF, but a small amount of NaCl remained in the THF solution of $CH_3NH_2BH_3$ after filtering (see the Experimental section 4.7.2), although we could not see any residual NaCl in the PXRD pattern of $CH_3NH_2BH_3$ (Figure S5 in Annex). Also, NaCl clearly appeared on the amorphous background of $NaAlH_4$–5 $CH_3NH_2BH_3$ (Figure 4.1).

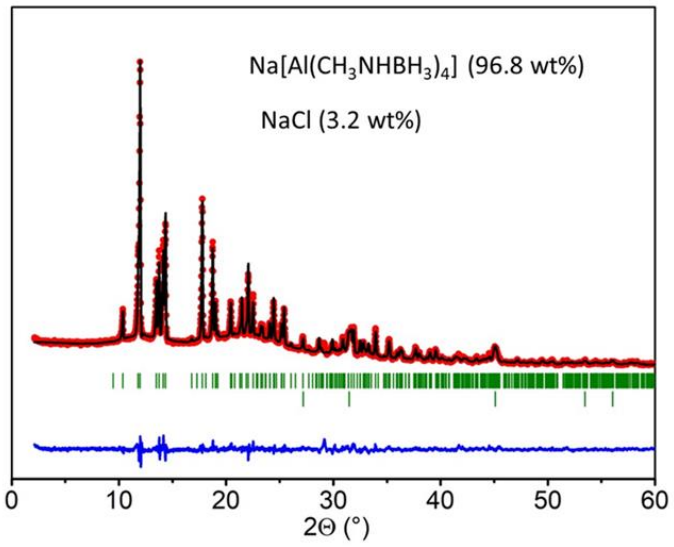

Figure 4.2 Rietveld refinement of the HR-PXRD diffractogram of $NaAlH_4$–$4CH_3NH_2BH_3$ containing $Na[Al(CH_3NHBH_3)_4]$ (upper green marker), NaCl (lower green marker) (λ = 1.54056 Å). Observed data (Y_{obs}, red curve), Rietveld refinement profile (Y_{calc}, black curve), and difference plot (Y_{obs} - Y_{calc}, blue curve). Agreement factors, corrected for background, are R_{exp} = 9.41 %, R_{wp} = 16.3 %, R_p = 18.8%, χ^2 = 3.

$Na[Al(CH_3NHBH_3)_4]$ crystallizes in a monoclinic unit cell with the space group $P2_1/n$. In this anionic complex, the central Al^{3+} ion is tetrahedrally coordinated by four N atoms from four $[CH_3NHBH_3]^-$ anions (Figure 4.3A), similarly to the previously reported $Na[Al(NH_2BH_3)_4]$ and $K[Al(NH_2BH_3)_4]$.[44, 49] The Al–N distances were between 1.922(11) and 1.990(12) Å, which were a little bit longer than in $Na[Al(NH_2BH_3)_4]$ (1.840(9)–1.929(8) Å) and $K[Al(NH_2BH_3)_4]$ (1.838(9)–1.909(9) Å). This could be explained by the introduction of the bulky methyl substituents on the N atoms, making longer Al–N bonds necessary to offer sufficient space for the $[CH_3NHBH_3]^-$ anions. The Na atoms have a distorted triangular bipyramidal coordination geometry formed by five surrounding BH_3 groups from the $[CH_3NHBH_3]^-$ anions (Figure. 4.3B), unlike the usual octahedral environments reported for $Na[Al(NH_2BH_3)_4]$, $Na_2[Mg(NH_2BH_3)_4]$, and $Na_2[Ca(NH_2BH_3)_4]$.[41, 44, 50] In $Na[Al(CH_3NHBH_3)_4]$, all the $[CH_3NHBH_3]^-$ units exhibited a bridging coordination mode, linking Al^{3+} and Na^+ ions, leading to the formation of a 3D polymeric structure (Figure 4.4). Given the smaller number of N–H bonds, fewer dihydrogen bonds were formed in $Na[Al(CH_3NHBH_3)_4]$, compared to in the non-substituted $Na[Al(NH_2BH_3)_4]$ (Table 4.3).

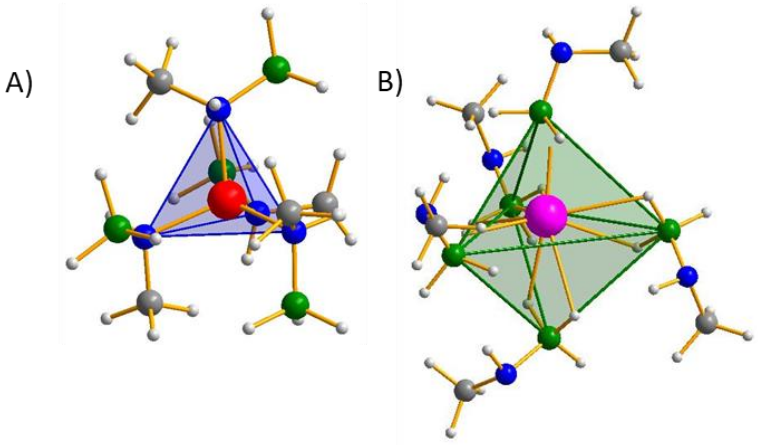

Figure 4.3 Ball and stick plots of the tetrahedral $[Al(CH_3NHBH_3)_4]^-$ anion (A) and distorted triangular bipyramidal coordination of Na+ cation (B); Color code: N = blue, B = green, C = grey, H = light grey, Al = red, and Na = pink.

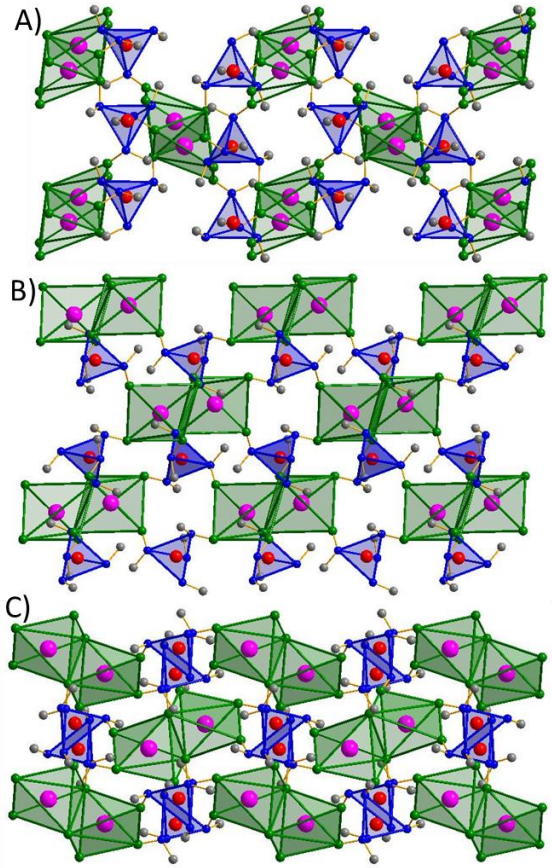

Figure 4.4 Crystal packing of Al and Na coordination polyhedra in the structure of $Na[Al(CH_3NHBH_3)_4]$ along the a (A), b (B), and c (C) axis. Color code: N = blue, B = green, C = grey, H = light grey, Al = red, and Na = pink. Hydrogen atoms are omitted for clarity.

The Fourier-transform infrared (FTIR) spectrum of $Na[Al(CH_3NHBH_3)_4]$ exhibited characteristic bands of B–H (bending from 962 to 1218 cm^{-1} and stretching from 2168 to 2450 cm^{-1}), N–H (bending at 1595 cm^{-1} and stretching from 3200 to 3298 cm^{-1}), C–H (bending at 1405–1495 cm^{-1} and stretching around 2864–3035 cm^{-1}), and C–N (stretching in the 859–965 cm^{-1} range) vibration modes, similar to those of $CH_3NH_2BH_3$ (Figure 4.5).[55] Furthermore, new bands were present between 502 and 640 cm^{-1}, which could be assigned to the Al–N stretching modes. In addition, the signal at 3166 cm^{-1} corresponding to the symmetrical stretching mode of N–H in the $CH_3NH_2BH_3$

precursor disappeared, whereas the signal corresponding to the N–H bending mode was shifted from 1320 cm^{-1} in the $CH_3NH_2BH_3$ precursor to 1364 cm^{-1}, consistent with the removal of one H atom and the formation of a coordination bond between N and Al. Moreover, the signal of the B–N stretching mode in $Na[Al(CH_3NHBH_3)_4]$ was widened and blue-shifted compared to $CH_3NH_2BH_3$. This phenomenon, which was also reported for $Na[Al(NH_2BH_3)_4]$,[44] indicated slightly stronger B–N bonds, which was in accordance with the shorter bonds observed in the crystal structure (Table 4.4).

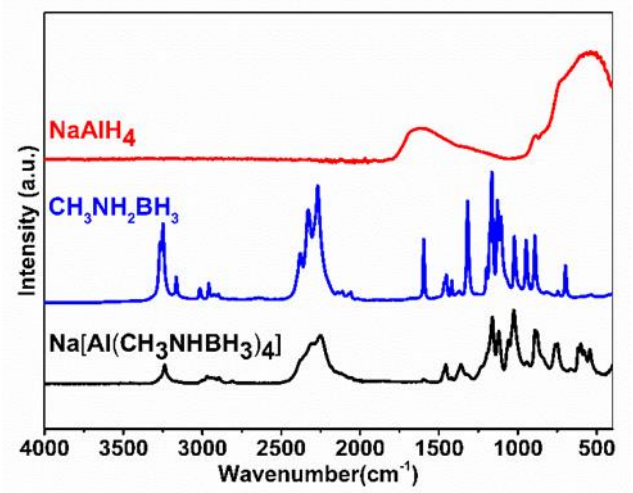

Figure 4.5 ATR-IR spectra of $Na[Al(CH_3NHBH_3)_4]$, $CH_3NH_2BH_3$ and $NaAlH_4$.

4.3 Investigation of the reaction mechanism and isolation of the intermediate

Compared to the reported $Na[Al(NH_2BH_3)_4]$, the methyl substituted $Na[Al(CH_3NHBH_3)_4]$ could be obtained with a shorter milling time while keeping all the other reaction parameters unchanged (see Table 4.1). This indicated a higher reactivity of $NaAlH_4$ with $CH_3NH_2BH_3$ than with its unsubstituted counterpart. Indeed, the electronic contribution of the methyl group to the N atom likely made the dehydrogenation with $NaAlH_4$ easier. Furthermore, the composites of $NaAlH_4$ with 4 eq. of $CH_3NH_2BH_3$ became liquid after just several milling cycles (Figure 4.6 and 4.13), in part because of the lower melting point of $CH_3NH_2BH_3$ (56 °C)[56] compared to NH_3BH_3 (112–

114 °C),[16] in which most likely the eutectic mixtures enabled a better interaction between the reactants. In contrast, while milling $NaAlH_4$ with 4 eq. of unsubstituted NH_3BH_3 the mixture remained solid throughout the synthesis.

Table 4.1 Milling conditions reported for the synthesis of $Na[Al(NH_2BH_3)_4]$ and used for the synthesis of the new $Na[Al(CH_3NHBH_3)_4]$ complex.

Parameter	$Na[Al(NH_2BH_3)_4]$	$Na[Al(CH_3NHBH_3)_4]$
Rotation speed (rpm)	600	600
Milling time (min)	3	3
Break time (min)	5	5
Number of cycles	240	120
Ball to powder mass ratio	30:1	30:1

Figure 4.6 Photographs of product after different amounts of milling cycles based on Approach A shown in Table 4.2.

To gain more insights into the reaction mechanism, the gas pressure and temperature were monitored in situ during the mechanochemical reaction between $NaAlH_4$ and 4 eq. of $CH_3NH_2BH_3$ (Figure 4.7 A and S6 in annex). About 3.93 mole of gas was released per mole of $NaAlH_4$ during the milling process, which was close to the amount of gas expected (4 eq.), according to the following equation:

$$NaAlH_4 + 4\ CH_3NH_2BH_3 \longrightarrow Na[Al(CH_3NHBH_3)_4] + 4\ H_2\uparrow$$

Interestingly, the pressure rise during the synthesis of $Na[Al(CH_3NHBH_3)_4]$ showed two distinct steps, illustrated by the two colors in Figure 4.7A. About 2.83 eq. of gas per Al was released during the first step. Since this may suggest the formation of an intermediate involving 3 $CH_3NH_2BH_3$ per $NaAlH_4$, we performed the milling under softer conditions, as described in the Experimental part 4.7.4, and the reaction was stopped after the first step of gas release, as could be observed from the *in-situ* follow-up of the pressure and temperature during the reaction (Figure 4.7A). Upon crystallization of the obtained product, we isolated crystalline powder, enabling us to determine the crystal structure of the intermediate by high-resolution PXRD. The structure revealed the composition $Na[AlH(CH_3NHBH_3)_3]$, in which 3 out of 4 hydrogen atoms in the starting complex hydride were exchanged for methylamidoboranes. This allows us to present the reaction of $Na[Al(CH_3NHBH_3)_4]$ synthesis as occurring in two steps, as shown in Figure 4.7B.

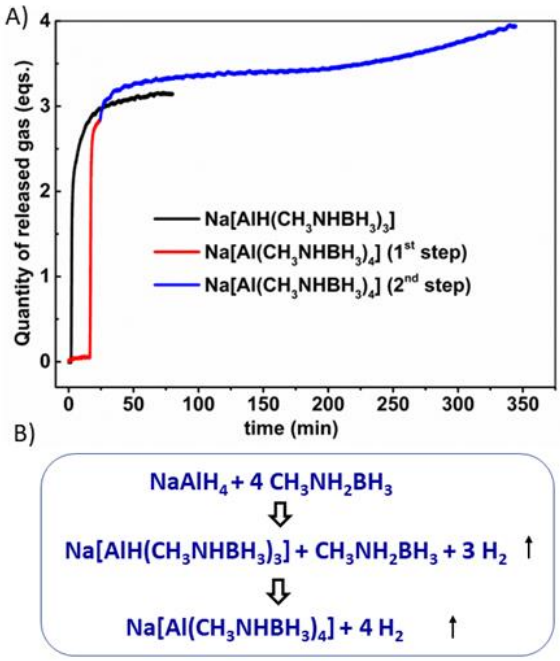

Figure 4.7 (A) The quantity of gas released during the synthesis of $Na[Al(CH_3NHBH_3)_4]$ and $Na[AlH(CH_3NHBH_3)_3]$, at 600 and 500 rpm milling for 2 and 1-step reactions respectively, and (B) the corresponding reaction steps for $NaAlH_4$ + $4CH_3NH_2BH_3$ mixture.

In 2013, the existence of $Li_3[AlH_2(NH_2BH_3)_4]$ was proposed but its structure has not been determined yet. The intermediate we identified in the present work is thus the first characterized example of a crystalline Al-based complex coordinated both with hydride and amidoborane. In $Na[AlH(CH_3NHBH_3)_3]$, aluminum is coordinated to three N atoms from the $[CH_3NHBH_3]^-$ anions and one hydride to form a distorted tetrahedron (Figure 4.8A). The Na^+ cation is surrounded by five H atoms from three different BH_3 groups (Figure 4.8B). More accurate H positions could be obtained from the DFT optimization, and thus the coordination environment for Na^+ may actually differ. The $[CH_3NHBH_3]^-$ units in the intermediate connect Al^{3+} and Na^+ ions in a bridging manner to form a 2D sheet (Figure 4.9) instead of the 3D polymeric structure in $Na[Al(CH_3NHBH_3)_4]$.

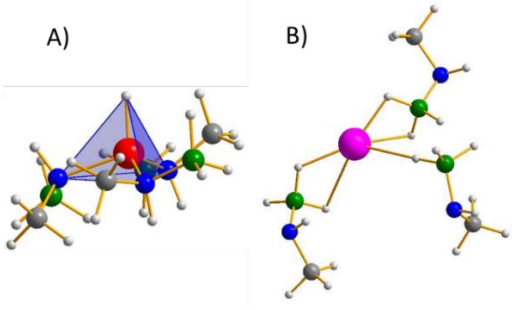

Figure 4.8 Ball and stick plots of the tetrahedral (A) $[AlH(CH_3NHBH_3)_3]^-$ and (B) $[Na(CH_3NHBH_3)_3]^{2-}$ Color code: N = blue, B = green, C = grey, H = light grey, Al = red, and Na = pink.

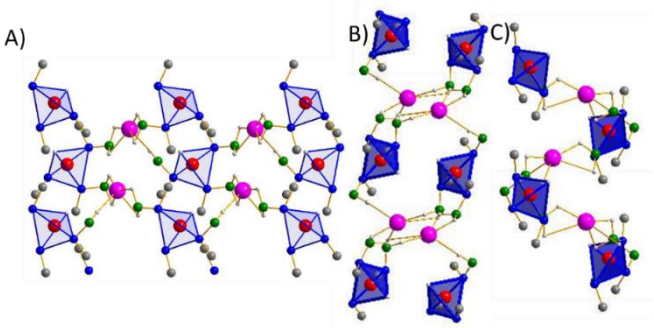

Figure 4.9 Crystal packing of Al and Na coordination polyhedra in the structure of $Na[AlH(CH_3NHBH_3)_3]$ along the a (A), b (B), and c (C) axis. Color code: N = blue, B = green, C = grey, H = light grey, Al = red, and Na = pink. Hydrogen atoms are omitted for clarity.

4.4 The thermal decomposition of $Na[Al(CH_3NHBH_3)_4]$

4.4.1 The stability of $Na[Al(CH_3NHBH_3)_4]$ in air

Before we investigated the thermal dehydrogenation of $Na[Al(CH_3NHBH_3)_4]$, we examined the stability of $Na[Al(CH_3NHBH_3)_4]$ in air based on the PXRD pattern analysis (Figure 4.10). The results indicate that $Na[Al(CH_3NHBH_3)_4]$ remains stable in air for at least 15 min without any decomposition. However, after being exposed to air for 25 min, peaks corresponding to MeAB appeared. After 1.5 hours, the peaks associated with $Na[Al(CH_3NHBH_3)_4]$ disappeared completely. This suggests that $Na[Al(CH_3NHBH_3)_4]$ decomposes entirely when exposed to air for 1.5 hours. Additionally, MeAB is identified as the main crystalline phase of the product, resulting from the reaction between $Na[Al(CH_3NHBH_3)_4]$ and air (or moisture present in the air).

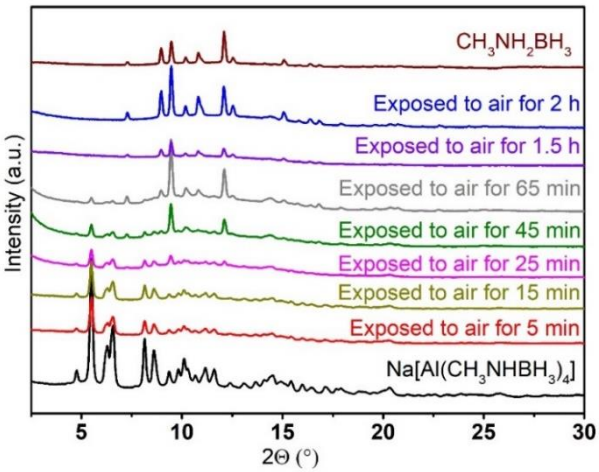

Figure 4.10 PXRD pattern of $CH_3NH_2BH_3$, $Na[Al(CH_3NHBH_3)_4]$, $Na[Al(CH_3NHBH_3)_4]$ exposed to air for different duration (λ = 0.71073 Å).

4.4.2 The thermal decomposition of $Na[Al(CH_3NHBH_3)_4]$

The lower number of N–H bonds and thus fewer dihydrogen bonds formed in $Na[Al(CH_3NHBH_3)_4]$ compared to $Na[Al(NH_2BH_3)_4]$ could potentially lead to a lower thermal stability of this complex (Table 4.3). Indeed, the thermal decomposition occurred in a single step with a very significant weight loss starting at about 100 °C, accompanied by a weight oscillation due to the so-

called “jet” effect (productions of gas or particles in a fast exothermic reaction), Figure 4.11A. Based on PXRD and IR analyses (Figure 4.11B and C), the solid decomposition products obtained after heating at 100 °C were identified as crystalline $NaBH_4$ along with some amorphous phase(s). This decomposition contrasted with the generation of pure hydrogen by $Na[Al(NH_2BH_3)_4]$, which ended up equally by formation of $NaBH_4$ and amorphous phase(s). The large weight loss of about 48% during the decomposition of the methyl-substituted analogue was much beyond the expected value for the release of pure H_2 (12.4 % and 126 g/L for the gravimetric and volumetric hydrogen density of $Na[Al(CH_3NHBH_3)_4]$ respectively, including the hydrogen of the methyl group). This clearly indicated that other heavier gaseous species were produced along with hydrogen, making $Na[Al(CH_3NHBH_3)_4]$ not suitable for hydrogen storage on its own.

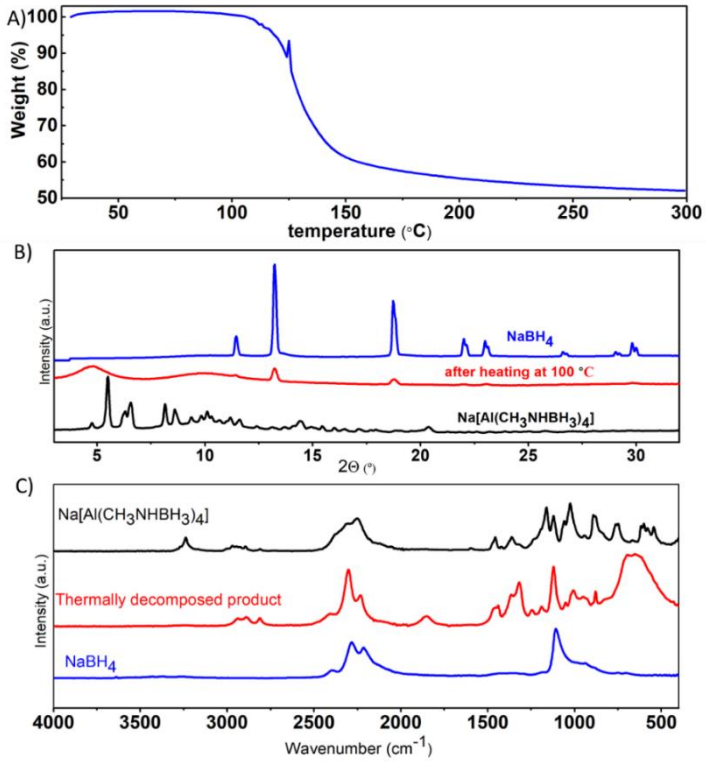

Figure 4.11 (A) TG analysis of $Na[Al(CH_3NHBH_3)_4]$ showing significant weight loss; (B) PXRD patterns (λ = 0.71073 Å) and (C) IR spectra of the product upon heating at 100 °C, compared to the starting $Na[Al(CH_3NHBH_3)_4]$ and $NaBH_4$.

4.5 The thermal dehydrogenation of RHCs based on $Na[Al(CH_3NHBH_3)_4]$

Many hydrides possessing a high H–content are not suitable as hydrogen carriers on their own, either due to their high decomposition temperatures, or to the release of different species along with hydrogen, as in the title system. However, a combination of two hydrides may generate pure hydrogen at moderate temperatures, in a reaction unique to the combination.[12, 57-61] Some theoretical studies are aiming to screen for such combinations, usually within the reaction enthalpy window (30-60 kJ/mol) suitable for reversible hydrogen adsorption/desorption;[62] the most promising systems are verified experimentally. The shortcoming of this approach is the absence of structure information (used in modeling) for some known hydrides and for the new phases being discovered. Indeed, a new hydrogen-rich solid may lead to numerous new combinations that avoided scoring in this screening process. It seems important to verify the properties of RHCs once the new H-rich phase is discovered. Therefore, we prepared and characterized the thermal properties of the RHCs based on $Na[Al(CH_3NHBH_3)_4]$ and NaH or $NaNH_2$.

4.5.1 The thermal dehydrogenation of $Na[Al(CH_3NHBH_3)_4]$ + 12NaH

To provide enough hydride ions to match the hydridic H from BH_3, we decided to use 12 eq. of NaH per Al (7.79% and 96 g/L for the gravimetric and volumetric hydrogen densities of the composite $Na[Al(CH_3NHBH_3)_4]$ + 12NaH respectively, including the hydrogen of the methyl group). The components were ball milled for 1 hour at 100 rpm. The obtained RHC possessed a considerably different thermal decomposition profile compared to the pure $Na[Al(CH_3NHBH_3)_4]$. The TGA curve showed two distinct weight loss steps from room temperature to 400 °C (Figure 4.12A), remarkably without the jet effect seen for the pure complex hydride. About 6.2 wt.% was lost during the first step from room temperature to 180 ˚C, which was close to the theoretical hydrogen content (5.45 wt.%, excluding hydrogen in the methyl groups) of the RHC. The dehydrogenation process of the first step was further characterized through mass spectrometry between 40 °C and 180 °C, revealing the hydrogen release, without the detection of ammonia, diborane, methane, or methylamine (Figure 4.12B).

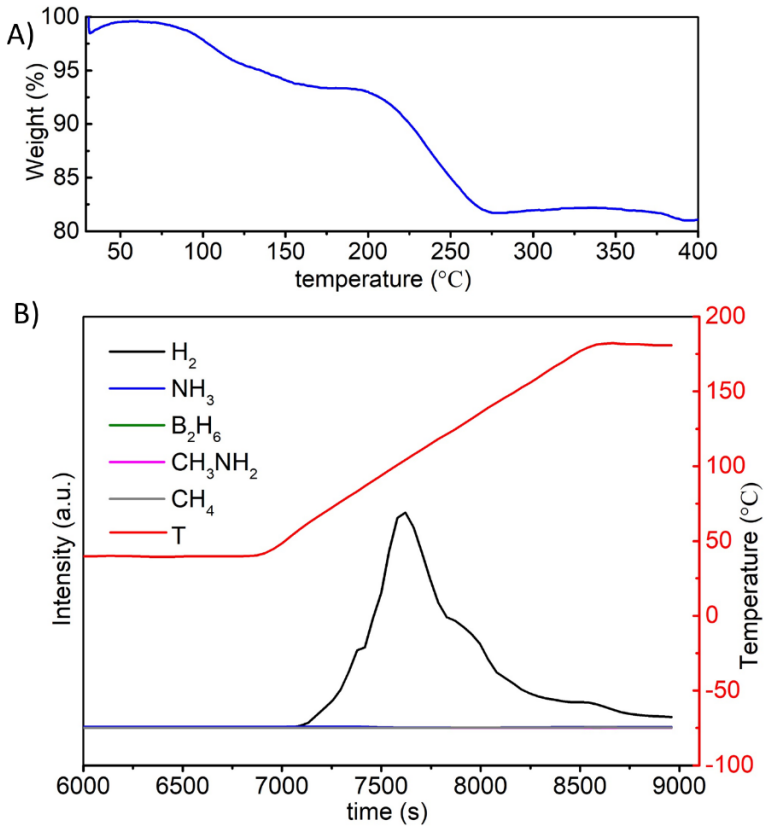

Figure 4.12 TGA (A) and MS (B) analyses for the RHC made of $Na[Al(CH_3NHBH_3)_4]$ + 12NaH.

4.5.2 The thermal dehydrogenation of $Na[Al(CH_3NHBH_3)_4]$ + $6NaNH_2$

Differently from NaH, $NaNH_2$ plays the role of a proton donor. In this case, 6 eq. of $NaNH_2$ was needed to provide enough protic $H^{\delta+}$ for the formation of H_2 from the $B–H^{\delta-}$ moieties contained in $Na[Al(CH_3NHBH_3)_4]$ (8.70% and 102 g/L for the gravimetric and volumetric hydrogen densities of the composite $Na[Al(CH_3NHBH_3)_4]$ + $6NaNH_2$ respectively, including the hydrogen of the methyl group). The RHC formed by the combination of $Na[Al(CH_3NHBH_3)_4]$ with 6 eq. of $NaNH_2$ showed one thermal decomposition step between room temperature and 400 °C, similar to the pure $Na[Al(CH_3NHBH_3)_4]$, but without the jet effect. However, the formation of the RHC lowered the amount of released gaseous products, as only about 10 wt.% was released upon heating to 400 °C (Figure 4.13A). The gaseous species released between 40 °C and

180 °C were also identified by means of mass spectrometry, similar to the RHC with NaH. We weighed a sample of this RHC before and after the MS characterization and found about 6.8 wt.% was lost up to 180 °C, at a theoretical hydrogen content of 6.1 wt.%, excluding the hydrogen in the methyl groups. We believe that the CH_3 group did not participate in the dehydrogenation reaction in both the RHCs, despite the experimental weight losses appearing slightly higher than the theoretical values. In this case, also, no ammonia, diborane, nitrogen, methane, or methylamine were detected by MS (Figure 4.13B and S13, 14 in Annex), in contrast with pristine $NaNH_2$, which released nitrogen and ammonia at about 140 °C (Figure. S11 in Annex).

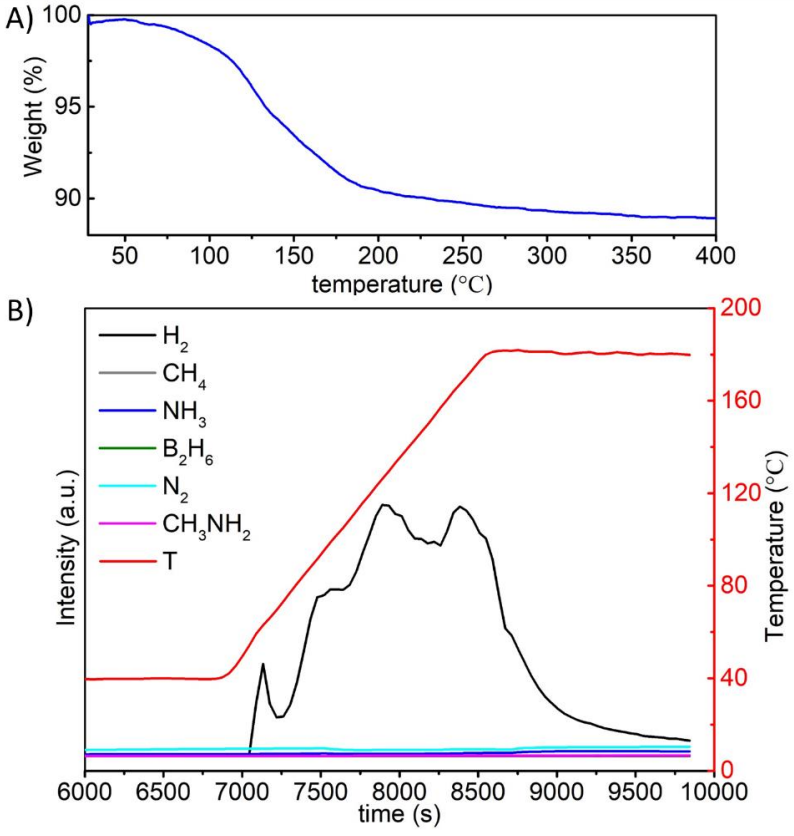

Figure 4.13 TGA (A) and MS (B) analyses for the RHC made of $Na[Al(CH_3NHBH_3)_4]$ + $6NaNH_2$.

In summary, although the pure $Na[Al(CH_3NHBH_3)_4]$ complex did not release pure hydrogen upon thermal treatment, the studied RHCs with 12 eq.

of NaH and with 6 eq. of $NaNH_2$ allowed obtaining pure hydrogen between 40 °C and 180 °C, proving that the concept of RHCs works very well for this Al-based system. Further study is necessary to test for possible hydrogen reversibility, which may require a use of catalysts, thus going beyond the scope of this work.

4.6 Conclusion

Al-based amidoborane $Na[Al(CH_3NHBH_3)_4]$ was obtained by a mechanochemical reaction between $NaAlH_4$ and $CH_3NH_2BH_3$. Compared to the previously reported $Na[Al(NH_2BH_3)_4]$, the introduction of a weak electron-donating CH_3 group favored the formation of Al-based amidoboranes. The reaction occurred in two steps, and the $Na[AlH(CH_3NHBH_3)_3]$ intermediate was isolated and characterized by PXRD, giving new insights into the formation of Al-based amidoboranes. Al^{3+} was tetrahedrally coordinated in both new compounds; $Na[AlH(CH_3NHBH_3)_3]$ is the first example of Al simultaneously coordinated to amidoborane and hydrogen.

Large weight losses were observed upon the thermal decomposition of $Na[Al(CH_3NHBH_3)_4]$, evidence that other gas phase by-products were forming along with hydrogen. The formation of reactive hydride composites with either 12 eq. of NaH or 6 eq. of $NaNH_2$ decreased the weight losses observed up to 180 °C to the theoretical hydrogen capacity of the systems. Moreover, we did not detect the formation of by-products such as NH_3, B_2H_6, CH_4, CH_3NH_2, or N_2 by mass spectrometry during the thermal decomposition of the RHCs. This calls for further study of the hydrogen reversibility in these systems, as well as highlighting the potential for cheap and light Al-based systems for solid-state hydrogen storage.

4.7 Experimental section

4.7.1 Chemicals

All the samples were obtained from commercially available $NaAlH_4$ (93%), $NaBH_4$ (97%), $CH_3NH_2{\cdot}HCl$ (98%), and anhydrous THF (>99.9%), which were purchased from Sigma Aldrich Co. Ltd. All the operations were performed in a glovebox with a high-purity argon atmosphere.

4.7.2 Synthesis of $CH_3NH_2BH_3$ (MeAB)[63]

See Chapter 3, Experimental section 3.7.4

4.7.3 Synthesis of $Na[Al(CH_3NHBH_3)_4]$

First, 1 eq. of $NaAlH_4$ (46 mg, 0.85 mmol) and 4 eq. of $CH_3NH_2BH_3$ (154.7 mg, 3.4 mmol) were placed into an 80 mL stainless-steel vial and with three 10 mm diameter stainless-steel balls and milled in a planetary ball mill (Fritsch Pulverisette 7 Premium line). Evolution of the gas pressure and temperature during the reaction was performed using the Easy GTM detection system accessory (Fritsch). The optimized synthesis parameters (milling speed, time, number of cycles, and ball to power mass ratio) are listed in Table 4.2. The sample used for complete characterization was obtained by applying the parameters for approach A with the purity of 96.8 %, in Table 4.2, this synthesis is reproducible.

Table 4.2 Parameters used for the optimization of the synthesis of $Na[Al(CH_3NHBH_3)_4]$.

Parameter	A	B	C	D
Rotation speed (rpm)	600	600	500	250
Milling time(min)	3	3	3	3
Break time(min)	5	5	2	2
Number of cycles	≥90	120	200	240
Ball to powder mass ratio	60:1	30：1	60:1	60:1

Composite $NaAlH_4$–$CH_3NH_2BH_3$: 1 eq. of $NaAlH_4$ (109.2 mg, 2.0 mmol) and 1 eq. of $CH_3NH_2BH_3$ (90.8 mg, 2.0 mmol) were placed into an 80 mL stainless steel vial with three 10 mm diameter stainless steel balls (ball-to-powder mass ratio of 60:1). The reactants were then milled in a planetary ball mill (Fritsch Pulverisette 7 Premium line), with a rotation speed of 600 rpm for 100 milling cycles of 3 min interrupted by 5 min cooling breaks.

Composite $NaAlH_4$–$2CH_3NH_2BH_3$: 1 eq. of $NaAlH_4$ (75 mg, 1.4 mmol) and 2 eq. of $CH_3NH_2BH_3$ (124.9 mg, 2.8 mmol) were placed into an 80 mL stainless steel vial with three 10 mm diameter stainless steel balls (ball-to-powder mass ratio of 60:1). The reactants were then milled in a planetary ball

mill (Fritsch Pulverisette 7 Premium line), with a rotation speed of 600 rpm for 140 milling cycles of 3 min interrupted by 5 min cooling breaks.

Composite $NaAlH_4$–$3CH_3NH_2BH_3$: 1 eq. of $NaAlH_4$ (46 mg, 0.85 mmol) and 3 eq. of $CH_3NH_2BH_3$ (116 mg, 2.6 mmol) were placed into an 80 mL stainless steel vial with three 10 mm diameter stainless steel balls (ball-to-powder mass ratio of 60:1). The reactants were then milled in a planetary ball mill (Fritsch Pulverisette 7 Premium line), with a rotation speed of 600 rpm for 140 milling cycles of 3 min interrupted by 5 min cooling breaks.

Composite $NaAlH_4$–$5CH_3NH_2BH_3$: 1 eq. of $NaAlH_4$ (46 mg, 0.85 mmol) and 5 eq. of $CH_3NH_2BH_3$ (191.0 mg, 4.2 mmol) were placed into an 80 mL stainless steel vial with three 10 mm diameter stainless steel balls (ball-to-powder mass ratio of 60:1). The reactants were then milled in a planetary ball mill (Fritsch Pulverisette 7 Premium line), with a rotation speed of 600 rpm for 200 milling cycles of 3 min interrupted by 5 min cooling breaks.

4.7.4 Isolation of $Na[AlH(CH_3NHBH_3)_3]$

Some crystalline $Na[AlH(CH_3NHBH_3)_3]$ was obtained by using the following method. First, a mixture of 1 eq. of $NaAlH_4$ and 4 eq. of $CH_3NH_2BH_3$ was loaded into an 80 mL stainless-steel vial with three 10 mm diameter stainless-steel balls and milled in a planetary ball mill (Fritsch Pulverisette 7 Premium line). Evolution of the gas pressure and temperature during the reaction was performed using the Easy GTM detection system accessory (Fritsch). The rotation speed was set to 500 rpm and the ball to powder mass ratio was 60: 1. The synthesis was performed using 15 milling cycles of 3 min interrupted by 2 min cooling breaks, to yield a colorless liquid (Figure 4.14). This liquid was then exposed to the dry atmosphere of an argon-filled glovebox for about 2 weeks, to yield some light gray powder. Upon heating this powder at 50 °C under vacuum in a tubular oven, crystalline $Na[AlH(CH_3NHBH_3)_3]$ was obtained.

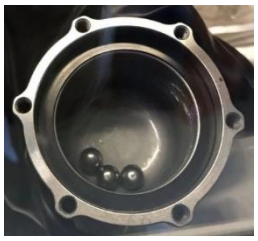

Figure 4.14 Photograph of sample used for isolating the $Na[AlH(CH_3NHBH_3)_3]$ intermediate after 15 cycles of milling before drying.

4.7.5 Powder X-ray diffraction (PXRD)

Samples were filled into 0.7 mm thin-walled glass capillaries (Hilgenberg GmbH) in an argon-filled glovebox and subsequently sealed with grease before removing them from the glovebox. The capillaries were then cut and immediately put into wax on a goniometer head without allowing air to enter the capillary.

Diffraction data were immediately recorded on a MAR345 image-plate detector equipped with an Incoated Mo (λ = 0.71073 Å) Microfocus (ImS) system operating at 50 kV and 1000 mA. The obtained 2D images were azimuthally integrated by the Fit2D program using LaB_6 as the calibrant. High-resolution (HR)-PXRD patterns were collected in 0.5 mm diameter glass capillaries on a STOE STADI P COMBI diffractometer using Cu-Ka1 (λ = 1.54056 Å) radiation (40 kV, 40 mA, graphite primary monochromator). The diffracted beam was recorded on a DECTRIS MYTHEN 1K strip detector.

4.7.6 Crystal structure determination

The HR-PXRD data for $Na[Al(CH_3NHBH_3)_4]$ and $Na[AlH(CH_3NHBH_3)_3]$ were indexed in monoclinic unit cells and their structures were solved by global optimization using FOX software.[64] The anions were modeled by conformationally-free z-matrices restrained by the bond distances and angles. Since the coordinated N-atom of methylamidoborane is chiral, we examined all the combinations of these chiral centers within the Al-centered anions. The resulting structures showed the best fit to the data, but also satisfied the crystal-chemical expectations, such as the formation of dihydrogen bonds N-H/H–B and coordination of Na^+ by H atoms of the BH_3 groups. Rietveld

refinements were done in Fullprof,[65] treating the amidoboranes as separate rigid bodies within the complex anion and refining Na and Al as free atoms. The symmetry was confirmed with the ADDSYM routine in the program PLATON.[66]

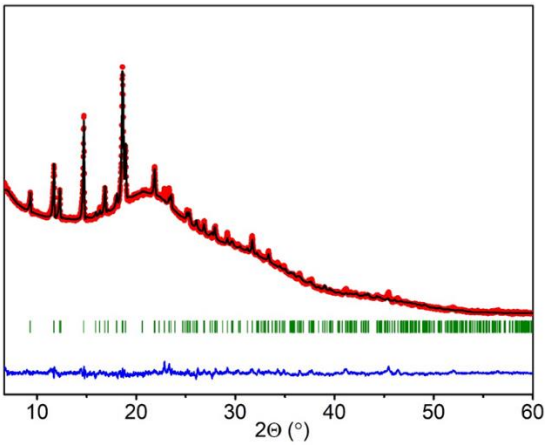

Figure 4.15 Rietveld refinement of the HR-PXRD diffractogram of $Na[AlH(CH_3NHBH_3)_3]$ (λ = 1.54056 Å). Observed data (Yobs, red curve), Rietveld refinement profile (Ycalc, black curve), and difference plot (Yobs - Ycalc, blue curve). Agreement factors, corrected for background, are R_{exp} = 11.92 %, R_{wp} = 22.4 %, R_p = 38.3 %, χ2 = 3.52.

Table 4.3 $N–H^{\delta+}…H^{\delta-}–B$ bond lengths and N-H…H angles in $Na[Al(NH_2BH_3)_4]$, $Na[AlH(CH_3NHBH_3)_3]$ and $Na[Al(CH_3NHBH_3)_4]$ complexes.

Complex	$N-H^{\delta+}…H^{\delta-}-B$	D(H···H)/Å	∠(N-H···H)/ °
$Na[Al(NH_2BH_3)_4]$	N(1)–H(11) …H(15)–B(1)	2.06	169.0
	N(1)–H(12) …H(25)–B(2)	2.18	134.4
	N(2)–H(22) …H(13)–B(1)	2.16	139.3
	N(3)–H(31) …H(35)–B(3)	2.24	137.2
	N(3)–H(32) …H(15)–B(1)	2.28	157.6
	N(4)–H(41) …H(23)–B(2)	1.96	143.9
	N(4)–H(42) …H(45)–B(4)	2.00	162.1
$Na[AlH(CH_3NHBH_3)_3]$	N(31)–H(31) …H(01)–Al(1)	2.43	139.6
$Na[Al(CH_3NHBH_3)_4]$	N(21)–H(21) …H(44)–B(41)	2.09	149.2
	N(31)–H(31) …H(14)–B(11)	2.34	160.4
	N(41)–H(41) …H(33)–B(31)	2.15	141.5
	N(41)–H(41) …H(32)–B(31)	2.21	142.3

Table 4.4 B-N bond lengths in $CH_3NH_2BH_3$, $Na[AlH(CH_3NHBH_3)_3]$ and $Na[Al(CH_3NHBH_3)_4]$

$CH_3NH_2BH_3$	$Na[AlH(CH_3NHBH_3)_3]$	$Na[Al(CH_3NHBH_3)_4]$
1.58(7)	1.46(3)	1.57(1)
	1.54(2)	1.54(7)
	1.47(3)	1.52(7)
		1.57(0)

4.7.7 Fourier-transform infrared spectroscopy (FTIR)

Attenuated total reflectance (ATR)-IR spectra were measured with a Bruker Alpha spectrometer equipped with a Platinum ATR sample holder (diamond crystal, single bounce) housed in an argon-filled glovebox.

4.7.8 Thermogravimetric analysis (TGA)

TGA measurements were performed using a Netzsch STA 449 F3 TGA/DSC equipped with a stainless-steel oven hosted in an argon-filled glovebox. Samples were loaded into an Al_2O_3 crucible and heated at a rate of 5 K min^{-1} under an argon atmosphere (100 mL min^{-1}).

4.7.9 Mass spectrometry

Mass spectrometry measurements were performed using a Hiden Catlab reactor combined with a Quantitative Gas Analyzer (QGA) Hidden quadrupole mass spectrometer, which is installed outside of the glovebox. Before the experiment, the samples were loaded into a quartz tube in between two layers of glass cotton under the protective atmosphere of an argon-filled glovebox. The two extremities of the quartz tube were sealed with Parafilm before removing from the glovebox. The quartz tube was then installed in the sample holder outside the glovebox after quickly removing the Parafilm, and the argon flow (40 mL min^{-1}) was switched on immediately to prevent contact of the sample with air. Samples were heated to 40 °C, and kept isothermally for ~2 h to stabilize the temperature. Heating was then performed at a rate of 5 °C min^{-1} up to 180 °C followed by an one hour isotherm. Gas evolution was monitored by recording the highest intensity peak for each gas, i.e., m/z of 2,

15, 17, 18, 26, 28, and 30 for H_2, CH_4, NH_3, H_2O, B_2H_6, N_2, and CH_3NH_2 respectively.

Table 4.5 The molar mass, density, the molar volume and hydrogen densities of $Na[Al(CH_3NHBH_3)_4]$, NaH and $NaNH_2$ and their composites.

System	M (g/mole)	δ (g/cm^3)	V (cm^3)	Gravimetric density (%)	Volumetric density (g/L)
$Na[Al(CH_3NHBH_3)_4]$	225.5	1.014	222.4	12.42	126
NaH	24	1.47	16.3	4.17	61
$NaNH_2$	39	1.39	28.1	5.13	71
$Na[Al(CH_3NHBH_3)_4]$ + 12 NaH	513.5	-	418.3	7.79	96
$Na[Al(CH_3NHBH_3)_4]$ + 6 $NaNH_2$	459.5	-	390.7	8.70	102

References

1. Møller, K. T.; Jensen, T. R.; Akiba, E.; Li, H.-w., Hydrogen - a Sustainable Energy Carrier. *Progress in Natural Science: Materials International* **2017**, *27*, 34-40.
2. Abe, J. O.; Popoola, A. P. I.; Ajenifuja, E.; Popoola, O. M., Hydrogen Energy, Economy and Storage: Review and Recommendation. *International Journal of Hydrogen Energy* **2019**, *44*, 15072-15086.
3. Dawood, F.; Anda, M.; Shafiullah, G. M., Hydrogen Production for Energy: An Overview. *International Journal of Hydrogen Energy* **2020**, *45*, 3847-3869.
4. Ren, J.; Musyoka, N. M.; Langmi, H. W.; Mathe, M.; Liao, S., Current Research Trends and Perspectives on Materials-Based Hydrogen Storage Solutions: A Critical Review. *International Journal of Hydrogen Energy* **2017**, *42*, 289-311.
5. Milanese, C., et al., Complex Hydrides for Energy Storage. *International Journal of Hydrogen Energy* **2019**, *44*, 7860-7874.
6. Wang, K.; Pan, Z.; Yu, X., Metal B-N-H Hydrogen-Storage Compound: Development and Perspectives. *Journal of Alloys and Compounds* **2019**, *794*, 303-324.

7. Hirscher, M., et al., Materials for Hydrogen-Based Energy Storage – Past, Recent Progress and Future Outlook. *Journal of Alloys and Compounds* **2020**, *827*, 153548.
8. Castilla-Martinez, C. A.; Moury, R.; Ould-Amara, S.; Demirci, U. B., Destabilization of Boron-Based Compounds for Hydrogen Storage in the Solid-State: Recent Advances. *Energies* **2021**, *14*.
9. Chen, Z.; Ma, Z.; Zheng, J.; Li, X.; Akiba, E.; Li, H.-W., Perspectives and Challenges of Hydrogen Storage in Solid-State Hydrides. *Chinese Journal of Chemical Engineering* **2021**, *29*, 1-12.
10. He, T.; Cao, H.; Chen, P., The Roles of Alkali/Alkaline Earth Metals in the Materials Design and Development for Hydrogen Storage. *Accounts of Materials Research* **2021**, *2*, 726-738.
11. Tarhan, C.; Çil, M. A., A Study on Hydrogen, the Clean Energy of the Future: Hydrogen Storage Methods. *Journal of Energy Storage* **2021**, *40*, 102676.
12. Dematteis, E. M., et al., Hydrogen Storage in Complex Hydrides: Past Activities and New Trends. *Progress in Energy* **2022**, *4*, 032009.
13. Grinderslev, J. B.; Amdisen, M. B.; Skov, L. N.; Møller, K. T.; Kristensen, L. G.; Polanski, M.; Heere, M.; Jensen, T. R., New Perspectives of Functional Metal Borohydrides. *Journal of Alloys and Compounds* **2022**, *896*, 163014.
14. Moradi, R.; Groth, K. M., Hydrogen Storage and Delivery: Review of the State of the Art Technologies and Risk and Reliability Analysis. *International Journal of Hydrogen Energy* **2019**, *44*, 12254-12269.
15. Stephens, F. H.; Pons, V.; Tom Baker, R., Ammonia–Borane: The Hydrogen Source Par Excellence? *Dalton Transactions* **2007**, 2613-2626.
16. Staubitz, A.; Robertson, A. P. M.; Manners, I., Ammonia-Borane and Related Compounds as Dihydrogen Sources. *Chemical Reviews* **2010**, *110*, 4079-4124.
17. Demirci, U. B., Ammonia Borane, a Material with Exceptional Properties for Chemical Hydrogen Storage. *International Journal of Hydrogen Energy* **2017**, *42*, 9978-10013.
18. Akbayrak, S.; Özkar, S., Ammonia Borane as Hydrogen Storage Materials. *International Journal of Hydrogen Energy* **2018**, *43*, 18592-18606.
19. Demirci, U. B., Ammonia Borane: An Extensively Studied, Though Not yet Implemented, Hydrogen Carrier. *Energies* **2020**, *13*.

20. Figen, A. K.; Filiz, B. C., Capacity of Ammonia Borane to Store Hydrogen. In *Reference Module in Materials Science and Materials Engineering*, Elsevier: **2020** Doi:10.1016/B978-0-12-803581-8.11758-8.

21. Baitalow, F.; Baumann, J.; Wolf, G.; Jaenicke-Rößler, K.; Leitner, G., Thermal Decomposition of B–N–H Compounds Investigated by Using Combined Thermoanalytical Methods. *Thermochimica Acta* **2002**, *391*, 159-168.

22. Stephens, F. H.; Baker, R. T.; Matus, M. H.; Grant, D. J.; Dixon, D. A., Acid Initiation of Ammonia–Borane Dehydrogenation for Hydrogen Storage. *Angewandte Chemie International Edition* **2007**, *46*, 746-749.

23. Demirci, U. B., Mechanistic Insights into the Thermal Decomposition of Ammonia Borane, a Material Studied for Chemical Hydrogen Storage. *Inorganic Chemistry Frontiers* **2021**, *8*, 1900-1930.

24. Chua, Y. S.; Chen, P.; Wu, G.; Xiong, Z., Development of Amidoboranes for Hydrogen Storage. *Chemical Communications* **2011**, *47*, 5116-5129.

25. Wang, K.; Zhang, J.-G.; Man, T.-T.; Wu, M.; Chen, C.-C., Recent Process and Development of Metal Aminoborane. *Chemistry – An Asian Journal* **2013**, *8*, 1076-1089.

26. Owarzany, R.; Leszczyński, J. P.; Fijalkowski, J. K.; Grochala, W., Mono- and Bimetalic Amidoboranes. *Crystals* **2016**, *6*.

27. Castilla-Martinez, C. A.; Moury, R.; Demirci, U. B., Amidoboranes and Hydrazinidoboranes: State of the Art, Potential for Hydrogen Storage, and Other Prospects. *International Journal of Hydrogen Energy* **2020**, *45*, 30731-30755.

28. Diyabalanage, H. V. K.; Shrestha, R. P.; Semelsberger, T. A.; Scott, B. L.; Bowden, M. E.; Davis, B. L.; Burrell, A. K., Calcium Amidotrihydroborate: A Hydrogen Storage Material. *Angewandte Chemie International Edition* **2007**, *46*, 8995-8997.

29. Xiong, Z., et al., High-Capacity Hydrogen Storage in Lithium and Sodium Amidoboranes. *Nature Materials* **2007**, *7*, 138.

30. Spielmann, J.; Jansen, G.; Bandmann, H.; Harder, S., Calcium Amidoborane Hydrogen Storage Materials: Crystal Structures of Decomposition Products. *Angewandte Chemie International Edition* **2008**, *47*, 6290-6295.

31. Wu, H.; Zhou, W.; Yildirim, T., Alkali and Alkaline-Earth Metal Amidoboranes: Structure, Crystal Chemistry, and Hydrogen Storage Properties. *Journal of the American Chemical Society* **2008**, *130*, 14834-14839.

32. Xiong, Z.; Wu, G.; Chua, Y. S.; Hu, J.; He, T.; Xu, W.; Chen, P., Synthesis of Sodium Amidoborane ($NaNH_2BH_3$) for Hydrogen Production. *Energy & Environmental Science* **2008**, *1*, 360-363.

33. Diyabalanage, H. V. K., et al., Potassium(I) Amidotrihydroborate: Structure and Hydrogen Release. *Journal of the American Chemical Society* **2010**, *132*, 11836-11837.

34. Zhang, Q.; Tang, C.; Fang, C.; Fang, F.; Sun, D.; Ouyang, L.; Zhu, M., Synthesis, Crystal Structure, and Thermal Decomposition of Strontium Amidoborane. *The Journal of Physical Chemistry C* **2010**, *114*, 1709-1714.

35. Luo, J.; Kang, X.; Wang, P., Synthesis, Formation Mechanism, and Dehydrogenation Properties of the Long-Sought $Mg(NH_2BH_3)_2$ Compound. *Energy & Environmental Science* **2013**, *6*, 1018-1025.

36. Kazakov, I. V.; Butlak, A. V.; Shelyganov, P. A.; Suslonov, V. V.; Timoshkin, A. Y., Reversible Structural Transformations of Rubidium and Cesium Amidoboranes. *Polyhedron* **2017**, *127*, 186-190.

37. Owarzany, R.; Jaroń, T.; Leszczyński, P. J.; Fijalkowski, K. J.; Grochala, W., Amidoboranes of Rubidium and Caesium: The Last Missing Members of the Alkali Metal Amidoborane Family. *Dalton Transactions* **2017**, *46*, 16315-16320.

38. Shcherbina, N. A.; Kazakov, I. V.; Timoshkin, A. Y., Synthesis and Characterization of Barium Amidoborane. *Russian Journal of General Chemistry* **2017**, *87*, 2875-2877.

39. Hawthorne, M. F.; Jalisatgi, S. S.; Safronov, A. V.; Lee, H. B.; Wu, J. *Chemical Hydrogen Storage Using Polyhedral Borane Anions and Aluminum-Ammonia-Borane Complexes*; United States, 2010-10-01, **2010**.

40. Fijalkowski, K. J.; Genova, R. V.; Filinchuk, Y.; Budzianowski, A.; Derzsi, M.; Jaroń, T.; Leszczyński, P. J.; Grochala, W., $Na[Li(NH_2BH_3)_2]$ – the First Mixed-Cation Amidoborane with Unusual Crystal Structure. *Dalton Transactions* **2011**, *40*, 4407-4413.

41. Kang, X.; Luo, J.; Zhang, Q.; Wang, P., Combined Formation and Decomposition of Dual-Metal Amidoborane $NaMg(NH_2BH_3)_3$ for High-Performance Hydrogen Storage. *Dalton Transactions* **2011**, *40*, 3799-3801.

42. Wu, H.; Zhou, W.; Pinkerton, F. E.; Meyer, M. S.; Yao, Q.; Gadipelli, S.; Udovic, T. J.; Yildirim, T.; Rush, J. J., Sodium Magnesium Amidoborane: The First Mixed-Metal Amidoborane. *Chemical Communications* **2011**, *47*, 4102-4104.

43. Xia, G.; Tan, Y.; Chen, X.; Guo, Z.; Liu, H.; Yu, X., Mixed-Metal (Li, Al) Amidoborane: Synthesis and Enhanced Hydrogen Storage Properties. *Journal of Materials Chemistry A* **2013**, *1*, 1810-1820.

44. Dovgaliuk, I.; Jepsen, L. H.; Safin, D. A.; Łodziana, Z.; Dyadkin, V.; Jensen, T. R.; Devillers, M.; Filinchuk, Y., A Composite of Complex and Chemical Hydrides Yields the First Al-Based Amidoborane with Improved Hydrogen Storage Properties. *Chemistry – A European Journal* **2015**, *21*, 14562-14570.

45. Yang, J.; Beaumont, P. R.; Humphries, T. D.; Jensen, C. M.; Li, X., Efficient Synthesis of an Aluminum Amidoborane Ammoniate. *Energies* **2015**, *8*.

46. Biliškov, N.; Borgschulte, A.; Užarević, K.; Halasz, I.; Lukin, S.; Milošević, S.; Milanović, I.; Novaković, J. G., In-Situ and Real-Time Monitoring of Mechanochemical Preparation of $Li_2Mg(NH_2BH_3)_4$ and $Na_2Mg(NH_2BH_3)_4$ and Their Thermal Dehydrogenation. *Chemistry – A European Journal* **2017**, *23*, 16274-16282.

47. Chernysheva, A.; Shelyganov, P.; V. Kazakov, I.; Timoshkin, A., *Complex Amidoboranes M2[M1(NH_2BH_3)$_4$] (M1 = Al, Ga; M2 = Li, Na, K, Rb, Cs)*, **2017**; Vol. 87, p 665-669.

48. Nakagawa, Y.; Shinzato, K.; Nakagawa, T.; Nakajima, K.; Isobe, S.; Goshome, K.; Miyaoka, H.; Ichikawa, T., Synthesis, Structural Characterization, and Hydrogen Desorption Properties of $Na[Al(NH_2BH_3)_4]$. *International Journal of Hydrogen Energy* **2017**, *42*, 6173-6180.

49. Møller, K. T.; Jørgensen, M.; Andreasen, J. G.; Skibsted, J.; Łodziana, Z.; Filinchuk, Y.; Jensen, T. R., Synthesis and Thermal Decomposition of Potassium Tetraamidoboranealuminate, $K[Al(NH_2BH_3)_4]$. *International Journal of Hydrogen Energy* **2018**, *43*, 311-321.

50. Milanović, I.; Biliškov, N.; Užarević, K.; Lukin, S.; Etter, M.; Halasz, I., Mechanochemical Synthesis and Thermal Dehydrogenation of Novel Calcium-Containing Bimetallic Amidoboranes. *ACS Sustainable Chemistry & Engineering* **2021**, *9*, 2089-2099.

51. James, S. L., et al., Mechanochemistry: Opportunities for New and Cleaner Synthesis. *Chemical Society Reviews* **2012**, *41*, 413-447.

52. Huot, J.; Ravnsbæk, D. B.; Zhang, J.; Cuevas, F.; Latroche, M.; Jensen, T. R., Mechanochemical Synthesis of Hydrogen Storage Materials. *Progress in Materials Science* **2013**, *58*, 30-75.

53. Do, J.-L.; Friščić, T., Mechanochemistry: A Force of Synthesis. *ACS Central Science* **2017**, *3*, 13-19.

54. Huot, J., et al. Mechanochemistry of Metal Hydrides: Recent Advances *Materials* **2019**, DOI: 10.3390/ma12172778.

55. Leardini, F.; Valero-Pedraza, M. J.; Perez-Mayoral, E.; Cantelli, R.; Bañares, M. A., Thermolytic Decomposition of Ethane 1,2-Diamineborane Investigated by Thermoanalytical Methods and in Situ Vibrational Spectroscopy. *The Journal of Physical Chemistry C* **2014**, *118*, 17221-17230.

56. Framery, E.; Vaultier, M., Efficient Synthesis and NMR Data of N- or B-Substituted Borazines. *Heteroatom Chemistry* **2000**, *11*, 218-225.

57. Yang, J.; Sudik, A.; Wolverton, C., Destabilizing $LiBH_4$ with a Metal (M = Mg, Al, Ti, V, Cr, or Sc) or Metal Hydride (MH_2 = MgH_2, TiH_2, or CaH_2). *The Journal of Physical Chemistry C* **2007**, *111*, 19134-19140.

58. Liu, Y.; Zhong, K.; Gao, M.; Wang, J.; Pan, H.; Wang, Q., Hydrogen Storage in a $LiNH_2$−MgH_2 (1:1) System. *Chemistry of Materials* **2008**, *20*, 3521-3527.

59. Jepsen, L. H.; Ley, M. B.; Lee, Y.-S.; Cho, Y. W.; Dornheim, M.; Jensen, J. O.; Filinchuk, Y.; Jørgensen, J. E.; Besenbacher, F.; Jensen, T. R., Boron–Nitrogen Based Hydrides and Reactive Composites for Hydrogen Storage. *Materials Today* **2014**, *17*, 129-135.

60. Qiu, S.; Chu, H.; Zou, Y.; Xiang, C.; Xu, F.; Sun, L., Light Metal Borohydrides/Amides Combined Hydrogen Storage Systems: Composition, Structure and Properties. *Journal of Materials Chemistry A* **2017**, *5*, 25112-25130.

61. Ali, N. A.; Sazelee, N. A.; Ismail, M., An Overview of Reactive Hydride Composite (RHCs) for Solid-State Hydrogen Storage Materials. *International Journal of Hydrogen Energy* **2021**, *46*, 31674-31698.
62. Alapati, S. V.; Johnson, J. K.; Sholl, D. S., Identification of Destabilized Metal Hydrides for Hydrogen Storage Using First Principles Calculations. *The Journal of Physical Chemistry B* **2006**, *110*, 8769-8776.
63. Dovgaliuk, I.; Møller, K. T.; Robeyns, K.; Louppe, V.; Jensen, T. R.; Filinchuk, Y., Complexation of Ammonia Boranes with Al^{3+}. *Inorganic Chemistry* **2019**, *58*, 4753-4760.
64. Favre-Nicolin, V.; Cerny, R., Fox, `Free Objects for Crystallography': A Modular Approach to Ab Initio Structure Determination from Powder Diffraction. *Journal of Applied Crystallography* **2002**, *35*, 734-743.
65. Rodríguez-Carvajal, J., Recent Advances in Magnetic Structure Determination by Neutron Powder Diffraction. *Physica B: Condensed Matter* **1993**, *192*, 55-69.
66. Spek, A., Single-Crystal Structure Validation with the Program Platon. *Journal of Applied Crystallography* **2003**, *36*, 7-13.

Chapter 5

Enhancing Hydrogen (H_2) Release from Boron-nitrogen-hydrogen Metal Oligomers via Di-methylene Substitution

Abstract

Boron-nitrogen-hydrogen (B-N-H) metal oligomers derived from ammonia borane or its derivatives show significant potential for hydrogen storage due to their high hydrogen content. In this chapter, we focus on improving the release of hydrogen (H_2) from metal oligomers by the novel sodium oligomer using NaH and di-methylene-substituted ammonia borane ($BH_3NH_2CH_2CH_2NH_2BH_3$, EDAB). The investigation of thermal dehydrogenation using thermal gravimetric analysis and mass spectrometry indicate that this newly formed oligomer can release ~7.4 wt.% pure hydrogen from room temperature up to 260 ˚C. These results confirmed that the di-methylene substituent on the nitrogen atoms of ammonia borane effectively suppresses the release of unwanted gases during thermal decomposition at moderate temperatures, similar to the observed action of the methyl group in Chapter 3. Notably, the di-methylene substituent on nitrogen significantly increases the hydrogen storage capacity compared to the methyl group. Our findings demonstrate that di-methylene substitution on nitrogen atoms of ammonia borane is an effective strategy to suppress the release of commonly encountered undesired gaseous by-products during the thermal dehydrogenation of B-N-H compounds, which opens up the potential for the design of promising hydrogen storage materials.

5.1 Introduction

Hydrogen has been considered a promising energy carrier for new sustainable and eco-friendly alternative energy storage due to the highest energy density per unit mass (120 MJ/kg)[1], eco-friendly environment, and abundance. Still, developing a compact, safe, and cost-efficient storage method is challenging for the wide practical application of hydrogen as main energy carrier. Chemical hydrogen storage methods[2-4] usually have the advantage of high gravimetric and volumetric hydrogen densities, such as $LiBH_4$ which has 18.5 wt.% and 122 g/L gravimetric and volumetric hydrogen densities, respectively[5]. However, the release of hydrogen by some chemical hydrogen storage methods generally requires high temperatures. Among chemical hydrogen storage materials, ammonia borane (NH_3BH_3 or AB) is a good precursor for synthesizing new compounds used for hydrogen storage. NH_3BH_3 has high hydrogen content (19.6 wt.%), with three hydridic and protic hydrogens on the N and B atoms. Their recombination favors hydrogen release. In addition, AB has high stability under ambient conditions, low toxicity, and high solubility in common solvents. These properties make it convenient for reacting with other chemicals in various conditions. The thermal decomposition of AB is multistep process (especially the third step occurs at over 500 °C), its decomposition is exothermic and thus irreversible, and it releases multiple volatile byproducts such as NH_3, $N_3B_3H_6$, and B_2H_6, making the chemical de/re-hydrogenation process really challenging. In addition, the thermal decomposition of AB is furthermore paired with severe foaming and volume expansion.[6-9] Thus, this limits its application for hydrogen storage. However, the chemical modification of AB through replacing one of the H atoms in the $–NH_3$ group of NH_3BH_3 by a metal, forming metal amidoboranes (MABs)[10-14] or the oligomers ($M[B_3N_2]$)[15-19] showed improved hydrogen storage properties, especially the decreased decomposition temperature and the increased purity of H_2. Hence, it is more advantageous to employ AB as a precursor for the design and synthesis of new compounds intended for hydrogen storage rather than utilizing it directly as a hydrogen storage material.

Apart from the metal amidoboranes and metal oligomers of AB, the hydrogen storage properties of some derivatives of AB with the modification

by the alkyl-groups have also been studied and reported. The simplest one, $CH_3NH_2BH_3$ (MeAB), has a lower melting point (58 °C)[20] than AB (112-114 °C)[8] and exhibits a high degree of volatility, with weight losses in excess of 80 % observed in TG experiments using flowing gas. Another example is $BH_3NH_2CH_2CH_2NH_2BH_3$ (EDAB), a dimer-like of MeAB. EDAB has a higher melting point (119 °C)[21] than AB and MeAB. EDAB releases ~10 wt.% of pure H_2 at temperatures ranging from 100 °C to 200 °C in two moderately exothermic steps. Although EDAB is more stable than AB at temperatures lower than 100 °C; however, the rates of hydrogen release are faster for EDAB than for AB at temperatures higher than 120 °C.[22] Other examples such as diethylenetriamine-borane ($C_4H_{13}N_3 \cdot 3BH_3$, DETAB), triethylenetetramine-borane ($C_6H_{18}N_4 \cdot 4BH_3$, TETAB) and tetraethylenepentamine-borane ($C_8H_{23}N_5 \cdot 5BH_3$, TEPAB) (their formulas are shown in Figure 5.8) reported by Zhang et al[23], and 1,2/1,3-di-aminopropane borane (1,2/1,3-TMDAB) studied by Leigang and co-workers,[24] all released pure hydrogen with a faster dehydrogenation rate than AB. All of the above examples indicate that the introduction of alkyl-groups has a positive effect on the properties of AB towards its application in hydrogen storage.

In Chapter 3, we conducted a study on the hydrogen release properties of $Na[BH_3(CH_3NH)BH_2(CH_3NH)BH_3]$ ($Na[B_3(MeN)_2]$), which is a methyl-substituted derivative of $Na[BH_3NH_2BH_2NH_2BH_3]$ ($Na[B_3N_2]$). The introduction of a methyl group on nitrogen atoms of $BH_3NH_2BH_2NH_2BH_3^-$ enhanced the purity of the released hydrogen.[19] This encouraged us to consider the introduction of other alkyl-groups to improve the properties of hydrogen storage of metal amidoborane or metal oligomer complexes. With this in mind, we attempt the investigation of the synthesis, structure characterization and hydrogen releasing of the novel metal oligomer compounds, derived from EDAB, $(CH_2NH_2BH_3)_2$, which can be seen as a dimeric form of MeAB, $(CH_3NH_2BH_3)$. Compared to MeAB, EDAB exhibits a more complicated and potentially diverse reaction pathway with MH (M = Li and Na). Also, there is limited literature on how this compound reacts with metal hydrides. Interestingly, EDAB has a lower so-called "dead mass" than MeAB. Therefore, we explored the synthesis based on the reaction between MH/MNH_2 (M = Li and Na) and EDAB. Only the metal oligomer compound was obtained successfully from the reaction between NaH and EDAB. The structure of this

novel metal oligomer was characterized using powder X-ray diffraction (PXRD), IR and ^{11}B NMR spectra and its thermal decomposition was investigated through thermal gravimetric analysis (TGA) and mass spectrometry. Compared to $Na[B_3N_2]$, this new oligomer releases purer hydrogen without formation of NH_3, B_2H_6, or other large fragments. Moreover, when compared to $Na[B_3(MeN)_2]$ (~4.6 wt.%), this new oligomer exhibited a higher capacity for releasing pure hydrogen (~7.4 wt.%).

5.2 Optimization of the reaction between NaH and EDAB

The reaction pathways between NaH/LiH and AB were reported to depend highly on the specific conditions.[25-27] To date, there is only one preliminary investigation of the reaction between NaH and EDAB conducted by Leardini and co-workers[28]. They performed the reaction under mechano-chemical conditions in a Spex 8000 high-energy shaker mill. By analyzing the amount of gas released during milling and comparing the PXRD pattern of the product with the reactant, they proposed that the obtained product was $NaBH_3NHCH_2CH_2NH_2BH_3$ (NaEDAB). Only one nitrogen lost a hydrogen in EDAB. However, the other amine group remained intact. Compared to the neat EDAB, NaEDAB gives rise to milder exothermic H_2 release at moderate temperatures and an endothermic desorption process at higher temperatures. These results provide encouraging indications for conducting more detailed investigations into the reactions between NaH/LiH, as well as $NaNH_2$/$LiNH_2$ and EDAB to discover novel compounds suitable for hydrogen storage.

To investigate the reaction between NaH and EDAB, we employed a wet chemical synthesis approach. In a typical procedure, NaH and EDAB with different molar ratios were suspended in toluene and stirred at a given temperature. Initially, we screened the NaH:EDAB molar ratios of 2:1 (sample **Na-i**), 1:1 (sample **Na-ii**), 1:1.5 (sample **Na-iii**) and 1:2 (sample **Na-iv**) using the PXRD analysis. It revealed new peaks and the presence of unreacted NaH in the PXRD patterns in all tested ratios (Figure 5.1A). Comparing the PXRD pattern of **Na-i** with that of **Na-ii**, we noticed a reduced amount of unreacted NaH in the latter. This indicates that the reaction ratio is closer to 1:1 than to 2:1. As we increased the amount of EDAB in the NaH-1.5EDAB and NaH-2EDAB systems, we observed the appearance of additional new peaks

alongside $NaBH_4$ in the PXRD patterns of samples **Na-iii** and **Na-iv**, signifying the occurrence of a new reaction. However, since a significant amount of $NaBH_4$ was formed in samples **Na-iii** and **Na-iv**, we did not focus our investigation on these systems or systems with higher amounts of EDAB.

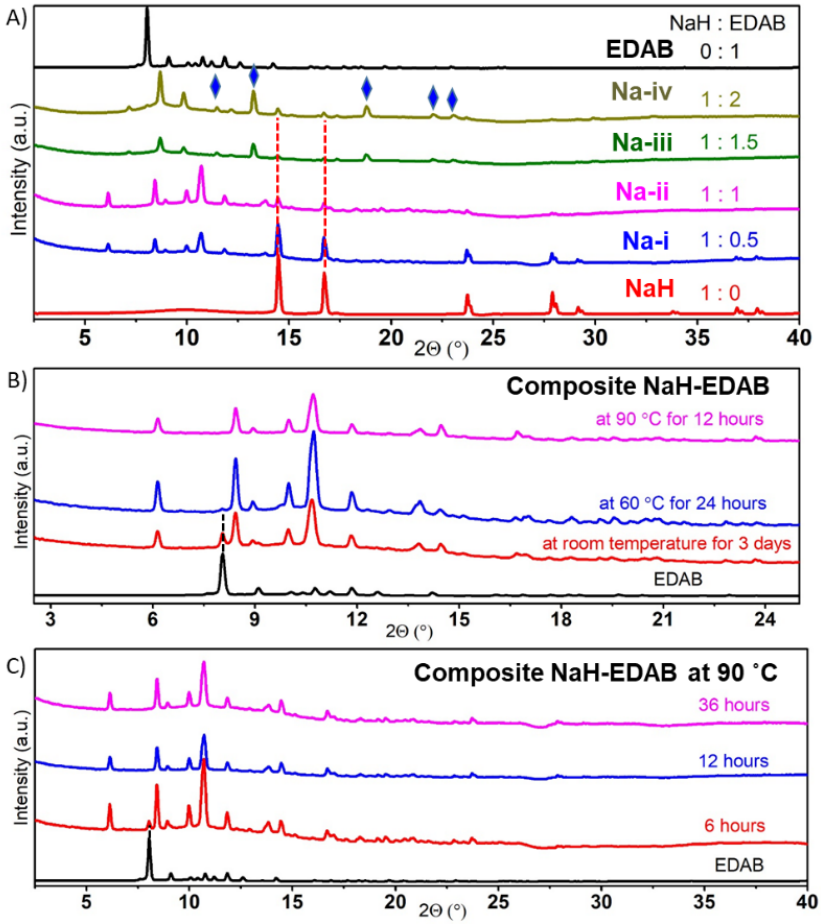

Figure 5.1 PXRD patterns of the product of the reaction between NaH and EDAB in different ratios (A); different temperatures (B) and different reaction times (C) (the peaks corresponding to $NaBH_4$ pointed by blue diamond in Figure A; the residue NaH in Figure A highlighted by the red dashed line; EDAB in Figures B and C highlighted by the black dash line; λ = 0.71073 Å).

To synthesize better quality sample **Na-ii**, we optimized the reaction temperature and time. NaH-EDAB mixtures were suspended in toluene and stirred at different temperatures for various amounts of time. We found that

this reaction could occur at temperatures of 90°C, 60°C, and even at room temperature, albeit with varying completion times (Figure 5.1B). The mixture reached an almost complete conversion after 6 hours at 90°C (Figure 5.1C). However, a duration of 3 days was insufficient for the reaction to reach completion at room temperature. Consequently, we ultimately synthesized Sample **Na-ii** for further structural analysis and property studies, employing a reaction temperature of 90°C for 12 hours in toluene (details provided in Table 5.1).

Table 5.1 The optimized reaction conditions for synthesis of sample **Na-ii**.

Sample	NaH:EDAB	Temperature	Reaction time	Solvent
Na-ii	1:1	90 ˚C	12 hours	Toluene

We also attempted the reaction between $NaNH_2$ and EDAB using both wet chemical synthesis (sample **Na-v**) and mechanical chemical synthesis (sample **Na-vi**) methods. However, we were unable to obtain a new single phase in either case. Notably, the PXRD pattern of sample **Na-v** appeared similar to that of samples **Na-iii** and **Na-iv** (Figure 5.9 and 5.1A). This led us to consider the possibility that the decomposition of EDAB may have been promoted by $NaNH_2$ or a small amount of NaH present in samples **Na-v**, **Na-iii**, and **Na-iv**. It is worth mentioning that EDAB alone remained stable in toluene at 90°C for 24 hours (Figure 5.10).

It was challenging to collect sample **Na-vi** due to its a sticky appearence. Furthermore, we explored the reaction between LiH and EDAB using various molar ratios, synthesis methods, and temperatures (Figure 5.11 and 5.12); however, no reaction was observed. Similarly, the reaction between $LiNH_2$ and EDAB, attempted through wet chemical synthesis (sample **Li-vii**), did not proceed (Figure 5.13). Meanwhile, the mechanical chemical synthesis (sample **Li-viii**) did not yield collectible products due to the formation of a greasy-like substance.

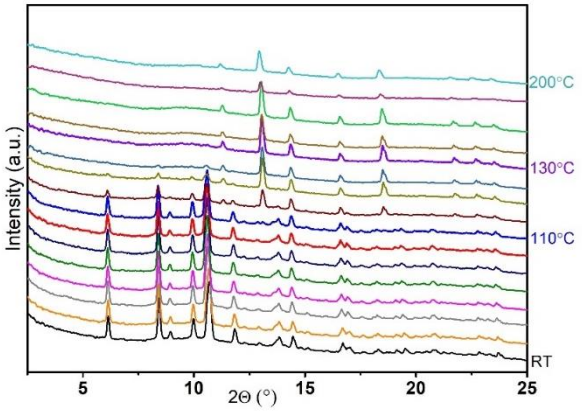

Figure 5.2 XRD data collected upon temperature ramp for sample **Na-ii** (λ = 0.71073 Å).

The phase purity of sample **Na-ii**, obtained after 12 hours of stirring at 90 ˚C, was verified through X-ray diffraction (PXRD) collected upon the ramping temperature. The peaks of $NaBH_4$ occurred at approximately 110˚C, while the complete set of peaks corresponding to sample **Na-ii** vanished simultaneously at around 130˚C (Figure 5.2). Based on the temperature ramping PXRD experiment, we deduce that sample **Na-ii** predominantly consists of a single phase, with the exception of a few peaks of the unreacted NaH.

5.3 Structure characterization of sample Na-ii

The obtained sample **Na-ii** was characterized by infrared (IR) and ^{11}B NMR spectroscopies (Figure 5.3). In the IR spectrum, a notable change was observed in the N-H stretching band, with the disappearance of the asymmetry (3142 cm^{-1}) observed in the $BH_3NH_2CH_2CH_2NH_2BH_3$ precursor. Additionally, the spectrum of sample **Na-ii** exhibited a single peak corresponding to the N-H stretching band at 3261 cm^{-1}. IR spectrum indicates that one hydrogen on each nitrogen of $BH_3NH_2CH_2CH_2NH_2BH_3$ has been removed.

Considering the Lewis acid and base reaction between NaH and EDAB, two equivalents of H^- from NaH are required to combine with the $H^{\delta+}$ on the N atoms of EDAB, resulting in the formation of H_2. However, in the case of sample **Na-ii**, only one equivalent of NaH or less (taking into account the

remaining NaH) was available. Therefore, it can be inferred that polymerization occurred either intermolecularly or intramolecularly in this system.

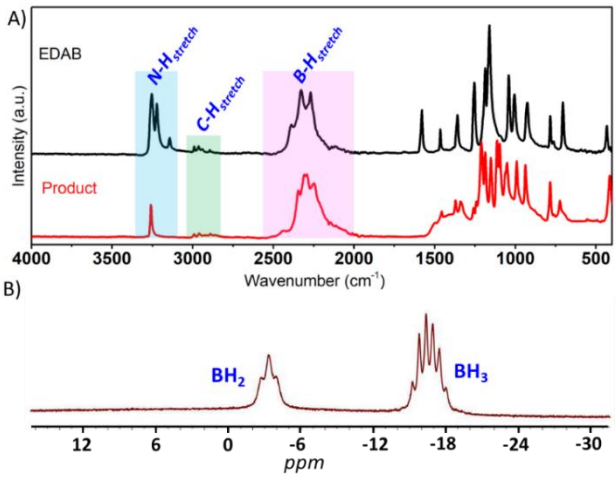

Figure 5.3 A) IR spectra of EDAB and sample **Na-ii**; B) ^{11}B NMR spectrum of sample **Na-ii**.

The broad band observed in the region of 2800-3008 cm^{-1} corresponds to the C-H stretching, while the band in the range of 2000-2500 cm^{-1} corresponds to the B-H stretching. There is no significant difference compared to the $BH_3NH_2CH_2CH_2NH_2BH_3$ precursor for the above signals in the IR spectrum. However, the B-N stretching signal located in the area of 661-754 cm^{-1} exhibited broadening for sample **Na-ii**, unlike that in $BH_3NH_2CH_2CH_2NH_2BH_3$ which showed only one B-N band at 704 cm^{-1}. This suggests the presence of two different B-N bonds in sample **Na-ii**, similar to what has been observed in $Na[B_3(MeN)_2]$ (reference [19]).

The ^{11}B NMR spectrum of sample **Na-ii** displayed two main boron signals (Figure 5.3B) at -3.34 ppm and -16.67 ppm, which can be attributed to the BH_2 and BH_3 groups, respectively. This observation is consistent with the results obtained from the IR spectra. The ratio of these two types of boron species, BH_2 and BH_3, was determined to be 1:2 based on the integration of their respective signal areas.

Based on the analysis of the IR spectra and ^{11}B NMR spectrum of sample **Na-ii**, and the reaction products for NaH-$3NH_3BH_3$ and NaH-$3CH_3NH_2BH_3$

systems, we propose the following reaction mechanism between 2 equivalents of NaH and 3 equivalents of EDAB.

Furthermore, we suggest the formula of sample **Na-ii** to be a metal oligomer containing a ten-membered (B-N-C) ring (Figure 5.4). To confirm our conjecture and gain further insights into the structure, we plan to conduct high-resolution PXRD measurements or attempt to grow single crystals to determine the crystal structure.

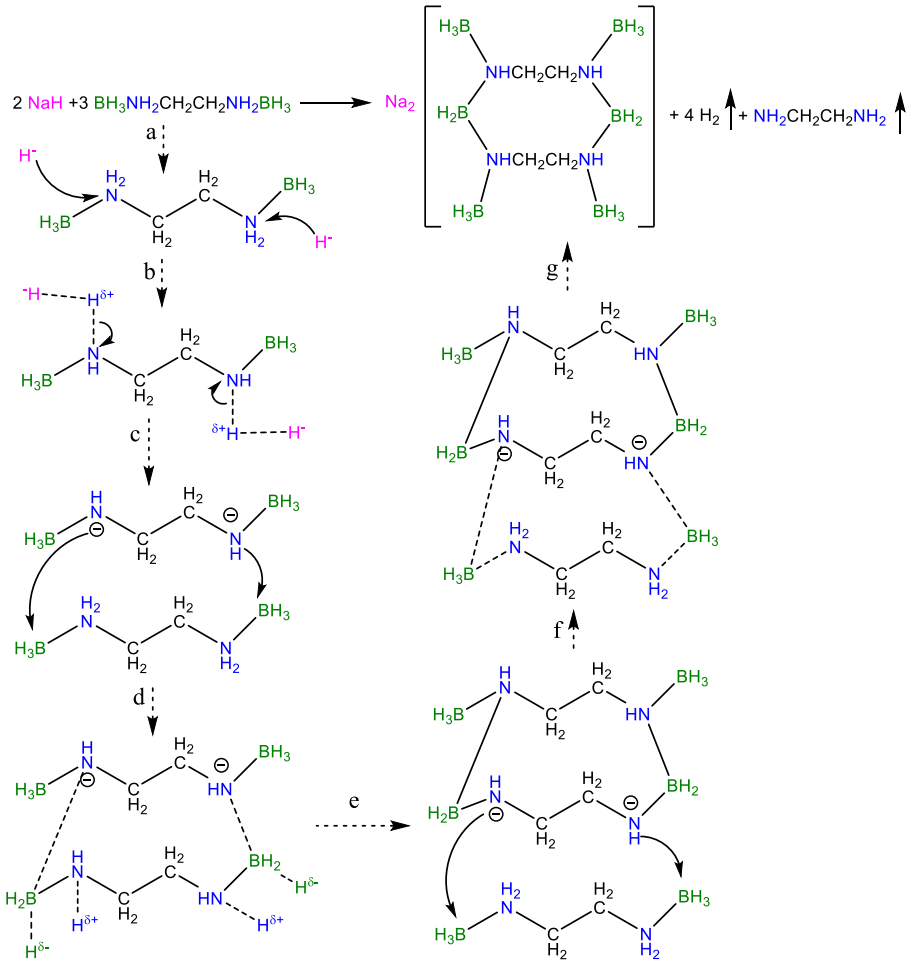

Figure 5.4 Proposed mechanism of the formation of Sample **Na-ii**.

5.4 Thermal decomposition of sample Na-ii

5.4.1 Stability of sample Na-ii in air

Prior to investigating the thermal decomposition of sample **Na-ii**, we examined its stability in ambient air using PXRD. The results revealed that sample **Na-ii** exhibited exceptional stability under these conditions. Even after being exposed to air for a period of 2 weeks (Figure 5.5), no additional crystalline phases were observed. This indicates that sample **Na-ii** possesses a robust capacity to resist moisture in the surrounding environment.

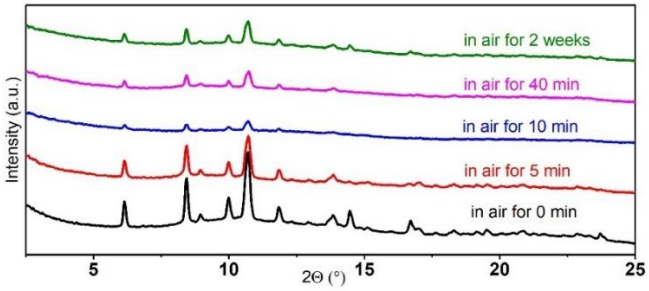

Figure 5.5 PXRD pattern of sample **Na-ii** and of the sample exposures to air for different times (λ = 0.71073 Å).

5.4.2 Thermal decomposition of sample Na-ii

The thermal stability of sample **Na-ii** was investigated by thermogravimetric analysis (TGA) under an inert nitrogen atmosphere from room temperature to 260 ˚C. Prior to the TGA analysis, sample **Na-ii** was subjected to vacuum at 90 ˚C for 36 hours to eliminate residual toluene and possibly $NH_2CH_2CH_2NH_2$, thus preventing their influence on the thermal dehydrogenation of the main phase. The absence of toluene and $NH_2CH_2CH_2NH_2$ in sample **Na-ii** was confirmed by the IR spectrum (Figure 5.3A).

During the TGA analysis, a slight mass increase was observed before the onset of the thermal decomposition, followed by a subsequent decrease starting at around 60 ˚C (Figure 5.6A). This initial mass increase could be attributed to air absorption prior to nitrogen purging. Notably, a single-step thermal decomposition process occurred steadily from room temperature to 260 °C. In contrast to the precursor EDAB and the methyl-substituted oligomer

$Na[B_3(MeN)_2]$[19], sample **Na-ii** did not exhibit weight oscillations (so-called jet effect) during the thermal decomposition within the RT-260 °C range. This indicates that sample **Na-ii** effectively mitigates rapid volume expansion during thermal decomposition.

The overall mass loss of sample **Na-ii** from room temperature to 260 ˚C was approximately 7.4% (Figure 5.6A), which closely matches the theoretical hydrogen content excluding the hydrogen on carbon, as indicated by our proposed formula (8.2% in theory) in Figure 5.4. Upon heating to 240 ˚C, the solid decomposition product was identified as crystalline $NaBH_4$, along with some unknown crystalline and potentially amorphous compounds, as determined by IR and PXRD analyses (Figure 5.6B and C). The formation of $NaBH_4$ after thermal decomposition mirrors the behavior observed in the metal oligomers ($M[B_3N_2]$, M = Li-Cs[15, 16]) obtained from NH_3BH_3 and the methyl-substituted oligomer $Na[B_3(MeN)_2]$[19] (as discussed in Chapter 3).

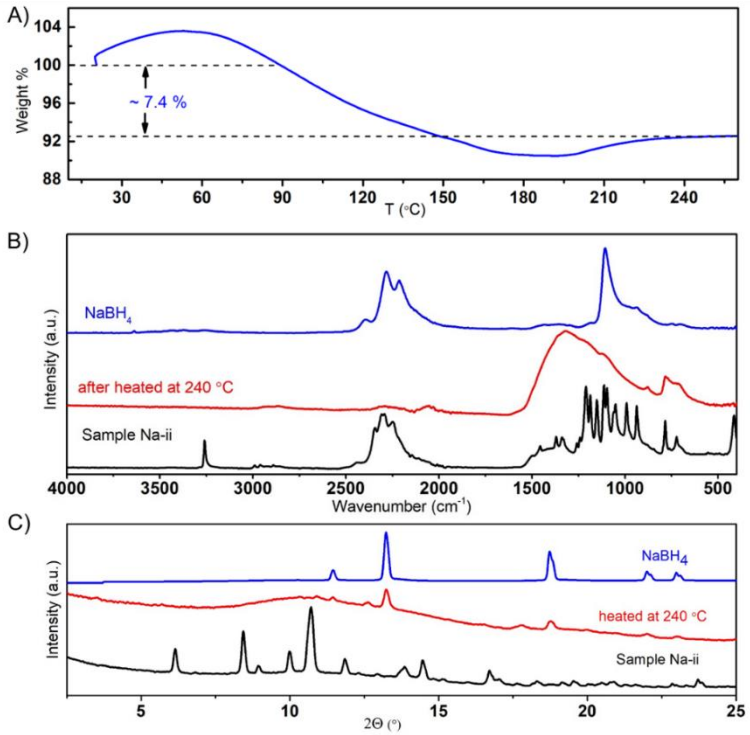

Figure 5.6 TG analysis of sample **Na-ii** (A); IR (B) and PXRD pattern (C) of sample **Na-ii**, the product of thermal decomposition and $NaBH_4$ (λ = 0.71073 Å).

5.5 Thermal dehydrogenation of sample Na-ii

The purity of the gases released during the thermal dehydrogenation of sample **Na-ii** was assessed using temperature-programmed mass spectrometry in the temperature range of 40 ˚C to 240 ˚C. The analysis revealed that only hydrogen gas was detected, while NH_3, B_2H_6, $NH_2CH_2CH_2NH_2$, and the solvent toluene were not released during the decomposition (Figure 5.7). This confirms that the di-methylene-substituted oligomer, sample **Na-ii**, releases approximately 7.4 wt.% of pure hydrogen when heated to 260 ˚C.

In comparison to the unsubstituted metal oligomer $Na[B_3N_2]$[15], which is derived from NaH and NH_3BH_3, the incorporation of a di-methylene group on the nitrogen atoms in sample **Na-ii** effectively suppresses the generation of undesired by-products during thermal hydrogen desorption. Furthermore, when compared to the methyl-substituted metal oligomer $Na[B_3(MeN)_2]$[19], obtained from NaH and $CH_3NH_2BH_3$, the di-methylene-substituted oligomer, sample **Na-ii**, exhibits an increased capacity for releasing pure hydrogen at moderate temperatures (~7.4 wt.% for sample **Na-ii**, ~4.6 wt.% for $Na[B_3(MeN)_2]$).

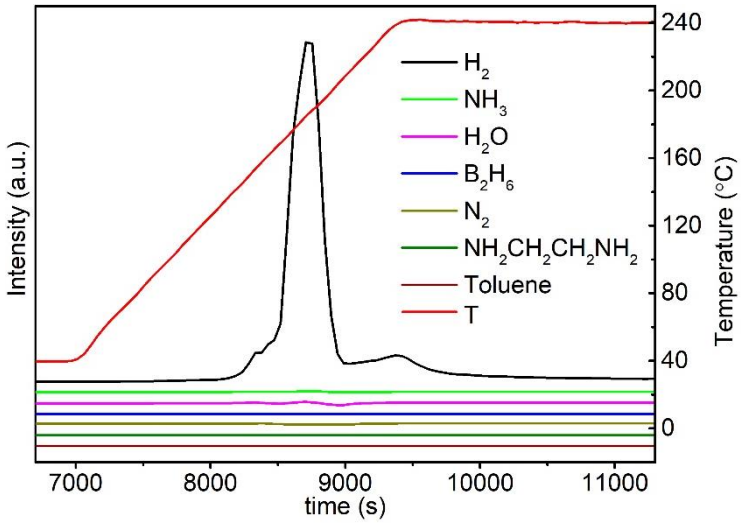

Figure 5.7 Mass spectrometry data on the decomposition of sample **Na-ii**.

5.6 Conclusion

We have successfully synthesized a novel di-methylene-substituted metal oligomer by reacting NaH with EDAB ($BH_3NH_2CH_2CH_2NH_2BH_3$). Based on infrared (IR) and ^{11}B NMR spectra analysis, we have proposed a tentative formula for this new compound. Compared to the unsubstituted metal oligomer $Na[B_3N_2]$, our newly synthesized compound can release approximately 7.4 wt.% of pure hydrogen below 260 °C. Furthermore, when compared to the methyl-substituted sodium oligomer $Na[B_3(MeN)_2]$, the di-methylene-substituted metal oligomer, sample **Na-ii**, demonstrates an even higher hydrogen storage capacity than we anticipated. This strongly suggests that incorporating methyl and di-methylene substituents on the nitrogen atoms of similar compounds holds great promise in mitigating the generation of undesired volatile by-products during thermal hydrogen release.

5.7 Experimental section

5.7.1 Chemicals

All the samples were obtained from commercially available NaH (95 %), LiH (95 %), $NaNH_2$ (> 90 %), $NaBH_4$ (97 %), $NH_2CH_2CH_2NH_2{\cdot}2HCl$ (98 %), and anhydrous THF (⩾99.9 %), Toluene (99.85 %), which were purchased from SigmaAldrich Co. Ltd. DMSO-d_6 (99.8 %) was purchased from Eurisotop, and $LiNH_2$ (95 %) was purchased from Alfa Aesar (China) Chemical Co., Ltd. All the operations were performed in a glovebox with a high-purity argon atmosphere.

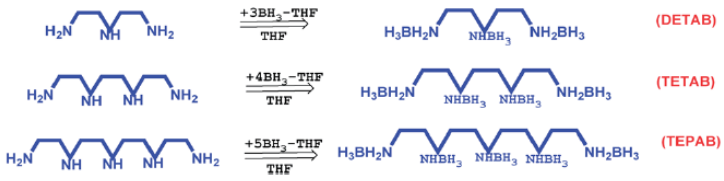

Figure 5.8 The formulas of DETAB, TETAB and TPEAB.[23]

5.7.2 Synthesis of $BH_3NH_2CH_2CH_2NH_2BH_3$ (EDAB)

EDAB was obtained through a procedure adapted from the literature.[21] In brief, the synthesis was performed as follows. Powdered $NaBH_4$ (1.40 g, 37

mmol), $NH_2CH_2CH_2NH_2 \cdot 2HCl$ (2.40 g, 18 mmol), and THF (250 mL) were added to a 500 mL, three-neck, round bottom flask. The obtained suspension was then vigorously stirred at room temperature under an argon atmosphere for 48 hours. Then the solid by-product (NaCl) was removed from the reaction mixture by filtration, and the solvent of the collected filtrate was removed by evaporation under reduced pressure (using a rotary evaporator) to obtain EDAB. The white solid was washed with diethyl ether three times and then dried under a vacuum for 4 hours to eliminate residual solvents. The product was characterized by means of ^{1}H, ^{13}C, and ^{11}B NMR and PXRD (Figure S15–18).

5.7.3 Optimization of the reaction between NaH and EDAB.

Sample Na-i: 2 eq. of NaH (67.2 mg, 2.8 mmol), 1 eq. of EDAB (122.8 mg, 1.4 mmol) and anhydrous Toluene (20 mL) were added to a 50 mL, one-neck round-bottom Schlenk flask. The obtained suspension was then vigorously stirred at 90 ˚C under an argon atmosphere for 24 hours. Then the solvent was removed by vacuum. And the white solid was dried under a vacuum for another 5 hours at 80 ˚C to eliminate residual solvents. The product was characterized by means of PXRD (Figure 5.1A).

Sample Na-ii: 1 eq. of NaH (33.6 mg, 1.4 mmol), 1 eq. of EDAB (122.8 mg, 1.4 mmol), and anhydrous Toluene (15 mL) were added to a 50 mL, one-neck round-bottom Schlenk flask. The obtained suspension was then vigorously stirred at 90 ˚C under an argon atmosphere for 24 hours. Then the solvent was removed by vacuum. And the white solid was dried under a vacuum for another 5 hours at 80 ˚C to eliminate residual solvents. The product was characterized by means of PXRD (Figure 5.1A). This synthesis method is reproducible.

Sample Na-iii: 1 eq. of NaH (22.4 mg, 0.9 mmol), 1.5 eq. of EDAB (122.8 mg, 1.4 mmol), and anhydrous Toluene (15 mL) were added to a 50 mL, one-neck round-bottom Schlenk flask. The obtained suspension was then vigorously stirred at 90 ˚C under an argon atmosphere for 24 hours. Then the solvent was removed by vacuum. And the white solid was dried under a vacuum for another 5 hours at 80 ˚C to eliminate residual solvents. The product was characterized by means of PXRD (Figure 5.1A).

Sample Na-iv: 1 eq. of NaH (16.8 mg, 0.7 mmol), 2 eq. of EDAB (122.8 mg, 1.4 mmol), and anhydrous Toluene (15 mL) were added to a 50 mL, one-neck round-bottom Schlenk flask. The obtained suspension was then vigorously stirred at 90 ˚C under an argon atmosphere for 24 hours. Then the solvent was removed by vacuum. And the white solid was dried under a vacuum for another 5 hours at 80 ˚C to eliminate residual solvents. The product was characterized by means of PXRD (Figure 5.1A).

Optimized the condition of sample Na-ii: 1 eq. of NaH (33.6 mg, 1.4 mmol), 1 eq. of EDAB (122.8 mg, 1.4 mmol), and anhydrous Toluene (15 mL) were added to a 50 mL, one-neck round-bottom Schlenk flask. The obtained suspension was then vigorously stirred at room temperature, 60 ˚C and 90 ˚C under an argon atmosphere for 3 days, 24 hours and 12 hours, respectively. Then the solvent was removed by vacuum. And the white solid was dried under a vacuum for another 5 hours at 80 ˚C to eliminate residual solvents. The product was characterized by means of PXRD (Figure 5.1B).

1 eq. of NaH (33.6 mg, 1.4 mmol), 1 eq. of EDAB (122.8 mg, 1.4 mmol), and anhydrous Toluene (15 mL) were added to a 50 mL, one-neck round-bottom Schlenk flask. The obtained suspension was then vigorously stirred at 90 ˚C under an argon atmosphere for 6 hours, 12 hours, 36 hours, respectively. Then the solvent was removed by vacuum. And the white solid was dried under a vacuum for another 5 hours at 80 ˚C to eliminate residual solvents. The product was characterized by means of PXRD (Figure 5.1C).

5.7.4 Reaction between $NaNH_2$ and EDAB

Sample Na-v: 1 eq. of powdered $NaNH_2$ (50.7 mg, 1.3 mmol), 1 eq. of powder EDAB (114.0 mg, 1.3 mmol), and anhydrous Toluene (20 mL) were added to a 50 mL, one-neck round-bottom Schlenk flask. The obtained suspension was then vigorously stirred at 90 ˚C under an argon atmosphere for 24 hours. Then the solvent was removed by vacuum. And the white solid was dried under a vacuum for another 3 hours at 80 ˚C to eliminate residual solvents. The product was characterized by means of PXRD (Figure 5.9).

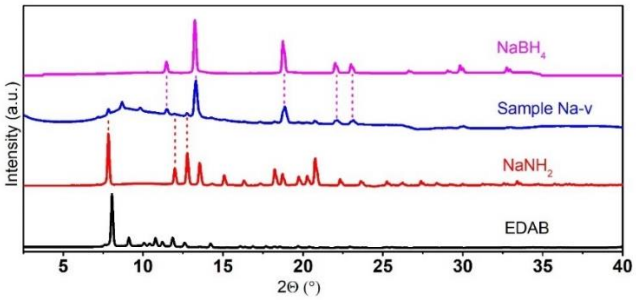

Figure 5.9 PXRD patterns of EDAB, $NaNH_2$, sample **Na-v**, and $NaBH_4$ (the peaks corresponding to $NaNH_2$ and $NaBH_4$ in product pointed by red and pink dash lines, respectively. λ = 0.71073 Å).

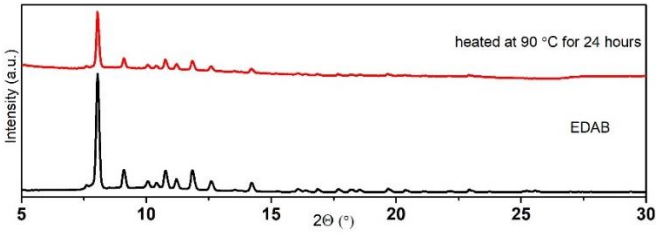

Figure 5.10 PXRD pattern of EDAB, and EDAB heated for 24 hours at 90 ˚C (λ = 0.71073 Å).

Sample Na-vi: 1 eq. of powdered $NaNH_2$ (50.7 mg, 1.3 mmol), 1 eq. of powder EDAB (114.0 mg, 1.3 mmol) were placed into an 80 mL stainless steel vial and with three 10 mm diameter stainless steel balls and milled in a planetary ball mill (Fritsch Pulverisette 7 Premium line). Evolution of the gas pressure and temperature during the reaction was performed using the Easy GTM detection system accessory (Fritsch). The rotation speed was set to 600 rpm and the ball-to-powder mass ratio was 75:1. The synthesis was performed using 200 milling cycles of 5 min milling interrupted by 3 min cooling breaks. The final product is too sticky to collect.

5.7.5 Reaction between LiH and EDAB

Sample Li-i: 2 eq. of LiH (15.9 mg, 2.0 mmol) and 1 eq. of EDAB (87.8 mg, 1.0 mmol) was placed into an 80 mL stainless steel vial with three 10 mm diameter stainless steel balls and milled in a planetary ball mill (Fritsch Pulverisette 7 Premium line). The evolution of the gas pressure and temperature during the reaction was performed using the Easy GTM detection system accessory (Fritsch). The rotation speed was set to 600 rpm and the

ball-to-powder mass ratio was 120:1. The synthesis was performed using 115 milling cycles of 10 min milling interrupted by 5 min cooling breaks. The product was characterized by means of PXRD (Figure 5.11).

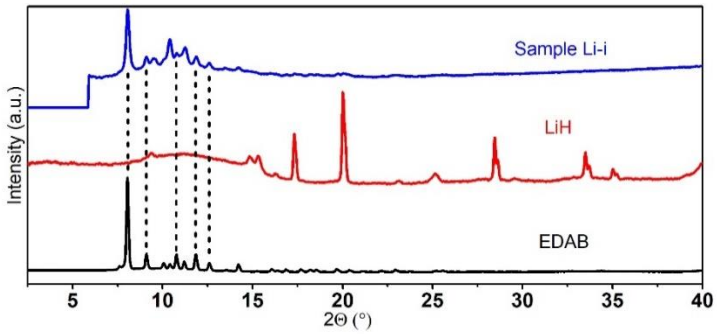

Figure 5.11 PXRD patterns of EDAB, LiH and sample **Li-i** (λ = 0.71073 Å).

Sample Li-ii and Li-iii: 2 eq. of LiH (31.8 mg, 4.0 mmol) and 1 eq. of EDAB (175.6 mg, 2.0 mmol) and anhydrous THF (20 mL) or Toluene (20 mL) were added to a 50 mL, one-neck round-bottom Schlenk flask. The obtained suspension was then vigorously stirred at room temperature (THF used as solvent) under an argon atmosphere for 48 hours (sample **Li-ii**), at 90 ˚C (Toluene used as solvent) under an argon atmosphere for 24 hours (sample **Li-iii**), respectively. Then the solvent was removed by vacuum. And the white solid was dried under a vacuum for another 5 hours to eliminate residual solvents. The product was characterized by means of PXRD (Figure 5.12).

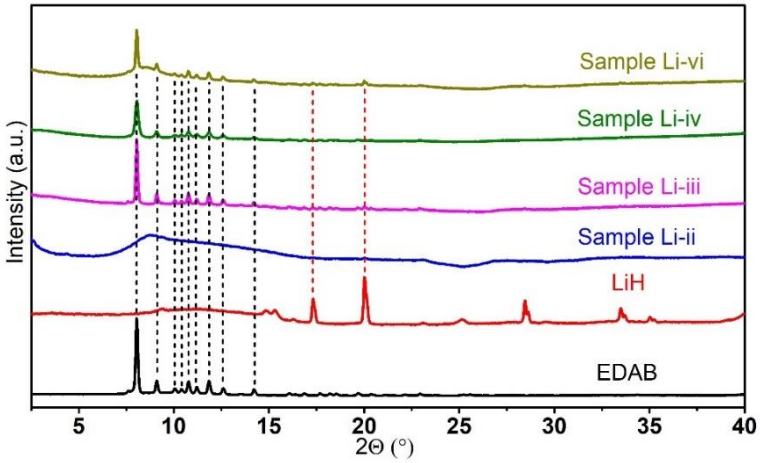

Figure 5.12 PXRD patterns of EDAB, LiH, samples **Li-ii**, **Li-iii**, **Li-iv** and **Li-vi** (λ = 0.71073 Å).

Sample Li-iv: 1 eq. of LiH (12.5 mg, 1.6 mmol) and 1 eq. of EDAB (137.8 mg, 1.6 mmol) was placed into an 80 mL stainless steel vial and with three 10 mm diameter stainless steel balls and milled in a planetary ball mill (Fritsch Pulverisette 7 Premium line). The evolution of the gas pressure and temperature during the reaction was performed using the Easy GTM detection system accessory (Fritsch). The rotation speed was set to 500 rpm and the ball-to-powder mass ratio was 80:1. The synthesis was performed using 20 milling cycles of 30 min milling interrupted by 15 min cooling breaks. The product was characterized by means of PXRD (Figure 5.12).

Sample Li-v and Li-vi: 1 eq. of LiH (12.5 mg, 1.6 mmol) and 1 eq. of EDAB (137.8 mg, 1.6 mmol) and anhydrous THF (20 mL) or Toluene (20 mL) were added to a 50 mL, one-neck round-bottom Schlenk flask. The obtained suspension was then vigorously stirred at room temperature (THF used as solvent) under an argon atmosphere for 48 hours (sample **Li-v**), at 90 ˚C (Toluene used as solvent) under an argon atmosphere for 24 hours (sample **Li-vi**), respectively. Then the solvent was removed by vacuum. sample **Li-v** was too sticky to collect after 5 hours under a vacuum. However, sample **Li-vi** was dried under a vacuum for another 5 hours to eliminate residual solvents. The product was characterized by means of PXRD (Figure 5.12).

5.7.6 The reaction between $LiNH_2$ and EDAB

Sample Li-vii: 1 eq. of powdered $LiNH_2$ (33.4 mg, 1.4 mmol), 1 eq. of powder EDAB (127 mg, 1.4 mmol), and anhydrous Toluene (20 mL) were added to a 50 mL, one-neck round-bottom Schlenk flask. The obtained suspension was then vigorously stirred at 90 ˚C under an argon atmosphere for 24 hours. Then the solvent was removed by vacuum. And the white solid was dried under a vacuum for another 3 hours at 80 ˚C to eliminate residual solvents. The product was characterized by means of PXRD (Figure 5.13).

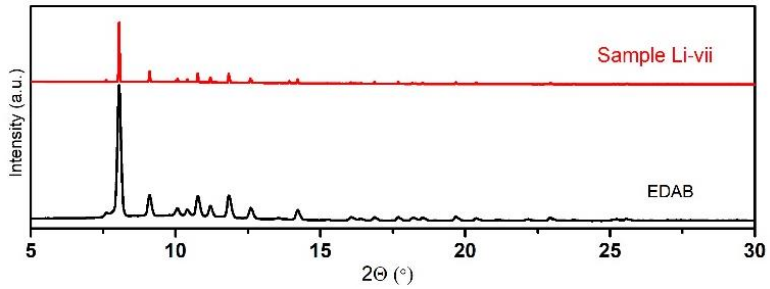

Figure 5.13 PXRD pattern of EDAB and sample **Li-vii** (λ = 0.71073 Å).

Sample Li-viii: 1 eq. of powdered $LiNH_2$ (33.4 mg, 1.4 mmol), 1 eq. of powder EDAB (127 mg, 1.4 mmol), was placed into an 80 mL stainless steel vial and with three 10 mm diameter stainless steel balls and milled in a planetary ball mill (Fritsch Pulverisette 7 Premium line). The evolution of the gas pressure and temperature during the reaction was performed using the Easy GTM detection system accessory (Fritsch). The rotation speed was set to 600 rpm and the ball-to-powder mass ratio was 75:1. The synthesis was performed using 200 milling cycles of 5 min milling interrupted by 3 min cooling breaks. The product is too sticky to collect.

5.7.7 Powder X-ray diffraction (PXRD):

Samples were carefully filled into 0.7 mm thin-walled glass capillaries (Hilgenberg GmbH) within an argon-filled glovebox. To prevent contact with air, the capillaries were sealed with grease before being taken out of the glovebox. The sealed capillaries were then cut and promptly placed into wax on a goniometer head, ensuring that no air entered the capillary. Diffraction data were immediately collected using a MAR345 image-plate detector equipped with an Incoatec Mo (λ = 0.71073 Å) Microfocus (IμS 2.0) X-ray source operating at 50 kV and 1000 μA. The resulting two-dimensional images were azimuthally integrated using the Fit2D software, with LaB_6 serving as a calibrant.

5.7.8 Fourier transform infrared spectroscopy (FTIR):

Attenuated total reflectance (ATR)-IR spectra were recorded using a Bruker Alpha spectrometer. The spectrometer was equipped with a Platinum ATR sample holder, which featured a diamond crystal for single bounce

measurements. The entire experimental setup was located within an argon-filled glovebox to maintain an inert atmosphere during the measurements.

5.7.9 Nuclear magnetic resonance (NMR):

^{1}H, ^{11}B and ^{13}C NMR were recorded on a Bruker Avance 500 MHz spectrometer (^{1}H NMR 500 MHz, ^{11}B NMR 160 MHz, and ^{13}C NMR 126 MHz).

5.7.10 Thermogravimetric analysis (TGA):

TGA measurements were conducted using a Mettler Toledo TGA/SDTA 851e instrument. The samples were loaded into Al_2O_3 crucibles and subjected to a heating rate of 5 K/min under a nitrogen flow of 100 mL/min.

5.7.11 Mass spectrometry:

Mass spectrometry measurements were performed using a Hiden Catlab reactor combined with a Quantitative Gas Analyser (QGA) Hidden quadrupole mass spectrometer, which is installed outside of the glovebox. Before the experiment, samples were loaded into a quartz tube in between two layers of glass cotton under the protective atmosphere of an argon-filled glovebox. The two extremities of the quartz tube were sealed with Parafilm before being removed from the glovebox. The quartz tube was then installed in the sample holder outside the glovebox after quickly removing the Parafilm and the argon flow (20 mL/min) was switched on immediately to prevent contact of the sample with air. Samples were heated to 40 °C and kept isothermally for ~2 hours to stabilize the temperature. Heating was then performed at a rate of 5 °C/min up to 240 °C corresponding to sample **Na-ii**, followed by a 1-hour isotherm. Gas evolution was monitored by recording the highest intensity peak for each gas, i.e. m/z of 2, 17, 18, 26, 28, 30, and 91 for H_2, NH_3, H_2O, B_2H_6, N_2, $NH_2CH_2CH_2NH_2$ and toluene, respectively. H_2O and N_2 were monitored to check if the sample contacted air or not.

References

1. Ren, J.; Musyoka, N. M.; Langmi, H. W.; Mathe, M.; Liao, S., Current Research Trends and Perspectives on Materials-Based Hydrogen Storage

Solutions: A Critical Review. *International Journal of Hydrogen Energy* **2017**, *42*, 289-311.

2. Milanese, C., et al., Complex Hydrides for Energy Storage. *International Journal of Hydrogen Energy* **2019**, *44*, 7860-7874.

3. Chen, Z.; Ma, Z.; Zheng, J.; Li, X.; Akiba, E.; Li, H.-W., Perspectives and Challenges of Hydrogen Storage in Solid-State Hydrides. *Chinese Journal of Chemical Engineering* **2021**, *29*, 1-12.

4. Dematteis, E. M., et al., Hydrogen Storage in Complex Hydrides: Past Activities and New Trends. *Progress in Energy* **2022**, *4*, 032009.

5. Li, H.-W.; Yan, Y.; Orimo, S.-i.; Züttel, A.; Jensen, C. M. Recent Progress in Metal Borohydrides for Hydrogen Storage *Energies* **2011**, DOI: 10.3390/en4010185.

6. Wolf, G.; Baumann, J.; Baitalow, F.; Hoffmann, F. P., Calorimetric Process Monitoring of Thermal Decomposition of B–N–H Compounds. *Thermochimica Acta* **2000**, *343*, 19-25.

7. Baitalow, F.; Baumann, J.; Wolf, G.; Jaenicke-Rößler, K.; Leitner, G., Thermal Decomposition of B–N–H Compounds Investigated by Using Combined Thermoanalytical Methods. *Thermochimica Acta* **2002**, *391*, 159-168.

8. Staubitz, A.; Robertson, A. P. M.; Manners, I., Ammonia-Borane and Related Compounds as Dihydrogen Sources. *Chemical Reviews* **2010**, *110*, 4079-4124.

9. Demirci, U. B., Mechanistic Insights into the Thermal Decomposition of Ammonia Borane, a Material Studied for Chemical Hydrogen Storage. *Inorganic Chemistry Frontiers* **2021**, *8*, 1900-1930.

10. Wang, K.; Zhang, J.-G.; Man, T.-T.; Wu, M.; Chen, C.-C., Recent Process and Development of Metal Aminoborane. *Chemistry – An Asian Journal* **2013**, *8*, 1076-1089.

11. Owarzany, R.; Leszczyński, J. P.; Fijalkowski, J. K.; Grochala, W., Mono- and Bimetalic Amidoboranes. *Crystals* **2016**, *6*.

12. Castilla-Martinez, C. A.; Moury, R.; Demirci, U. B., Amidoboranes and Hydrazinidoboranes: State of the Art, Potential for Hydrogen Storage, and Other Prospects. *International Journal of Hydrogen Energy* **2020**, *45*, 30731-30755.

13. Milanović, I.; Biliškov, N.; Užarević, K.; Lukin, S.; Etter, M.; Halasz, I., Mechanochemical Synthesis and Thermal Dehydrogenation of Novel Calcium-Containing Bimetallic Amidoboranes. *ACS Sustainable Chemistry & Engineering* **2021**, *9*, 2089-2099.

14. Zhang, T.; Steenhaut, T.; Li, X.; Devred, F.; Devillers, M.; Filinchuk, Y., Aluminum Methylamidoborane Complexes: Mechanochemical Synthesis, Structure, Stability, and Reactive Hydride Composites. *Sustainable Energy & Fuels* **2023**, *7*, 1119-1126.

15. Fijalkowski, K. J.; Jaroń, T.; Leszczyński, P. J.; Magos-Palasyuk, E.; Palasyuk, T.; Cyrański, M. K.; Grochala, W., $M(BH_3NH_2BH_2NH_2BH_3)$ – the Missing Link in the Mechanism of the Thermal Decomposition of Light Alkali Metal Amidoboranes. *Physical Chemistry Chemical Physics* **2014**, *16*, 23340-23346.

16. Owarzany, R.; Fijalkowski, K. J.; Jaroń, T.; Leszczyński, P. J.; Dobrzycki, Ł.; Cyrański, M. K.; Grochala, W., Complete Series of Alkali-Metal $M(BH_3NH_2BH_2NH_2BH_3)$ Hydrogen-Storage Salts Accessed Via Metathesis in Organic Solvents. *Inorganic Chemistry* **2016**, *55*, 37-45.

17. Chen, X.-M.; Jiang, X.; Jing, Y.; Chen, X., Synthesis and Dehydrogenation of Organic Salts of a Five-Membered B/N Anionic Chain, a Novel Ionic Liquid. *Chemistry – An Asian Journal* **2021**, *16*, 2475-2480.

18. Owarzany, R.; Jaroń, T.; Kazimierczuk, K.; Malinowski, P. J.; Grochala, W.; Fijalkowski, K. J., Towards Hydrogen-Rich Ionic $(NH_4)(BH_3NH_2BH_2NH_2BH_3)$ and Related Molecular $NH_3BH_2NH_2BH_2NH_2BH_3$. *Dalton Transactions* **2023**, *52*, 3586-3595.

19. Zhang, T.; Steenhaut, T.; Devillers, M.; Filinchuk, Y. Release of Pure H_2 from $Na[BH_3(CH_3NH)BH_2(CH_3NH)BH_3]$ by Introduction of Methyl Substituents *Inorganics* **2023**, DOI: 10.3390/inorganics11050202.

20. Bowden, M. E.; Brown, I. W. M.; Gainsford, G. J.; Wong, H., Structure and Thermal Decomposition of Methylamine Borane. *Inorganica Chimica Acta* **2008**, *361*, 2147-2153.

21. Leardini, F.; Valero-Pedraza, M. J.; Perez-Mayoral, E.; Cantelli, R.; Bañares, M. A., Thermolytic Decomposition of Ethane 1,2-Diamineborane Investigated by Thermoanalytical Methods and in Situ Vibrational Spectroscopy. *The Journal of Physical Chemistry C* **2014**, *118*, 17221-17230.

22. Neiner, D.; Karkamkar, A.; Bowden, M.; Joon Choi, Y.; Luedtke, A.; Holladay, J.; Fisher, A.; Szymczak, N.; Autrey, T., Kinetic and Thermodynamic Investigation of Hydrogen Release from Ethane 1,2-Di-Amineborane. *Energy & Environmental Science* **2011**, *4*, 4187-4193.

23. Zhang, L.; Li, S.; Tan, Y.; Tang, Z.; Guo, Z.; Yu, X., Synthesis and Hydrogen Release Properties of Alkyl-Substituted Amine-Boranes. *Journal of Materials Chemistry A* **2014**, *2*, 10682-10687.

24. Li, L.; Gu, Q.; Tang, Z.; Chen, X.; Tan, Y.; Li, Q.; Yu, X., Two Novel Derivatives of Ammonia Borane for Hydrogen Storage: Synthesis, Structure, and Hydrogen Desorption Investigation. *Journal of Materials Chemistry A* **2013**, *1*, 12263-12269.

25. Chen, X.-M.; Wang, J.; Liu, S.-C.; Zhang, J.; Wei, D.; Chen, X., Controllable Syntheses of B/N Anionic Aminoborane Chain Complexes by the Reaction of NH_3BH_3 with NaH and the Mechanistic Study. *Dalton Transactions* **2019**, *48*, 14984-14988.

26. Xiong, Z., et al., High-Capacity Hydrogen Storage in Lithium and Sodium Amidoboranes. *Nature Materials* **2007**, *7*, 138.

27. Wu, C.; Wu, G.; Xiong, Z.; Han, X.; Chu, H.; He, T.; Chen, P., $LiNH_2BH_3{\cdot}NH_3BH_3$: Structure and Hydrogen Storage Properties. *Chemistry of Materials* **2010**, *22*, 3-5.

28. Leardini, F.; Mirabile Gattia, D.; Montone, A.; Cuevas, F.; Perez-Mayoral, E.; Valero-Pedraza, M. J.; Bañares, M. A.; Cantelli, R., A Step Forward to the Dehydrogenation Reversibility of Amine-Borane Adducts by Coupling Sodium and Hydrocarbon Groups. *International Journal of Hydrogen Energy* **2015**, *40*, 2763-2767.

Chapter 6

Synthesis, Structural Characterization, and Hydrogen Release of Al-Based Amidoboranes Derived from $MAlH_4$-EDAB

Abstract

Over the past two decades, the high hydrogen content and favorable dehydrogenation conditions of multi-metallic amidoboranes have gained significant attention for their potential in hydrogen storage. Among them, Al-based multi-amidoboranes have shown promise because of their high polarizing power, lightweight nature, and abundant natural presence. In this chapter, we successfully synthesized two novel tetrahedrally coordinated Al-based amidoboranes, namely $Li[Al(BH_3NHCH_2CH_2NHBH_3)_2]$ and $Na[Al(BH_3NHCH_2CH_2NHBH_3)_2]$, using $BH_3NH_2CH_2CH_2NH_2BH_3$ (EDAB) as a precursor. Additionally, we also attempted to synthesize octahedral-coordinated Al-based amidoboranes using EDAB. The structure of $Na[Al(BH_3NHCH_2CH_2NHBH_3)_2]$ was determined through modeling based on synchrotron powder X-ray diffraction. Additionally, the formation of the Al-N bond in $Li[Al(BH_3NHCH_2CH_2NHBH_3)_2]$ and $Na[Al(BH_3NHCH_2CH_2NHBH_3)_2]$ was confirmed with IR spectra. $Na[Al(BH_3NHCH_2CH_2NHBH_3)_2]$ is more stable in air than $Li[Al(BH_3NHCH_2CH_2NHBH_3)_2]$. Importantly, thermal gravimetric analysis and mass spectrum characterization confirmed that both compounds release hydrogen without the presence of ammonia, diborane, or ethylenediamine. Our work represents the first example of Al-based amidoboranes with chelation coordination geometry, which provides an

essential foundation for understanding the relationship of complex multi-metallic amidoboranes in terms of synthesis, structure, and properties.

6.1 Introduction

Compounds based on boron–nitrogen–hydrogen (B-N-H)[1, 2] have emerged as promising hydrogen storage materials due to the lightweight nature of boron and nitrogen, as well as their ability to accommodate multiple hydrogen atoms. This is attributed to the hydridic and protic characteristics of the B-H and N-H bonds, which facilitate the release of hydrogen. One representative example of B-N-H material is ammonia borane[3, 4] (NH_3BH_3 or AB), which can release up to 19.6 wt.% of hydrogen, exhibits low toxicity and demonstrates good stability under ambient conditions.

However, the thermal decomposition of NH_3BH_3 occurs in multiple steps, typically at around 120 °C, 200 °C, and above 500 °C, leading to the generation of toxic volatile by-products such as B_2H_6, NH_3, and $N_3B_3H_6$. The decomposition process is often accompanied by severe foaming and volume expansion. Various strategies have been explored to address these limitations, including chemical modifications of NH_3BH_3 molecules to create derivatives. This approach has resulted in the synthesis of novel compounds like alkali amidoboranes [5-8], alkaline earth amidoboranes[9-13], and multi-metallic amidoboranes[14-25], which exhibit improved characteristics for hydrogen storage applications. For instance, KNH_2BH_3 releases approximately 5.8 wt.% of pure hydrogen from room temperature up to 160 °C[6]. $Mg(NH_2BH_3)_2$ can release approximately 10 wt.% of high-purity H_2 upon heating to 300 °C[13]. Furthermore, $Na_2Mg(NH_2BH_3)_4$ has the ability to release 8.4 wt.% of predominantly hydrogen, with minor amounts of ammonia and borazine[16].

Compared to mono-metallic amidoboranes, multi-metallic amidoboranes offer greater versatility in forming new compounds. So far, multi-metallic amidoboranes have been categorized into Li-, Mg-, Ca-, and Al-based amidoboranes based on the central coordination metals. Our works focus on the synthesis and chemical modification of Al-based amidoboranes, driven by the high polarizing power defined by the exceptional charge-to-radius ratio, low weight, and high natural abundance of Al.

Our initial investigation on Al-based amidoboranes led to the discovery of $Na[Al(NH_2BH_3)_4]$[22], which exhibits a two-step hydrogen release process (at 120 °C and 168 °C), releasing approximately 9 wt.% of high-purity hydrogen. Furthermore, the amorphous residue obtained after the thermal decomposition of $Na[Al(NH_2BH_3)_4]$ demonstrated the ability to reversibly absorb around 27% of the released hydrogen at 250 °C and a hydrogen pressure of 150 bar. Subsequently, we conducted a study on the formation, structure, and hydrogen release properties of its derivative, $Na[Al(CH_3NHBH_3)_4]$[25]. This compound was synthesized from $NaAlH_4$ and $CH_3NH_2BH_3$ (MeAB), and the introduction of a methyl group (-CH_3) on the nitrogen of NH_3BH_3 stabilized an intermediate compound, $Na[AlH(CH_3NHBH_3)_3]$, shedding light on the formation process of such compounds. Notably, the energy input required for the formation of $Na[Al(CH_3NHBH_3)_4]$ was lower than that of the unsubstituted $Na[Al(NH_2BH_3)_4]$, which can be attributed to the presence of the methyl group. $Na[Al(CH_3NHBH_3)_4]$ does not release high-purity hydrogen during its thermal decomposition, but forms reactive hydride composites with NaH and $NaNH_2$ desorbing pure H_2 under relatively mild conditions.

To further advance the development of Al-based amidoboranes and gain a deeper understanding of the relationships between synthesis, structure, and hydrogen release properties, we conducted additional modifications on $Na[Al(NH_2BH_3)_4]$. In this section, we will introduce our new Al-based amidoboranes, namely $Li[Al(BH_3NHCH_2CH_2NHBH_3)_2]$, and $Na[Al(BH_3NHCH_2CH_2NHBH_3)_2]$, providing comprehensive details about their synthesis, structural characterization, and thermal dehydrogenation properties.

For the synthesis of $Li[Al(BH_3NHCH_2CH_2NHBH_3)_2]$ and $Na[Al(BH_3NHCH_2CH_2NHBH_3)_2]$, we employed $BH_3NH_2CH_2CH_2NH_2BH_3$ (EDAB) as one of the precursors. EDAB offers greater accessibility than NH_3BH_3, as it can be derived from commercially available and cost-effective precursors. Additionally, the presence of the weak electron-donating methylene substituent influences the coordination bonds between the nitrogen and aluminum atoms in the final complex, similar to the behaviour observed in $Na[Al(CH_3NHBH_3)_4]$. EDAB exhibits a dimer-like structure derived from $CH_3NH_2BH_3$, facilitating the formation of a chelate complex with aluminum.

This characteristic contributes to the creation of a more stable framework for Al-based amidoboranes, suppressing the release of significant fragments during thermal decomposition, as observed in $Na[Al(CH_3NHBH_3)_4]$[25].

6.2 The syntheses of four- and six-coordinated Al-based amidoboranes with EDAB

The crystal structures of the reported Al-based amidoborane complexes in a tetrahedral coordination geometry include $Na[Al(NH_2BH_3)_4]$, $K[Al(NH_2BH_3)_4]$, $Na[AlH(CH_3NHBH_3)_3]$ and $Na[Al(CH_3NHBH_3)_4]$. These complexes can be synthesized by ball milling $NaAlH_4$ or $KAlH_4$ with 4 equivalents of NH_3BH_3 or $CH_3NH_2BH_3$. Mechanochemical synthesis is preferred over wet chemical methods for the synthesis of hydrogen storage materials, as it avoids the use of coordinating or high-boiling-point solvents, which can often complicate the process.

It has been reported that the reaction between 1 equivalent of $LiAlH_4$ and 4 equivalents of NH_3BH_3 under ball milling conditions is excessively violent. Furthermore, the lower melting point of $CH_3NH_2BH_3$ (58 °C)[26] compared to NH_3BH_3 (112-114 °C)[27] results in $NaAlH_4$-$4CH_3NH_2BH_3$ composites exhibiting higher reactivity than $NaAlH_4$-$4NH_2BH_3$. As a result, ball milling may not be suitable for the synthesis of $Li[Al(CH_3NHBH_3)_4]$. In contrast, $BH_3NH_2CH_2CH_2NH_2BH_3$ (EDAB) demonstrates higher thermal stability and a slightly higher melting point (119 °C)[28] compared to NH_3BH_3 and $CH_3NH_2BH_3$. Therefore, the reaction between $LiAlH_4$ and EDAB is expected to go easier than between $LiAlH_4$ and $CH_3NH_2BH_3$ and/or NH_3BH_3. Thus, we attempted the ball milling synthesis of a novel Al-based amidoborane complex with Li and Na, using $LiAlH_4$/$NaAlH_4$ and EDAB.

While aluminum can adopt four-coordinated and six-coordinated geometries generally, this study focuses on the four-coordinated Al-based amidoboranes. However, we briefly mention our attempts to synthesize six-coordinated Al-based amidoboranes using the respective metal alanates and EDAB.

6.2.1 Synthesis of $Li[Al(BH_3NHCH_2CH_2NHBH_3)_2]$

Initially, we conducted ball milling experiments using $LiAlH_4$-2EDAB composites under the same conditions as for the synthesis of $Na[Al(NH_2BH_3)_4]$ and $Na[Al(CH_3NHBH_3)_4]$, as indicated for the sample **Li-A** in Table 6.1. Unlike the drastic pressure increase observed during the milling of $LiAlH_4$-$4NH_3BH_3$, no sudden pressure jump was observed in the case of Na-containing system. The powder X-ray diffraction (PXRD) pattern (Figure 6.1, sample **Li-A**) revealed the presence of a few new peaks alongside the residual reactants, suggesting that the reaction between $LiAlH_4$ and 2 EDAB could occur under these milling conditions. However, a longer milling time or more intense milling conditions seem to be necessary to complete the reaction. This indicates that EDAB exhibits lower reactivity in this reaction than NH_3BH_3 and $CH_3NH_2BH_3$.

To enhance the yield of the new product from the milled $LiAlH_4$-2EDAB composites, we optimized the milling conditions, as shown in Table 6.1. Method **E** resulted in high yields of new crystalline phase(s), although a small amount of EDAB remained also in these systems. We attempted to prolong the milling time (samples **Li-F** in Table 6.1) to obtain a pure product based on the method **E**. However, an excessively long milling time led to diminished intensities of the diffraction peaks (Figure 6.1, samples **Li-F**).

Table 6.1 Parameters used for the optimization of the synthesis of $Li[Al(BH_3NHCH_2CH_2NHBH_3)_2]$ and the reported milling conditions for the synthesis of $Na[Al(NH_2BH_3)_4]$ and $Na[Al(CH_3NHBH_3)_4]$.

Samples	Rotation speed (rpm)	Milling time (min)	Break time (min)	Number of cycles	Ball to powder mass ratio
$Na[Al(NH_2BH_3)_4]$[22]	600	3	5	240	30:1
$Na[Al(CH_3NHBH_3)_4]$[25]	600	3	5	120	30:1
Li-A	600	3	5	240	30:1
Li-B	600	3	5	50	100:1
Li-C	600	3	5	240	60:1
Li-D	500	30	15	30	80:1
Li-E	500	30	15	50	80:1
Li-F	500	30	15	60	80:1

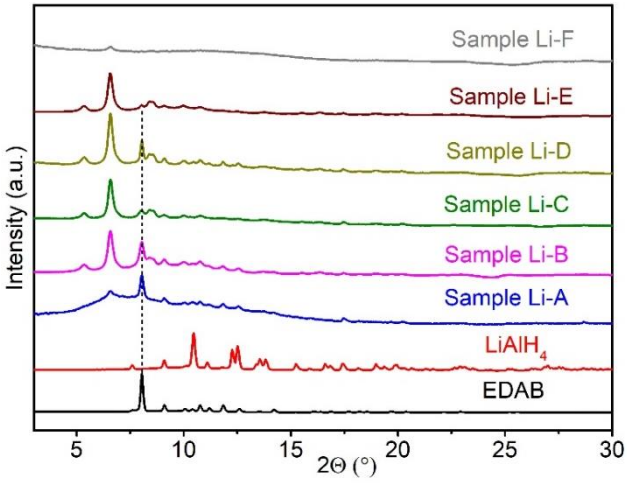

Figure 6.1 PXRD patterns of EDAB, $LiAlH_4$, and samples Li-A, B, C, D, E and F (the main peak of residual EDAB in samples Li-A, B, C, D and E was pointed by black dash line, λ = 0.71073 Å).

Variable-temperature PXRD measurements were conducted to determine the number of phases associated with the newly observed peaks. Interestingly, all the peaks observed in the PXRD pattern of sample **Li-E** vanished simultaneously at approximately 130 °C (Figure 6.2). This indicates that these peaks correspond to a single phase. The pressure and temperature were carefully monitored throughout the milling process of $LiAlH_4$-2EDAB (refer to the synthesis section and Table 6.4). The results revealed the release of approximately 3.3 equivalents of gas per mole of $LiAlH_4$, which closely matches the expected gas quantity (4 equivalents) based on Equation 6.1.

$$LiAlH_4 + 2\ BH_3NH_2CH_2CH_2NH_2BH_3 \longrightarrow Li[Al(BH_3NHCH_2CH_2NHBH_3)_2] + 4\ H_2\uparrow$$

Equation 6.1

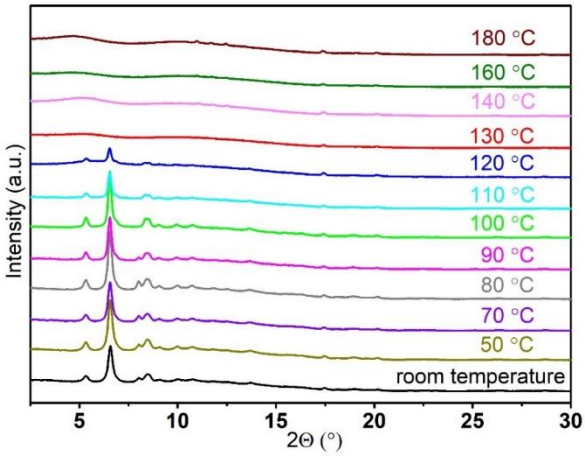

Figure 6.2 Temperature ramp followed by PXRD for $Li[Al(BH_3NHCH_2CH_2NHBH_3)_2]$ (λ = 0.71073 Å).

In the structure characterization section, we also performed the IR spectra analysis of the sample **Li-E**, comparing it with that of $Na[Al(BH_3NHCH_2CH_2NHBH_3)_2]$. Interestingly, the IR spectra of sample **Li-E** exhibited a striking similarity to that of $Na[Al(BH_3NHCH_2CH_2NHBH_3)_2]$. This observation, combined with the findings from ramping PXRD measurements and the analysis of released gases during synthesis, strongly suggests that $Li[Al(BH_3NHCH_2CH_2NHBH_3)_2]$ was successfully synthesized under the milling conditions employed for the sample **Li-E**.

6.2.2 Synthesis of $Na[Al(BH_3NHCH_2CH_2NHBH_3)_2]$

In our quest to obtain Al-based amidoboranes with Na^+ as a counterion, we explored the wet chemical synthesis approach by reacting $NaAlH_4$ and EDAB. Previous reports indicated that $Na[Al(NH_2BH_3)_4]$ could be obtained in THF at room temperature within 3 hours[29]. Following this, we conducted the synthesis of $Na[Al(BH_3NHCH_2CH_2NHBH_3)_2]$ in anhydrous THF with varying stirring times (as shown in Table 6.2). Specifically, we combined 1 eq. of $NaAlH_4$ and 2 eq. of EDAB in anhydrous THF at room temperature and allowed the reaction to proceed for 24, 48, and 72 hours, yielding respectively samples **Na-A**, **Na-B**, and **Na-C** in Table 6.2 (further details are provided in the synthesis section 6.6.7).

Table 6.2 Parameters used for the optimization of the synthesis of $Na[Al(BH_3NHCH_2CH_2NHBH_3)_2]$ at room temperature. (Boiling points are given to show which solvents will be easier to eliminate)

Samples	Reaction time (h)	Solvent(s) (boiling point)
Na-A	24	THF (66 °C)
Na-B	48	THF (66 °C)
Na-C	72	THF (66 °C)
Na-D	48	Toluene (110.6 °C)
Na-E	48	Hexane (69 °C)
Na-F	48	Diethyl ether (34.6 °C)
Na-G	48	1,4-dioxane (101 °C)
Na-H	48	Dichloromethane (39.6 °C)
Na-I	48	Acetonitrile (82 °C)
Na-J	48	5/6 Toluene + 1/6 THF (-)

Our results demonstrate that $Na[Al(BH_3NHCH_2CH_2NHBH_3)_2]$ could indeed be formed in THF at room temperature, albeit with a longer reaction time compared to its analog $Na[Al(NH_2BH_3)_4]$. We monitored the progress of the reaction using PXRD patterns (Figure 6.3). After 24 hours of reaction (sample **Na-A**), new peaks appeared on the PXRD, indicating the formation of new compounds. Extending the reaction time to 48 and 72 hours (samples **Na-B** and **Na-C**), the peaks attributed to EDAB completely disappeared, while the new peaks matched those observed in sample **Na-A**. This confirms that the reaction between $NaAlH_4$ and EDAB was completed within 48 hours.

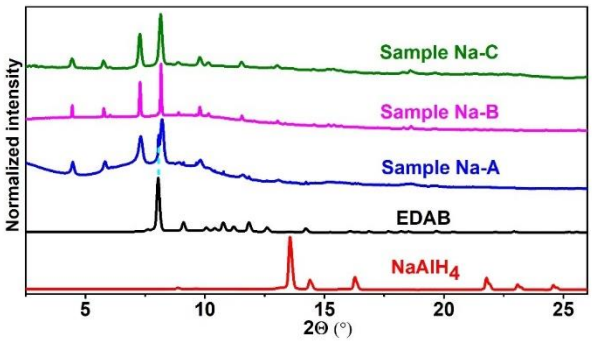

Figure 6.3 PXRD patterns of $NaAlH_4$, EDAB, and of samples Na-A, B and C (the residual EDAB in sample Na-A was pointed by light blue dash line, λ = 0.71073 Å).

To verify the purity of the newly synthesized compound, we performed temperature ramping synchrotron PXRD from room temperature to 225 °C (Figure 6.4). The results demonstrated that all the peaks observed in sample **Na-B** gradually decreased and eventually vanished simultaneously at approximately 121 °C and 165 °C, respectively. This observation suggests that sample **Na-B** consists of a single phase, confirming its purity.

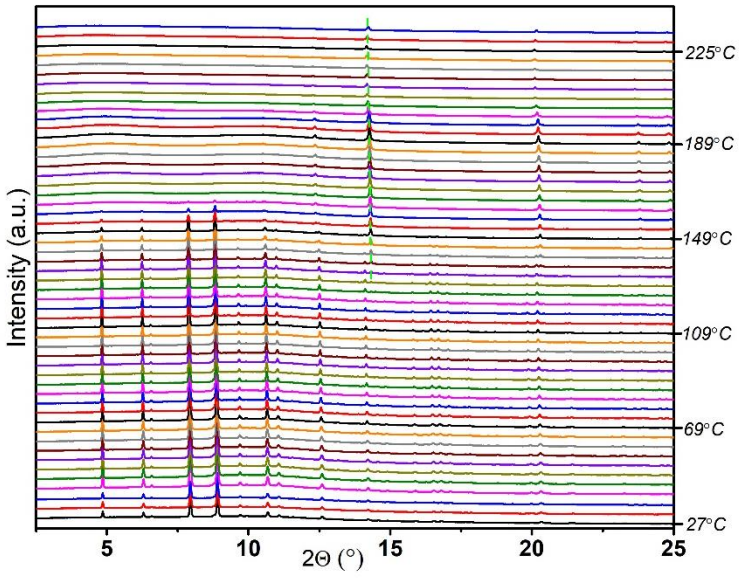

Figure 6.4 Temperature ramping PXRD pattern of $Na[Al(BH_3NHCH_2CH_2NHBH_3)_2]$ (the green dot line point one of the peaks of $NaBH_4$, λ = 0.77509 Å).

For structural characterization, we employed synchrotron PXRD data and conducted modeling to determine the structure of this novel Al-based amidoborane complex, $Na[Al(BH_3NHCH_2CH_2NHBH_3)_2]$. Additionally, we analyzed the IR spectra to provide additional support for our structural conclusions. Notably, the synthesis of $Na[Al(BH_3NHCH_2CH_2NHBH_3)_2]$ requires a significantly longer stirring time (over 24 hours) compared to the synthesis of $Na[Al(NH_2BH_3)_4]$, which can be obtained within 3 hours at room temperature. This indicates that EDAB exhibits higher inertness than AB when reacted with $NaAlH_4$. Consequently, our attempts to synthesize $Na[Al(BH_3NHCH_2CH_2NHBH_3)_2]$ via mechanochemical synthesis were

unsuccessful, despite employing the most rigorous milling conditions in our ball mill. The subsequent sections will provide further details regarding our ball-milling experiments.

The successful formation of $Na[Al(BH_3NHCH_2CH_2NHBH_3)_2]$ in THF can be attributed to two main factors. Firstly, both EDAB and $NaAlH_4$ can dissolve in THF, although $NaAlH_4$ exhibits poor solubility that facilitates efficient contact between the two reactants. Secondly, the THF solvent coordinates with Na^+ and enhances the stability of $Na[Al(BH_3NHCH_2CH_2NHBH_3)_2]$. To validate these assumptions, we conducted the reaction in various solvents, including solvents with poor solubility but lacking coordination points (O atom) such as toluene (sample **Na-D**) and hexane (sample **Na-E**), solvents with poor solubility but possessing coordination points (O atom) like diethyl ether (sample **Na-F**) and 1,4-dioxane (sample **Na-G**), solvents with poor solubility but having other coordination points like dichloromethane (sample **Na-H**) and acetonitrile (sample **Na-I**), and a mixture of toluene and THF (sample **Na-J**).

The experimental results revealed that the reaction between $NaAlH_4$ and EDAB did not take place in toluene and hexane (sample **Na-D** and **E** in Figure 6.5). Similarly, no reaction occurred in diethyl ether or dichloromethane (samples **Na-F** and **H** in Figure 6.5). When 1,4-dioxane was used as the solvent, EDAB interacted with the solvent instead of coordinating with aluminum (sample **Na-G** in Figure 6.6). In acetonitrile, the formation of an amorphous product was observed (sample **Na-I** in Figure 6.5). As anticipated, $Na[Al(BH_3NHCH_2CH_2NHBH_3)_2]$ was partially formed in the mixture of toluene and THF (sample **Na-J** in Figure 6.7). All of these observations confirm the importance of both the solubility of the reactants and the coordination of THF with Na in the successful formation of $Na[Al(BH_3NHCH_2CH_2NHBH_3)_2]$. This should also be why we failed to synthesize the title compound mechanochemically.

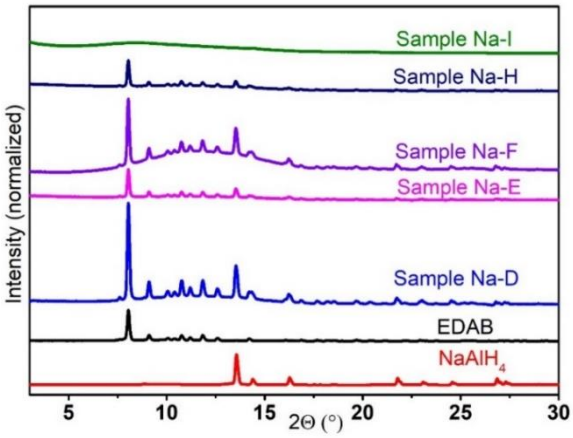

Figure 6.5 PXRD patterns of $NaAlH_4$, EDAB, and samples Na-D, E, F, H and I (λ = 0.71073 Å).

To obtain a THF-free sample of $Na[Al(BH_3NHCH_2CH_2NHBH_3)_2]$, we subjected the sample to vacuum treatment at room temperature and 50 °C (Figure 6.8). Unfortunately, the PXRD patterns of the resulting products remained unchanged, resembling those of sample **Na-B** even after vacuum treatment at both temperatures. We also conducted mass spectrometry characterization on sample **Na-B** and observed that the release of coordinated THF by Na^+ occurred at a higher temperature (~95 ˚C) compared to the release of hydrogen (~68 ˚C) (Figure 6.23). These findings indicate that removing THF from sample **Na-B** through heating or vacuum treatment is challenging, if not impossible.

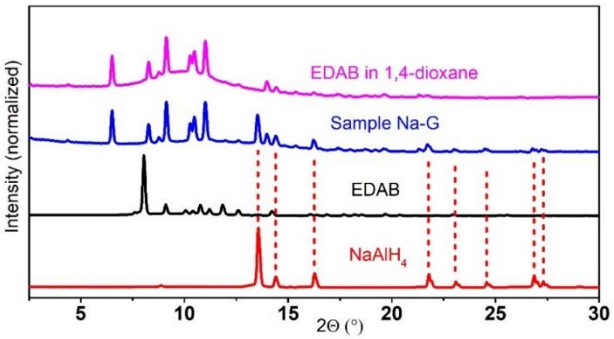

Figure 6.6 PXRD patterns of $NaAlH_4$, EDAB, and samples Na-G, and EDAB stirred in 1,4-dioxane for 2 days (the residual $NaAlH_4$ was pointed by red dash line, λ = 0.71073 Å).

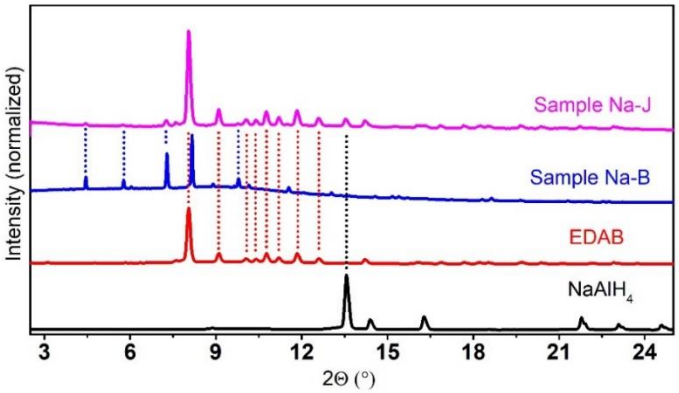

Figure 6.7 PXRD patterns of $NaAlH_4$, EDAB, and samples Na-B, and J (formed $Na[Al(BH_3NHCH_2CH_2NHBH_3)_2]$, residual EDAB and $NaAlH_4$ were pointed by blue, red and black dash line, λ = 0.71073 Å).

Additionally, we attempted to wash sample **Na-B** with lower boiling-point solvents such as CH_2Cl_2 and diethyl ether to eliminate the coordinated THF molecules. Regrettably, these efforts proved ineffective in removing THF from $Na[Al(BH_3NHCH_2CH_2NHBH_3)_2]$ (Figure 6.8). Consequently, we were compelled to investigate the thermal de-hydrogenation of $Na[Al(BH_3NHCH_2CH_2NHBH_3)_2]$ in the presence of THF as our next step.

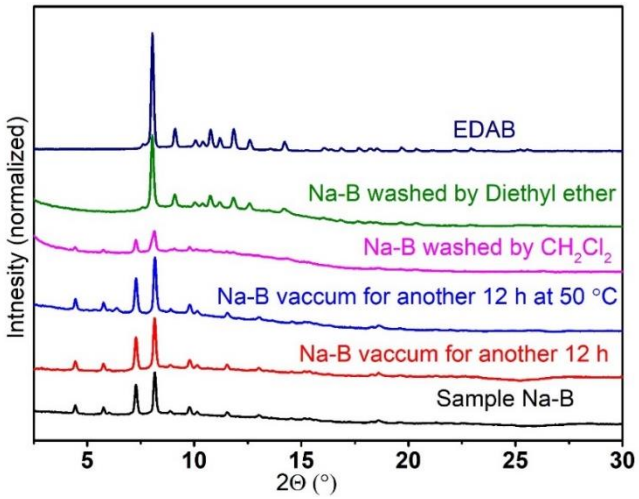

Figure 6.8 PXRD patterns of sample Na-B, sample Na-B vacuum-treated for 12 h at room temperature (red line) and at 50 °C (blue line), washed by CH_2Cl_2 (pink) and diethyl ether (green), and EDAB (λ = 0.71073 Å).

Initially, we failed to synthesize $Na[Al(BH_3NHCH_2CH_2NHBH_3)_2]$ through ball milling. Despite our rigorous efforts to mill the composites of $NaAlH_4$-2EDAB under various milling conditions, including extended milling time, harder milling balls, and higher milling speed—the desired reaction did not occur. This outcome contrasts the successful reactions observed in its parent composites, $NaAlH_4$-4AB and $NaAlH_4$-4MeAB (Table 6.3 and Figure 6.9). These results reaffirm that EDAB exhibits lower reactivity in this reaction when compared to AB and MeAB.

Table 6.3 Parameters used for the synthesis of $Na[Al(BH_3NHCH_2CH_2NHBH_3)_2]$ by ball milling (SS is short of stainless steel, TC is short of tungsten carbide).

Sample	Na-K	Na-L	Na-M	Na-N
Speed	600	600	1000	500
Milling time (min)	3	30	3	3
Break time (min)	2	30	5	2
Milling cycles	90	20	35	22
Ball powder mass ratio	60:1	120:1	120:1	120:1
materials	SS	SS	SS	TC

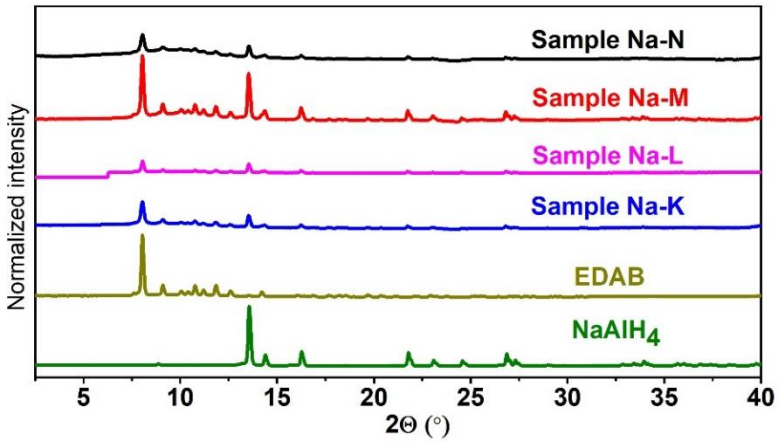

Figure 6.9 PXRD patterns of $NaAlH_4$, EDAB, and samples **Na-K**, **L**, **M**, **N** (λ = 0.71073 Å).

6.2.3 Attempted synthesis of $Li_3[Al(BH_3NHCH_2CH_2NHBH_3)_3]$

$$Li_3AlH_6 + 3\ BH_3NH_2CH_2CH_2NH_2BH_3 \longrightarrow Li_3[Al(BH_3NHCH_2CH_2NHBH_3)_3] + 6\ H_2\uparrow \quad \text{Equation 6.2}$$

We attempted to perform the reaction between Li_3AlH_6 and 3 EDAB according to the Equation 6.2 by ball milling the composites at high speed for an extended period (refer to Experiment section 6.6.8, sample **Li3-A**). However, we observed that the pressure did not increase during milling. This observation suggests that the Li_3AlH_6-3EDAB composites are too inert to undergo a reaction via ball milling, similar to the behavior observed for the $NaAlH_4$-2EDAB system. Consequently, we explored alternative approaches by conducting the reaction in organic solvents.

We conducted the reaction in THF at room temperature (sample **Li3-B**), at 60 ˚C (sample **Li3-C**), and in toluene at 90 ˚C (sample **Li3-D**). After stirring for 48 hours at room temperature in THF, we attempted to collect the composites; however, drying them proved challenging. Upon analyzing sample **Li3-C** by PXRD, we observed a mixture of amorphous materials and metallic aluminum (Figure 6.10). The NH stretching bond in the IR spectra resembled that of EDAB (Figure 6.11), indicating that the desired reaction did not occur.

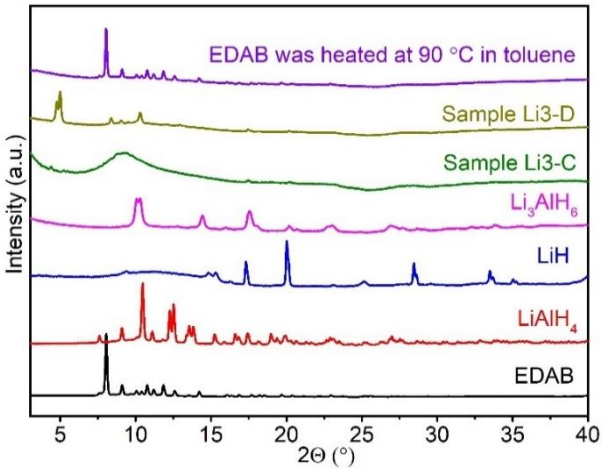

Figure 6.10 PXRD pattern of samples Li3-C, Li3-D, $LiAlH_4$, LiH and reactants (λ = 0.71073 Å).

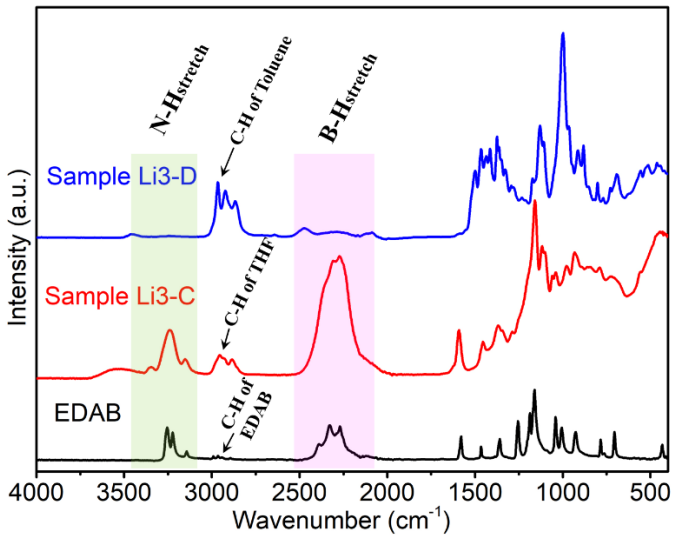

Figure 6.11 IR spectra of sample Li3-C, Li3-D and EDAB.

The product in sample **Li3-D** exhibited unusual characteristics. It did not correspond to the thermally decomposed product of EDAB at 90 ˚C nor the product of the reaction between LiH and EDAB. This was evident from the stability of EDAB at 90 ˚C in toluene (Figure 6.10) and the absence of a reaction between LiH and EDAB at 90 ˚C in toluene (Chapter 5). The PXRD pattern of sample **Li3-D** revealed the presence of new peaks compared to the reactants, $LiAlH_4$ and LiH (Figure 6.10). However, the disappearance of the NH and BH stretching bonds in the IR spectra (Figure 6.11) was a unique phenomenon not observed in other Al-based amidoborane compounds.

6.2.4 Attempted synthesis of $Na_3[Al(BH_3NHCH_2CH_2NHBH_3)_3]$

$$Na_3AlH_6 + 3\ BH_3NH_2CH_2CH_2NH_2BH_3 \longrightarrow Na_3[Al(BH_3NHCH_2CH_2NHBH_3)_3] + 6\ H_2\uparrow \quad \text{Equation 6.3}$$

Similar to the synthesis of $Li_3[Al(BH_3NHCH_2CH_2NHBH_3)_3]$, we also attempted to synthesize $Na_3[Al(BH_3NHCH_2CH_2NHBH_3)_3]$ using both ball milling and wet synthesis methods.

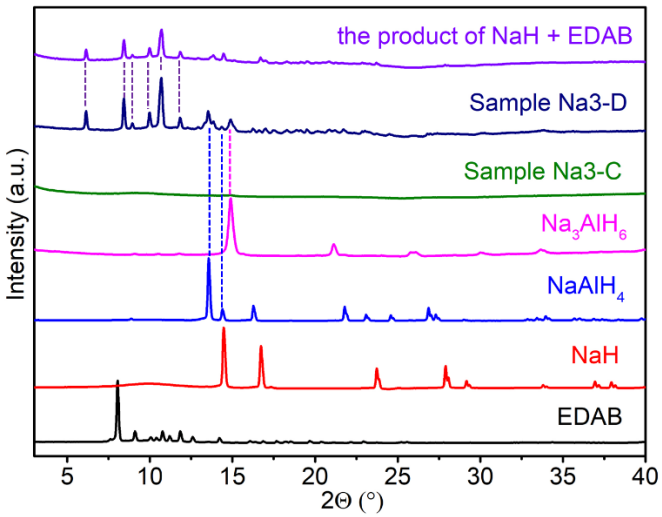

Figure 6.12 PXRD pattern of EDAB, NaH, $NaAlH_4$, Na_3AlH_6, samples Na3-C, Na3-D, and the product from NaH + EDAB (λ = 0.71073 Å).

Initially, we attempted to synthesize $Na_3[Al(BH_3NHCH_2CH_2NHBH_3)_3]$ through ball milling of the composites of Na_3AlH_6-3EDAB for an extended period at high speed (refer to Experiment section 6.6.9, sample **Na3-A**). However, analysis of the PXRD pattern revealed that the desired reaction did not occur. This observation indicates that the Na_3AlH_6-3EDAB composites exhibit a high level of inertness, preventing them from reacting with each other via ball milling, similar to the behavior observed in the $NaAlH_4$-2EDAB and Li_3AlH_6-3EDAB systems. As a result, we decided to explore alternative approaches by investigating the reaction in organic solvents.

We carried out the reaction in THF at room temperature (sample **Na3-B**), at 60 ˚C (sample **Na3-C**), and in toluene at 90 ˚C (sample **Na3-D**). After stirring for 48 hours at room temperature in THF, we encountered difficulties in drying and collecting the samples. The PXRD analysis of sample **Na3-C** revealed that it consisted of amorphous material(s) (Figure 6.12). On the other hand, the product obtained from sample **Na3-D** was a mixture of unreacted Na_3AlH_6, $NaAlH_4$, and the product resulting from the reaction between NaH and EDAB (Figure 6.12). This suggests that Na_3AlH_6 partially decomposed to NaH and $NaAlH_4$ under these conditions.

6.2.5 Attempted synthesis of $Na_2Li[Al(BH_3NHCH_2CH_2NHBH_3)_3]$

$$Na_2LiAlH_6 + 3\ BH_3NH_2CH_2CH_2NH_2BH_3 \longrightarrow Na_2Li[Al(BH_3NHCH_2CH_2NHBH_3)_3] + 6\ H_2\uparrow$$ Equation 6.4

We also explored the synthesis of six-coordinated Al-based amidoboranes by reacting Na_2LiAlH_6 with 3 equivalents of EDAB, following Equation 6.4 mentioned above. However, the desired reaction did not occur through ball milling (Sample **Na2Li-A**), similar to the results obtained with Li_3AlH_6 + 3EDAB and Na_3AlH_6 + 3EDAB systems.

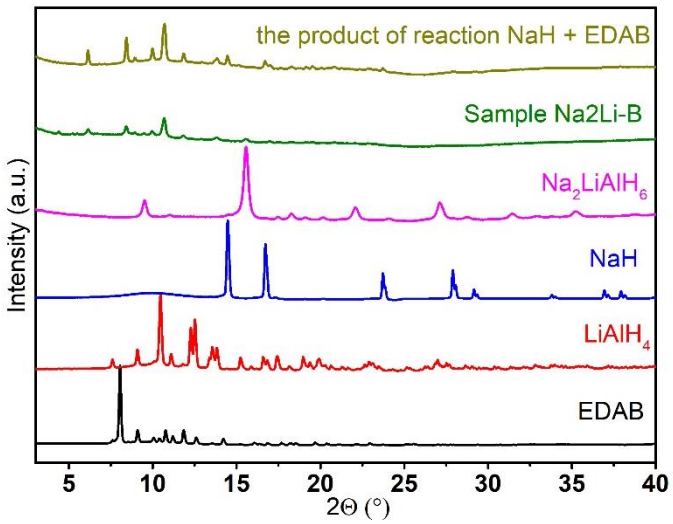

Figure 6.13 PXRD pattern of EDAB, $LiAlH_4$, NaH, Na_2LiAlH_6, sample Na_2Li-B and the product of the reaction between NaH and EDAB (λ = 0.71073 Å).

When the reaction between Na_2LiAlH_6 and 3 equivalents of EDAB was conducted in THF at room temperature, the obtained product (sample **Na2Li-B**) was identified as the product resulting from the reaction between NaH and EDAB (Figure 6.13). This outcome is consistent with the reaction observed between Na_3AlH_6 and 3 equivalents of EDAB in toluene at 90 ˚C. These findings suggest that Na_2LiAlH_6 undergoes decomposition to NaH and $LiAlH_4$ at room temperature in THF.

Based on our attempts to synthesize six-coordinated Al-based amidoboranes using EDAB, we can conclude that these three compounds (Li_3AlH_6, Na_3AlH_6, and Na_2LiAlH_6) are not sufficiently stable to react with EDAB in organic solvents. Therefore, it is necessary to consider alternative, more stable alanates for such reactions. Alternatively, the stability of these three six-coordinated alanates could be enhanced by subjecting them to high hydrogen pressure before their reaction with EDAB. Exploring other methods to increase their stability is also worth an investigation.

6.3 Characterization of $M[Al(BH_3NHCH_2CH_2NHBH_3)_2]$ (M = Li, Na)

6.3.1 Structure of $Na[Al(BH_3NHCH_2CH_2NHBH_3)_2]$

The crystal structure of $Li[Al(BH_3NHCH_2CH_2NHBH_3)_2]$ could not be determined due to the limited number of diffraction peaks and their significant broadening. Therefore, the structure of $Li[Al(BH_3NHCH_2CH_2NHBH_3)_2]$ was characterized through IR spectra, which will be discussed later.

Fortunately, the crystal structure of $Na[Al(BH_3NHCH_2CH_2NHBH_3)_2]$ with THF was successfully determined using synchrotron powder X-ray diffraction (SR-PXRD). Although some details still need further finishing (disordered coordinated THF), the main structural framework has been resolved. We are currently making efforts to grow single crystals to acquire more comprehensive information about the structure, including the disorder of the THF molecule. Based on the SR-PXRD data, the crystal structure of $Na[Al(BH_3NHCH_2CH_2NHBH_3)_2]$ with THF was modeled in a tetragonal unit cell with space group P*4/n*. In this anionic complex, each $[BH_3NHCH_2CH_2NHBH_3]^{2-}$ anion provides two pairs of electrons from two nitrogen atoms, forming a chelate coordinated with the central Al^{3+} ions. This arrangement contributes to the enhanced stability of the compound $Na[Al(BH_3NHCH_2CH_2NHBH_3)_2]$ compared to its analogs, $Na[Al(NH_2BH_3)_4]$ and $Na[Al(CH_3NHBH_3)_4]$.

The central Al^{3+} ion is tetrahedrally coordinated by four nitrogen atoms (Figure 6.14A), exhibiting a geometry similar to previously reported compounds such as $Na[Al(NH_2BH_3)_4]$[22], $K[Al(NH_2BH_3)_4]$[24], and

$Na[Al(CH_3NHBH_3)_4]$[25]. The Al-N distances were fixed at 1.95 Å, slightly longer than those observed in $Na[Al(NH_2BH_3)_4]$ (1.840(9)-1.929(8) Å) and $K[Al(NH_2BH_3)_4]$ (1.838(9)-1.909(9) Å), but similar to $Na[Al(CH_3NHBH_3)_4]$ (1.922(1)-1.990(1) Å).

The Na atoms exhibit a square pyramidal coordination geometry (Figure 6.14B), with each atom surrounded by four BH_3 groups from four different $[Al(BH_3NHCH_2CH_2NHBH_3)_2]^-$ anions, as well as one oxygen atom from the THF solvent molecule. This arrangement differs from the usual octahedral environments observed in compounds like $Na[Al(NH_2BH_3)_4]$[22], $Na_2[Mg(NH_2BH_3)_4]$[16], and $Na_2[Ca(NH_2BH_3)_4]$[19], as well as the triangular bipyramidal environment in $Na[Al(CH_3NHBH_3)_4]$[25].

The THF exhibits disorder around the 4-fold symmetry axis, which could be better resolved by studying a single crystal. Similar to the reported $Na[Al(NH_2BH_3)_4]$ and $Na[Al(CH_3NHBH_3)_4]$, all $[BH_3NHCH_2CH_2NHBH_3]^{2-}$ units display a bridging coordination mode, connecting Al^{3+} and Na^+ ions, resulting in the formation of a three-dimensional polymeric structure (Figure 6.14C,D, and E).

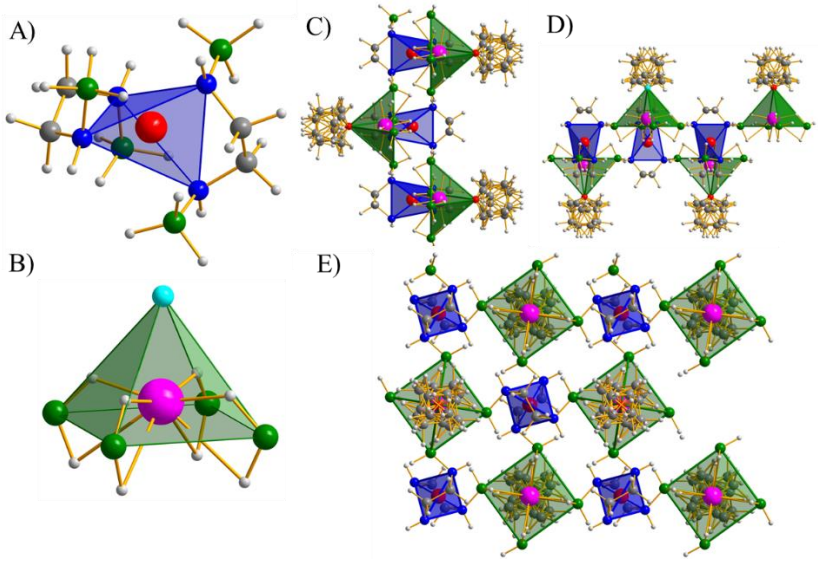

Figure 6.14 The coordinated geometry of Al^{3+} (A), Na^+ (B), crystal packing along with a (C), b (D) and c (E) axis (Color code: N = blue, B = green, C = grey, H = light grey, O = sky blue, Al = red, and Na = pink)

6.3.2 The IR spectra of M[Al(BH$_3$NHCH$_2$CH$_2$NHBH$_3$)$_2$] (M = Li and Na)

To characterize the structure of Li[Al(BH$_3$NHCH$_2$CH$_2$NHBH$_3$)$_2$] and compare it with Na[Al(BH$_3$NHCH$_2$CH$_2$NHBH$_3$)$_2$], we conducted ATR-IR spectra measurements on LiAlH$_4$, NaAlH$_4$, EDAB, Li[Al(BH$_3$NHCH$_2$CH$_2$NHBH$_3$)$_2$], and Na[Al(BH$_3$NHCH$_2$CH$_2$NHBH$_3$)$_2$]. The IR spectra of Li[Al(BH$_3$NHCH$_2$CH$_2$NHBH$_3$)$_2$] and Na[Al(BH$_3$NHCH$_2$CH$_2$NHBH$_3$)$_2$] exhibit characteristic peaks in comparison to the reactant EDAB, indicating structural differences among these compounds (Figure 6.15).

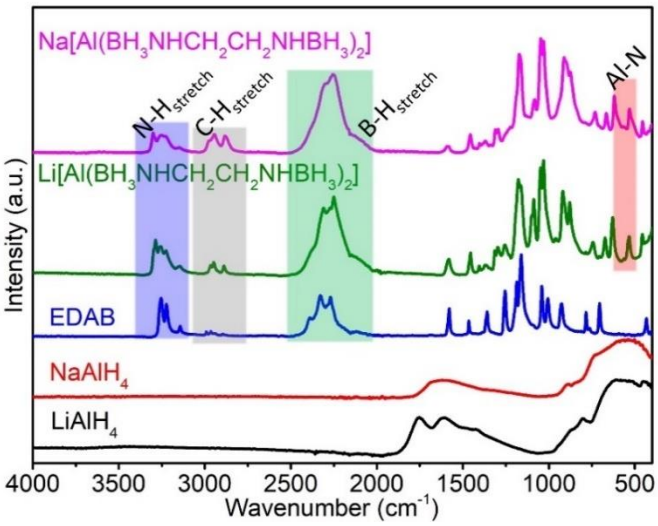

Figure 6.15 The IR spectra of LiAlH$_4$, NaAlH$_4$, EDAB, Li[Al(BH$_3$NHCH$_2$CH$_2$NHBH$_3$)$_2$] and Na[Al(BH$_3$NHCH$_2$CH$_2$NHBH$_3$)$_2$] (stretch bond areas of N-H, C-H and B-H are pointed by blue, gray and green rectangle; Al-N bond is pointed by red rectangle).

The IR spectra show the presence of stretching modes for N-H (3114 – 3346 cm^{-1}), C-H (2838 – 3010 cm^{-1}), and B-H (2033 – 2499 cm^{-1}) in both Li[Al(BH$_3$NHCH$_2$CH$_2$NHBH$_3$)$_2$] and Na[Al(BH$_3$NHCH$_2$CH$_2$NHBH$_3$)$_2$]. There is no significant difference compared to the precursor EDAB. Additionally, new peaks appear in these two new complexes within the Al-N bond region (highlighted by the red rectangle) between 400 and 800 cm^{-1}, similar to other compounds such as Li[Al(NH$_2$)$_4$][30], Na[Al(NH$_2$)$_4$][31, 32], Na[Al(NH$_2$BH$_3$)$_4$][22], and

$Na[Al(CH_3NHBH_3)_4]$[25]. All above suggest that $Li[Al(BH_3NHCH_2CH_2NHBH_3)_2]$ has the similar tetrahedrally coordinated Al-N chelated geometry.

Furthermore, the intensity of the C-H stretching bond in $Na[Al(BH_3NHCH_2CH_2NHBH_3)_2]$ is higher than that in $Li[Al(BH_3NHCH_2CH_2NHBH_3)_2]$ and EDAB (as indicated by the gray area in Figure 6.15). This observation can be attributed to THF molecules coordinating with Na^+ in $Na[Al(BH_3NHCH_2CH_2NHBH_3)_2]$. This finding is consistent with the structural analysis and the results of thermal decomposition, which will be discussed in the following section.

6.4 Thermal decomposition of $M[Al(BH_3NHCH_2CH_2NHBH_3)_2]$ (M = Li, Na)

6.4.1 Stability of $Li[Al(BH_3NHCH_2CH_2NHBH_3)_2]$ in air

Before studying the thermal decomposition of $Li[Al(BH_3NHCH_2CH_2NHBH_3)_2]$, we conducted a PXRD analysis to assess its stability in the air. The results revealed that $Li[Al(BH_3NHCH_2CH_2NHBH_3)_2]$ is highly sensitive to air. After being exposed to air for just a minute, the peaks attributed to the free EDAB noticeably increased. Furthermore, after 15 minutes, the signals corresponding to $Li[Al(BH_3NHCH_2CH_2NHBH_3)_2]$ completely disappeared (Figure 6.16). Only the peaks of EDAB were observed in the PXRD pattern, indicating that the Al-N bond was broken upon contact of $Li[Al(BH_3NHCH_2CH_2NHBH_3)_2]$ with air. This process can be illustrated as shown in Figure 6.17. The OH-groups from water coordinate to Al successfully competing with $[BH_3NHCH_2CH_2NHBH_3]^{2-}$, while the protic H from water balanced the charge of $[BH_3NHCH_2CH_2NHBH_3]^{2-}$, resulting in the reformation of $BH_3NH_2CH_2CH_2NH_2BH_3$.

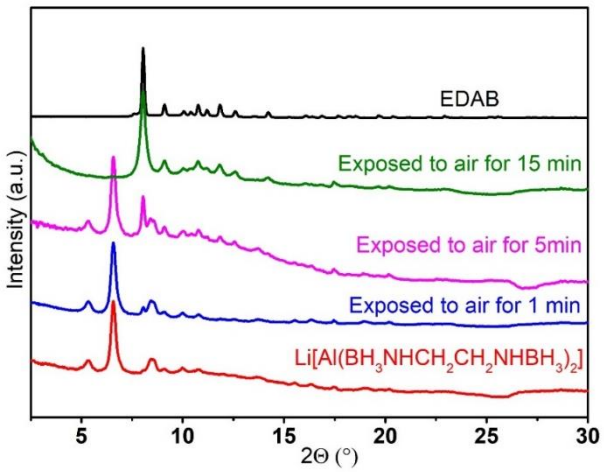

Figure 6.16 PXRD pattern of EDAB, $Li[Al(BH_3NHCH_2CH_2NHBH_3)_2]$, $Li[Al(BH_3NHCH_2CH_2NHBH_3)_2]$ exposed to air for 1, 5 and 15 min (λ = 0.71073 Å).

$$4\ LiAlH_4 + (14+x)\ H_2O + 2\ CO_2 \longrightarrow [LiAl_2(OH)_6]_2CO_3 \cdot x\ H_2O + Li_2CO_3 + 16\ H_2 \uparrow$$ Equation 6.5[33]

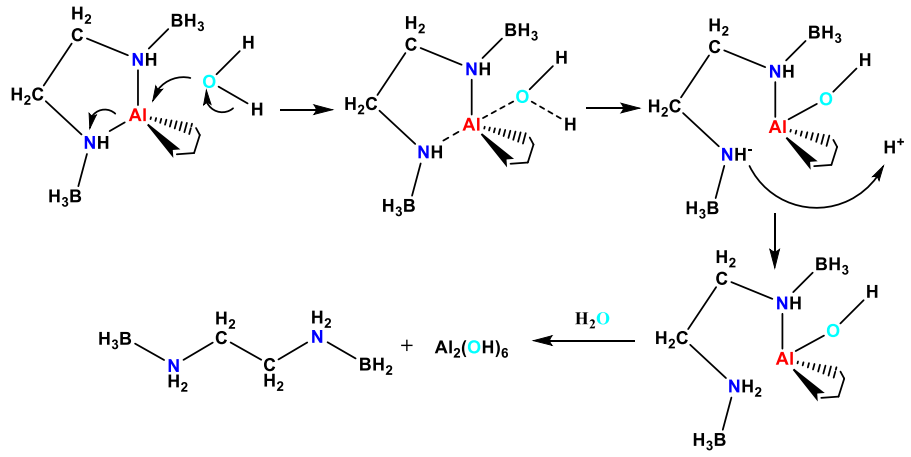

$$4\ Li[Al(BH_3NHCH_2CH_2NHBH_3)_2] + (14+x)\ H_2O + 2\ CO_2 \longrightarrow [LiAl_2(OH)_6]_2CO_3 \cdot x\ H_2O + 8\ BH_3NH_2CH_2CH_2NH_2BH_3\ (EDAB) + Li_2CO_3$$ Equation 6.6

Figure 6.17 Proposed hydrolysis process of $Li[Al(BH_3NHCH_2CH_2NHBH_3)_2]$ exposed to air.

We compared the IR spectrum of $Li[Al(BH_3NHCH_2CH_2NHBH_3)_2]$ exposed to air with that of EDAB, $LiAlH_4$, and $LiAlH_4$ exposed to air (Figure 6.18). It was observed that the products formed when $Li[Al(BH_3NHCH_2CH_2NHBH_3)_2]$ was exposed to air resembled a mixture of EDAB and $LiAlH_4$ exposed to air (highlighted by the sky blue rectangle in Figure 6.18). Therefore, we propose that the reaction between $Li[Al(BH_3NHCH_2CH_2NHBH_3)_2]$ and air moisture follows the Equation 6.6 depicted in Figure 6.17, this proposal is based on the reported Equation 6.5 for $LiAlH_4$ exposed to air. We also examined the behaviour of $Na[Al(NH_2BH_3)_4]$ and $Na[Al(CH_3NHBH_3)_4]$ in air. Similar to $Li[Al(BH_3NHCH_2CH_2NHBH_3)_2]$, the respective reactants NH_3BH_3 and $CH_3NH_2BH_3$ of $Na[Al(NH_2BH_3)_4]$ and $Na[Al(CH_3NHBH_3)_4]$ were re-formed upon exposure to air (S9 in Annex and Figure 4.10 in Chapter 4).

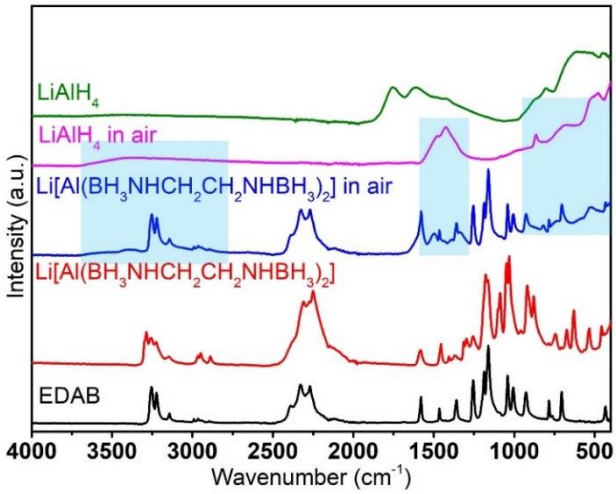

Figure 6.18 IR spectra of EDAB, $Li[Al(BH_3NHCH_2CH_2NHBH_3)_2]$, $Li[Al(BH_3NHCH_2CH_2NHBH_3)_2]$ exposed to air, $LiAlH_4$ exposed to air and $LiAlH_4$ (the new band appeared in spectra of $Li[Al(BH_3NHCH_2CH_2NHBH_3)_2]$ exposed to air and $LiAlH_4$ exposed to air were highlighted with sky blue rectangles.).

6.4.2 Thermal dehydrogenation of $Li[Al(BH_3NHCH_2CH_2NHBH_3)_2]$

The thermal stability of $Li[Al(BH_3NHCH_2CH_2NHBH_3)_2]$ was examined using thermogravimetric analysis (TGA) under an inert argon atmosphere, covering a temperature range from room temperature to 280 °C. The TGA results showed that the thermal decomposition of

$Li[Al(BH_3NHCH_2CH_2NHBH_3)_2]$ started at approximately 104 °C. In contrast to the starting compound EDAB[28], the thermal decomposition of $Li[Al(BH_3NHCH_2CH_2NHBH_3)_2]$ did not exhibit weight oscillation (jet effect) during the process (Figure 6.19A), which is considered a drawback to be addressed in the thermal dehydrogenation of NH_3BH_3 and its derivatives.

Based on PXRD and IR analyses, the solid decomposition products obtained after heating at 280 °C were identified as amorphous phase(s) lacking N-H and B-H bonds, but containing metallic aluminum, which comes from $LiAlH_4$ decomposition (Figure 6.19 B and C). The mass loss during the thermal decomposition of $Li[Al(BH_3NHCH_2CH_2NHBH_3)_2]$ was approximately 6.6 wt.%, which is within the expected value for the release of pure H_2 (7.8 % for theoretical hydrogen content of $Li[Al(BH_3NHCH_2CH_2NHBH_3)_2]$, excluding hydrogen on carbon, Table S.1 in the annex.

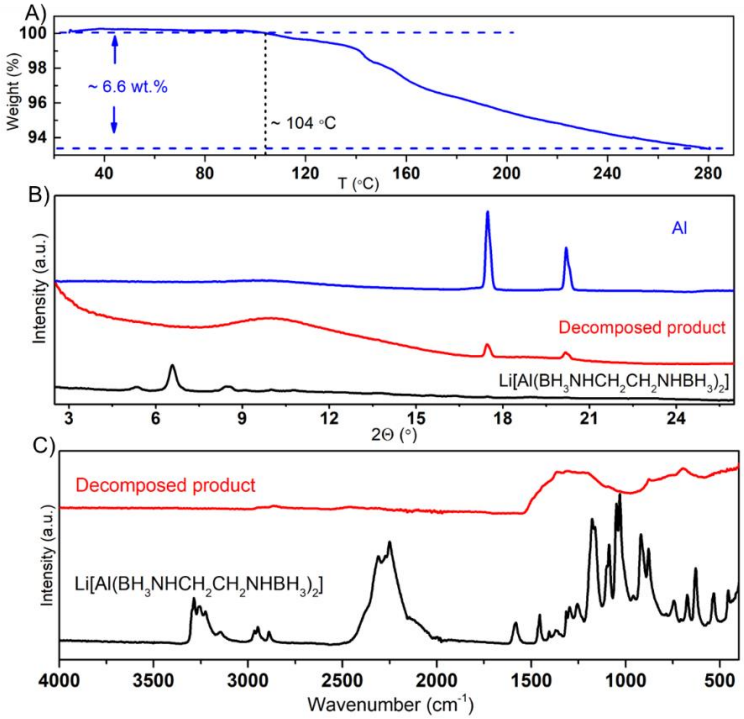

Figure 6.19 Thermogravimetric analysis (TGA) of $Li[Al(BH_3NHCH_2CH_2NHBH_3)_2]$ (A); PXRD pattern of $Li[Al(BH_3NHCH_2CH_2NHBH_3)_2]$, the thermally decomposed product and aluminum (B); ATR-IR spectra of $Li[Al(BH_3NHCH_2CH_2NHBH_3)_2]$ and of the thermally decomposed product (C) (λ = 0.71073 Å).

The purity of the gas released during the thermal dehydrogenation of $Li[Al(BH_3NHCH_2CH_2NHBH_3)_2]$ was analysed using temperature-programmed mass spectrometry (TPMS) in the temperature range from room temperature to 280 °C. The TPMS analysis was performed within a glovebox under argon atmosphere to prevent a contamination by moisture, as $Li[Al(BH_3NHCH_2CH_2NHBH_3)_2]$ is highly sensitive to it. Due to the small size of the crucible, the signals' intensities for the released gases in the mass spectrometry results were not as high as in our other experiments. Nevertheless, the hydrogen signals were visible, despite the challenges associated with detecting hydrogen due to its light weight. No signals corresponding to other gases were observed, confirming that ammonia (NH_3), diborane (B_2H_6), ethylenediamine ($NH_2CH_2CH_2NH_2$), and THF were not released during the decomposition process. Only hydrogen was detected (Figure 6.20).

These findings indicate that $Li[Al(BH_3NHCH_2CH_2NHBH_3)_2]$ releases approximately 6.6 wt.% of pure hydrogen when heated to 280 °C. The successful formation of this novel Al-based amidoborane compound suggests that it effectively suppresses the release of unwanted by-products during thermal hydrogen desorption, surpassing the performance of NH_3BH_3.

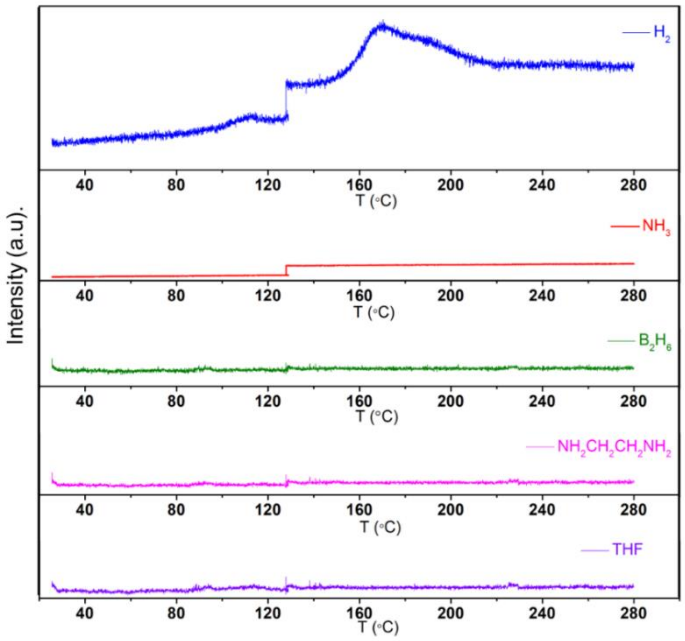

Figure 6.20 Mass spectrometry results for $Li[Al(BH_3NHCH_2CH_2NHBH_3)_2]$.

6.4.3 Stability of $Na[Al(BH_3NHCH_2CH_2NHBH_3)_2]$ in air

The air stability of $Na[Al(BH_3NHCH_2CH_2NHBH_3)_2]$ was investigated based on PXRD analysis and compared to $Li[Al(BH_3NHCH_2CH_2NHBH_3)_2]$ $Na[Al(BH_3NHCH_2CH_2NHBH_3)_2]$ demonstrated higher stability in ambient air. No changes were observed in the PXRD pattern of $Na[Al(BH_3NHCH_2CH_2NHBH_3)_2]$ during the initial 30 minutes of exposure to air. However, after 1 hour, the peaks corresponding to EDAB appeared, and after 2.5 hours of exposure, the PXRD pattern of $Na[Al(BH_3NHCH_2CH_2NHBH_3)_2]$ completely transformed into that of EDAB.

The coordination of THF to Na^+ in $Na[Al(BH_3NHCH_2CH_2NHBH_3)_2]$ may contribute to better binding of $[BH_3NHCH_2CH_2NHBH_3]^{2-}$ to Al^{3+}. This may hinder the interaction of water molecules with both Al and Na, leading to increased stability of $Na[Al(BH_3NHCH_2CH_2NHBH_3)_2]$ over a longer duration in ambient air.

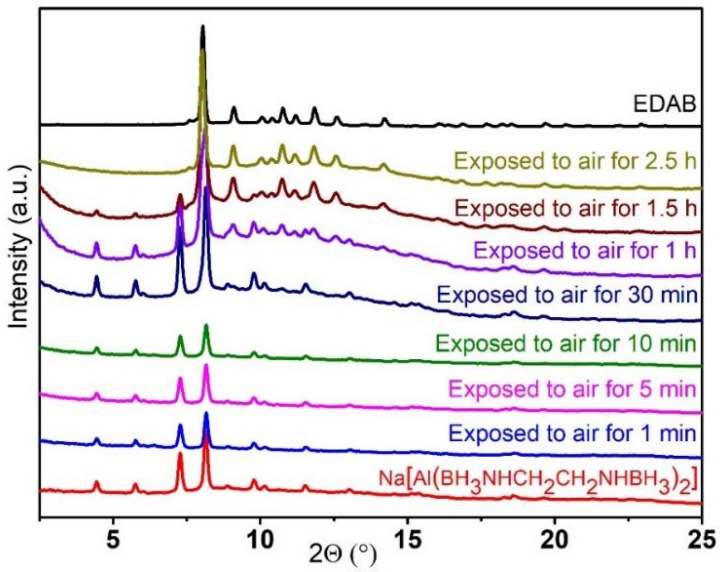

Figure 6.21 The PXRD pattern of $Na[Al(BH_3NHCH_2CH_2NHBH_3)_2]$, $Na[Al(BH_3NHCH_2CH_2NHBH_3)_2]$ exposed to air for different times and the pattern of EDAB (λ = 0.71073 Å).

6.4.4 Thermal dehydrogenation of $Na[Al(BH_3NHCH_2CH_2NHBH_3)_2]$

Due to the good stability of $Na[Al(BH_3NHCH_2CH_2NHBH_3)_2]$ in air, we studied the thermal stability of $Na[Al(BH_3NHCH_2CH_2NHBH_3)_2]$ under an inert nitrogen atmosphere by an instrument installed outside of a glovebox (at room temperature and on heating to 240 °C). The thermal decomposition of $Na[Al(BH_3NHCH_2CH_2NHBH_3)_2]$ was found to occur in a single step, initiated at approximately 55 °C, and exhibiting a continuous weight loss without oscillation (jet effect), in contrast to the behaviour observed in the case of EDAB[28]. Compared to $Li[Al(BH_3NHCH_2CH_2NHBH_3)_2]$, decomposing at 104 °C, $Na[Al(BH_3NHCH_2CH_2NHBH_3)_2]$ started to decompose at a lower temperature (55 °C). This should be caused by the different intermolecular interactions in these two compounds. After heating to 240 °C, the solid decomposition products were identified as the known crystalline $NaBH_4$ along with some unknown crystalline and amorphous phases containing C-H bonds (Figure 6.22 B and C). The formation of BH_4^- during the thermal decomposition is similar to $Na[Al(NH_2BH_3)_4]$[22] and $Na[Al(CH_3NHBH_3)_4]$[25]. The mass loss during the thermal decomposition of $Na[Al(BH_3NHCH_2CH_2NHBH_3)_2]$ from room temperature to 240 °C was ~13.3 wt.%. This value exceeds the hydrogen content of $Na[Al(BH_3NHCH_2CH_2NHBH_3)_2]$, which is 5.4 wt.% (excluding H on carbon). This should be caused by the release of THF coordinated to Na^+ evolving along with hydrogen during the thermal decomposition.

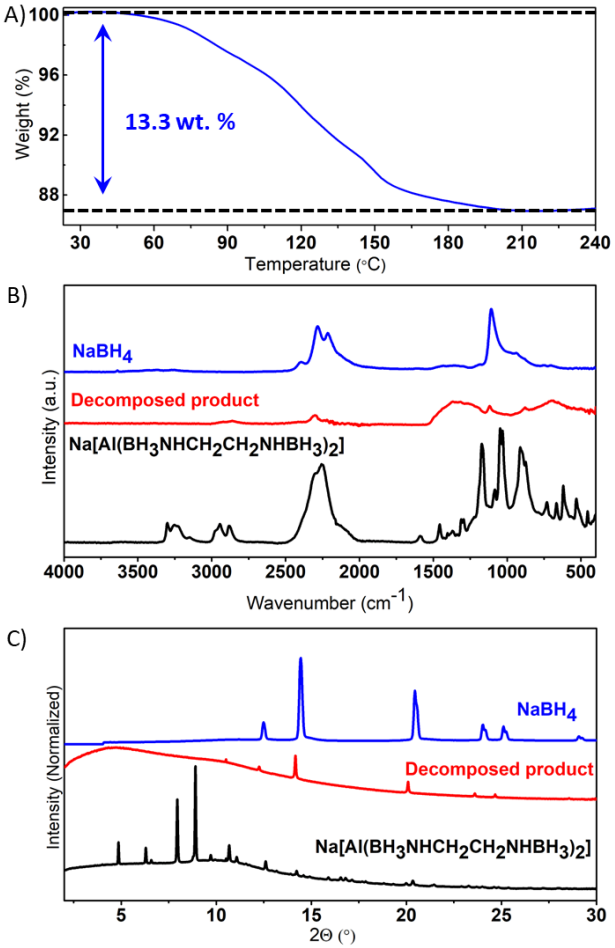

Figure 6.22 Thermogravimetric analysis (TGA) of $Na[Al(BH_3NHCH_2CH_2NHBH_3)_2]$ (A); ATR-IR spectra of $Na[Al(BH_3NHCH_2CH_2NHBH_3)_2]$, thermal decomposed production and $NaBH_4$ (B); XRD pattern of $Na[Al(BH_3NHCH_2CH_2NHBH_3)_2]$, thermally decomposed product and the pattern of $NaBH_4$ (C) (λ = 0.77509 Å).

To better understand the dehydrogenation process of $Na[Al(BH_3NHCH_2CH_2NHBH_3)_2]$, we performed mass spectrometry analysis in the temperature range from 40 °C to 240 °C. The results revealed that hydrogen and THF were released. Notably, we didn't find the signals of ammonia (NH_3), diborane (B_2H_6), or ethylenediamine ($NH_2CH_2CH_2NH_2$) that are usually released along with H_2 during the thermal de-hydrogenation of NH_3BH_3 and of its derivatives (Figure. 6.23). In addition, we found H_2 released

from about 68 °C and THF release started at about 95 °C (Figure 6.23). This is why we cannot remove THF by vacuum at elevated temperatures like 50 °C. Overall, the formation of $Na[Al(BH_3NHCH_2CH_2NHBH_3)_2]$ suppressed the liberation of common by-products such as NH_3, B_2H_6.

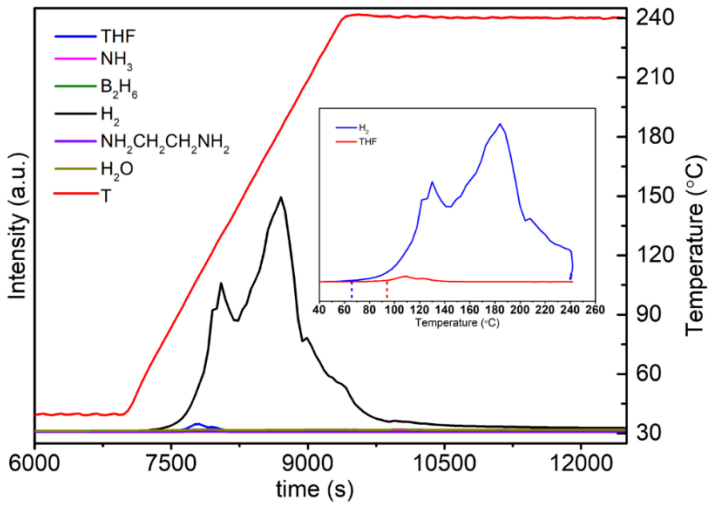

Figure 6.23 Mass spectrometry results for $Na[Al(BH_3NHCH_2CH_2NHBH_3)_2]$.

6.5 Conclusion

We successfully synthesized $Li[Al(BH_3NHCH_2CH_2NHBH_3)_2]$ and $Na[Al(BH_3NHCH_2CH_2NHBH_3)_2]$ using mechanochemical synthesis and a wet chemical approach from 1 equivalent of $MAlH_4$ (M = Li) and 2 equivalents of $BH_3NH_2CH_2CH_2NH_2BH_3$, respectively. In comparison to AB and MeAB, $BH_3NH_2CH_2CH_2NH_2BH_3$ exhibited higher inertness and required more energy input to form an Al-N bond when reacting with $NaAlH_4$. This favors the reaction between the otherwise extremely reactive $LiAlH_4$ and $BH_3NH_2CH_2CH_2NH_2BH_3$ through mechanochemical synthesis and thus avoids the explosive reaction that occurrs between $LiAlH_4$ and NH_3BH_3.

In the structure of $Na[Al(BH_3NHCH_2CH_2NHBH_3)_2]$, the Al^{3+} ion is tetrahedrally coordinated to two $[BH_3NHCH_2CH_2NHBH_3]^{2-}$ anions through nitrogen atoms and forming chelates. The formation of the Al-N bond in $Li[Al(BH_3NHCH_2CH_2NHBH_3)_2]$ and $Na[Al(BH_3NHCH_2CH_2NHBH_3)_2]$ was confirmed through IR spectroscopy.

Thermogravimetric analysis (TGA) and mass spectrometry revealed that $Li[Al(BH_3NHCH_2CH_2NHBH_3)_2]$ releases 6.6 wt.% of pure hydrogen from room temperature to 280 °C. The TGA and mass spectrometry analysis of $Na[Al(BH_3NHCH_2CH_2NHBH_3)_2]$ indicated that the released hydrogen was contaminated with THF. Nevertheless, the formation of $Li[Al(BH_3NHCH_2CH_2NHBH_3)_2]$ and $Na[Al(BH_3NHCH_2CH_2NHBH_3)_2]$ effectively suppressed the release of by-products that typically contaminate hydrogen during the thermal dehydrogenation of NH_3BH_3 and its derivatives, such as NH_3 and B_2H_6.

In this work, it has been confirmed that the substitution on the N-side of AB allows to form stable chelate complexes exhibiting an effective suppression of the release of the common gaseous impurities. Furthermore, these examples provide valuable insights into the structure of chelated coordinated aluminum amidoborane compounds.

6.6 Experimental section

6.6.1 Chemicals

All the samples were obtained from commercially available NaH (95 %), LiH (95 %), $NaAlH_4$ (93%), $LiAlH_4$ (> 98 %), $NaBH_4$ (97%), $NH_2CH_2CH_2NH_2{\cdot}2$ HCl (98 %), and anhydrous THF (⩾ 99.9%), toluene (99.85%), hexane (≥99.9 %), diethyl ether (≥99.5 %), 1,4-dioxane (≥99.5 %), CH_2Cl_2 (99.5 %) and CH_3CN (≥99.9 %), which were purchased from SigmaAldrich Co. Ltd. All the operations were performed in a glovebox with a high-purity argon atmosphere.

6.6.2 Synthesis of EDAB ($BH_3NH_2CH_2CH_2NH_2BH_3$)

See Chapter 5, Experimental section 5.7.2.

6.6.3 Synthesis of Li_3AlH_6

$$LiAlH_4 + 2\ LiH \longrightarrow Li_3AlH_6$$ Equation 6.7

Li_3AlH_6 was synthesized through the mechanochemical reaction between LiH and $LiAlH_4$ following a method described in the literature[34]. To initiate the

reaction, 151.8 mg (4 mmol) of $LiAlH_4$ and 63.6 mg (8 mmol) of LiH were loaded into an 80 mL stainless steel milling vial along with three steel balls (10 mm in diameter, a total mass 12 g). Ball milling was performed using a planetary ball mill (Fritsch Pulverisette 7 Premium line) under an argon atmosphere of one bar, with a rotation speed of 500 rpm for a during of 10 hours. This process yielded a black powder. The obtained PXRD pattern matched the reported results (Figure S19 in annex)

6.6.4 Synthesis of Na_3AlH_6

$$NaAlH_4 + 2\ NaH \longrightarrow Na_3AlH_6$$ Equation 6.8

Na_3AlH_6 was synthesized through the mechanochemical reaction between NaH and $NaAlH_4$ following a similar method to the synthesis of Li_3AlH_6. For the reaction, 303.6 mg $NaAlH_4$ (5.6 mmol) and 229.4 mg NaH (9.6 mmol) with a molar ratio of 1: 1.7 were loaded into a 40 mL stainless steel milling vial along with three steel balls (10 mm in diameter, total mass 12 g). The ball milling process was conducted using a planetary ball mill (Fritsch Pulverisette 7 Premium line) under an argon atmosphere at 1 bar, with a rotation speed of 500 rpm for a during of 10 hours. The PXRD data is presented in the Supporting Information (specifically in Figure S20), which agrees with the reported pattern.

6.6.5 Synthesis of Na_2LiAlH_6

$$LiAlH_4 + 2\ NaH \longrightarrow Na_2LiAlH_6$$ Equation 6.9

Na_2LiAlH_6 was synthesized by means of a mechanochemical reaction between NaH and $LiAlH_4$, employing a similar method as described in literature [35]. In this synthesis, 302.6 mg (8.0 mmol) $LiAlH_4$ and 382.3 mg (16.0 mmol) NaH, with a molar ratio of 1: 2, were loaded into an 80 mL stainless steel milling vial containing three steel balls (15 mm in diameter, total mass 43 g). The ball milling process was carried out using a planetary ball mill (Fritsch Pulverisette 7 Premium line) under an argon atmosphere at 1 bar, with a rotation speed of 500 rpm for a during of 8 hours. The PXRD data is presented

in the Supporting Information (specifically in Figure S21), which is consistent with the reported results.

6.6.6 Synthesis of $Li[Al(BH_3NHCH_2CH_2NHBH_3)_2]$

Sample Li-E: 1 eq. of $LiAlH_4$ (26.9 mg, 0.7 mmol) and 2 eq. of EDAB (124.63 mg, 1.4 mmol) were placed into an 80 mL stainless steel vial and with three 10 mm diameter stainless steel balls and milled in a planetary ball mill (Fritsch Pulverisette 7 Premium line). Evolution of the gas pressure and temperature during the reaction was performed using the Easy GTM detection system accessory (Fritsch). The rotation speed was set to 500 rpm and the ball-to-powder mass ratio was 80:1. The synthesis was performed using 50 milling cycles of 30 min milling interrupted by 15 min cooling breaks, to yield dark gray powder. The product was characterized by means of PXRD (Figure. 6.1). The reproducibility of this synthesis methods has been confirmed.

Table 6.4. The start and the end of pressure and temperature, and the amount of released gas during synthesis of sample **Li-E** using Easy-GTM system.

P_{start} (bar)	T_{start} (°C)	P_{end} (bar)	T_{end} (°C)	Δn_{gas}(mmol)	$\Delta n_{gas}/n_{LiAlH4}$
1.0	23.6	1.7	23.1	2.4	3.3

Other samples were synthesized through a similar method of sample **Li-E** with different parameters (milling speed, time, number of cycles and ball to power mass ratio) as listed in Table 6.1.

6.6.7 Synthesis of $Na[Al(BH_3NHCH_2CH_2NHBH_3)_2]$

Powdered $NaAlH_4$ (81 mg, 1.5 mmol), EDAB (263.3 mg, 3.0 mmol), and anhydrous THF (30 mL) were added to a 100 mL, one-neck round bottom Schlenk flask. The obtained suspension was then vigorously stirred at room temperature under an argon atmosphere for 24 (sample **Na-A**), 48 (sample **Na-B**) and 72 hours (sample **Na-C**), respectively. Then the solvent was removed by vacuum. And the white solid was dried under vacuum for another 5 hours to eliminate residual solvents. The product was characterized by means of PXRD (Figure. 6.3).

Samples Na-D, **E**, **F**, **G**, **H**, and **I**: the procedure similar as that of Sample **Na-B**. Powdered $NaAlH_4$ (81 mg, 1.5 mmol), EDAB (263.3 mg, 3.0 mmol), and anhydrous Toluene, Hexane, Diethyl ether, 1,4-dioxane, CH_2Cl_2, or CH_3CN (30 mL) were added to a 100 mL, one-neck round bottom Schlenk flask. The obtained suspension was then vigorously stirred at room temperature under an argon atmosphere for 48 hours. Then the solvent was removed by vacuum. And the white solid was dried under vacuum for another 5 hours to eliminate residual solvents. The products were characterized by means of PXRD (Figure. 6.5-6.6).

Sample Na-J: the procedure similar to that of sample **Na-B**. Powdered $NaAlH_4$ (81 mg, 1.5 mmol), EDAB (263.3 mg, 3.0 mmol), anhydrous Toluene (25 mL), and anhydrous THF (5 mL) were added to a 100mL, one-neck round bottom Schlenk flask. The obtained suspension was then vigorously stirred at room temperature under an argon atmosphere for 48 hours. Then the solvent was removed by vacuum. And the white solid was dried under vacuum for another 5 hours to eliminate residual solvents. The product was characterized by means of PXRD (Figure. 6.7).

Samples Na-K, L, M, and N: 1 eq. of $NaAlH_4$ and 2 eq. of EDAB were placed into an 80 mL stainless steel vial and with three 10 mm diameter stainless steel balls and milled in a planetary ball mill (Fritsch Pulverisette 7 Premium line). Evolution of the gas pressure and temperature during the reaction was performed using the Easy GTM detection system accessory (Fritsch). The milling parameters were set as shown in Table 6.3. And the product was characterized by means of PXRD (Figure. 6.9).

6.6.8 Synthesis of $Li_3[Al(BH_3NHCH_2CH_2NHBH_3)_3]$

Sample Li3-A: 1 eq. of Li_3AlH_6 (16.2 mg, 0.3 mmol) and 3 eq. of EDAB (79 mg, 0.9 mmol) were placed into an 80 mL stainless steel vial and with three 10 mm diameter stainless steel balls and milled in a planetary ball mill (Fritsch Pulverisette 7 Premium line). Evolution of the gas pressure and temperature during the reaction was performed using the Easy GTM detection system accessory (Fritsch). The rotation speed was set to 500 rpm and the ball-to-powder mass ratio was 120:1. The synthesis was performed using 20 milling cycles of 30 min milling interrupted by 30 min cooling breaks.

Samples Li3-B and Li3-C: 1 eq. of Li_3AlH_6 (16.2 mg, 0.3 mmol), 3 eq. of EDAB (79 mg, 0.9 mmol) and anhydrous THF (15 mL) were added to a 50 mL, one-neck round bottom Schlenk flask. The obtained suspension was then vigorously stirred at room temperature under an argon atmosphere for 48 hours (sample **Li3-B**), at 60 ˚C under an argon atmosphere for 24 hours (sample **Li3-C**), respectively. Then the solvent was removed by vacuum. And the white solid was dried under vacuum for another 5 hours to eliminate residual solvents. The product was characterized by means of PXRD (Figure 6.10).

Sample Li3-D: 1 eq. of Li_3AlH_6 (16.2 mg, 0.3 mmol), 3 eq. of EDAB (79 mg, 0.9 mmol) and anhydrous toluene (15 mL) were added to a 50 mL, one-neck round bottom Schlenk flask. The obtained suspension was then vigorously stirred at 90 ˚C under an argon atmosphere for 24 hours (sample **Li3-D**). Then the solvent was removed by vacuum. And the white solid was dried under vacuum for another 5 hours to eliminate residual solvents. The product was characterized by means of PXRD (Figure 6.10).

Heat-treated EDAB: EDAB (79 mg, 0.9 mmol) and anhydrous toluene (15 mL) were added to a 50 mL, one-neck round bottom Schlenk flask. Then vigorously stirred at 90 ˚C under an argon atmosphere for 24 hours. Then the solvent was removed by vacuum. And the white solid was dried under vacuum for another 5 hours to eliminate residual solvents. The product was characterized by means of PXRD (Figure 6.10).

6.6.9 Synthesis of $Na_3[Al(BH_3NHCH_2CH_2NHBH_3)_3]$

Sample Na3-A: 1 eq. of Na_3AlH_6 (30.6 mg, 0.3 mmol) and 3 eq. of EDAB (79 mg, 0.9 mmol) were placed into an 80 mL stainless steel vial and with three 10 mm diameter stainless steel balls and milled in a planetary ball mill (Fritsch Pulverisette 7 Premium line). Evolution of the gas pressure and temperature during the reaction was performed using the Easy GTM detection system accessory (Fritsch). The rotation speed was set to 600 rpm and the ball-to-powder mass ratio was 100:1. The synthesis was performed using 25 milling cycles of 30 min milling interrupted by 30 min cooling breaks.

Samples Na3-B and Na3-C: 1 eq. of Na_3AlH_6 (30.6 mg, 0.3 mmol), 3 eq. of EDAB (79 mg, 0.9 mmol) and anhydrous THF (15 mL) were added to a 50 mL, one-neck round bottom Schlenk flask. The obtained suspension was then

vigorously stirred at room temperature under an argon atmosphere for 48 hours (sample **Na3-B**), or at 60 ˚C under an argon atmosphere for 48 hours (sample **Na3-C**), respectively. Then the solvent was removed by vacuum. And the white solid was dried under vacuum for another 5 hours to eliminate residual solvents. The product was characterized by means of PXRD (Figure 6.12).

Sample Na3-D: 1 eq. of Na_3AlH_6 (30.6 mg, 0.3 mmol), 3 eq. of EDAB (79 mg, 0.9 mmol) and anhydrous Toluene (15 mL) were added to a 50 mL, one-neck round bottom Schlenk flask. The obtained suspension was then vigorously stirred at 90 ˚C under an argon atmosphere for 24 hours (sample **Na3-D**). Then the solvent was removed by vacuum. And the white solid was dried under vacuum for another 5 hours to eliminate residual solvents. The product was characterized by means of PXRD (Figure 6.12).

6.6.10 Synthesis of $Na_2Li[Al(BH_3NHCH_2CH_2NHBH_3)_3]$

Sample Na2Li-A: 1 eq. of Na_2LiAlH_6 (37.0 mg, 0.4 mmol) and 3 eq. of EDAB (113 mg, 1.3 mmol) were placed into an 80 mL stainless steel vial and with three 10 mm diameter stainless steel balls and milled in a planetary ball mill (Fritsch Pulverisette 7 Premium line). Evolution of the gas pressure and temperature during the reaction was performed using the Easy GTM detection system accessory (Fritsch). The rotation speed was set to 500 rpm and the ball-to-powder mass ratio was 80:1. The synthesis was performed using 20 milling cycles of 30 min milling interrupted by 15 min cooling breaks.

Sample Na2Li-B: 1 eq. of Na_2LiAlH_6 (37.0 mg, 0.4 mmol), 3 eq. of EDAB (113 mg, 1.3 mmol) and anhydrous THF (15 mL) were added to a 50 mL, one-neck round bottom Schlenk flask. The obtained suspension was then vigorously stirred at room temperature under an argon atmosphere for 24 hours (sample **Na2Li-B**). Then the solvent was removed by vacuum. And the white solid was dried under vacuum for another 5 hours to eliminate residual solvents. The product was characterized by means of PXRD (Figure 6.13).

6.6.11 Powder X-ray diffraction

Samples were carefully filled into 0.7 mm thin-walled glass capillaries (Hilgenberg GmbH) within an argon-filled glovebox. To prevent contact with air, the capillaries were sealed with grease before being taken out of the

glovebox. The sealed capillaries were then cut and promptly placed into wax on a goniometer head, ensuring that no air entered the capillary. Diffraction data were immediately collected using a MAR345 image-plate detector equipped with an Incoatec Mo (λ = 0.71073 Å) Microfocus (IμS 2.0) X-ray source operating at 50 kV and 1000 μA. The resulting two-dimensional images were azimuthally integrated using the Fit2D software, with LaB_6 serving as a calibrant.

Synchrotron PXRD patterns were collected with a PILATUS@SNBL diffractometer (SNBL, ESRF, Grenoble, France) equipped with a Dectris PILATUS 2M single-photon counting pixel area detector (λ = 0.77509 Å). Powder patterns were obtained by using raw data processed by the SNBL Toolbox software using data for LaB_6 standard.

6.6.12 Crystal structure determination:

The synchrotron PXRD data for $Na[Al(BH_3NHCH_2CH_2NHBH_3)_2]$ was indexed in tetragonal unit cells and its structure was solved by global optimization using FOX software.[36] The anions were modelled by conformationally-free z-matrices restraining bond distances and angles. Rietveld refinements were done in Fullprof,[37] treating amidoboranes as separate rigid bodies within the complex anion and refining Na and Al as free atoms. The symmetry was confirmed with ADDSYM routine in the program PLATON.[38]

6.6.13 Fourier transform infrared spectroscopy (FTIR)

Attenuated total reflectance (ATR)-IR spectra were recorded using a Bruker Alpha spectrometer. The spectrometer was equipped with a Platinum ATR sample holder, which featured a diamond crystal for single bounce measurements. The entire experimental setup was located within an argon-filled glovebox to maintain an inert atmosphere during the measurements.

6.6.14 Thermogravimetric analysis (TGA)

TGA measurements for Sample $Li[Al(BH_3NHCH_2CH_2NHBH_3)_2]$ was conducted using a Netzsch STA 449 F3 TGA/DSC. The TGA/DSC was equipped with a stainless-steel oven and located within an argon-filled

glovebox to ensure an inert atmosphere during the measurements. The sample was loaded into Al_2O_3 crucibles and subjected to a heating rate of 5 K/min under an argon flow of 100 mL/min.

TGA measurements for Sample $Na[Al(BH_3NHCH_2CH_2NHBH_3)_2]$ was conducted using a Mettler Toledo TGA/SDTA 851e instrument. The sample was placed in Al_2O_3 crucibles and subjected to a heating rate of 5 K/min under a Nitrogen flow of 100 mL/min.

6.6.15 Mass spectrometry

Mass spectrometry analysis of $Li[Al(BH_3NHCH_2CH_2NHBH_3)_2]$ with the use of a Hiden Analytical HPR-20 QMS sampling system, which is installed in a glovebox. The samples were loaded into an Al_2O_3 crucible and heated from room temperature to 300 °C (5 K/min) in an argon flow of 100 mL/min. Gas evolution was monitored by recording the highest intensity peak for each gas, i.e. m/z of 2, 17, 26, 30, and 42 for H_2, NH_3, H_2O, B_2H_6, N_2, $NH_2CH_2CH_2NH_2$, THF respectively.

Mass spectrometry measurements for $Na[Al(BH_3NHCH_2CH_2NHBH_3)_2]$ were performed using a Hiden Catlab reactor combined with a Quantitative Gas Analyser (QGA) Hidden quadrupole mass spectrometer, which is installed outside of the glovebox. Before the experiment, samples were loaded into a quartz tube in between two layers of glass cotton under the protective atmosphere of an argon-filled glovebox. The two extremities of the quartz tube were sealed with Parafilm before removed from the glovebox. The quartz tube was then installed in the sample holder outside the glovebox after quickly removing the Parafilm and the argon flow (40 mL/min) was switched on immediately to prevent contact of the sample with air. Samples were heated to 40 °C and kept isothermally for ~ 2 h to stabilize the temperature. Heating was then performed at a rate of 5 °C/min up to 240 °C corresponding to $Na[Al(BH_3NHCH_2CH_2NHBH_3)_2]$, followed by a 1 h isotherm. Gas evolution was monitored by recording the highest intensity peak for each gas, i.e. m/z of 2, 17, 18, 26, 28, 30, and 42 for H_2, NH_3, H_2O, B_2H_6, N_2, $NH_2CH_2CH_2NH_2$, THF respectively. Monitored H_2O and N_2 to check if sample contacted air or not.

References

1. Hamilton, C. W.; Baker, R. T.; Staubitz, A.; Manners, I., B–N Compounds for Chemical Hydrogen Storage. *Chemical Society Reviews* **2009**, *38*, 279-293.

2. Huang, Z.; Autrey, T., Boron–Nitrogen–Hydrogen (B-N-H) Compounds: Recent Developments in Hydrogen Storage, Applications in Hydrogenation and Catalysis, and New Syntheses. *Energy & Environmental Science* **2012**, *5*, 9257-9268.

3. Wolf, G.; Baumann, J.; Baitalow, F.; Hoffmann, F. P., Calorimetric Process Monitoring of Thermal Decomposition of B–N–H Compounds. *Thermochimica Acta* **2000**, *343*, 19-25.

4. Baitalow, F.; Baumann, J.; Wolf, G.; Jaenicke-Rößler, K.; Leitner, G., Thermal Decomposition of B–N–H Compounds Investigated by Using Combined Thermoanalytical Methods. *Thermochimica Acta* **2002**, *391*, 159-168.

5. Xiong, Z., et al., High-Capacity Hydrogen Storage in Lithium and Sodium Amidoboranes. *Nature Materials* **2007**, *7*, 138.

6. Diyabalanage, H. V. K., et al., Potassium(I) Amidotrihydroborate: Structure and Hydrogen Release. *Journal of the American Chemical Society* **2010**, *132*, 11836-11837.

7. Wu, C.; Wu, G.; Xiong, Z.; Han, X.; Chu, H.; He, T.; Chen, P., $LiNH_2BH_3{\cdot}NH_3BH_3$: Structure and Hydrogen Storage Properties. *Chemistry of Materials* **2010**, *22*, 3-5.

8. Owarzany, R.; Jaroń, T.; Leszczyński, P. J.; Fijalkowski, K. J.; Grochala, W., Amidoboranes of Rubidium and Caesium: The Last Missing Members of the Alkali Metal Amidoborane Family. *Dalton Transactions* **2017**, *46*, 16315-16320.

9. Diyabalanage, H. V. K.; Shrestha, R. P.; Semelsberger, T. A.; Scott, B. L.; Bowden, M. E.; Davis, B. L.; Burrell, A. K., Calcium Amidotrihydroborate: A Hydrogen Storage Material. *Angewandte Chemie International Edition* **2007**, *46*, 8995-8997.

10. Zhang, Q.; Tang, C.; Fang, C.; Fang, F.; Sun, D.; Ouyang, L.; Zhu, M., Synthesis, Crystal Structure, and Thermal Decomposition of Strontium Amidoborane. *The Journal of Physical Chemistry C* **2010**, *114*, 1709-1714.

11. Shcherbina, N. A.; Kazakov, I. V.; Timoshkin, A. Y., Synthesis and Characterization of Barium Amidoborane. *Russian Journal of General Chemistry* **2017**, *87*, 2875-2877.

12. Chua, Y. S.; Wu, G.; Xiong, Z.; Karkamkar, A.; Guo, J.; Jian, M.; Wong, M. W.; Autrey, T.; Chen, P., Synthesis, Structure and Dehydrogenation of Magnesium Amidoborane Monoammoniate. *Chemical Communications* **2010**, *46*, 5752-5754.

13. Luo, J.; Kang, X.; Wang, P., Synthesis, Formation Mechanism, and Dehydrogenation Properties of the Long-Sought $Mg(NH_2BH_3)_2$ Compound. *Energy & Environmental Science* **2013**, *6*, 1018-1025.

14. Fijalkowski, K. J.; Genova, R. V.; Filinchuk, Y.; Budzianowski, A.; Derzsi, M.; Jaroń, T.; Leszczyński, P. J.; Grochala, W., $Na[Li(NH_2BH_3)_2]$ – the First Mixed-Cation Amidoborane with Unusual Crystal Structure. *Dalton Transactions* **2011**, *40*, 4407-4413.

15. Kang, X.; Luo, J.; Zhang, Q.; Wang, P., Combined Formation and Decomposition of Dual-Metal Amidoborane $NaMg(NH_2BH_3)_3$ for High-Performance Hydrogen Storage. *Dalton Transactions* **2011**, *40*, 3799-3801.

16. Wu, H.; Zhou, W.; Pinkerton, F. E.; Meyer, M. S.; Yao, Q.; Gadipelli, S.; Udovic, T. J.; Yildirim, T.; Rush, J. J., Sodium Magnesium Amidoborane: The First Mixed-Metal Amidoborane. *Chemical Communications* **2011**, *47*, 4102-4104.

17. Chua, Y. S.; Li, W.; Wu, G.; Xiong, Z.; Chen, P., From Exothermic to Endothermic Dehydrogenation – Interaction of Monoammoniate of Magnesium Amidoborane and Metal Hydrides. *Chemistry of Materials* **2012**, *24*, 3574-3581.

18. Biliškov, N.; Borgschulte, A.; Užarević, K.; Halasz, I.; Lukin, S.; Milošević, S.; Milanović, I.; Novaković, J. G., In-Situ and Real-Time Monitoring of Mechanochemical Preparation of $Li_2Mg(NH_2BH_3)_4$ and $Na_2Mg(NH_2BH_3)_4$ and Their Thermal Dehydrogenation. *Chemistry – A European Journal* **2017**, *23*, 16274-16282.

19. Milanović, I.; Biliškov, N.; Užarević, K.; Lukin, S.; Etter, M.; Halasz, I., Mechanochemical Synthesis and Thermal Dehydrogenation of Novel Calcium-Containing Bimetallic Amidoboranes. *ACS Sustainable Chemistry & Engineering* **2021**, *9*, 2089-2099.

20. Hawthorne, M. F.; Jalisatgi, S. S.; Safronov, A. V.; Lee, H. B.; Wu, J. *Chemical Hydrogen Storage Using Polyhedral Borane Anions and Aluminum-Ammonia-Borane Complexes*; United States, 2010-10-01, 2010.
21. Xia, G.; Tan, Y.; Chen, X.; Guo, Z.; Liu, H.; Yu, X., Mixed-Metal (Li, Al) Amidoborane: Synthesis and Enhanced Hydrogen Storage Properties. *Journal of Materials Chemistry A* **2013**, *1*, 1810-1820.
22. Dovgaliuk, I.; Jepsen, L. H.; Safin, D. A.; Łodziana, Z.; Dyadkin, V.; Jensen, T. R.; Devillers, M.; Filinchuk, Y., A Composite of Complex and Chemical Hydrides Yields the First Al-Based Amidoborane with Improved Hydrogen Storage Properties. *Chemistry – A European Journal* **2015**, *21*, 14562-14570.
23. Yang, J.; Beaumont, P. R.; Humphries, T. D.; Jensen, C. M.; Li, X., Efficient Synthesis of an Aluminum Amidoborane Ammoniate. *Energies* **2015**, *8*.
24. Møller, K. T.; Jørgensen, M.; Andreasen, J. G.; Skibsted, J.; Łodziana, Z.; Filinchuk, Y.; Jensen, T. R., Synthesis and Thermal Decomposition of Potassium Tetraamidoboranealuminate, $K[Al(NH_2BH_3)_4]$. *International Journal of Hydrogen Energy* **2018**, *43*, 311-321.
25. Zhang, T.; Steenhaut, T.; Li, X.; Devred, F.; Devillers, M.; Filinchuk, Y., Aluminum Methylamidoborane Complexes: Mechanochemical Synthesis, Structure, Stability, and Reactive Hydride Composites. *Sustainable Energy & Fuels* **2023**, *7*, 1119-1126.
26. Bowden, M. E.; Brown, I. W. M.; Gainsford, G. J.; Wong, H., Structure and Thermal Decomposition of Methylamine Borane. *Inorganica Chimica Acta* **2008**, *361*, 2147-2153.
27. Staubitz, A.; Robertson, A. P. M.; Manners, I., Ammonia-Borane and Related Compounds as Dihydrogen Sources. *Chemical Reviews* **2010**, *110*, 4079-4124.
28. Leardini, F.; Valero-Pedraza, M. J.; Perez-Mayoral, E.; Cantelli, R.; Bañares, M. A., Thermolytic Decomposition of Ethane 1,2-Diamineborane Investigated by Thermoanalytical Methods and in Situ Vibrational Spectroscopy. *The Journal of Physical Chemistry C* **2014**, *118*, 17221-17230.
29. Nakagawa, Y.; Shinzato, K.; Nakagawa, T.; Nakajima, K.; Isobe, S.; Goshome, K.; Miyaoka, H.; Ichikawa, T., Synthesis, Structural

Characterization, and Hydrogen Desorption Properties of $Na[Al(NH_2BH_3)_4]$. *International Journal of Hydrogen Energy* **2017**, *42*, 6173-6180.

30. Jacobs, H.; Jänichen, K.; Hadenfeldt, C.; Juza, R., Lithiumaluminiumamid, $LiAl(NH_2)_4$, Darstellung, Röntgenographische Untersuchung, Infrarotspektrum Und Thermische Zersetzung. *Zeitschrift für anorganische und allgemeine Chemie* **1985**, *531*, 125-139.

31. Lutz, H. D.; Lange, N.; Jacobs, H.; Nöcker, B., Gitterschwingungsspektren. Lxxi. Wasserstoffbrückenbindungen Und Synergetischer Effekt in Kristallinen Amiden Am Beispiel Von $NaAl(NH_2)_4$. *Zeitschrift für anorganische und allgemeine Chemie* **1992**, *613*, 83-87.

32. Jacobs, H.; Nöcker, B., Neubestimmung Von Struktur Und Eigenschaften Isotyper Natriumtetraamidometallate Des Aluminiums Und Galliums. *Zeitschrift für anorganische und allgemeine Chemie* **1993**, *619*, 381-386.

33. Ashton, E.; Oakley, W. C.; Brack, P.; Dann, S. E., Evaluation of the Vapor Hydrolysis of Lithium Aluminum Hydride for Mobile Fuel Cell Applications. *ACS Applied Energy Materials* **2022**, *5*, 8336-8345.

34. Liu, S.-S.; Zhang, Y.; Sun, L.-X.; Zhang, J.; Zhao, J.-N.; Xu, F.; Huang, F.-L., The Dehydrogenation Performance and Reaction Mechanisms of Li_3AlH_6 with TiF_3 Additive. *International Journal of Hydrogen Energy* **2010**, *35*, 4554-4561.

35. Wang, F.; Liu, Y.; Gao, M.; Luo, K.; Pan, H.; Wang, Q., Formation Reactions and the Thermodynamics and Kinetics of Dehydrogenation Reaction of Mixed Alanate Na_2LiAlH_6. *The Journal of Physical Chemistry C* **2009**, *113*, 7978-7984.

36. Favre-Nicolin, V.; Cerny, R., Fox, `Free Objects for Crystallography': A Modular Approach to Ab Initio Structure Determination from Powder Diffraction. *Journal of Applied Crystallography* **2002**, *35*, 734-743.

37. Rodríguez-Carvajal, J., Recent Advances in Magnetic Structure Determination by Neutron Powder Diffraction. *Physica B: Condensed Matter* **1993**, *192*, 55-69.

38. Spek, A., Single-Crystal Structure Validation with the Program Platon. *Journal of Applied Crystallography* **2003**, *36*, 7-13.

Chapter 7

Attempts to synthesize $M_3[Al(NH_2BH_3)_6]$

Abstract

Six-coordinated Al-based amidoborane compounds hold significant potential in the fields of hydrogen storage and the development of Al-based amidoborane complexes. In this chapter, we present our exploration into the modification and synthesis of known and new six-coordinated Al-based amidoborane compounds. Owing to the big size of the $[Al(NH_2BH_3)_6]^{3-}$ anion, the larger Na cations or mixed cation Li/Na mixtures can match it. The smaller Li matches the slightly smaller anion $[AlH_2(NH_2BH_3)_4]^{3-}$. Based on the PXRD and IR analysis, the synthesis conditions for samples Na3Al-04, Na3Al-13 and Na2LiAl-01 (see the text) can be served as the reference for future synthesis of such complexes.

7.1 Introduction

Metal amidoboranes[1, 2] show improved hydrogen storage properties than the pristine NH_3BH_3 in the temperature or /and the purity of released H_2[3-5]. The multi-metallic amidoboranes make it more diversified to synthesize new amidoborane complexes compared with the mono-metallic amidoboranes[6-9]. These multi-metallic amidoborane complexes can be categorized into various groups based on the central metal, which acts as a stronger Lewis acid. These groups include Li-based[6], Mg-based[7, 8, 10, 11], Ca-based[12], and Al-based[13-18] multi-metallic amidoborane complexes.

Al-based amidoborane complexes attracted our attention due to their high polarizing power, low weight, and high natural abundance. What's more, Al^{3+} is capable of coordinating the initial B- and N-based complex hydrides and their dehydrogenation products, thus serving as a template (or a matrix) for potentially reversible dehydrogenation[19]. Moreover, Al^{3+} functions as a stronger Lewis acid compared to Li^+, Mg^{2+}, and Ca^{2+}, thereby facilitating the formation of homoleptic coordinate environments for the central metals and the counterion metals with $NH_{(2)}$ groups and BH_3 groups, respectively. For instance, in all of the reported Al-Based amidoborane compounds ($Na[Al(NH_2BH_3)_4]$, $K[Al(NH_2BH_3)_4]$ and $Na[Al(CH_3NHBH_3)_4]$), Al^{3+} homoleptic coordinated with four N of four anion $NH_2BH_3^-$ and Na^+ interacted with $H^{\delta-}$ of BH_3 groups. This allows us to predict the potential structure of the new and unknown multi-metallic amidoborane complexes. In contrast, in $Li_2[Ca(NH_2BH_3)_4]$, Ca^{2+} demonstrates mixed coordination by two N atoms from two anion $NH_2BH_3^-$ ions and $H^{\delta-}$ from four BH_3 groups, while Li^+ exhibits mixed coordination with $H^{\delta-}$ from two BH_3 groups due to the similarity in Lewis acidity between Li^+ and Ca^{2+}. Notably, $Na[Al(NH_2BH_3)_4]$ shows promising hydrogen storage properties especially the high purity of released hydrogen and high gravimetric density, which encourage us to pay more attention to studying the new Al-based amidoborane complexes and deeply understand the relationship between the hydrogen storage properties and structure.

Previous reports have predominantly concentrated on the synthesis, properties, as well as structure of four-coordinated Al-based amidoborane compounds, like $Li[Al(NH_2BH_3)_4]$ and $K[Al(NH_2BH_3)_4]$. However, there has been limited research on the synthesis and properties of six-coordinated Al-

based amidoborane compounds, particularly with regard to their structure. Consequently, the primary focus of this chapter is on the attempt to synthesize hexacoordinated Al-based amidoborane complexes.

Existing investigations have identified two reported hexacoordinated Al-based amidoborane complexes, namely $Li[AlH_2(NH_2BH_3)_4]$[14] and $[Al(NH_3)_6][Al(NH_2BH_3)_6]$[20]. These complexes have been characterized based on NMR, IR, and PXRD patterns; however, detailed information regarding their crystal structure is lacking. In order to elucidate the structure of six-coordinated Al-based amidoboranes, it is imperative to synthesize new and distinct Al-based amidoborane complexes. To ensure the high hydrogen content and minimize the influence of other molecules like NH_3, we have specifically focused on synthesizing simple light metals (Na^+ and Li^+) Al-based amidoborane complexes. The analysis of the obtained samples primarily involved PXRD and IR techniques. Although we didn't get the pure desired product, the analyzed results and different methods are important to make the synthesis of the six-coordinated Al-based amidoboranes successful in the future.

7.2 Exploring the synthesis of $Li_3[Al(NH_2BH_3)_6]$

To the best of our knowledge, there have been no reports regarding the successful synthesis of $Li_3[Al(NH_2BH_3)_6]$. In 2013, Guanglin and co-workers investigated the hydrogen performance of composites containing Li_3AlH_6-4 NH_3BH_3, Li_3AlH_6-5NH_3BH_3 and Li_3AlH_6-6NH_3BH_3. The post-milled Li_3AlH_6-4 NH_3BH_3 obtained after milling was tentatively identified as $Li_3[AlH_2(NH_2BH_3)_4]$ based on PXRD, ^{11}B NMR, and IR analyses. However, they encountered difficulties in indexing the structure of $Li_3[AlH_2(NH_2BH_3)_4]$ due to sample impurities.

In our work, we made modifications to the synthesis process (as outlined in Table 7.1) of $Li_3[AlH_2(NH_2BH_3)_4]$ and obtained a sample (referred to as Sample **Li3Al-06** in Figure 7.1) without the presence of peaks corresponding to $LiBH_3NH_2BH_2NH_2BH_3$ (indicated by the gray dashed line in Figure 7.1), which was observed in the previously reported sample from 2013. However, due to the weak diffraction signals exhibited by this sample, we could not determine its structure based on the PXRD data measured using our Mar 345

diffractometer. We plan to conduct Synchrotron PXRD analysis in future studies to investigate the purity and determine the structure. This advanced technique will provide more accurate and detailed information about the sample, enabling us to screen for impurities and elucidate the structure of $Li_3[AlH_2(NH_2BH_3)_4]$.

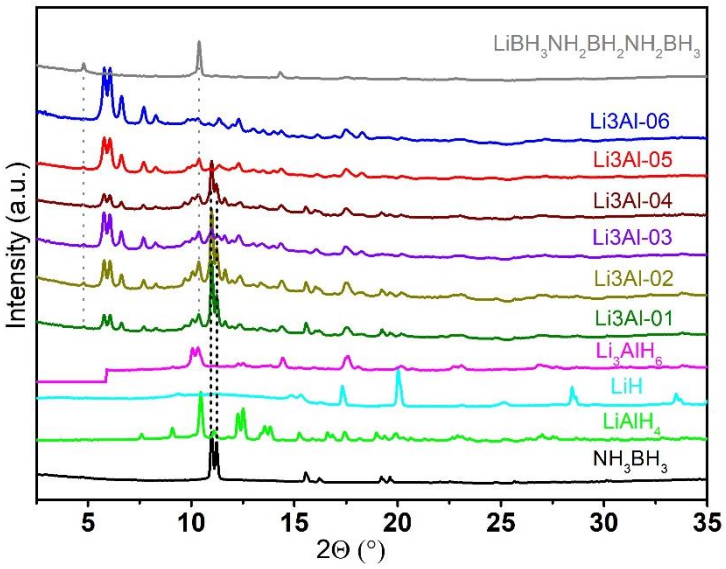

Figure 7.1 PXRD pattern of NH_3BH_3, $LiAlH_4$, LiH, Li_3AlH_6, Sample Li3Al-01 to Li3Al-06 and $LiBH_3NH_2BH_2NH_2BH_3$ (the residual NH_3BH_3 and the formed $LiBH_3NH_2BH_2NH_2BH_3$ pointed by the black dash line and gray dash line, respectively; λ = 0.71073 Å)

We also attempted to synthesize $Li_3[AlH_2(NH_2BH_3)_4]$ using wet chemical approaches as described in Experimental section 7.5.3. Regrettably, our efforts yielded an amorphous product when stirring composites of Li_3AlH_6-4 NH_3BH_3 in THF at both room temperature and 60 °C (as shown in Figure 7.2). This limits the analysis of the structure based on the crystal structure.

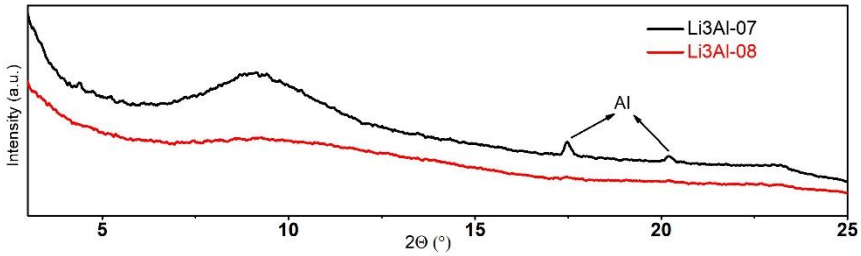

Figure 7.2 PXRD pattern of Sample Li3Al-07 and Li3Al-08 (λ = 0.71073 Å)

Based on the findings presented in Chapter 4, it was discovered that $Na[AlH(CH_3NHBH_3)_3]$ serves as an intermediate product in the reaction between $NaAlH_4$ and $CH_3NH_2BH_3$. This observation led us to question whether $Li_3[AlH_2(NH_2BH_3)_4]$ is the final product resulting from the reaction between Li_3AlH_6 and NH_3BH_3. Consequently, we attempted to obtain the ultimate product, $Li_3[Al(NH_2BH_3)_6]$, using both mechanochemical and wet chemical synthesis methods.

In the mechanochemical synthesis, we conducted the reaction using Li_3AlH_6-$6NH_3BH_3$ (Sample **Li3Al-09**) and $Li_3[AlH_2(NH_2BH_3)_4]$-$2NH_3BH_3$ (Sample **Li3Al-10**). However, neither of these attempts proved successful. Instead, the products obtained from both methods were identified as $Li_3[AlH_2(NH_2BH_3)_4]$ rather than $Li_3[Al(NH_2BH_3)_6]$. This outcome suggests that $Li_3[AlH_2(NH_2BH_3)_4]$ is more stable than $Na[AlH(CH_3NHBH_3)_3]$, which was transferred into the final product $Na[Al(CH_3NHBH_3)_4]$ by prolonging milling time.

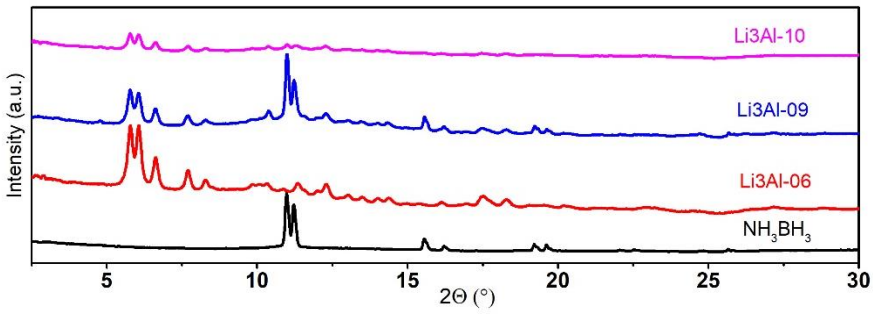

Figure 7.3 PXRD pattern of Sample Li3Al-09 and Li3Al-10 (λ = 0.71073 Å).

Regarding the wet chemical synthesis, it was observed that the final crystalline product obtained from the reaction of Li_3AlH_6-$6NH_3BH_3$ in THF for

48 hours or in Toluene at 60°C for 24 hours (Sample **Li3Al-12** and **Li3Al-14** in Figure 7.4) is identified as $LiBH_3NH_2BH_2NH_2BH_3$. It has been previously reported that $LiBH_3NH_2BH_2NH_2BH_3$ is the product resulting from the reaction between 1 equivalent of LiH and 3 equivalents of NH_3BH_3, as well as the thermally decomposed product of $LiNH_2BH_3$.[21]

In the case of Sample **Li3Al-12** and **Li3Al-14**, it is speculated that Li_3AlH_6 decomposed to form LiH, which subsequently reacted with NH_3BH_3 to produce $LiBH_3NH_2BH_2NH_2BH_3$. However, according to PXRD analysis, a new unknown crystalline phase was formed when Li_3AlH_6 reacted with NH_3BH_3 in THF at 60 °C (Sample **Li3Al-13**). Unfortunately, we were unable to index the sample successfully, hindering the determination of its specific structure. In future investigations, we intend to characterize this unknown crystalline phase further using solid-state NMR and elemental analysis techniques.

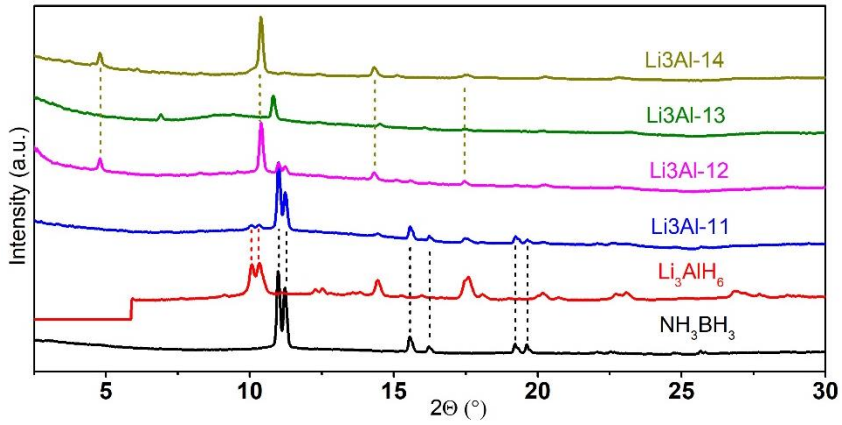

Figure 7.4 PXRD pattern of Sample Li3Al-11-Li3Al-14 (λ = 0.71073 Å).

In summary, the mechanochemical synthesis methods indicate a preference for the formation of $Li_3[AlH_2(NH_2BH_3)_4]$ rather than $Li_3[Al(NH_2BH_3)_6]$ in the reaction between Li_3AlH_6 and NH_3BH_3. This preference could be attributed to the challenges posed by arranging six $NH_2BH_3^-$ anions around Al^{3+} due to crowding, or the limited size of Li ions in adequately coordinating the large anion $[Al(NH_2BH_3)_6]^{3-}$. To overcome these limitations, we have decided to explore the synthesis of metallic six-coordinated aluminum amidoborane complexes by utilizing a combination of Na and Na-Li mixed cations as an alternative to Li.

7.3 Exploring the synthesis of $Na_3[Al(NH_2BH_3)_6]$

Initially, we conducted a screening of various ratios between Na_3AlH_6 and NH_3BH_3 through mechanochemical synthesis approaches (as depicted in Figure 7.5). The composites Na_3AlH_6-$4NH_3BH_3$ resulted in a mixture of amorphous and crystalline phase(s), characterized by six broad peaks observed in the PXRD pattern (designated as Sample **Na3Al-01**). As for the composites Na_3AlH_6-$5NH_3BH_3$, more crystalline phases were obtained (designated as Sample **Na3Al-02**), with some of the crystalline phases observed in Sample **Na3Al-01** still present. The residue Na_3AlH_6 existed in both Sample **Na3Al-01** and **Na3Al-02**, which suggests $Na_3[AlH_2(NH_2BH_3)_4]$ and $Na_3[AlH(NH_2BH_3)_5]$ are not the thermodynamic products in this case. This is different from that of $Li_3[AlH_2(NH_2BH_3)_4]$, which confirmed our indication that Li^+ is too small to cover the big anion $[Al(NH_2BH_3)_6]^{3-}$.

Notably, the product obtained from the post-milled composites Na_3AlH_6-6 NH_3BH_3 (referred to as Sample **Na3Al-03**) exhibited significant differences when compared to Sample **Na3Al-01** and Sample **Na3Al-02**, as evidenced by the analysis of the PXRD pattern. In Sample **Na3Al-03**, several new peaks emerged, providing valuable information for determining its structure. Consequently, due to these promising observations, our focus shifted towards investigating the reaction involving Na_3AlH_6-$6NH_3BH_3$.

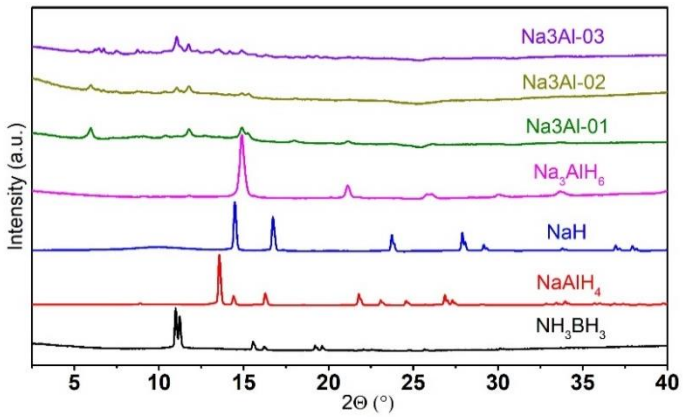

Figure 7.5 PXRD pattern of Sample NH_3BH_3, $NaAlH_4$, NaH, Na_3AlH_6, Na3Al-01 to Na3Al-03 (λ = 0.71073 Å).

We modified the milling conditions of the composites Na_3AlH_6-$6NH_3BH_3$, as outlined in Table 7.2. The resulting samples, Na3Al-04 to Na3Al-07, were

characterized using PXRD analysis (as shown in Figure 7.6A). In all of the samples, the peaks corresponding to $NaBH_3NH_2BH_2NH_2BH_3$ were present. It is known that $NaBH_3NH_2BH_2NH_2BH_3$ is either a product of the reaction between NaH and 3 equivalents of NH_3BH_3 or a thermally decomposed product of $NaNH_2BH_3$,[21] similar to $LiBH_3NH_2BH_2NH_2BH_3$. This suggests that during the ball milling process with NH_3BH_3, a portion of Na_3AlH_6 decomposed to NaH and $NaAlH_4$.

However, we did not observe any peaks corresponding to $Na[Al(NH_2BH_3)_4]$ in any of the aforementioned samples. Notably, an IR band in the range of 520-650 cm^{-1} was present in the spectrum of Sample Na3Al-04 (Figure 7.6B), which is indicative of the Al-N bond. Based on this observation, we propose that $Na_3[Al(NH_2BH_3)_6]$ formed under the milling conditions employed for Sample Na3Al-04. Nevertheless, further analysis of the structure and modification of the synthesis approach will be pursued in our future investigations.

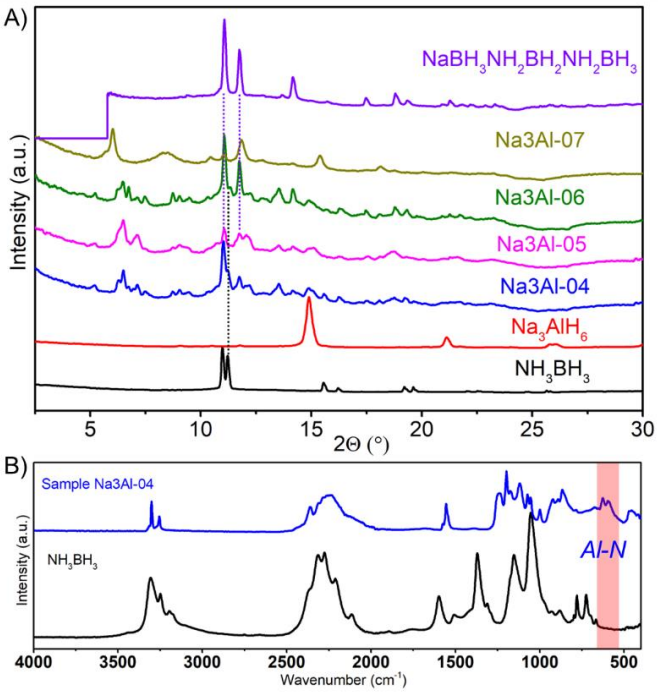

Figure 7.6 (A). PXRD pattern of Sample NH_3BH_3, Na_3AlH_6, Na3Al-04 to Na3Al-07 (λ = 0.71073 Å); (B). IR spectra of NH_3BH_3 and Na3Al-04 (Al-N bond highlighted by the red rectangle).

Similar to the reaction between 1 equivalent of Li_3AlH_6 and 6 equivalents of NH_3BH_3 in organic solvents, the composites Na_3AlH_6-$6NH_3BH_3$ also resulted in the formation of $NaBH_3NH_2BH_2NH_2BH_3$ instead of the desired product when conducted in THF and toluene (as observed in **Sample Na3Al-08**, **Na3Al-09**, and **Na3Al-10**, as shown in Figure 7.7).

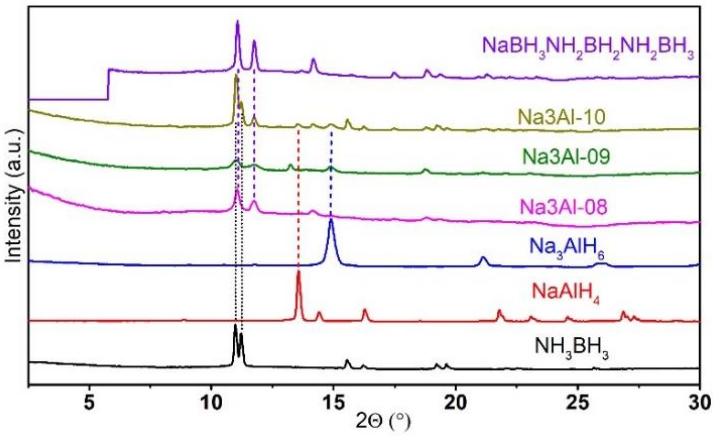

Figure 7.7 PXRD pattern of NH_3BH_3, $NaAlH_4$, Na_3AlH_6, Sample **Na3Al-08** to **Na3Al-10** (λ = 0.71073 Å, residue NH_3BH_3 pointed by the black dash line, the formed $NaBH_3NH_2BH_2NH_2BH_3$ highlighted by the purple dash line, $NaAlH_4$ pointed by the red dash line and residue Na_3AlH_6 highlighted by blue dash line).

We employed the previously reported synthesis of $Na[Al(NH_2BH_3)_4]$ and $NaNH_2BH_3$ compounds as a starting point for our attempts to synthesize $Na_3[Al(NH_2BH_3)_6]$. Following the reaction equation described in Equation 7.7 of the experimental section 7.5.6, we conducted ball milling experiments. Based on the PXRD pattern analysis, Sample **Na3Al-13** resembles Sample **Na3Al-04**, which is formed from Na_3AlH_6 and NH_3BH_3. Notably, the byproduct $NaBH_3NH_2BH_2NH_2BH_3$ coexisted with $Na_3[Al(NH_2BH_3)_6]$ in Sample **Na3Al-13**.

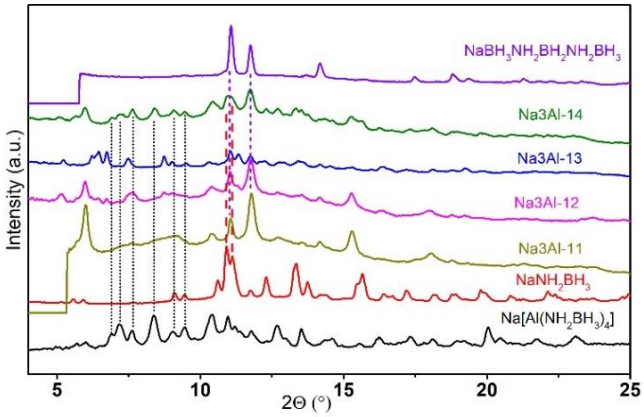

Figure 7.8 PXRD pattern of $Na[Al(NH_3BH_3)_4]$, $NaNH_2BH_3$, Sample **Na3Al-11** to **Na3Al-14** and $NaBH_3NH_2BH_2NH_2BH_3$ (λ = 0.71073 Å, unreacted $Na[Al(NH_3BH_3)_4]$ and $NaNH_2BH_3$ pointed by black and red dash line, respectively; the formed $NaBH_3NH_2BH_2NH_2BH_3$ pointed by purple dash line.).

The synthesis of $Na_3[Al(NH_2BH_3)_6]$ is still being investigated to discover more optimal reaction conditions that can minimize side reactions. The current methods are primarily hindered by the formation of $NaBH_3NH_2BH_2NH_2BH_3$, as observed in the above-mentioned reaction equations. $NaNH_2BH_3$ can be obtained through the reaction of NaH with NH_3BH_3 or through the reaction of $NaNH_2$ and NH_3BH_3. It has been reported that the former method often results in a mixture containing a small amount of $NaBH_3NH_2BH_2NH_2BH_3$, while the latter method yields $NaNH_2BH_3$ without any detectable signals of $NaBH_3NH_2BH_2NH_2BH_3$.[22] Therefore, one potential solution to obtain pure $Na_3[Al(NH_2BH_3)_6]$ could involve using $NaNH_2BH_3$ generated from the reaction between $NaNH_2$ and NH_3BH_3. Further exploration is required to validate this approach.

7.4 Exploring the synthesis of $Na_2Li[Al(NH_2BH_3)_6]$

We also explored the use of Na_2LiAlH_6 as another precursor for synthesizing six-coordinated Al-based amidoborane complexes. We conducted ball milling reactions between 1 eq. of Na_2LiAlH_6 and 6 eq. of NH_3BH_3 (Sample **Na2LiAl-01**), 1 eq. of Na_2LiAlH_6 and 5 eq. of NH_3BH_3 (Sample **Na2LiAl-02**), and 1 eq. of Na_2LiAlH_6 and 4 eq. of NH_3BH_3 (Sample **Na2LiAl-03**). Upon post-milling characterization, the composites Na_2LiAlH_6-4

NH_3BH_3 (Sample **Na2LiAl-03**) and Na_2LiAlH_6-$5NH_3BH_3$ (Sample **Na2LiAl-02**) exhibited fewer wide peaks in the PXRD pattern compared to the composites Na_2LiAlH_6-$6NH_3BH_3$ (Sample **Na2LiAl-01**). In addition, the unreacted Na_2LiAlH_6 appeared in Sample **Na2LiAl-02** and **Na2LiAl-03** (Figure 7.9A), which suggests the amount of NH_3BH_3 is not enough in the composites Na_2LiAlH_6-$4NH_3BH_3$ and Na_2LiAlH_6-$5NH_3BH_3$. This is the same as that of the reaction between Na_3AlH_6 and NH_3BH_3. There is the signal of locked at the range of the Al-N bond in the IR spectrum of Sample **Na2LiAl-01** (Figure 7.9B), which indicates $Na_2Li[Al(NH_2BH_3)_6]$ formed under such reaction conditions. However, the weak diffraction of Sample **Na2LiAl-01** necessitates more rigorous measurement techniques to assess its purity and structural characterization. Furthermore, the PXRD pattern of Sample **Na2LiAl-04**, which is the product of the reaction between 1 eq. of Na_2LiAlH_6 and 6 eq. of NH_3BH_3 in THF, closely resembles that of $NaBH_3NH_2BH_2NH_2BH_3$. This suggests that Na_2LiAlH_6 decomposes to NaH and $LiAlH_4$ in organic solvents, similar to the behavior observed with Li_3AlH_6 and Na_3AlH_6.

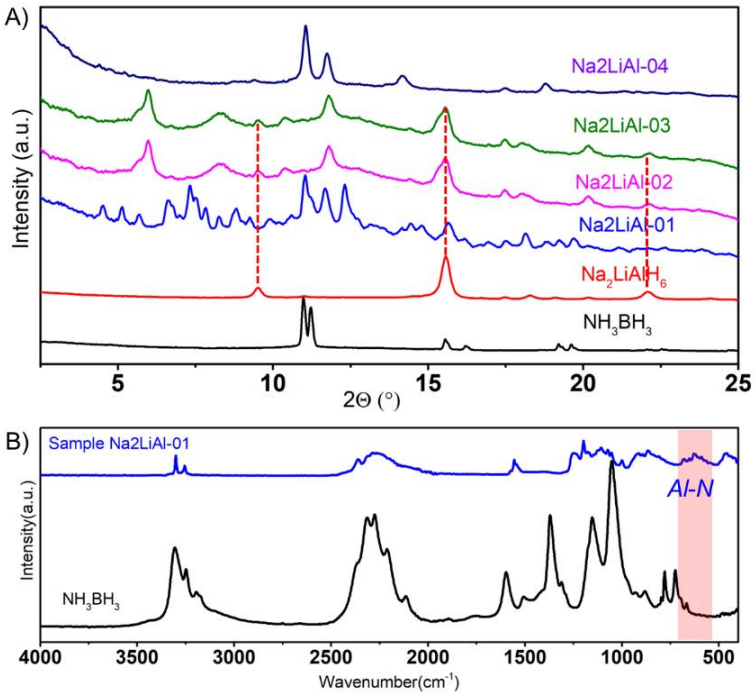

Figure 7.9 PXRD pattern of Sample NH_3BH_3, Na_2LiAlH_6, Na2LiAl-01-Na2LiAl-04 (λ = 0.71073 Å).

In summary, $Li_3[AlH_2(NH_2BH_3)_4]$ has been identified as the thermodynamic product for the Li-based counter-anion six-coordinated Al-based amidoborane complex. We will further investigate the structural details by determining the modified Sample **Li3Al-06**. By introducing Na and Na-Li mixed cations with a slightly larger radius, the $[Al(NH_2BH_3)_6]^{3-}$ anion becomes more stable compared to $[AlH_2(NH_2BH_3)_4]^{3-}$ and $[AlH(NH_2BH_3)_5]^{3-}$. However, the alanates Li_3AlH_6, Na_3AlH_6 and Na_2LiAlH_6 decompose into $MAlH_4$ and MH in organic solvents, which limits their applicability for synthesizing six-coordinated Al-based amidoborane complexes in such solvents. Therefore, mechanochemical synthesis is preferred for the synthesis of these complexes. In our exploration, the synthesis conditions of Sample **Na3Al-04**, **Na3Al-13**, and **Na2LiAl-01** can serve as references for future optimization or new synthesis methods for such six-coordinated Al-based amidoborane complexes.

7.5 Experimental section

7.5.1 Chemicals

All the samples were obtained from commercially available NaH (95 %), LiH (95 %), $NaAlH_4$ (93 %), $LiAlH_4$ (>98 %), $NaBH_4$ (97 %), NH_3BH_3 (97 %), and anhydrous THF (⩾99.9%), Toluene (99.85%), which were purchased from SigmaAldrich Co. Ltd. DMSO-d_6 (99.8%) was purchased from Eurisotop. All the operations were performed in a glovebox with a high-purity argon atmosphere.

7.5.2 Synthesis of Li_3AlH_6

See Chapter six experimental section 6.6.3.

7.5.3 Syntheses of Samples Li3Al-01 to Li3Al-14

$$Li_3AlH_6 + 4\ NH_3BH_3 \longrightarrow Li_3[AlH_2(NH_2BH_3)_4] + 4\ H_2\uparrow$$ Equation 7.1

Samples Li3Al-01, Li3Al-02, Li3Al-03, Li3Al-04 and Li3Al-05: 1 eq. of Li_3AlH_6 (91.0 mg, 1.7 mmol) and 4 eq. of AB (208.9 mg, 6.8 mmol) were introduced into an 80 mL stainless steel vial. The vial was equipped with three

10 mm diameter stainless steel balls and subjected to milling in a planetary ball mill (Fritsch Pulverisette 7 Premium line). Monitoring of gas pressure and temperature evolution throughout the reaction was accomplished using the Easy GTM detection system accessory (Fritsch). The milling conditions were fixed as Table 7.1 and resulted in the formation of a dark gray powder (Figure 7.1).

Sample Li3Al-06: 1 eq. of Li_3AlH_6 (45.5 mg, 0.84 mmol) and 4 eq. of AB (104.5 mg, 3.4 mmol) were introduced into an 80 mL stainless steel vial. The vial was equipped with three 10 mm diameter stainless steel balls and subjected to milling in a planetary ball mill (Fritsch Pulverisette 7 Premium line). Monitoring of gas pressure and temperature evolution throughout the reaction was accomplished using the Easy GTM detection system accessory (Fritsch). The rotation speed was fixed at 500 rpm, and the ball-to-powder mass ratio was maintained at 80:1. The synthesis process involved 15 milling cycles, each consisting of 30 minutes of milling followed by 30 minutes of cooling breaks, resulting in the formation of a dark gray powder (Figure 7.1).

Table 7.1 The conditions of ball milling for composites Li_3AlH_6-$4NH_3BH_3$.

Sample	speed	Milling time	Break time	cycles	Ratio of ball to powder
Li3Al-01	350	30	30	3	40:1
Li3Al-02	350	30	30	6	40:1
Li3Al-03	350	30	30	35	40:1
Li3Al-04	250	30	30	35	40:1
Li3Al-05	500	30	30	16	40:1
Li3Al-06	500	30	30	15	80:1

Samples Li3Al-07 and Li3Al-08: 1 eq. of Li_3AlH_6 (45.5 mg, 0.84 mmol) and 4 eq. of AB (104.5 mg, 3.4 mmol), and anhydrous THF (20 mL) were added to a 100 mL, one-neck round bottom Schlenk flask. The obtained suspension was then vigorously stirred at room temperature (Sample **Li3Al-07**) and 60 ˚C (Sample **Li3Al-08**) under an argon atmosphere for 48 hours, respectively. Then the solvent was removed by vacuum. And the solid was

dried under vacuum for another 5 hours to eliminate residual solvents. The product was characterized by means of PXRD (Figure. 7.2).

$$Li_3AlH_6 + 6\ NH_3BH_3 \longrightarrow Li_3[Al(NH_2BH_3)_6] + 6H_2\uparrow$$ Equation 7.2

Sample Li3Al-09: 1 eq. of Li_3AlH_6 (91 mg, 1.7 mmol) and 6 eq. of AB (313.4 mg, 10.1 mmol) were introduced into an 80 mL stainless steel vial. The vial was equipped with three 10 mm diameter stainless steel balls and subjected to milling in a planetary ball mill (Fritsch Pulverisette 7 Premium line). Monitoring of gas pressure and temperature evolution throughout the reaction was accomplished using the Easy GTM detection system accessory (Fritsch). The rotation speed was fixed at 500 rpm, and the ball-to-powder mass ratio was maintained at 30:1. The synthesis process involved 35 milling cycles, each consisting of 30 minutes of milling followed by 30 minutes of cooling breaks, resulting in the formation of a dark gray powder (Figure 7.3).

$$Li_3[AlH_2(NH_2BH_3)_4] + 2\ NH_3BH_3 \longrightarrow Li_3[Al(NH_2BH_3)_6] + 2\ H_2\uparrow$$ Equation 7.3

Sample Li3Al-10: 1 eq. of $Li_3[AlH_2(NH_2BH_3)_4]$ (109.9 mg, 0.65 mmol) and 2 eq. of AB (61.7 mg, 1.3 mmol) were introduced into an 80 mL stainless steel vial. The vial was equipped with three 10 mm diameter stainless steel balls and subjected to milling in a planetary ball mill (Fritsch Pulverisette 7 Premium line). Monitoring of gas pressure and temperature evolution throughout the reaction was accomplished using the Easy GTM detection system accessory (Fritsch). The rotation speed was fixed at 500 rpm, and the ball-to-powder mass ratio was maintained at 80:1. The synthesis process involved 15 milling cycles, each consisting of 30 minutes of milling followed by 30 minutes of cooling breaks, resulting in the formation of a dark gray powder (Figure 7.3).

Samples Li3Al-11, Li3Al-12, and Li3Al-13: 1 eq. of Li_3AlH_6 (32 mg, 0.6 mmol) and 6 eq. of AB (110 mg, 3.6 mmol), and anhydrous THF (15 mL) were added to a 50 mL, one-neck round bottom Schlenk flask. The obtained suspension was then vigorously stirred at room temperature for 12 hours (Sample **Li3Al-11**), 48 hours (Sample **Li3Al-12**) and 60 ˚C for 24 hours (Sample **Li3Al-13**) under an argon atmosphere, respectively. Then the solvent was removed under vacuum. And the solid was dried under vacuum for another 5 hours to eliminate residual solvents. The product was characterized by means of PXRD (Figure. 7.4).

Sample Li3Al-14: 1 eq. of Li_3AlH_6 (32 mg, 0.6 mmol) and 6 eq. of AB (110 mg, 3.6 mmol), and anhydrous Toluene (15 mL) were added to a 50 mL, one-neck round bottom Schlenk flask. The obtained suspension was then vigorously stirred at room temperature under an argon atmosphere for 24 hours. Then the solvent was removed under vacuum. And the solid was dried under vacuum for another 5 hours to eliminate residual solvents. The product was characterized by means of PXRD (Figure. 7.4).

7.5.4 Synthesis of Na_3AlH_6

See Chapter six experimental section 6.6.4.

7.5.5 Synthesis of $NaNH_2BH_3$

$$NaH + NH_3BH_3 \longrightarrow NaNH_2BH_3 + H_2\uparrow$$

Equation 7.4

1 eq. of NaH (131.8 mg, 5.5 mmol) and 1 eq. of AB (169.1 mg, 5.5 mmol) were introduced into an 80 mL stainless steel vial. The vial was equipped with three 10 mm diameter stainless steel balls and subjected to milling in a planetary ball mill (Fritsch Pulverisette 7 Premium line). Monitoring of gas pressure and temperature evolution throughout the reaction was accomplished using the Easy GTM detection system accessory (Fritsch). The rotation speed was fixed at 500 rpm, and the ball-to-powder mass ratio was maintained at 60:1. The synthesis process involved 15 milling cycles, each consisting of 10 minutes of milling followed by 5 minutes of cooling breaks, resulting in the formation of a white powder (Figure 7.10).

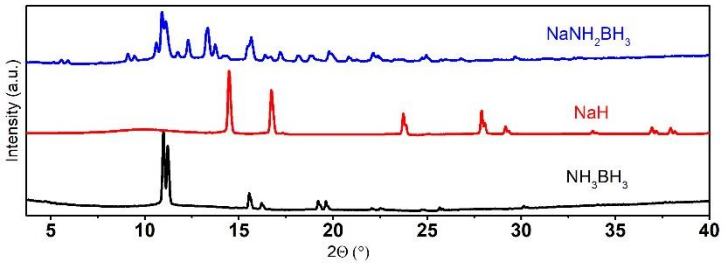

Figure 7.10 PXRD pattern of NH_3BH_3, NaH and $NaNH_2BH_3$ (λ = 0.71073 Å)

7.5.6 Syntheses of Samples Na3Al-01 to Na3Al-14

$$Na_3AlH_6 + 6\ NH_3BH_3 \longrightarrow Na_3[Al(NH_2BH_3)_6] + 6H_2 \uparrow$$ Equation 7.5

Samples Na3Al-01, Na3Al-02 and Na3Al-03: 1 eq. of Na_3AlH_6 (26.9 mg, 0.7 mmol) and 4 eq. of AB (124.63 mg, 1.4 mmol) (**Na3Al-01**), 1 eq. of Na_3AlH_6 (26.9 mg, 0.7 mmol) and 5 eq. of AB (124.63 mg, 1.4 mmol) (**Na3Al-02**), and 1 eq. of Na_3AlH_6 (26.9 mg, 0.7 mmol) and 6 eq. of AB (124.63 mg, 1.4 mmol) (**Na3Al-03**) were placed into an 80 mL stainless steel vial and with three 10 mm diameter stainless steel balls and milled in a planetary ball mill (Fritsch Pulverisette 7 Premium line), respectively. The gas pressure and temperature evolution during the reaction was performed using the Easy GTM detection system accessory (Fritsch). The rotation speed was set to 500 rpm and the ball-to-powder mass ratio was 80:1. The synthesis was performed using 20 milling cycles of 30 min milling interrupted by 15 min cooling breaks, to yield light gray powder (Figure 7.5).

Samples Na3Al-04 and Na3Al-05: 1 eq. of Na_3AlH_6 (106 mg, 1.0 mmol) and 6 eq. of AB (192 mg, 6.2 mmol) were introduced into an 80 mL stainless steel vial. The vial was equipped with three 10 mm diameter stainless steel balls and subjected to milling in a planetary ball mill (Fritsch Pulverisette 7 Premium line). Monitoring of gas pressure and temperature evolution throughout the reaction was accomplished using the Easy GTM detection system accessory (Fritsch). The milling conditions were fixed as Table 7.2 and result in the formation of a white powder (Figure 7.6A).

Samples Na3Al-06, Na3Al-07: 1 eq. of Na_3AlH_6 (53 mg, 0.5 mmol) and 6 eq. of AB (96 mg, 3.1 mmol) were introduced into an 80 mL stainless steel vial. The vial was equipped with three 10 mm diameter stainless steel balls and subjected to milling in a planetary ball mill (Fritsch Pulverisette 7 Premium line). Monitoring of gas pressure and temperature evolution throughout the reaction was accomplished using the Easy GTM detection system accessory (Fritsch). The milling conditions were fixed as Table 7.2 and result in the formation of a white powder (Figure 7.6A).

Table 7.2 The conditions of ball milling for composites Na_3AlH_6-$6NH_3BH_3$.

Sample	speed	Milling time	Break time	cycles	Ratio of ball to powder
Na3Al-04	250	30	30	40	40:1
Na3Al-05	350	30	30	40	40:1
Na3Al-06	350	30	30	40	80:1
Na3Al-07	500	30	15	40	80:1

Samples Na3Al-08, and Na3Al-09: 1 eq. of Na_3AlH_6 (53 mg, 0.5 mmol) and 6 eq. of AB (96 mg, 3.1 mmol), and anhydrous THF (15 mL) were added to a 50 mL, one-neck round bottom Schlenk flask. The obtained suspension was then vigorously stirred at room temperature (**Na3Al-08**) and 60 ˚C (**Na3Al-09**) for 48 hours under an argon atmosphere, respectively. Then the solvent was removed under vacuum. And the solid was dried under vacuum for another 5 hours to eliminate residual solvents. The product was characterized by means of PXRD (Figure. 7.7).

Sample Na3Al-10: 1 eq. of Na_3AlH_6 (53 mg, 0.5 mmol) and 6 eq. of AB (96 mg, 3.1 mmol), and anhydrous Toluene (15 mL) were added to a 50 mL, one-neck round bottom Schlenk flask. The obtained suspension was then vigorously stirred at 60 ˚C for 48 hours under an argon atmosphere, respectively. Then the solvent was removed under vacuum. And the solid was dried under vacuum for another 5 hours to eliminate residual solvents. The product was characterized by means of PXRD (Figure. 7.7).

$$Na[Al(NH_2BH_3)_4] + 2\ NaNH_2BH_3 \longrightarrow Na_3[Al(NH_2BH_3)_6] \quad \text{Equation 7.6}$$

Samples Na3Al-11 to Na3Al-14: 1 eq. of $Na[Al(NH_2BH_3)_4]$ (84.7 mg, 0.5 mmol) and 2 eq. of $NaNH_2BH_3$ (52.8 mg, 1.0 mmol) were introduced into an 80 mL stainless steel vial. The vial was equipped with three 10 mm diameter stainless steel balls and subjected to milling in a planetary ball mill (Fritsch Pulverisette 7 Premium line). Monitoring of gas pressure and temperature evolution throughout the reaction was accomplished using the Easy GTM detection system accessory (Fritsch). The milling conditions were fixed as Table 7.3 and result in the formation of a white powder (Figure 7.8).

Table 7.3 The parameters of synthesis Samples **Na3Al-11** to **Na3Al-14**.

Sample	speed	Milling time	Break time	cycles	Ratio of ball to powder
Na3Al-11	250	30	15	6	90:1
Na3Al-12	200	30	15	6	90:1
Na3Al-13	200	30	15	4	90:1
Na3Al-14	200	30	15	2	90:1

7.5.7 Synthesis of Na_2LiAlH_6

See Chapter six experimental section 6.6.5.

7.5.8 Syntheses of Samples Na_2LiAl-01 to Na_2LiAl-04

$$Na_2LiAlH_6 + 6\ NH_3BH_3 \longrightarrow Na_2Li[Al(NH_2BH_3)_6] + 6H_2\uparrow$$ Equation 7.7

Samples Na_2LiAl-01, Na_2LiAl-02 and Na_2LiAl-03: 1 eq. of Na_2LiAlH_6 (61.6 mg, 0.72 mmol) and 4 eq. of AB (88.4 mg, 2.9 mmol) (**Na2LiAl-03**), 1 eq. of Na_2LiAlH_6 (53.7 mg, 0.62 mmol), 5 eq. of AB (96.4 mg, 3.1 mmol) (**Na2LiAl-02**), and 1 eq. of Na_2LiAlH_6 (47.6 mg, 0.55 mmol), 6 eq. of AB (102.4 mg, 3.3 mmol) (**Na2LiAl-01**) were placed into an 80 mL stainless steel vial and with three 10 mm diameter stainless steel balls and milled in a planetary ball mill (Fritsch Pulverisette 7 Premium line), respectively. The evolution of the gas pressure and temperature during the reaction was performed using the Easy GTM detection system accessory (Fritsch). The rotation speed was set to 500 rpm and the ball-to-powder mass ratio was about 80:1. The synthesis was performed using 20 milling cycles of 30 min milling interrupted by 30 min cooling breaks, to yield dark gray powder (Figure 7.9A).

Sample Na_2LiAl-04: 1 eq. of Na_2LiAlH_6 (47.6 mg, 0.55 mmol), 6 eq. of AB (102.4 mg, 3.3 mmol) and anhydrous THF (30 mL) were added to a 100 mL, one-neck round bottom Schlenk flask. The obtained suspension was then vigorously stirred at room temperature for 24 hours under an argon atmosphere, respectively. Then the solvent was removed under vacuum. And the solid was dried under vacuum for another 5 hours to eliminate residual solvents. The product was characterized by means of PXRD (Figure. 7.9A).

References

1. Owarzany, R.; Leszczyński, P. J.; Fijalkowski, K. J.; Grochala, W. Mono- and Bimetalic Amidoboranes *Crystals* **2016**, DOI: 10.3390/cryst6080088.

2. Wang, K.; Pan, Z.; Yu, X., Metal B-N-H Hydrogen-Storage Compound: Development and Perspectives. *Journal of Alloys and Compounds* **2019**, *794*, 303-324.

3. Xiong, Z., et al., High-Capacity Hydrogen Storage in Lithium and Sodium Amidoboranes. *Nature Materials* **2007**, *7*, 138.

4. Diyabalanage, H. V. K., et al., Potassium(I) Amidotrihydroborate: Structure and Hydrogen Release. *Journal of the American Chemical Society* **2010**, *132*, 11836-11837.

5. Wu, C.; Wu, G.; Xiong, Z.; Han, X.; Chu, H.; He, T.; Chen, P., $LiNH_2BH_3{\cdot}NH_3BH_3$: Structure and Hydrogen Storage Properties. *Chemistry of Materials* **2010**, *22*, 3-5.

6. Fijalkowski, K. J.; Genova, R. V.; Filinchuk, Y.; Budzianowski, A.; Derzsi, M.; Jaroń, T.; Leszczyński, P. J.; Grochala, W., $Na[Li(NH_2BH_3)_2]$ – the First Mixed-Cation Amidoborane with Unusual Crystal Structure. *Dalton Transactions* **2011**, *40*, 4407-4413.

7. Chua, Y. S.; Li, W.; Wu, G.; Xiong, Z.; Chen, P., From Exothermic to Endothermic Dehydrogenation – Interaction of Monoammoniate of Magnesium Amidoborane and Metal Hydrides. *Chemistry of Materials* **2012**, *24*, 3574-3581.

8. Kang, X.-D.; Luo, J.-H.; Wang, P., Efficient and Highly Rapid Hydrogen Release from Ball-Milled 3 $NH_3BH_3/MMgH_3$ (M=Na, K, Rb) Mixtures at Low Temperatures. *International Journal of Hydrogen Energy* **2012**, *37*, 4259-4266.

9. Biliškov, N.; Borgschulte, A.; Užarević, K.; Halasz, I.; Lukin, S.; Milošević, S.; Milanović, I.; Novaković, J. G., In-Situ and Real-Time Monitoring of Mechanochemical Preparation of $Li_2Mg(NH_2BH_3)_4$ and $Na_2Mg(NH_2BH_3)_4$ and Their Thermal Dehydrogenation. *Chemistry – A European Journal* **2017**, *23*, 16274-16282.

10. Kang, X.; Luo, J.; Zhang, Q.; Wang, P., Combined Formation and Decomposition of Dual-Metal Amidoborane $NaMg(NH_2BH_3)_3$ for High-Performance Hydrogen Storage. *Dalton Transactions* **2011**, *40*, 3799-3801.

11. Wu, H.; Zhou, W.; Pinkerton, F. E.; Meyer, M. S.; Yao, Q.; Gadipelli, S.; Udovic, T. J.; Yildirim, T.; Rush, J. J., Sodium Magnesium Amidoborane: The First Mixed-Metal Amidoborane. *Chemical Communications* **2011**, *47*, 4102-4104.

12. Milanović, I.; Biliškov, N.; Užarević, K.; Lukin, S.; Etter, M.; Halasz, I., Mechanochemical Synthesis and Thermal Dehydrogenation of Novel Calcium-Containing Bimetallic Amidoboranes. *ACS Sustainable Chemistry & Engineering* **2021**, *9*, 2089-2099.

13. Hawthorne, M. F.; Jalisatgi, S. S.; Safronov, A. V.; Lee, H. B.; Wu, J. *Chemical Hydrogen Storage Using Polyhedral Borane Anions and Aluminum-Ammonia-Borane Complexes*; United States, 2010-10-01, **2010**.

14. Xia, G.; Tan, Y.; Chen, X.; Guo, Z.; Liu, H.; Yu, X., Mixed-Metal (Li, Al) Amidoborane: Synthesis and Enhanced Hydrogen Storage Properties. *Journal of Materials Chemistry A* **2013**, *1*, 1810-1820.

15. Dovgaliuk, I.; Jepsen, L. H.; Safin, D. A.; Łodziana, Z.; Dyadkin, V.; Jensen, T. R.; Devillers, M.; Filinchuk, Y., A Composite of Complex and Chemical Hydrides Yields the First Al-Based Amidoborane with Improved Hydrogen Storage Properties. *Chemistry – A European Journal* **2015**, *21*, 14562-14570.

16. Nakagawa, Y.; Shinzato, K.; Nakagawa, T.; Nakajima, K.; Isobe, S.; Goshome, K.; Miyaoka, H.; Ichikawa, T., Synthesis, Structural Characterization, and Hydrogen Desorption Properties of $Na[Al(NH_2BH_3)_4]$. *International Journal of Hydrogen Energy* **2017**, *42*, 6173-6180.

17. Møller, K. T.; Jørgensen, M.; Andreasen, J. G.; Skibsted, J.; Łodziana, Z.; Filinchuk, Y.; Jensen, T. R., Synthesis and Thermal Decomposition of Potassium Tetraamidoboranealuminate, $K[Al(NH_2BH_3)_4]$. *International Journal of Hydrogen Energy* **2018**, *43*, 311-321.

18. Zhang, T.; Steenhaut, T.; Li, X.; Devred, F.; Devillers, M.; Filinchuk, Y., Aluminum Methylamidoborane Complexes: Mechanochemical Synthesis, Structure, Stability, and Reactive Hydride Composites. *Sustainable Energy & Fuels* **2023**, *7*, 1119-1126.

19. Dovgaliuk, I.; Le Duff, C. S.; Robeyns, K.; Devillers, M.; Filinchuk, Y., Mild Dehydrogenation of Ammonia Borane Complexed with Aluminum Borohydride. *Chemistry of Materials* **2015**, *27*, 768-777.

20. Yang, J.; Beaumont, P. R.; Humphries, T. D.; Jensen, C. M.; Li, X., Efficient Synthesis of an Aluminum Amidoborane Ammoniate. *Energies* **2015**, *8*.

21. Fijalkowski, K. J.; Jaroń, T.; Leszczyński, P. J.; Magos-Palasyuk, E.; Palasyuk, T.; Cyrański, M. K.; Grochala, W., M($BH_3NH_2BH_2NH_2BH_3$) – the Missing Link in the Mechanism of the Thermal Decomposition of Light Alkali Metal Amidoboranes. *Physical Chemistry Chemical Physics* **2014**, *16*, 23340-23346.

22. Xiong, Z.; Wu, G.; Chua, Y. S.; Hu, J.; He, T.; Xu, W.; Chen, P., Synthesis of Sodium Amidoborane ($NaNH_2BH_3$) for Hydrogen Production. *Energy & Environmental Science* **2008**, *1*, 360-363.

Chapter 8

Conclusions and perspectives

8.1 General conclusions

The main goal of this thesis was to enhance the hydrogen storage properties of metal amidoborane derivatives by introducing the electron-donating groups, to understand the influence of the substituents on hydrogen storage performance at the molecular level, to further use this information towards design and synthesis of novel materials for compact, safe, and cost-effective hydrogen storage. To accomplish this, we used two different substituents on the N-side of AB producing AB-based precursors. Then we studied their alkali metal derivatives as well as Al-based amidoborane complexes.

The first substituent used in this study is the methyl (-CH_3) group. Interaction of $CH_3NH_2BH_3$ with NaH yielded an oligomer $Na[BH_3(CH_3NH)BH_2(CH_3NH)BH_3]$. As compared to the unsubstituted analogue containing $[BH_3NH_2BH_2NH_2BH_3]^-$ anion, the introduction of methyl groups on nitrogen atoms resulted in a decrease of the thermal dehydrogenation temperature and an enhancement in the purity of the released hydrogen. This can be attributed to the strengthening of the B-N bonds due to the introduction of methyl groups on the nitrogen atoms, which leads to a reduction of the release of volatile gases containing nitrogen and boron during thermal dehydrogenation. Furthermore, the introduction of methyl groups on the nitrogen atoms disrupts intermolecular dihydrogen bonding network and causes a kink in the B-N-B-N-B geometry, promoting the formation of intramolecular dihydrogen bonds. This likely facilitates the release of hydrogen molecules and suppresses the release of larger fragments during thermal decomposition. These findings confirm that the presence of small methyl groups on the nitrogen atoms has a positive effect on the hydrogen release by $Na[BH_3(CH_3NH)BH_2(CH_3NH)BH_3]$.

Reaction of $CH_3NH_2BH_3$ with $NaAlH_4$ leads to the formation of $Na[Al(CH_3NHBH_3)_4]$. The introduction of methyl groups facilitates the formation of Al-N bonds, resulting in a decrease in energy required for the synthesis of $Na[Al(CH_3NHBH_3)_4]$, making this material easier to make (consider also that MeAB is cheaper than AB). Furthermore, we were able to isolate the reaction intermediate, $Na[AlH(CH_3NHBH_3)_3]$, which provides valuable insights into the formation mechanism of Al-based amidoborane complexes. Unfortunately, methyl groups were unable to suppress the release of large fragments upon thermal decomposition. However, the formation of reactive hydrides composites with NaH and $NaNH_2$ enables to release pure hydrogen at moderate temperatures of ~180 ˚C.

Another alkyl group utilized in this study is the di-methylene chain ($-CH_2CH_2-$), which acts as a bridge connecting two ammonia boranes molecules, thereby forming the precursor $BH_3NH_2CH_2CH_2NH_2BH_3$. This molecule can be doubly deprotonated upon the reaction with metal hydrides. The results in Chapter 5 have confirmed that the introduction of di-methylene groups on nitrogen atoms has a similar positive impact on hydrogen release properties, particular in terms of purity, as observed with the introduction of methyl groups. In comparison to the methyl-substituted compound ($Na[BH_3(CH_3NH)BH_2(CH_3NH)BH_3]$), this sodium-based oligomer with di-methylene substitution has a more complex structure and is capable of releasing greater amount of pure hydrogen under moderate conditions.

Reaction of the di-methylene substituted precursor with lithium and sodium alanates leads to the formation of $[Al(BH_3NHCH_2NHBH_3)_2]^-$ complexes. The relative inertness of $BH_3NH_2CH_2CH_2NH_2BH_3$ makes it possible to react it with $LiAlH_4$ mechanochemically, while the reaction between NH_3BH_3 and $LiAlH_4$ has an explosive character. The obtained $Li[Al(BH_3NHCH_2CH_2NHBH_3)_2]$ releases ~6.6 wt.% of pure hydrogen at modest temperatures. The sodium salt, $Na[Al(BH_3NHCH_2CH_2NHBH_3)_2]$, can be obtained only from solutions, most conveniently in THF. This complex is stabilized by the coordinated THF, thus the thermally released hydrogen contains also this solvent. However, we can affirm that $M[Al(BH_3NHCH_2CH_2NHBH_3)_2]$ does not release NH_3 and B_2H_6, which often contaminate hydrogen during the thermal dehydrogenation of ammonia boranes and its derivatives. This confirms that the introduction of di-methylene

groups on nitrogen atoms of AB is capable of suppressing the formation of volatile by-products, having more profound effect and smaller dead mass than the methyl groups.

In summary, the introduction of weakly electron-donating groups such as -CH_3 and -CH_2CH_2- on the nitrogen atoms of the metal amidoborane complexes holds promise in making hydrogen stores capable to release large amounts of pure hydrogen at moderate temperatures. This benefit arises from the stronger N-B bonds in the forming complexes and the reorganization of intermolecular and intramolecular dihydrogen bonds. This approach can be extended to other mono- or multi-metallic amidoborane compounds and can likely be applied using other substituents.

8.2 Perspectives

Six-coordinated Al-based amidoborane compounds hold significant potential in the fields of hydrogen storage and in particular the development of Al-based amidoborane complexes. Our research has focused on attempting to synthesize the six-coordinated Al-based amidoborane compounds from NH_3BH_3 (Chapter 7) and $BH_3NH_2CH_2CH_2NH_2BH_3$ (Chapter 6). Based on the current findings, $Li_3[AlH_2(NH_2BH_3)_4]$ is more stable than $Li_3[Al(NH_2BH_3)_6]$, $Na_2Li[Al(NH_2BH_3)_6]$ and $Na_3[Al(NH_2BH_3)_6]$ are more stable than their intermediates such as $Na_2Li[AlH_2(NH_2BH_3)_4]$ and $Na_3[AlH_2(NH_2BH_3)_4]$. Besides, it is crucial to avoid the formation of $M[BH_3NH_2BH_2NH_2BH_3]$ (M = Li and Na) and the decomposition of M_3AlH_6 to successfully obtain the desired compounds in a pure form. To address these challenges, the following potential solutions can be explored in future synthesis attempts:

i. Utilizing MNH_2 instead of MH throughout the synthesis process to prevent undesired reactions between MH and NH_3BH_3.

ii. Implementing a pretreatment step for M_3AlH_6 under a high-pressure hydrogen atmosphere to enhance its stability.

iii. Selecting more stable alternatives than Na_2LiAlH_6 or Na_3AlH_6.

By considering these alternative approaches, we aim to overcome the hurdles encountered in synthesizing the desired compounds and further

advance the development of six-coordinated Al-based amidoborane compounds.

The positive impact of introducing -CH_3 and -CH_2CH_2- groups in the amidoborane anions has been investigated and confirmed in terms of enhancing hydrogen purity and decreasing the thermal decomposition temperature. However, our study on the thermal properties of these new compounds is limited due to the limited availability of differential scanning calorimetry (DSC) equipment to study compounds producing corrosive gases. Nevertheless, understanding the thermal behavior is crucial as it indicates the reversibility of these new compounds for hydrogen storage. Therefore, it is necessary to further investigate and compare effects of -CH_3 and -CH_2CH_2- on the heats involved in the decomposition of metal amidoboranes. It is predicted that electron-donating groups connected to the nitrogen atom and electron-withdrawing groups attached to the borane moiety of ammonia borane can decrease the exothermicity if not making the thermal decomposition endothermic. As a result, the newly obtained compounds from $CH_3NH_2BH_3$ and $BH_3NH_2CH_2CH_2NH_2BH_3$ in this thesis may exhibit thermal neutrality during their decomposition, which is advantageous for their re-hydrogenation. Future research should focus on exploring and characterizing the heats of decomposition and the hydrogen desorption reversibility of these compounds. Also, building upon the findings presented in Chapter 4, it is worthwhile to explore hydrogen storage properties (including reversibility) of reactive hydride composites based on our newly synthesized compounds.

To further investigate the impact of substituents on the hydrogen storage properties of metal amidoboranes, the phenyl group represents another viable candidate. Similar to -CH_3 and -CH_2CH_2-, the phenyl group also functions as a weak electron-donating group. However, in contrast to -CH_3 and -CH_2CH_2-, the phenyl group offers additional versatility, allowing for the synthesis of diverse analogues, as depicted in Figure 8.1. Based on current research, the introduction of weak electron-donating groups on nitrogen atoms has demonstrated a positive effect on hydrogen storage properties. This prompts the question of whether strong electron-donating groups, such as -OCH_3, could also be utilized for optimizing hydrogen storage performance. Additionally, it is worth exploring the potential of -CH_3, -CH_2CH_2-, phenyl, and

-OCH_3 groups in enhancing the hydrogen storage capabilities of other multi-metallic amidoborane complexes, including those based on Li, Mg, and Ca. By investigating the effects of these various substituents, we can gain a deeper understanding of their influence on hydrogen storage performance and potentially identify novel strategies for designing advanced hydrogen storage materials.

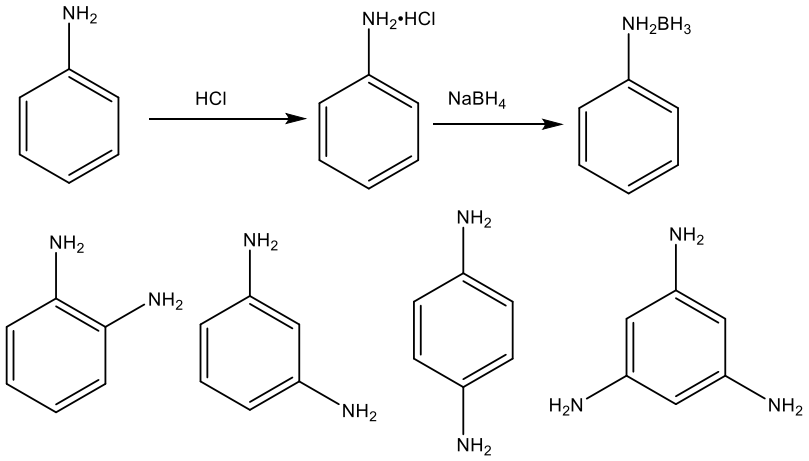

Figure 8.1 Synthesis of $PhNH_2BH_3$ and related compounds.

Annex

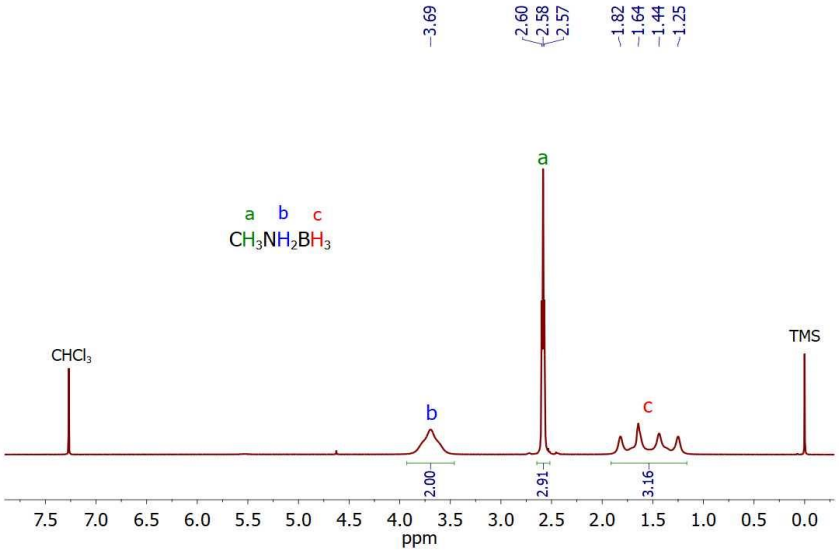

Figure S1 ^{1}H NMR spectrum of $CH_3NH_2BH_3$.

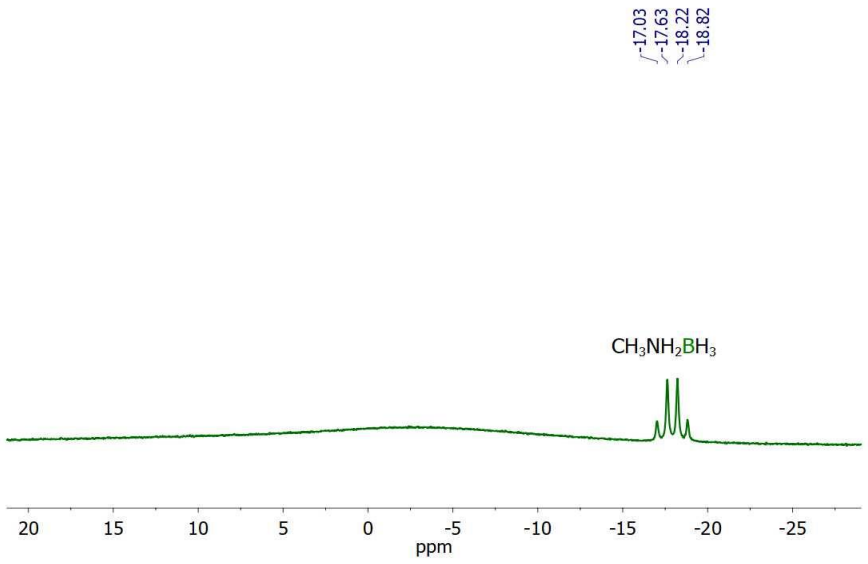

Figure S2 ^{11}B NMR spectrum of $CH_3NH_2BH_3$.

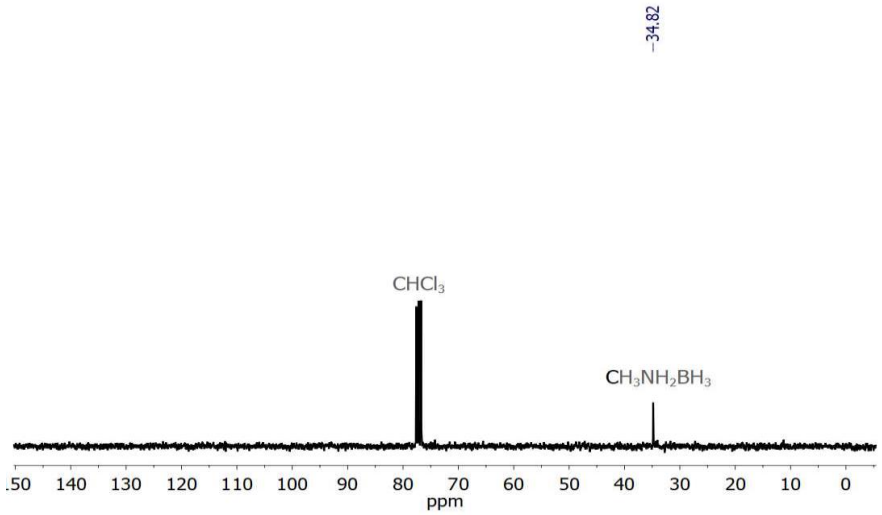

Figure S3 ^{13}C NMR spectrum of $CH_3NH_2BH_3$.

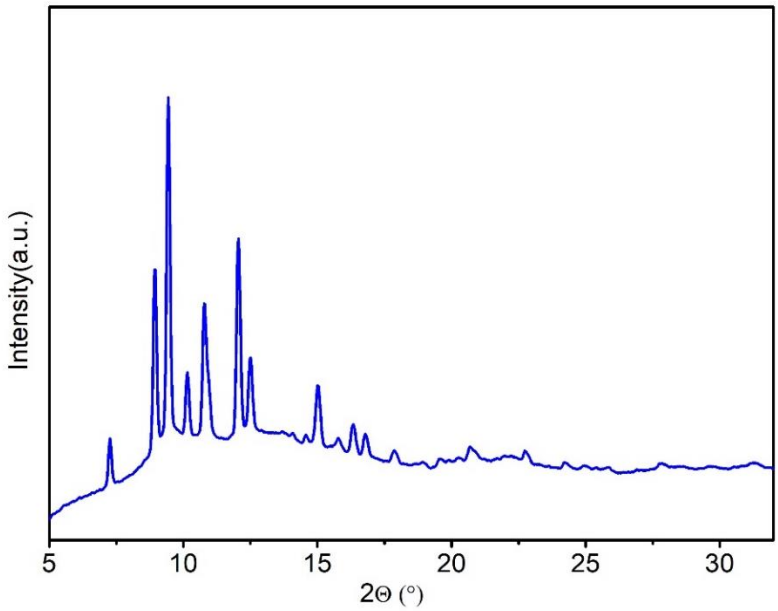

Figure S4 PXRD pattern of $CH_3NH_2BH_3$ (λ = 0.71073 Å).

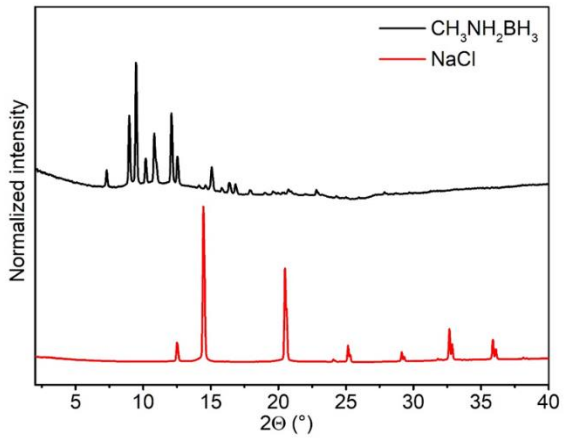

Figure S5 PXRD pattern of $CH_3NH_2BH_3$ and NaCl (λ = 0.71073 Å).

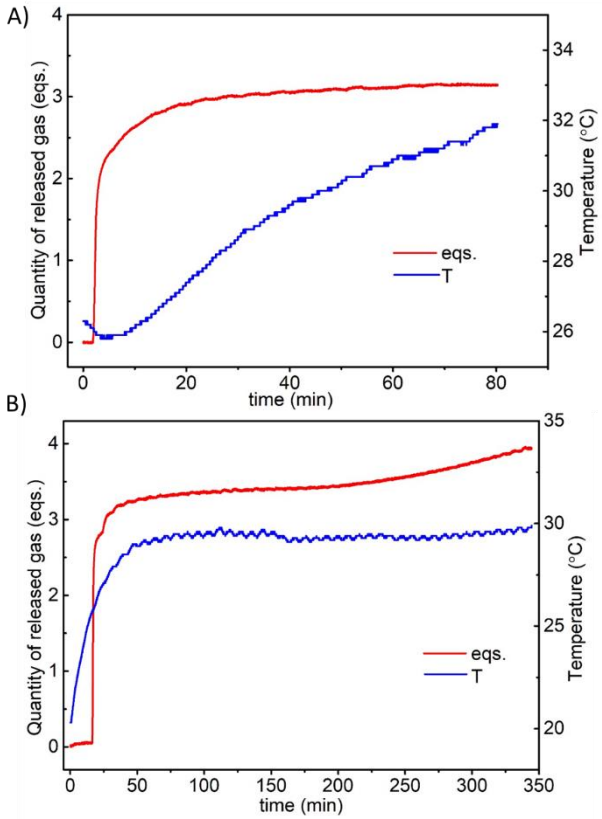

Figure S6 The quantity of gas per Al released and temperature during the synthesis of $Na[AlH(CH_3NHBH_3)_3]$ (A) and $Na[Al(CH_3NHBH_3)_4]$ (B).

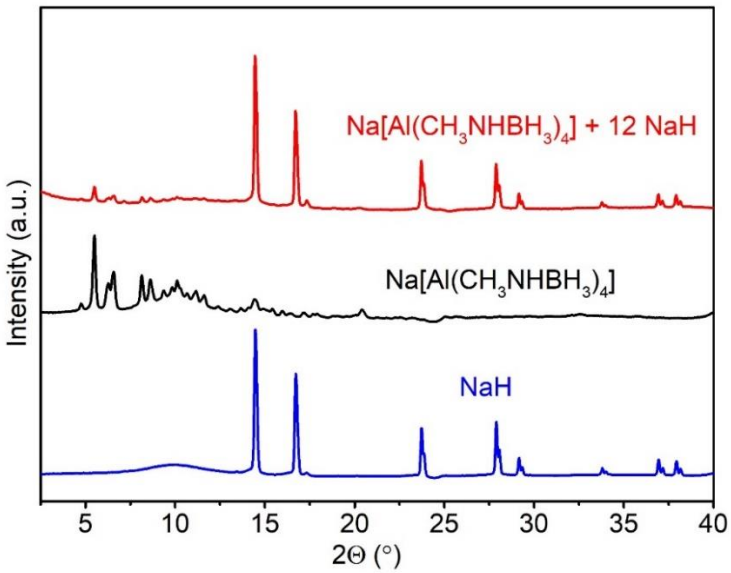

Figure S7 PXRD patterns of $Na[Al(CH_3NHBH_3)_4]$+ 12NaH, $Na[Al(CH_3NHBH_3)_4]$, and commercial NaH.

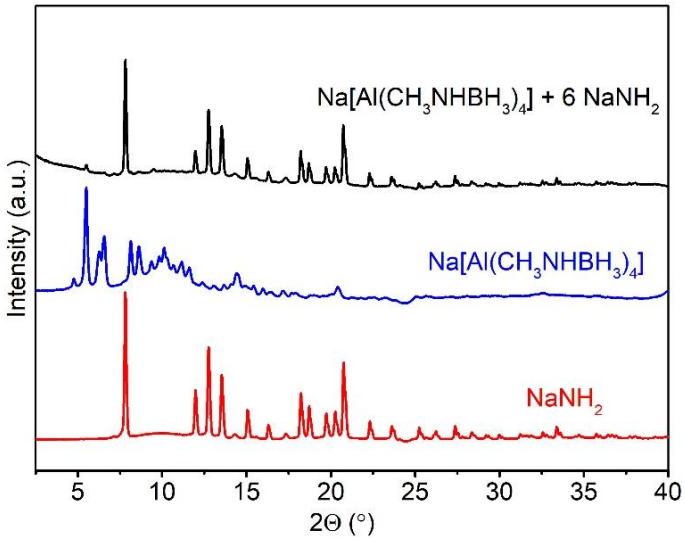

Figure S8 PXRD patterns of $Na[Al(CH_3NHBH_3)_4]$+ $6NaNH_2$, $Na[Al(CH_3NHBH_3)_4]$, and commercial $NaNH_2$.

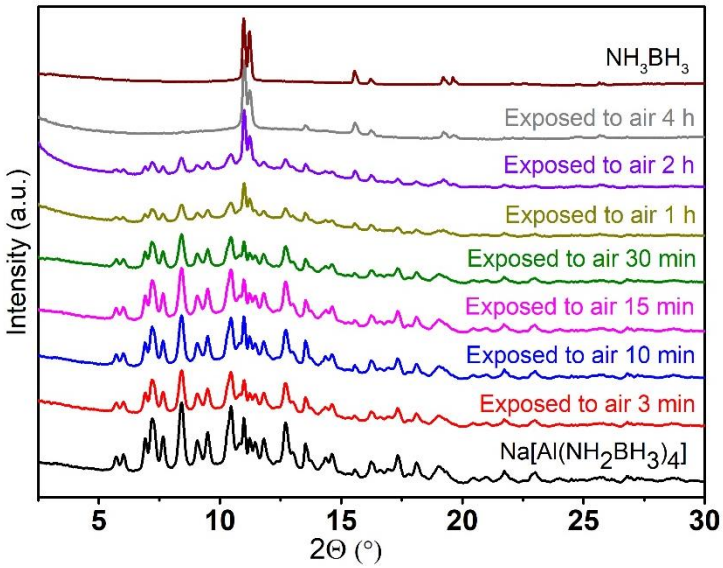

Figure S9 PXRD patterns of NH_3BH_3, $Na[Al(NH_2BH_3)_4]$, and $Na[Al(NH_2BH_3)_4]$ exposed to air for different duration (λ = 0.71073 Å).

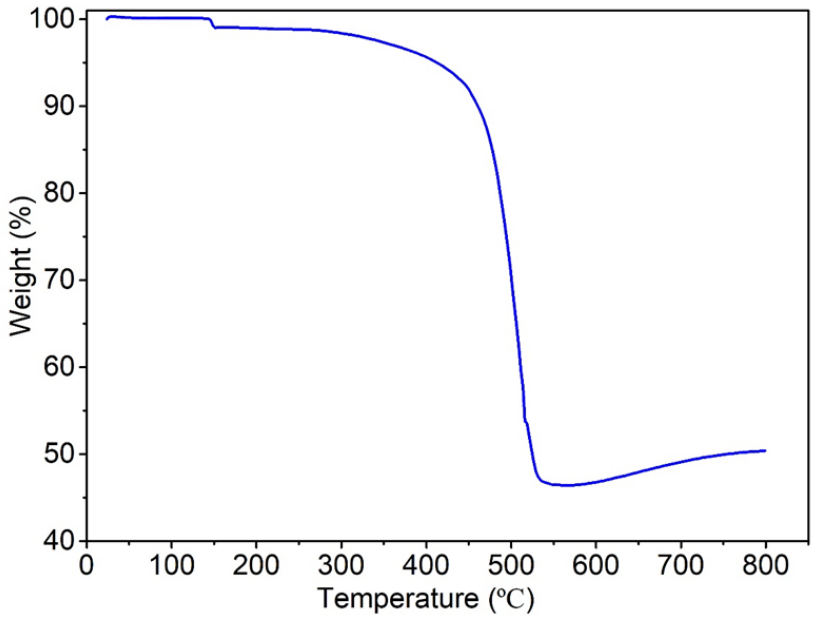

Figure S10 TGA curve of commercial $NaNH_2$.

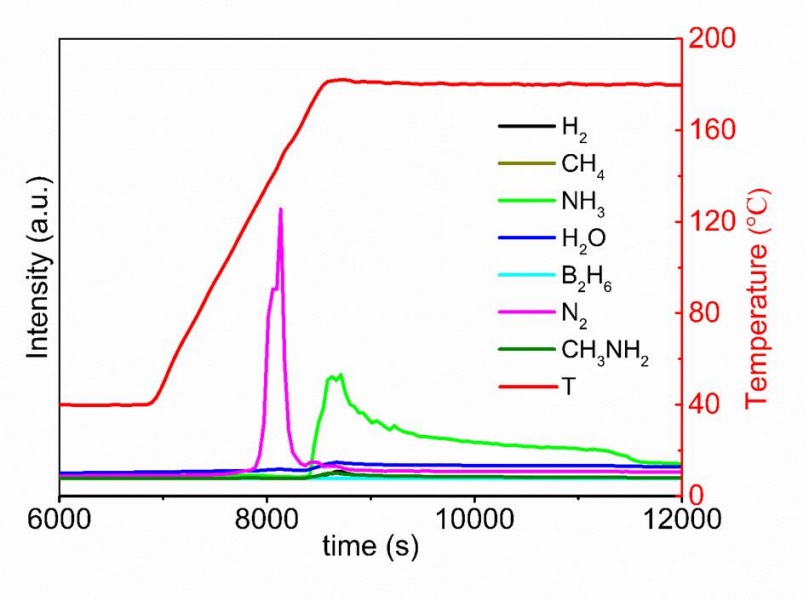

Figure S11 MS spectra of commercial $NaNH_2$.

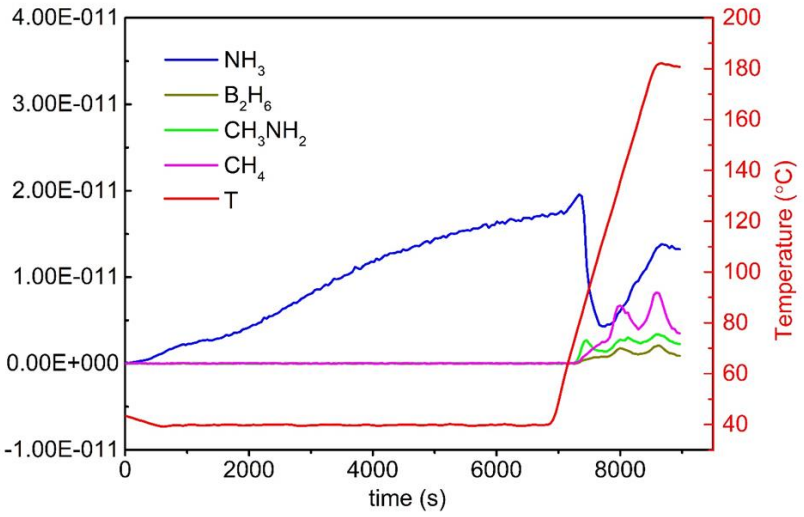

Figure S12 Zoom in the non-H_2 MS curve of $Na[Al(CH_3NHBH_3)_4]$ + 12NaH.

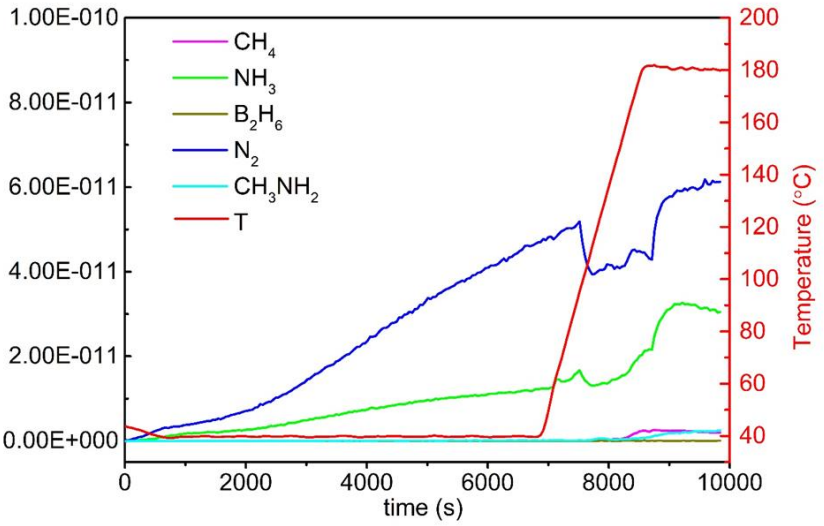

Figure S13 Zoom in the non-H_2 MS curve of $Na[Al(CH_3NHBH_3)_4]$ + $6NaNH_2$.

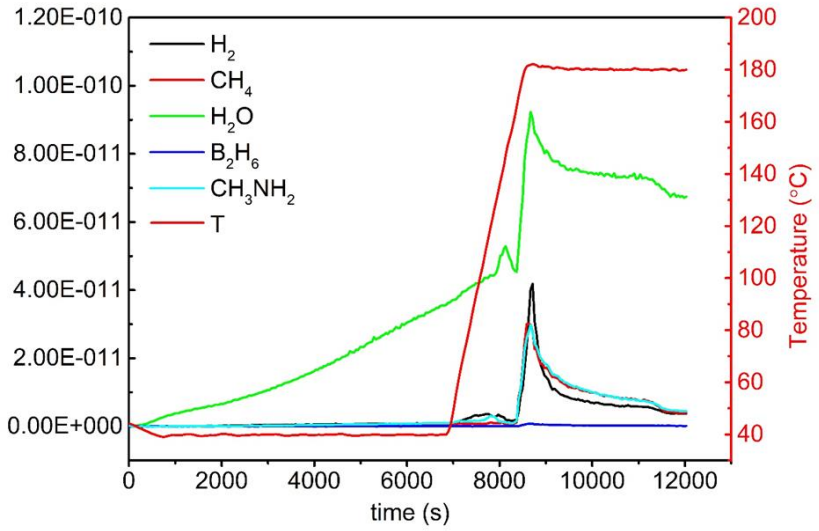

Figure S14 Zoom in the non-N_2 and NH_3 MS curve of commercial $NaNH_2$.

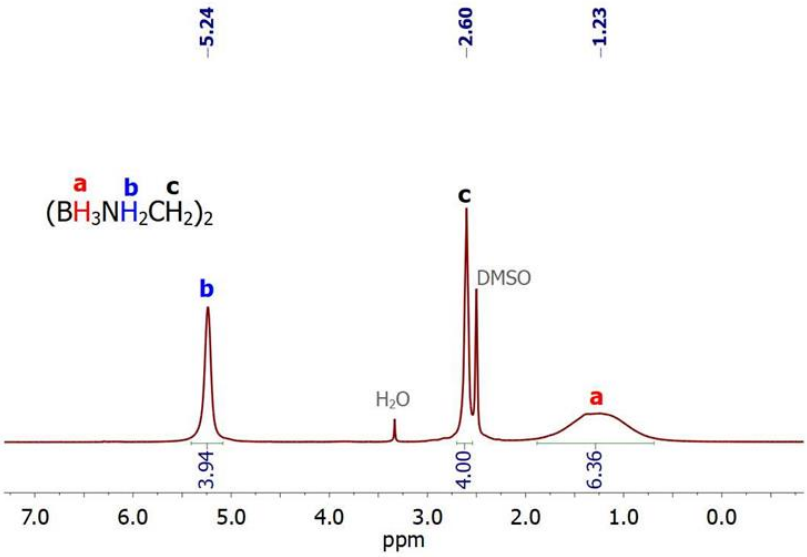

Figure S15 ^{1}H NMR spectrum of EDAB.

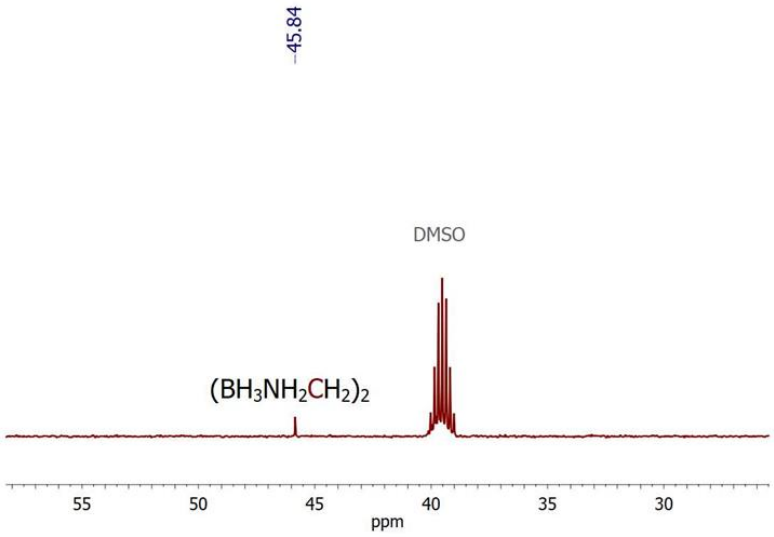

Figure S16 ^{13}C NMR spectrum of EDAB.

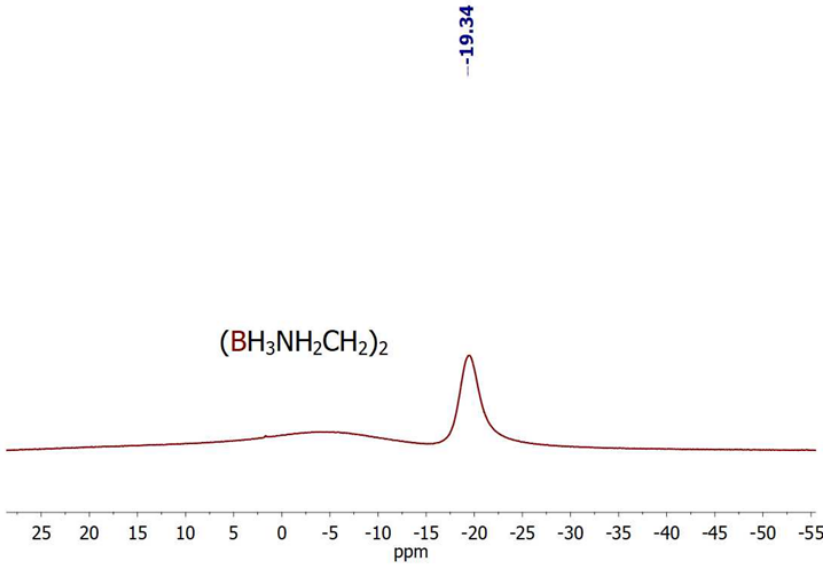

Figure S17 ^{11}B NMR spectrum of EDAB.

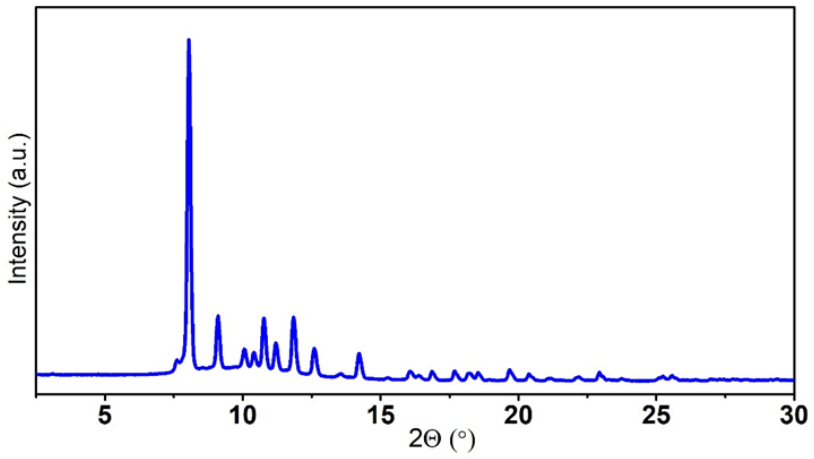

Figure S18 PXRD pattern of EDAB (λ = 0.71073 Å).

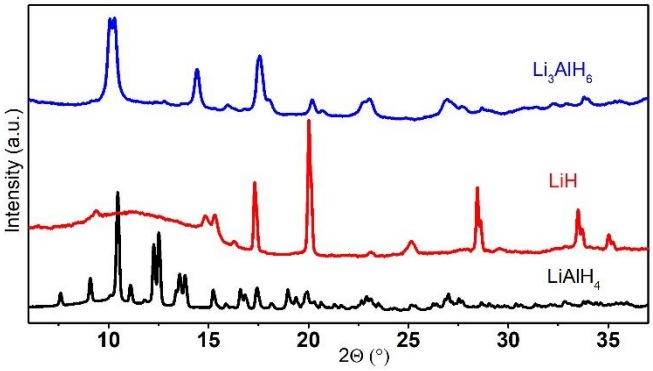

Figure S19 PXRD of Li_3AlH_6, LiH and $LiAlH_4$(λ = 0.71073 Å).

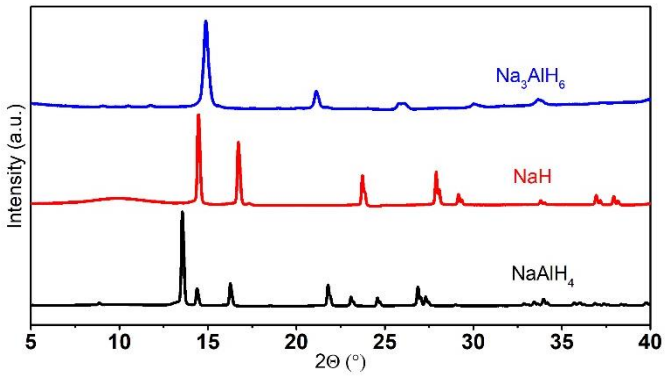

Figure S20 PXRD of Na_3AlH_6, NaH and $NaAlH_4$(λ = 0.71073 Å).

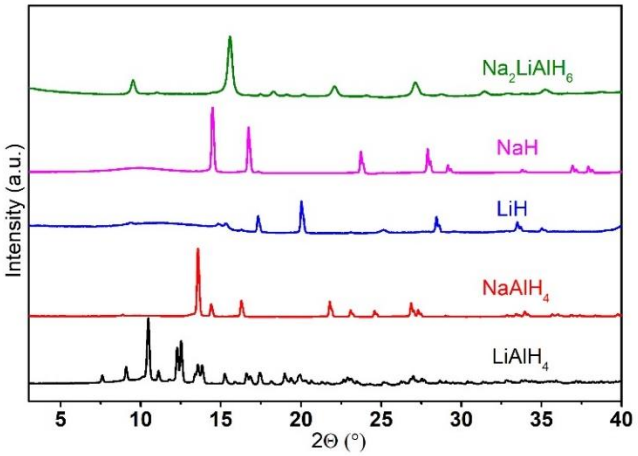

Figure S21 PXRD of Na_2LiAlH_6, NaH, LiH, $NaAlH_4$ and $LiAlH_4$(λ = 0.71073 Å).

Table S1 Calculated elemental content in $Li[Al(BH_3NHCH_2CH_2NHBH_3)_2]$.

M (g/mol)	Mass of B (%)	Mass of N (%)	Mass of C (%)	Mass of H (%)	Mass of H (excluding H on carbon) (%)
205.4	21.0	27.3	23.4	11.8	7.8

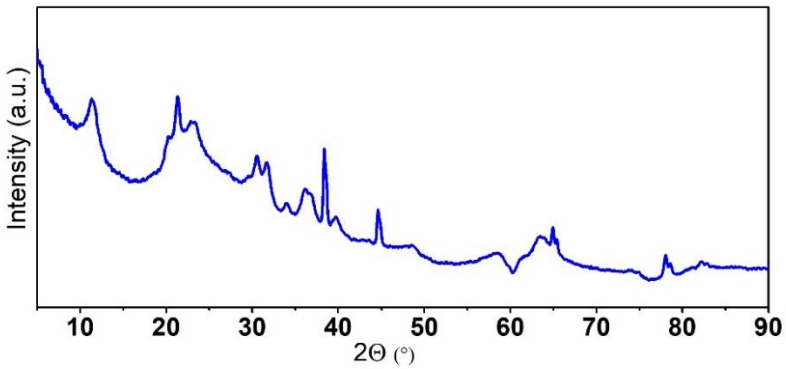

Figure S22 PXRD pattern of product(s) of $LiAlH_4$ exposed to air (λ = 0.71073 Å).